Controlling flexural waves using subwavelength perfect absorbers : application to Acoustic Black Holes

Julien Leng

UNIVERSITE BRETAGNE SCIENCES LOIRE POUR L'INGENIEUR

Le Mans Université

THESE DE DOCTORAT

LE MANS UNIVERSITE

COMUE UNIVERSITE BRETAGNE LOIRE

ECOLE DOCTORALE N° 602
Sciences pour l'Ingénieur
Discipline : 60
Spécialité : Acoustique

Julien LENG

Controlling flexural waves using subwavelength perfect absorbers: Application to Acoustic Black Holes

Manuscrit de soutenance
Unité de recherche : Laboratoire d'Acoustique de l'Université du Mans (LAUM, UMR CNRS 6613)
Thèse n° : 2019LEMA1027

Soutenance envisagée le 5 novembre 2019 sous réserve de l'autorisation des rapporteurs

Rapporteurs :	**Morvan OUISSE**	Pr. – Université Bourgogne Franche-Comté (Besançon, France)
	Olga UMNOVA	Reader – University of Salford (Salford, Royaume-Uni)
Examinateurs :	**Philippe ROUX**	D. R. CNRS – Institut des sciences de la Terre (Grenoble, France)
	Sergei SOROKIN	Pr. – Aalborg University (Aalborg, Danemark)
Directeur :	**François GAUTIER**	Pr. – Le Mans Université (Le Mans, France)
Co-directeur :	**Ruben PICO**	Pr. – Universitat Politècnica de València (Gandia, Espagne)
Co-encadrant :	**Vicent ROMERO-GARCIA**	C. R. CNRS – Le Mans Université (Le Mans, France)
Co-encadrant :	**Adrien PELAT**	M. C. – Le Mans Université (Le Mans, France)

Académie de Nantes

Le Mans Université, France
École doctorale Sciences Pour l'Ingénieur

Doctoral Thesis

Controlling flexural waves using subwavelength perfect absorbers: application to Acoustic Black Holes

by:

Julien Leng

A thesis submitted in partial fulfilment of the requirements for the degree of Doctor of Philosophy in Acoustics in the Acoustics Laboratory of Le Mans University UMR CNRS 6613

Defended on the 5th November 2019, subject to the authorisation of the reviewers, in front of the examining committee:

M. Ouisse	Pr. (Université Bourgogne Franche-Comté)	Reviewer
O. Umnova	Reader (University of Salford)	Reviewer
P. Roux	D. R. CNRS (Institut des Sciences de la Terre)	Examiner
S. Sorokin	Pr. (Aalborg University)	Examiner
F. Gautier	Pr. (Le Mans Université)	Supervisor
R. Pico	Pr. (Universitat Politècnica de València)	Co-supervisor
V. Romero-Garcia	C. R. CNRS (Le Mans Université)	Co-supervisor
A. Pelat	M. C. (Le Mans Université)	Co-supervisor

Abstract

The development of vibration control methods adapted to light structures is a scientific and technological challenge over past decades due to increasingly stringent economic and ecological standards. The classical passive solutions for vibration damping usually rely on adding mass into structures, therefore conflicting with the lightweight issues.

Meanwhile, recent promising studies in audible acoustics have focused on broadband wave absorption at low frequencies by means of subwavelength perfect absorbers. Their design requires the fulfilment of two conditions: (i) increasing the density of states at low frequencies by using local resonators, and (ii) matching the impedance with the background medium by controlling the ratio between the inherent losses of the resonator and the leakage of energy due to the aperture of the resonator to the propagating medium. Particularly, the impedance matching corresponds to the situation in which the amount of inherent losses in the resonator equals the amount of energy leakage, and is known as the critical coupling condition. Such absorbers have proven effective for the total absorption of the energy of an incident wave by audible acoustic metamaterials, and a generalisation of the method to elastodynamics fields could be of great interest to comply with the conflicting requirements for the vibration control of light structures.

This thesis aims at adapting the problem of perfect absorption for flexural waves in 1D and 2D systems with local resonators by using the critical coupling condition. First, 1D systems with simple geometries are studied to prove the efficiency of the method for flexural waves. This first preliminary study aims at opening up new avenues to the design of simple resonators for efficient flexural wave absorption, showing also the limits of absorption induced by the geometry used in the study. The 1D systems are then complexified by considering the study of the critical coupling of 1D Acoustic Black Holes resonators. This motivated its interpretation via the concept of critical coupling in order to provide the key features to future optimisation procedures of such a type of termination. Then, the 1D perfect absorbers are extended to 2D, extending the formalism of the critical coupling condition to 2D systems. The perfect absorption of the first axisymmetric mode of a circular resonator embedded in an infinite thin plate is firstly analysed. The multiple scattering of 2D systems is analysed to consider configurations close to practical applications. To that end, an infinite array of penetrable and dissipative circular scatterers, embedded in an infinite or semi-infinite 2D thin plate, i.e. a metaplate, is considered. Through this thesis, analytical models, full wave numerical simulations and experiments are used to validate the physical behavior of the presented systems, showing good agreement between them.

Keywords: Passive wave control, Flexural waves, Metamaterial, Locally resonant structure, Perfect absorption, Critical coupling, Acoustic Black Hole.

Résumé

Le développement de méthodes de contrôle des vibrations à basse fréquence adaptées aux structures légères est un défi scientifique et technologique des dernières décennies en raison des contraintes économiques et écologiques de plus en plus strictes. Les solutions passives classiques pour l'amortissement des vibrations reposent généralement sur l'ajout de masse dans les structures, ce qui va à l'encontre des problèmes d'allègements.

Parallèlement, de récentes études prometteuses dans le domaine de l'acoustique audible se sont concentrées sur l'absorption large bande des ondes à basse fréquence au moyen d'absorbeurs parfaits sub-longueurs d'onde. Leur conception nécessite de remplir deux conditions générales : (i) augmenter la densité d'état à basse fréquence en utilisant des résonateurs locaux, et (ii) adapter l'impédance au milieu de propagation en contrôlant le rapport entre les pertes inhérentes du résonateur et les fuites d'énergie dues à l'ouverture du résonateur vers le milieu de propagation. En particulier, l'adaptation d'impédance correspond à la situation dans laquelle la quantité de perte inhérente dans le résonateur est égale à celle des fuites d'énergie, et est connue sous le nom de condition de couplage critique. Ces absorbeurs ont prouvé leur efficacité pour l'absorption totale de l'énergie d'une onde incidente par des métamatériaux en acoustique audible, et une généralisation de la méthode pour le domaine élastodynamique pourrait être d'un grand intérêt pour répondre aux exigences contradictoires du contrôle des vibrations des structures légères à basse fréquence.

Cette thèse vise à adapter le problème d'absorption parfaite des ondes de flexion dans des systèmes 1D et 2D avec des résonateurs locaux en utilisant la condition de couplage critique. Les systèmes étudiés sont complexifiés progressivement pour comprendre pas à pas les principaux mécanismes physiques de l'absorption parfaite de l'énergie des ondes de flexion. Les systèmes 1D à géométries simples sont d'abord étudiés pour prouver l'efficacité de la méthode pour les ondes de flexion. Cette première étude préliminaire vise à ouvrir de nouvelles voies à la conception de résonateurs simples pour une absorption efficace des ondes de flexion, et montre également les limites d'absorption induites par la géométrie utilisée dans ce type d'étude. Les systèmes 1D sont ensuite complexifiés en considérant l'étude du couplage critique de Trou Noir Acoustique (TNA) 1D. Ceci a motivé l'interprétation de l'effet TNA à l'aide du concept de couplage critique afin de présenter des outils clés à de futures procédures d'optimisation pour ce type de terminaisons. Le formalisme de condition de couplage critique est ensuite étendu aux systèmes 2D. L'absorption parfaite du premier mode axisymétrique d'un résonateur circulaire inséré dans une plaque mince infinie est d'abord analysée. La diffusion multiple des systèmes 2D est analysée pour considérer des configurations plus réalistes, proches d'une application industrielle. Pour cela, une infinité de diffuseurs circulaires pénétrables insérés dans une plaque mince 2D infinie ou semi-infinie,

appelée métaplaque, est alors considérée. A travers cette thèse, des modèles analytiques, des simulations numériques et des expériences, montrant un bon accord entre eux, sont présentés afin de valider le comportement physique des systèmes présentés.

Mots clés: Contrôle passif d'onde, Absorption parfaite, Onde de flexion, Couplage critique, Métamatériau, Trou Noir Acoustique, Structure localement résonante.

Remerciements

Ces travaux de thèse n'ont pu être possible sans la présence et le soutien d'un grand nombre de personnes que je souhaite vivement remercier dans les paragraphes suivants. Toutes ces personnes font partie intégrante de cette thèse à mes yeux, et ont grandement contribué à la très riche expérience que j'ai vécue et aux rencontres que j'ai pu faire.

Je suis tout d'abord honoré d'avoir pu présenter ces travaux de thèse devant le jury présent lors de la soutenance. Je souhaite vivement remercier Olga Umnova et Morvan Ouisse pour l'intérêt qu'ils ont porté à ce travail en acceptant de le rapporter. Je remercie également Sergey Sorokin et Philippe Roux d'avoir assisté à la présentation de ce travail en tant qu'examinateurs. Je remercie particulièrement Philippe Roux d'avoir présidé le jury le jour de la soutenance, mais aussi d'avoir accepté de faire partie de mon Comité de Suivi Individuel lors de ces 3 années. Je remercie sincèrement son écoute, ses remarques et ses conseils lors de chaque comité.

Ces travaux ont été effectués au sein du Laboratoire d'Acoustique de l'Université du Mans (LAUM), dont je tiens à remercier les directeurs Joël Gilbert (directeur jusqu'en 2016) et Pierrick Lotton (directeur actuel), ainsi que tous les membres. Mes remerciements vont également à Le Mans ACoustique (LMAC) pour avoir accordé les financements permettant de réaliser cette thèse de doctorat. Je remercie particulièrement Jana Le Coz, assistante de direction à LMAC, d'avoir mis à disposition tous les moyens nécessaires pour financer mes déplacements et le matériel pour les travaux expérimentaux. J'ai pu travailler et m'épanouir quotidiennement à l'Ecole Nationale Supérieure d'Ingénieurs du Mans (ENSIM) où mon bureau se situait. Je remercie ainsi Pascal Leroux (directeur jusqu'en 2018) qui m'y a accueilli, Jean-François Tassin (directeur actuel) et tous les membres de l'ENSIM. J'adresse aussi mes remerciement à Mathieu Secail-Geraud pour m'avoir formé à l'utilisation du matériel expérimental et pour ses conseils, à Julien Nicolas pour l'usinage des pièces. Je remercie également l'Universitat Politècnica de València (UPV) de m'avoir accueilli lors de deux séjours très enrichissants à Gandia.

J'ai pu effectuer 3 ans d'enseignement durant cette thèse. J'ai ainsi eu l'occasion d'intégrer l'équipe d'enseignement en Licence Science Pour l'Ingénieur et à l'ENSIM. Je remercie particulièrement Laurent Simon, Bertrand Lihoreau, Christophe Ayrault, Frédéric Ablitzer, Omar Aklouche et Justine Carpentier avec qui j'ai pu collaborer et qui ont beaucoup apporté à mon expérience, à ma vision de l'enseignement et qui ont attisé mon goût à cette discipline.

Je souhaite remercier chaleureusement ma direction de thèse pour la confiance qu'ils m'ont accordée tout au long de ces 3 années. Je remercie François Gautier pour son accompagnement et ces conseils à travers nos discussions lors de réunions de travail qui m'ont été précieux. Je

tiens aussi à remercier son soutien lors de la dernière ligne droite de la thèse qui m'a permis de fournir les derniers efforts nécessaires pour conclure ces travaux. Je remercie également Adrien Pelat pour son implication et ses conseils qui ont contribué à l'aboutissement de cette thèse. Je remercie particulièrement son accueil et son implication lors de mon installation à l'ENSIM. Un grand merci à Rubén Picó Vila pour son enthousiasme à chaque réunion et nos discussions scientifiques très enrichissantes. Je n'oublierai jamais l'incroyable accueil que Rubén et sa femme Eva m'ont accordé à bras ouverts, ainsi que leur bienveillance, lors de mes séjours à Gandia. Les discussions journalières que j'ai pu avoir seul à seul avec Rubén, aussi bien d'une heure que de dix minutes, sur des points scientifiques ou sur mon quotidien à Gandia, m'ont permis d'évoluer dans les meilleures conditions possible au sein de l'UPV. Je tiens aussi à adresser mes remerciements à Jean-Philippe Groby dans ce paragraphe dédié à ma direction de thèse. Malgré le fait que son nom n'y soit pas inscrit officiellement, il fait partie intégrante de la direction de cette thèse à mes yeux. Merci à Jean-Philippe pour sa disponibilité, son soutien et toutes ces discussions scientifiques qui m'ont été plus que précieux pour aboutir à cette thèse. Il a aussi su trouver les mots pour me réconforter et pour me redonner de la force lors d'une période de remise en question et de doute de ma part. Je lui adresse pour cela mes plus sincères remerciements. Enfin, je souhaite remercier du fond du coeur Vicent Romero García pour tout ce qu'il a apporté dans cette thèse. Je serai à jamais reconnaissant de son entière implication et sa disponibilité du début jusqu'à la fin de cette thèse. Sa présence constante à chaque réunion ainsi que nos séances de travail seul à seul, où il a pu apporter de nombreux et précieux conseils, m'ont permis de garder cette rigueur scientifique tout au long de la thèse, et de me dépasser au quotidien. Vicent m'a aussi prouvé qu'une thèse ne se résume pas uniquement à de la science, mais est aussi une expérience humaine. Je souhaite exprimer ma profonde reconnaissance pour nos discussions sur mon avenir, ainsi que ses encouragements et son soutien lors de moments personnels difficiles.

Mon expérience en thèse n'aurait pas été la même sans les doctorants que j'ai pu cotoyer à l'ENSIM. Je remercie les "vieux" : Océane, Sylvain, Antoine,Omar, Justine, Torea, Thibault, Jules et Paul, mais aussi les "nouveaux", à savoir Guillaume, Jean-Baptiste, Erwan, Erwan et Meryem, pour leur sourire et l'animation qu'ils apportent dans la vie de laboratoire à l'ENSIM. Un merci à mes collègues de bureau : Justine, Torea et Jules avec qui j'ai pu partager des moments drôles et réconfortants au quotidien. Mes remerciements vont aussi à Paul qui a toujours su être à mon écoute, et avec qui j'ai partagé les mêmes moments, aussi bien joyeux que difficiles, de cette thèse. Nos séjours en congrès resteront de très bons souvenirs pour moi. Je remercie également les doctorants du côté de "l'UFR" : Samuel et Matthieu pour leur soutien.

Cette thèse a été ponctuée par une rencontre, celle avec Becci, qui a su m'accompagner au quotidien et partager les épreuves que j'ai traversées durant cette thèse. Le réconfort quotidien qu'elle a su m'apporter à travers sa patience, son sourire, sa bonne humeur et son soutien ont un prix inestimable à mes yeux. Je ne peux que la remercier infiniment.

Je remercie enfin ma famille : mes parents, mon frère Jérôme et ma soeur Johanna qui m'ont toujours entièrement soutenu dans tout ce que j'ai entrepris. Je remercie particulièrement mes parents pour toutes les valeurs qui m'ont inculqué et qui font que j'écris aujourd'hui ces lignes.

Encore merci à vous tous.

Table of contents

Chapter 1

Introduction

1.1 Challenges of vibration control for light structures

Weight reduction of structures is an important concern in the engineering domain. The european transport industry is one example through its more stringent carbon emission standards, imposed by the European Union's objective to further reduce CO_2 emissions through vehicle technology. These measures have obliged manufacturers to change their way of designing vehicles. The fuel consumption of a vehicle, and so its CO_2 emissions, is directly related to its mass: a heavy vehicle would need to consume more fuel to overcome forces resisting vehicle motion during a driving cycle than a lighter one. However, the lightening of the structure may be accompanied by an increase of vibration amplitude, which may be a source of structural damage as well as noise radiation. This structural damage usually corresponds to fatigue failures which are due to stresses coming from the dynamic loads of vibration on the structure. The loads do not necessarily need to stress the components above their yield point to cause damages, however a high number of cycles of vibration is sufficient to cause a mechanical failure. Noise radiation may be an even more significant problem as it may create undesirable effects on people and their hearing [1, 45]. This issue is therefore also a health concern: noise radiation may lead to a variety of effects including annoyance, reduced cognitive performance, sleep disturbance and hearing loss of those who are exposed to it [45]. The mitigation of the vibration amplitude to avoid all these inconveniences is nevertheless difficult to reconcile with the problematic of weight reduction, showing that the development of vibration control methods adapted to light structures is a crucial issue.

1.2 Overview of common methods for vibration control

The usual ways to control vibrations rely on active, semi-active or passive methods [151]. The physical mechanisms used in each of them are various and clearly different, but they can be grouped into few categories:

— changing the stiffness or mass of the structure in order to shift its resonance frequencies out of the range of the source frequency,
— reducing the vibration amplitude of the structure at its resonance frequencies,
— Adding secondary sources to mitigate the primary one by using destructive interferences.

This section aims at introducing the various damping methods. In particular, active and semi-active damping methods are briefly described below since this dissertation focuses only on passive damping methods. The description of the systems in this section is done according to three frequency ranges from the vibration point of view: the low, medium and high frequency ranges. Such frequencies ranges in vibration are not easy to define. However, a delimitation between each range can be made for any complex system by looking at the behaviour of its transfer function [136]. The low frequency range is characterised by a distinct resonant behaviour of the system with sharp and well defined resonance peaks in its transfer function. In the intermediary range, also called medium frequency range, the transfer function is sligthly smoothed and local groups of resonance peaks are observed due to the increase of the modal overlap. In the high frequency range, a smooth behaviour of the transfer function is commonly noticed and the diffuse field assumptions are reached. These ranges can also be delimited using the Modal Overlap Factor (MOF), which is defined as the ratio between the modal bandwidth at half amplitude $\Delta_{\text{-3dB}}$ and the average modal spacing between two consecutive modes Δf_n:

$$\text{MOF} = \frac{\Delta_{\text{-3dB}}}{\Delta f_n}. \tag{1.1}$$

The frequency ranges in vibrations may therefore be delimited as follows [54]:

— MOF $< 30\%$: the low-frequency range in which the structure admits a resonant behaviour,
— $30\% <$ MOF $< 100\%$: the mid-frequency range in which the modal overlap is higher,
— $100\% <$ MOF: the high-frequency range in which diffuse field assumptions are reached.

1.2.1 Active and semi-active control methods

Active damping methods are implemented by bonding piezoelectric transducers to a flexible structure using strong adhesive materials. These transducers can be used as actuators, sensors, or both. The transducers, when used as actuators strain when exposed to a voltage, and inversely produce a voltage when strained as sensors. A typical active damping method consists of applying a voltage to the actuator to minimise the unwanted vibration of the structure [9, 149]. The voltage is controlled by a sensor which is most of the time identical to the actuator and collocated on the structure to measure its vibration. The method has been developed for beams [60] and thin plates [58] and applications on reduced noise radiation [111] or vehicles have been proposed [56, 150], among others.

The semi-active damping methods, also known as piezoelectric shunt-damping, use piezoelectric transducers which are shunted by a passive electric circuit that dissipates mechanical energy of the structure. The difference between active and semi-active methods is that no active control of the voltage is performed in semi-active method. The pioneering work of Hagood and Von Flotow [87] showed that a single shunted piezo-electric patch simply made of a single resistance (resistive circuit shunting) or a serie RL circuit (resonant circuit shunting) can be used to dissipate the mechanical energy of a structure at one given frequency. Numerous works have then presented analysis of the efficiency of such systems for wave cancellation at a given frequency [46, 49], and methods of optimisation [13, 142] have been proposed. The extension over broader frequency bands has also been developed by complexifying the shunting circuits [14, 15, 194], and has been applied to beam [12], thin plate [34] and plate [29] systems.

The main interest of active and semi-active damping methods relies on the possibility to tune the parameters according to the frequency. However, their implementation requires a large number of active elements inducing substantial design costs and sometimes maintenance issues, which restricts their industrial implementation.

1.2.2 Passive damping methods

a) Intrinsic damping

As a structure vibrates, forces appear in the material, resulting in losses by heat dissipation and therefore to vibration damping. This dissipation can be characterised for a given material by a loss factor η. More precisely, η expresses the delay between stress and strain. Hence, the Hooke's law at the time t and in the formalism $e^{-i\omega t}$ reads as:

$$E = \frac{\sigma_0}{\epsilon_0 e^{i\eta}} = E_0 e^{-i\eta}, \qquad \eta > 0,$$

where E is the complex Young's modulus describing the damping properties of the material, σ_0 the force applied to the material, ϵ_0 its related strain, and the ratio σ_0 over ϵ_0 corresponds to the storage modulus or the lossless Young's modulus E_0 which describres the stiffness of the material. This complex Young's modulus is also used in another form which is obtained by applying the Taylor expansion of $e^{-i\eta}$ and by assuming low damping, such that:

$$E = E_0(1 - i\eta),$$

where the real part of E represents the elastic effect and the imaginary part represents the dissipation. The damping representation by means of a complex Young's modulus has been first introduced by Myklestad [131] and is now widely used to characterise and quantify damping properties of materials. A way to effectively reduce the vibration amplitude of a structure by using its intrinsic properties would consist in choosing materials with a high damping factor η. Unfortunately, most of materials having a high damping factor have also a weak storage modulus and vice-versa. Materials with good intrinsic damping properties are therefore soft, which limits their industrial implementation where materials with a good mechanical strength are sought. This relation between E_0 and η can be depicted in the form of an Ashby diagram as shown in Fig. 1.1. Such a type of diagram is a scatter plot of materials according to two or more properties [7], and is useful to compare the ratio between different properties for the materials selection in mechanical design. The materials located at the top-left of the diagram in Fig. 1.1 correspond to soft material with high loss factor ranging from polymeric foams to elastomers whereas materials located at the bottom-right correspond to stiff material with low loss factor such as ceramics and alloys.

b) Viscoelastic materials

Another way to take advantage of the intrinsic damping property of materials is to apply add-on type damping, which consists of gluing a viscoelastic material with a high loss factor on one side of the structure (Fig. 1.2). The bending of the structure produces extensional strains

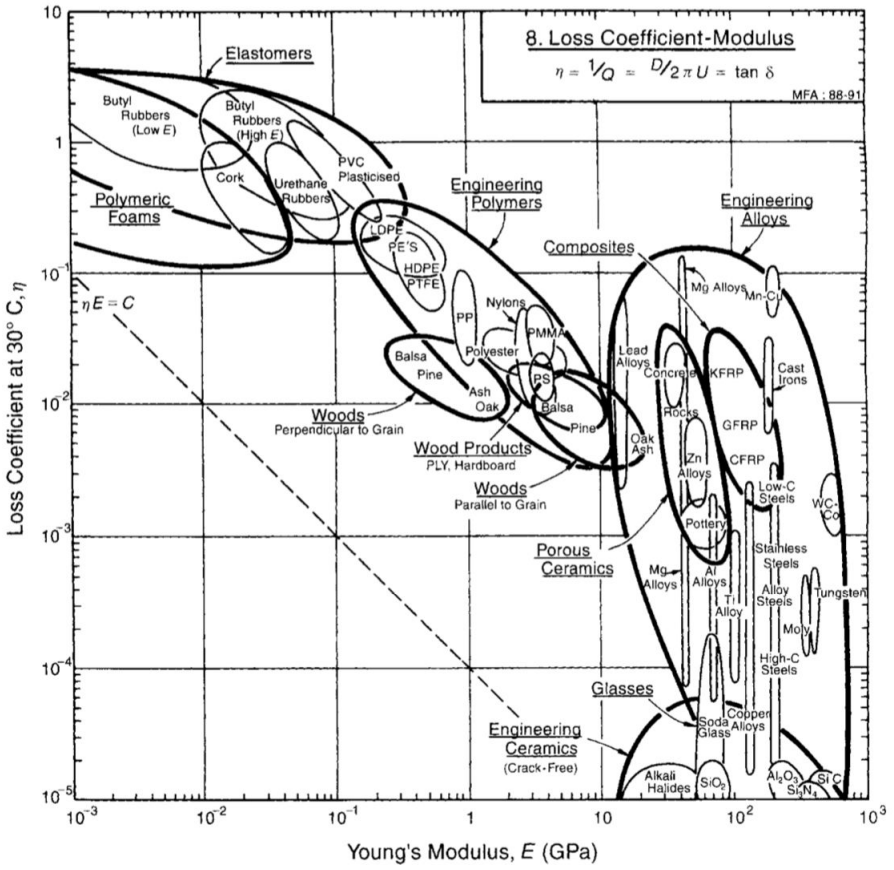

FIGURE 1.1 – Ashby diagram of the loss factor against the storage modulus [7]

in the viscoelastic layer in directions parallel to the structure surface, leading to energy storage and/or dissipation of vibration energy. This strategy ensures a good mechanical strength of the system by using a bearing structure, while introducing damping by means of the viscoelastic material. These viscoelastic materials are mainly polymeric materials, ranging from natural or synthetic rubber, through various adhesives to industrial plastics [102]. This damping mechanism has been first modeled by Oberst in the case of a simply supported beam layered by a viscoelastic material [135]. This model provides modal parameters of the first flexural modes of the composite system as well as its equivalent material and geometrical characteristics. This has been thereafter generalised by the Ross-Kerwin-Ungar (RKU) model for two layered and three layered models [154, 178].The development of measurement methods of the dynamic properties of damping materials have then emerged from the pioneering model of Oberst and RKU [173, 193]. These methods are not only limited to the characterisation of viscoelastic material for vibration applications, but are also used for porous materials in acoustic applications [95]. Various applications using RKU and Oberst models have been proposed such as the design of omnidirectional broadband insulating devices [40] and of Acoustic Black Holes [106] or the study of tyre/road interaction noise [139], to cite a few. More advanced methods have also been presented for measuring the dynamic properties of composite materials, including Virtual Field Methods [147] or Inverse Methods [186], as well as methods for characterising the vibrational behaviour of layered structure, such as higher-order theories [86, 152, 191] or dynamic stiffness approaches in Wave Finite Element method [38, 37], to name a few.

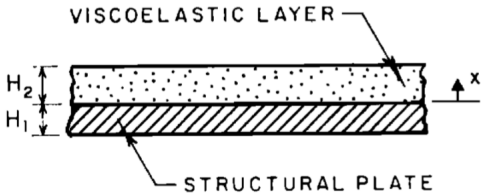

FIGURE 1.2 – Plate with attached viscoelastic layer. (Add-on type damping) [179]

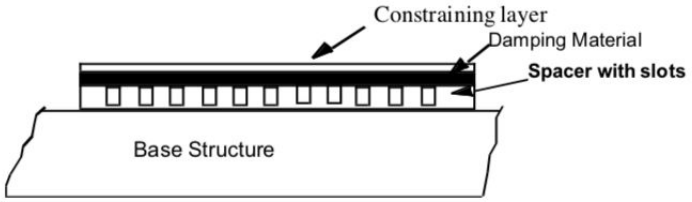

FIGURE 1.3 – Diagram of a stand-off layer damping system. [151]

Viscoelastic materials are mainly chosen in vibration control engineering. Commercial aircraft applications, for instance, use stand-off damping layers to provide damping treatment in fuselages. Such a type of treatment is a variation of the add-on type method and consists in spacing the damping layer with the structure in order to increase the shear deformation in the viscoelastic layer and, as a consequence, the damping capacity of the treatment (see Fig 1.3). Another example is that of automotive companies which use laminate material [203], which consists of bonding two pieces of metal together with a viscoelastic adhesive. This damping method differs from classic add-on treatments, since it consists of replacing the original panel with a new damping one. Figure 1.4 depicts the simulation of the vibration response of a car dash panel by using Finite Element Method for two materials: laminate and steel. The damping effect of the laminate material is characterised by a smooth vibration response, and clearly contrasts with the resonant behaviour of the steel panel.

The use of viscoelastic material in industrial applications has proven effective. However, it requires an addition of material most of the time, and as a consequence, mass to the structure, which is inconvenient on both an environmental and economic level.

c) Damping systems with graded properties

Materials with a graded impedance. Another approach to damp the vibration of structures is the use of systems with graded properties. This has been treated first in the work of Vemula *et al.* [181], in which they proposed to gradually change the impedance at the edges of a beam system along the propagation direction of flexural waves as shown in the left figure of Fig. 1.5. To do this, several beams with different materials are combined together leading to a decrease in impedance at the interfaces as the wave propagates toward the free end of the system. A large attenuation of the wave reflections at the edges of the structure is therefore obtained (see the right figure of Fig.1.5). The attenuation efficiency is directly linked to the type of impedance variation at the end of the beam. This attenuation is achieved over a wide band

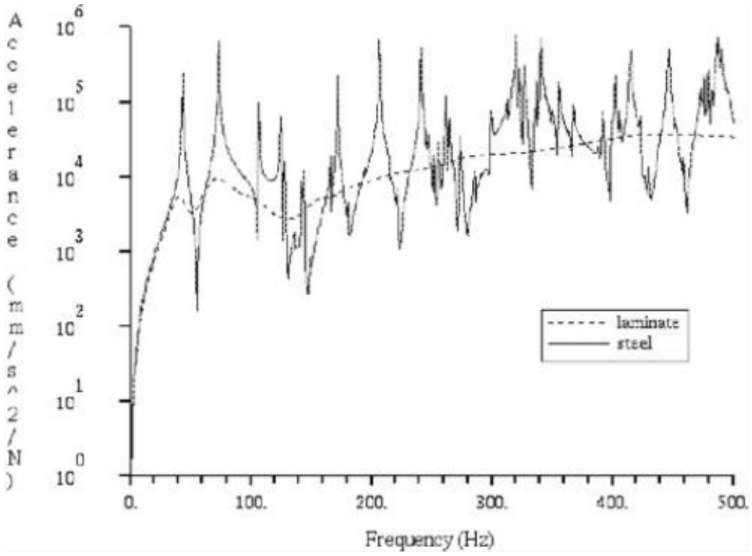

FIGURE 1.4 – FEM prediction of the vibration response of a car dash panel using laminate material (solid line) and steel (dashed line). [126]

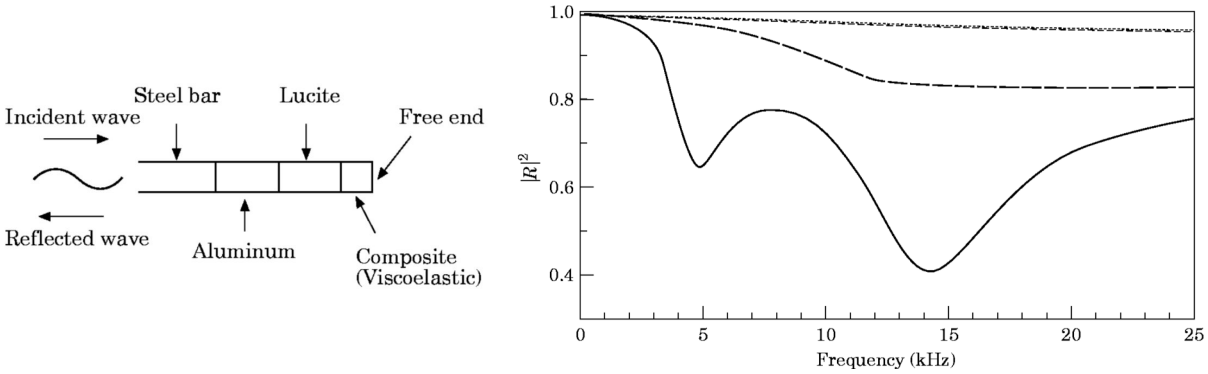

FIGURE 1.5 – Diagram of a graded impedance interface at the edge of a steel bar [181] (left). Reflected energy by four configurations of graded edges of a steel bar: (· · · ·) steel bar; (- - - -) steel bar, Al; (– – – –) steel bar, Al, Lucite; (——) steel bar, Al, Lucite, Composite. (right)

of frequencies and is more efficient for higher frequencies. However, it is accompanied by a large amplitude of the propagating waves, since the amplitude increases as the impedance decreases due to the conservation of the energy flux carried by the wave. The results have been observed experimentally and explained by means of an analytical model with a S-matrix formulation based on Mindlin and Kirchhoff theory for flexural waves. The method has thereafter been extended to longitudinal waves by Chen *et al.* [35] where the impedance mismatch is controlled by means of shape memory alloy (SMA) inserts, which are smart materials that change properties when heated. Other applications have also been proposed, such as wave cloaking [68] or non-destructive evaluation techniques [115]. In particular, Liew *et al.* studied in Ref. [115] the suppression of reflections at the boundaries of a beam waveguide by using Metal-Polymer Functionally Graded Materials (FGM). FGM is a two-component composite whose composition varies from one component to the other in a continuous manner, as shown in Fig 1.6).

FIGURE 1.6 – Picture of the Aluminium-Polycarbonate FGM used in Ref. [115] where light areas are aluminium while dark areas are polycarbonate.

Acoustic Black Holes. Using Euler-Bernoulli or thin beam theory, the bending wave impedance of a beam is expressed as EIk^2, where E is the Young's modulus, I the second moment of area and k the wavenumber. Another way to obtain a system with graded impedance than gradually changing the material is to modify k which is also dependent on the thickness of the system. Thus, the impedance of the beam can be graded if the thickness is continously changed. From this statement, Mironov proposed to take advantage of the beam properties by continuously decreasing the thickness toward the beam edge along the propagation direction of flexural waves [127] (see Fig.1.5). This thickness decrease follows a power-law and vanishes at the extremity of the beam. In the case where the varying thickness profile is expressed along the x-axis as $h(x) = \epsilon x^n$, the wavenumber k of the beam can be written as

$$k = \epsilon^{-1/2} \sqrt[4]{\frac{12\rho}{E\omega^2}} x^{-n/2}, \tag{1.2}$$

where ω is the circular frequency and ρ the mass density. The local phase velocity c_ϕ and group velocity c_γ therefore read as:

$$c_\phi = \frac{\omega}{k} = \sqrt{\epsilon} \sqrt[4]{\frac{E\omega^2}{12\rho}} x^{n/2}, \tag{1.3}$$

$$c_\gamma = \frac{\partial \omega}{\partial k} = \sqrt{n\epsilon} \sqrt[4]{\frac{E\omega^2}{3\rho}} x^{(n-1)/2}. \tag{1.4}$$

By tending x towards zero, or equivalently by tending h towards zero, c_ϕ and c_γ tend also towards zero. As a result, the flexural wave slows down by propagating along the termination due to the decrease of thickness until reaching a zero phase c_ϕ and group c_γ velocities at its extremity. The wave is therefore trapped at the extremity of the beam and is not reflected back. This slowdown is accompanied by a large amplitude of the propagating waves due to the conservation of the energy flux. The amplitude at the beam extremity may therefore become infinite in the conservative case due to its zero thickness, creating a singular point at the extremity. This wave trapping system is the so called Acoustic Black Hole (ABH). Such an ideal system is compact and lightweight since its does not require additional mass to provide absorption, but it needs a continuous decrease of the thickness until zero. The main limit of such a system in practice is that the thickness profile must be truncated. This leads to a non-null thickness at its tip and therefore to a significant reflection of the flexural waves. Krylov proposed the addition of a thin layer of viscoelastic material along the ABH profile to make up for the truncation [107, 106]. The combination of the power-law shaped wedge and the effect of a thin absorbing layer reduces significantly the wave reflection coefficient as compared to an uncovered ABH as shown in Fig. 1.8. He also showed the influence of the position of the truncation at the edge on the reflection coefficient. A longer ABH provides better absorbing performances than a shorter one for a given thickness power-law. These studies led to other devices in which the ABH effect

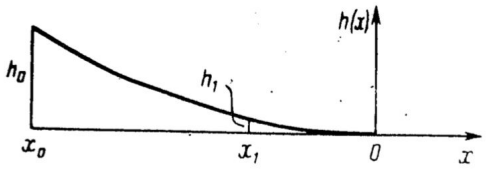

FIGURE 1.7 – Plate with a power-law tapered edge. x_1 and h_1 correspond to the coordinate of the ABH edge and its thickness in the practical case respectively. x_0 is the coordinate of the ABH edge in the ideal case where the thickness is null in this case [127].

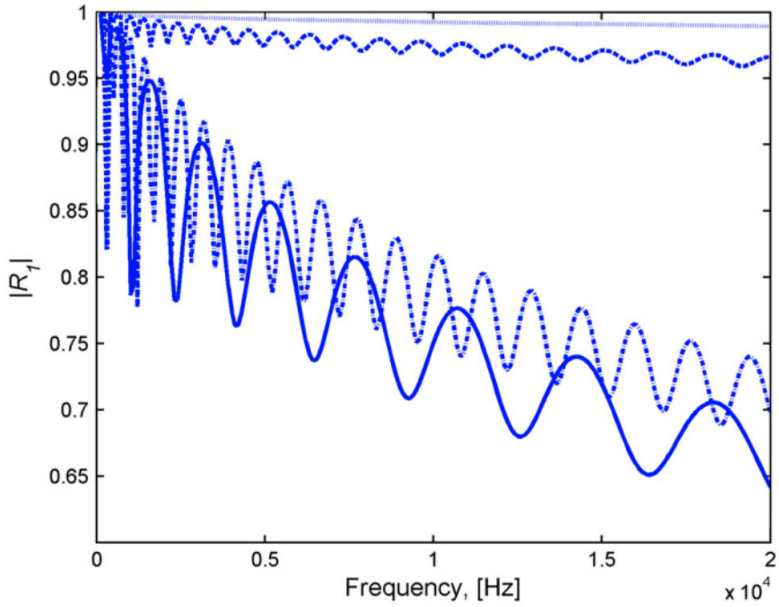

FIGURE 1.8 – Frequency dependence of the reflection coefficient $|R_1|$ for a beam with an ABH termination covered by a 700 μm absorbing film (solid curve) and 10 μm absorbing film (dash-dotted curve); with an ABH without absorbing film (dashed curve); and for a uniform beam with 700 mm absorbing film (dotted curve). [79]

and the presence of losses damping are combined such as spiral ABHs [112] which provide as good damping efficiency as classical ABHs with the same thickness profile while meeting the constraint of space limitation, compound ABHs which produce more effective ABH effect while ensuring better structural rigidity [207], and ABH resonant beam dampers which use the ABH as dynamic vibration absorbers [208]. The reflection coefficient of 1D ABH has been widely studied through various methods, including plane wave model [79], multimodal approaches [53], finite difference [54], finite element methods [159] and wavelet decomposition [171], among others. Other strategies have also been employed to enhance the ABH performance, such as the use of extended platforms to facilitate practical implementations of the ABH [11, 170], the use of constrained damping layers [51] or the use of beam non-linearities [55].

Krylov extended later on the operating principle of the ABH to axi-symmetric circular features which consist of circular pits with power-law varying thickness [105] (see Fig. 1.9). These systems can slow down and trap flexural waves similarly to 1D ABHs with omni-directional absorbing properties. However, the 2D thickness profile of the ABH must be truncated in practice

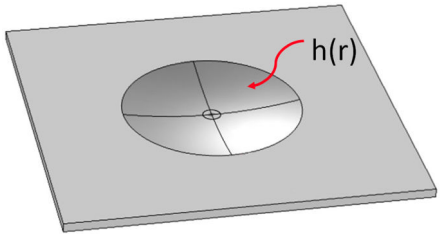

FIGURE 1.9 – Diagram of a typical 2D circular ABH with a radially dependent thickness profile h(r) and a central plateau. (adapted from [41])

similarly to the 1D ABH. Two cases can therefore be considered and have been firstly studied by Aklouche *et al.* [3]: having a hole at the center of the practical ABH due to the truncation, or filling the hole with a plateau of thickness equal to the residual thickness of the truncation. The efficiency of 2D ABHs as flexural vibration dampers has been experimentally highlighted for the first time as part of the thesis of Cuenca [47] and published in [21, 77, 79], thereafter. The focusing or trapping effect of 2D ABHs have been experimentally and numerically highlighted by Yan *et al.* in the ideal case, with a residual thickness and with a central plateau [201, 202]. They showed that the weaker efficiency of an ABH with a central plateau is due to the fact that only a portion of the incident wave is focused in the ABH in this case. Aklouche *et al.* studied the scattering properties of an ABH whose thickness follows a second order power-law in an infinite plate [4]. The results exhibited a cut-on wavenumber below which the trapping effect of the ABH is inefficient, showing the limits of such damping devices at low frequency. Other kinds of applications using the 2D ABH system such as insulating [40] and lensing [41, 210] devices have been also proposed. Studies introducing multiple ABHs embedded in periodic lattice configurations have also been carried out. These lattices form platonic crystals and give rise to unusual wave propagation properties such as double refraction [209] or lensing [210], to cite a few. The concept of platonic crystals and their properties are developed later in this chapter.

The main damping effect of such 1D and 2D systems appears in the mid-frequency and high-frequency range, as shown in Fig. 1.8. As a consequence the damping effect at low frequencies is weak and the ABH is not useful for a plethora of technological applications in which the low frequencies are the main source to be damped.

d) Tuned vibration absorbers

The use of Tuned Vibration Absorber (TVA) is also relevant to damp vibration. This device was invented by Frahm in 1911 [76] and consists in adding a reaction mass and a resilient element on the treated structure. In tonal applications, they are generally tuned to interefere with the structural vibration at the disturbance frequency. This leads to an alteration of the frequency response of the primary system and introduces another resonance in the composite system due to the additional degree of freedom provided by the TVA. Their design focuses on having a precise tuning of the mass and the damping to the disturbance frequency and on controlling the damping to an appropriate level in order to have reasonable displacement amplitude of the TVA mass. The damping effect of such a system may be broadband when the structure is lightly damped. TVA can be designed using the impedance coupling method [66] that uses the impedance of the TVA. This method avoids heavy computations of the complete

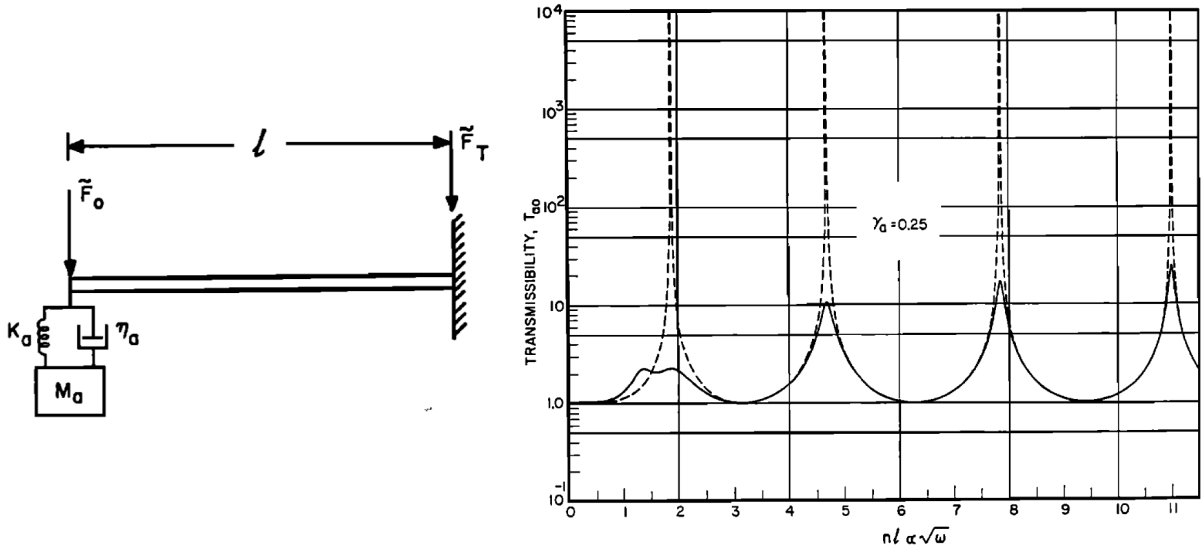

FIGURE 1.10 – Tuned Vibration Absorber attached to the end of a cantilever beam excited by a sinusoidally varying force at its free end [167] (left) and transmissibility across the beam according to dimensionless angular frequencies with (solid line) and without TVA (dashed line) [167] (right). An additional resonance provided by the TVA can be noticed below the first resonance frequency.

system since only the attachment point between the TVA and the background medium is computed. The simplest design of a TVA is a mass-spring oscillator with viscous damping on the structure to be treated or a mass with a viscoelastic spring system as shown in Fig. 1.5. Several design variations have been nonetheless proposed over the years such as a pendulum-type absorber [6] to control vibration of an inverted pendulum type structure, multi-degree of freedom TVA which showed an improvement in the response of the conventional TVA by the introduction of a significant trough in the frequency response function [168] and broadband performances [22].

TVA can also be used in the case of infinite media rather than finite structures [23]. The device is sometimes called Tuned Vibration Neutraliser (TVN) and aims to suppress propagating waves in the system rather than influence its resonant behaviour. It is then a scattering problem instead of a modal problem. The tuning of the resonance frequency of an undamped TVN has been analysed [23], showing that complete suppression of the flexural wave transmission can be achieved but a wave absorption of 50% can only be obtained with this kind of device [62].

TVA and TVN are very effective at reducing vibrations of industrial mechanical structures with relatively low cost. However, the damping effect of such systems at low frequency requires a large addition of mass, which leads again to the same problematics as mentioned above.

1.3 Control of the flexural wave propagation using periodic structures

The common methods described in the previous section lead to heavy and bulky solutions, or in the case of ABHs, to solution limited to the high frequency range. A new class of innovative

materials based on a periodic modulation of their properties has meanwhile emerged. These present promising results which may offer solutions to ecologic, health and economic issues in vibration control. This section aims at presenting an overview of periodic systems for controlling flexural waves. Two types of material regime are distinguished here: the diffraction regime due to the periodic modulation of the material properties and the metamaterial regime due to the introduction of local resonances in the material.

1.3.1 Diffraction regime : from photonic to platonic crystals

Brillouin observed in the mid 1950's that the propagation of any type of wave motion through a periodically modulated material is governed by a dispersion relation in which the wave vector is a periodic function of the frequency, producing band structures [25]. This observation paved the way to the design of photonic crystals in electromagnetic field. The pioneering work of Yablonovitch [200] and John [100] in the late 1980's showed that such periodic systems present bandgaps or stop bands, which correspond to frequency ranges in which wave propagation is forbidden. These works have been inspired by the quantum mechanical band theory in which the existence of energy bands and forbidden band have been highlighted. Unlike the energy bands, the forbidden band or forbidden bandgaps correspond to particular energy ranges in a solid in which the electrons cannot propagate. The analogies between the electromagnetic equations and those in acoustics and for elastic waves led to the emergence of phononic crystals a few years later presenting bandgaps for acoustic and elastic waves [109, 161]. The terminology *phonon* defines a quantum of vibrational energy in an elastic medium. It is used in the context of vibrations in crystal lattices in analogy to the notion of a photon in electromagnetics [94]. Such acoustic periodic systems can provide sound attenuation in the frequency ranges of the bandgaps and applications in sonic barriers for the human audible frequency range have been proposed by exploiting this property [82, 108, 110, 156], among others [57].

More recently, the properties of flexural waves in periodically-constrained thin elastic plates have been studied and bandgaps for flexural waves have been observed [65, 124]. These bandgaps can decrease the vibrational response of the plate over certain frequency ranges similarly to those of phononic crystals. McPhedran *et al.* proposed the name of *platonic* crystals [124] for this type of structured system. In addition to these platonic crystals, periodic arrays of holes in plates [130, 184], periodically undulated plates [176] or inclusions of different materials [162] have been proposed. The study has also been applied to beam systems [176, 190] and to Lamb waves in plates [32, 99]. Several methodologies for band structure calculations of platonic crystals have been investigated such as multiple scattering [130], Finite Element [88], Super Cell [180] or Plane Wave Expansion (PWE) method [176].

For all fields of physics, the bandgaps of periodic structures are due to Bragg interferences, which are destructive ones encountered at particular frequency ranges. The frequency range and the bandwidth of the gaps depend on the periodicity length scale a, which has to be comparable to the propagation wavelength λ. Thus, bandgaps at low frequencies require large and bulky structures which is inconvenient for industrial applications. This scale dependency can however be overcome by the use of locally resonant (LR) metamaterials on the sub-wavelength scale ($\lambda >> a$).

1.3.2 Metamaterial regime

A metamaterial is broadly and briefly defined as *an artificial media with unusual properties*. This definition is generally used since it captures the spirit of the subject. However, there is no consensus on the meaning of the words *unusual* and *artificial* and there is no definition that is universally accepted by everyone. Is a property defined as unusual by one person also unusual for another? Does metamaterial always concern artificial media? Anyway, there is consensus that the concept of metamaterial was first introduced in electromagnetics by Veselago in the late 1960's [182]. The refractive index value of a material had always been considered positive up to his work. Veselago hypothesised that the refractive index may also be negative if both the electric permittivity and the magnetic permeability of a material are negative. Materials with such properties are called *left-handed* material in reference to Fleming's left-hand rule in electromagnetism and can exhibit negative refractive index. Pendry *et al.* [145] proposed 30 years later left-handed materials by introducing local resonances in a periodic array. These resonances are introduced by means of split-ring metallic cylinders put in a square array. By doing so, a negative effective permeability was observed in a bandgap around the resonance frequency of the cylinder. This resonance frequency is far below the first Bragg frequency of the array, meaning that wave propagation in periodic media can be mitigated for wavelengths λ much longer than the lattice size a ($\lambda >> a$) by using local resonances. This was validated experimentally by Smith *et al.* [164, 165] later on. These works were then extended for the control of elastic and acoustic wave propagation.

Liu et al. [119] proposed a *locally resonant (LR) sonic crystal* in which the local resonances are introduced by rubber coated lead spheres. These spheres were embedded in an epoxy matrix and negative effective dynamic mass density was obtained for wavelengths that are two orders of magnitude larger than the lattice size a. The negative effective mass density produces exponential attenuation of the incoming wave amplitude through the sample, generating therefore bandgaps at the resonance frequency of the local resonators. The local resonances can also give rise to other original phenomena such as invisibility cloaks [33].

New classes of metamaterials that are not based on resonant properties have also emerged thanks to manufacturing progresses such as auxetic metamaterials [129] with negative Poisson's ratio that contract in transverse directions under uniaxial compressive loads, pentamode metamaterials [103] with near-zero modulus that behave like fluids despite the fact that they are solids, and origami inspired metamaterials [117], to cite a few.

The potential of LR materials to mitigate wave propagation at low frequency has aroused interest in the vibro-acoustic community to design devices for noise and vibration control. A wide number of periodic systems have been designed in order to observe bandgaps in LR thin plates. Local resonances in plates can be introduced by means of inclusions or by adding resonators on top of plate host structures. The 2D periodic arrangements of inclusions such as rubber discs [92], rubber-coated steel disc inclusions [104] or hemmed discs inclusions [195] have been investigated. Xiao *et al.* [197] and Claeys *et al.* [39] have analysed theoretically the potential of LR panels to obtain low-frequency vibrational bandgaps by using idealised mass-spring resonators onto a thin plate. Practicable resonators in LR plates have also been proposed beside the theoretical

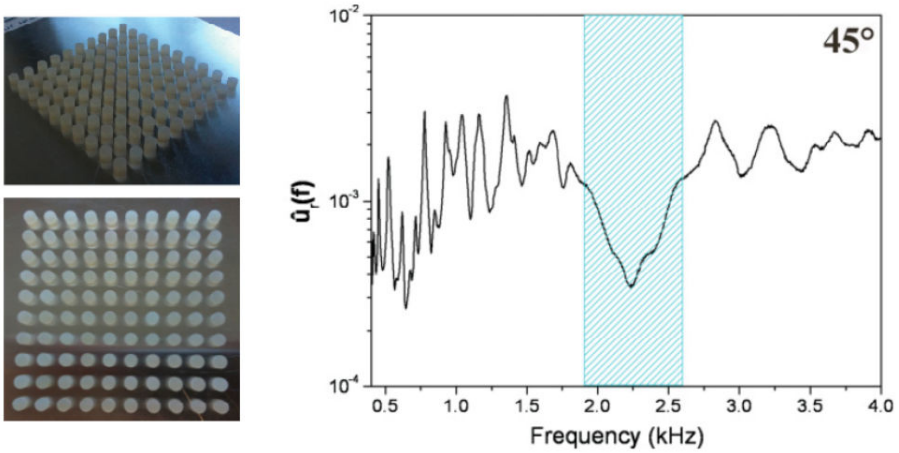

FIGURE 1.11 – LR plate with a 2D periodic array of silicon stub resonators proposed in [137] (left) and the corresponding averaged displacement field along the diagonal direction of the crystal. A significant attenuation of the transmitted wave field is observed at a particular frequency range, implying the presence of a BG at this frequency range. (right).

analyses with idealised mass-spring resonators. Wu *et al.* [183] proposed a LR plate consisting of a 2D periodic array of cylindrical aluminum stubbed resonators on a thin aluminum plate host structure to obtain flexural wave bandgaps. Oudich *et al.* [137] proposed silicone rubber stub resonators instead of aluminum ones (see Fig. 1.11). An attenuation at lower frequencies has therefore been obtained thanks to the less stiff property of silicone rubber compared to aluminum. Assouar *et al.* [8] also added masses on top of the rubber stubs in order to broaden and shift the LR bandgap at lower frequency. Various LR plates have been proposed such as 2D periodic array of beam-like resonators attached to a thin plate [196] as shown in Fig. 1.12. The same investigations have also been applied to LR beams with idealised mass-spring and other kinds of resonators [39, 118, 198].

A huge variety of original phenomena has also been observed in metamaterial plates similarly to acoustic metamaterial such as negative refraction [166], flexural wave focusing [71] or confinement [69], cloaking [70], lensing [30, 71] or waveguiding using periodically graded structured plates [31], among others.

For all fields, the bandgaps generated by locally resonant materials do not require periodicity, but arise from the addition of local sub-wavelength resonators to a hosting medium. Such materials can be small, lightweight and can operate in the low frequency regime. They are therefore of great interest since they can answer to both the current industrial problematic of damping vibration at low frequency and the problem of vibration control adapted to light structures.

1.4 Acoustic subwavelength perfect absorption

Recent studies in audible acoustics have focused on wave absorption at low frequencies by means of subwavelength locally resonant materials. In particular, the design of broadband subwavelength perfect absorbers, whose dimensions are much smaller than the wavelength of

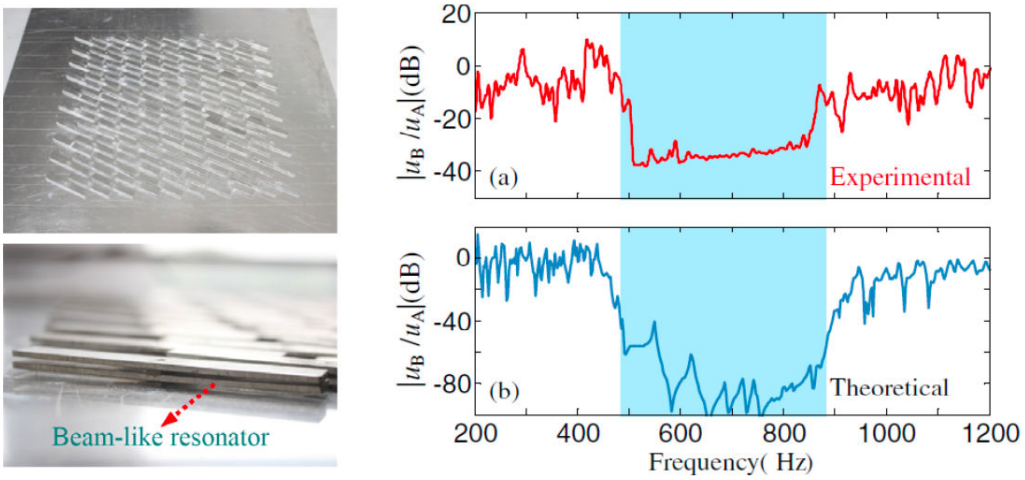

FIGURE 1.12 – LR plate with a 2D periodic array of beam-like resonators proposed in [196] (left) and out-of-plane vibration transmittance from a point in the middle of the crystal to another one at the edge (right). The results shows an attenuation of the wave field and implies the presence of a BG.

the frequency to be attenuated, have recently been proposed [84, 96, 98, 125, 153]. Such devices can totally absorb the energy of an incident wave and require solving the two complex problems: (*i*) increasing the density of states at low frequencies and (*ii*) matching the impedance with the background medium. On the one hand, the use of local resonators is a successful approach for increasing the density of states at low frequencies with reduced dimensions, as it has been shown in the field of metamaterials [42, 61, 67, 119, 140, 163, 174, 187]. On the other hand, the local resonators of such metamaterials are open and lossy ones. The field inside the local resonator can interact with an external wave field in the background medium through the interface that connects the resonator to the medium. This connection can be seen as an aperture through which wave energy can leak out from one system to another (see left figure of Fig. 1.13). The resonator is therefore considered as open to the background medium due to its energy leakage to the medium. Inherent losses can also be added inside the resonator by introducing an internal energy dissipation source. The impedance matching of such metamaterials can be controlled by the ratio between the inherent losses of the resonator and the leakage of energy [17]. Particularly, the impedance matching corresponds to the situation in which the amount of inherent losses in the resonator equals the amount of energy leakage, and is known as the critical coupling condition [205]. This situation occurs at the resonance frequency of the resonator and leads to a perfect absorption of the wave energy by the resonator at this specific frequency (see right figure of Fig. 1.13). This phenomenon has also been widely used to design perfect absorbers in different fields of physics [28, 199] other than acoustics.

1.5 Motivations and objectives of the work

The solutions proposed by the usual passive damping methods do not necessarily answer both the problematic of damping vibration at low frequency and the problem of vibration control adapted to light structures. These methods either respond to one of these two problematics, but neglect the other. For example, they can provide a satisfactory solution to face the problematic

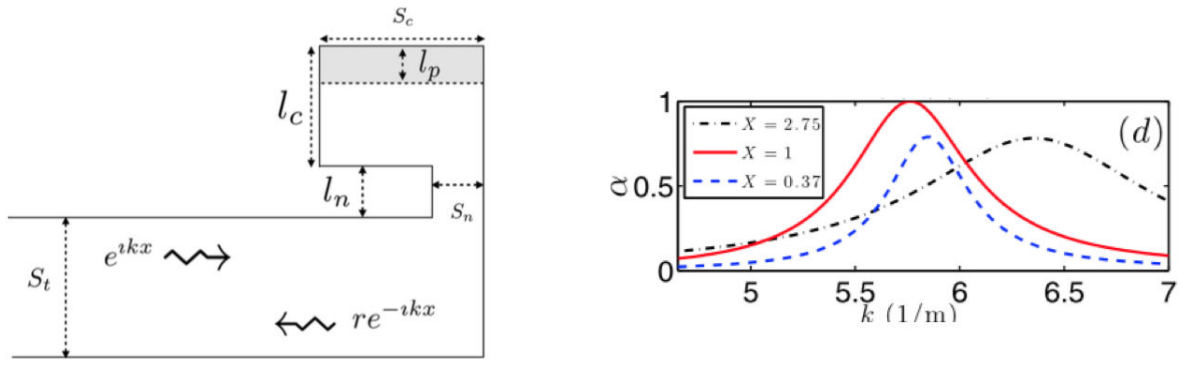

FIGURE 1.13 – (left) Diagram of the acoustic perfect absorber proposed in [153] made of a Helmholtz resonator loaded to a waveguide filled with air. The inherent losses in the resonator are controlled with a porous material of thickness l_p. The neck of the resonator of width S_n plays the role here of the aperture between the resonator and the waveguide. (right) Evaluation of the absorption coefficient by the Helmholtz resonator of three different configurations with different amount of losses. The solid line corresponds to the critical coupling situation in which the incident wave is totally absorbed by the resonator at its resonance frequency.

of damping vibration at low frequency, but imply heavy and/or bulky solutions. Conversely, these methods can comply to the lightweight constraint by taking advantage of the inherent properties of the structure, but cannot achieve good performances at low frequency. This constitutes therefore a motivation for this work. The objective being to understand, analyse and design 1D and 2D passive damping lightweight systems which can attenuate flexural vibrations at low frequencies, and more particularly at wavelengths much smaller than the characteristic length of the damping system.

1.5.1 Subwavelength absorber for flexural waves

Particular interest has been accorded to the design of subwavelength perfect absorbers. Such absorbers have proven their efficiency for the total absorption of the energy of an incident wave in audible acoustic metamaterials, and a generalisation of the method in elastodynamics field could be of great interest owing to the constraints previously mentioned. Hence, this work aims first of all at adapting the problem of perfect absorption for flexural waves in 1D elastic beams with local resonators by using the critical coupling condition. The design of systems with simple geometry are analysed to that purpose. They are composed of a main beam and an open resonator simply consisting of a reduction of the thickness of the main beam. The resonator is considered as open here since the field inside the resonator can interact with the one of the main beam through the aperture between both systems. A thin viscoelastic coating is also attached to it. The composite resonators present therefore both energy leakage due to the aperture of the resonator to the main beam which can be controlled by changing the thickness of the beams, and inherent losses due to the viscoelastic damping which is controlled by changing the properties of the viscoelastic coating. The resonators are chosen first as an integral part of the main beam in order to facilitate its implementation for the experimental validation of the method. Particularly, the absorption of energy is analysed by means of the Transfer Matrix Method (TMM) for the

two scattering problems: the reflection and the transmission of flexural waves. An experimental validation is also performed. This first preliminary study aims to open up new avenues to the design of simple resonators for efficient flexural wave absorption by means of the critical coupling condition, showing also the limits of absorption induced by the geometry used in the study.

The problem is then complexified by extending the method in the 2D case. To that end, an infinite array of penetrable circular scatterers embedded in an infinite or semi-infinite 2D thin plate is considered thereafter. This system constitutes a 2D metaplate in which the penetrable scatterers compose its resonant block. A 2D preliminary study is presented in which the perfect absorption of the first axisymmetric mode of a circular resonator embedded in an infinite thin plate is analysed. The resonator consists of a circular reduction of the thickness of the infinite plate, and a thin viscoelastic coating is attached to the resonator similarly to the the 1D case. This composite scatterer presents therefore leakage and inherent losses which can be controlled similarly to the resonators presented in the 1D case. This analysis is done through the balance between the energy leakage and the inherent losses in the resonator for the particular case of a concentric incident wave propagating towards the centre of the resonator. The composite is studied by means of a semi-analytical model based on the scattering method and is compared with numerical results using FEM methods. The optimised 2D resonator is therefore embedded in the form of an infinite array in a plate and two scattering problems are then studied by using the multiple scattering method: the reflection problem in a semi-infinite plate and the transmission problem in an infinite plate. This analysis aims at showing the adaptability of the method for the case of 2D problems and at getting closer to a practical application.

1.5.2 Adapting the Acoustic Black Hole for perfect absorption of flexural waves

The combination of the ABH effect and the presence of losses provides a good damping performance while reducing the weight of the initial structure. However, the efficiency of ABH devices is weak in low frequencies, thus limiting their application. Despite this drawback, the ABH effect remains of great interest in designing damping system by removing part of the system matter. This has acted as motivation to improve the absorbing efficiency of the ABH by using the critical coupling condition. The combination of the ABH effect at high frequencies with the perfect absorption obtained with the critical coupling condition at low frequencies would allow for a broadband absorber without adding mass in the system. To that end, a system composed of a main beam terminated by an open resonator which corresponds to an ABH of finite length is analysed. A thin viscoelastic coating is also attached to the resonator creating a composite material. The vibration response of the composite ABH is studied by discretising it with constant thickness piecewise elements. The composite presents resonances, energy leakage and inherent losses in the same way as the simple resonator described in the previous section. All these properties fulfill the conditions to design a subwavelength perfect absorber as mentioned in the previous section without altering the initial ABH effect since this effect originates only from the geometry of the system.

A new physical insight of the ABH efficiency emerged through the study of the critical coupling of a 1D ABH. The ABH effect may be interpreted as a consequence of the critical

coupling at one resonance frequency of the ABH and of the broadband quasi-perfect absorption at higher frequencies, thanks to the specific geometry of the resonator. This has motivated this work to interprete the Acoustic Black Hole effect based on the concept of critical coupling in order to provide the key to future optimisation procedures of such a type of terminations. Two strategies to optimise the absorption efficiency of an ABH termination at low frequency are proposed in this work, both consisting in applying the critical coupling condition. The first consists in tuning the losses introduced by the viscoelastic layer by shaping its thickness profile in order to achieve the critical coupling condition at several resonances of the ABH. The second strategy is based on the addition of a mass at the extremity of the ABH which decreases the first resonance frequency of the ABH. The critical coupling is then applied at this specific frequency to obtain a low frequency absorption by the termination. The approach of mass addition on a ABH has already been investigated by Aklouche *et al.* [3]. The study presented in this thesis gives new perspectives of this approach by using the concept of critical coupling.

1.5.3 Layout of the thesis

This thesis is organised in the form of 5 chapters, the complexity of each of which is gradually increased to understand step by step the main physical mechanisms of the perfect absorption of flexural wave energy. The content of the chapters are as follows.

Chapter 5 presents a survey of usual methods for vibration damping, paying attention to passive damping methods. A description of the methods to control the propagation of flexural waves using periodic materials has been made afterwards. Finally the objectives, motivations, and a brief overview of the work have been given.

Chapter 2 is devoted to the problem of perfect absorption of flexural waves in 1D elastic beams with simple local resonators by using the critical coupling condition for the two scattering problems: the reflection and the transmission of flexural waves. The design of an experimental prototype and the measurement of its reflection and absorption coefficients in the reflection problem are also presented, and are compared with a numerical model using Finite Element Method (FEM). This chapter refers to the article [114] published in New Journal of Physics and presented in Appendix.

Chapter 3 focuses on the link between the complex nature of the trapped modes within a 1D ABH and its reflection coefficient troughs, in terms of depth and frequency width. More specifically, the purpose of Chapter 3 is to analyse first the absorbing efficiency of the ABH by using the critical coupling condition. Two strategies to optimise the absorption efficiency of an ABH termination at low frequency are then proposed in this work, both consisting in applying the critical coupling condition. All the analytical results are validated with a FEM model.

Chapter 4 concerns the design of the resonant blocks of a metaplate by using the critical coupling condition. A preliminary study is presented in which the perfect absorption of the first axisymmetric mode of a circular resonator embedded in an infinite thin plate is analysed. The scattering of a resonator, consisting in a circular reduction of the thickness of the infinite plate on which a thin viscoelastic coating is attached, is studied. The problem is then complexified by

studying the scattering of a penetrable scatterer with radially varying thickness. The analysis is done by means of the multiple scattering method for multilayered systems.

Chapter 5 concerns the scattering of flexural waves by an infinite critically coupled array of circular inclusions embedded in a thin plate. This system composes a metaplate and the analysis of the absorbing efficency of this array is made for two configurations. The first configuration corresponds to a 2D transmission problem in which the array is embedded in an infinite thin plate, wheras the second corresponds to a 2D reflexion problem in which the scattered field by the array interacts with a simply supported plane boundary in a semi-infinite thin plate. The scattered field by the array is studied by means of the multiple scattering theory and by using a FEM model.

Chapter 6 gives the concluding remarks as well as perspectives for future works.

Chapter 2

Flexural wave absorption by open lossy resonators for the reflection and transmission problems

2.1 Introduction

The design of broadband subwavelength perfect absorbers has recently proven its efficiency in audible acoustics [84, 96, 98, 125, 153]. Such devices have dimensions that are much smaller than the wavelength of the frequency to be attenuated and can totally absorb the energy of an incident wave provided that the critical coupling condition between the absorber and the background medium is fulfilled (see Section 1.4). The critical coupling condition is relevant for applications in vibrations owing to the increasing need for damping materials at low frequencies in several branches of industry [61]. Current passive solutions in this field are mainly based on the use of viscoelastic coatings [172]. Another solution yields in TVAs [50, 24, 63] that is used to control flexural waves in beams. The tuning of the resonance frequency of an undamped TVA has been analysed [24], showing that complete suppression of the flexural wave transmission can be achieved. In most cases, TVAs have been used to minimise the transmission of a propagating wave [24], resulting in practice in heavy treatments at low frequencies. Less attention has been paid to the case of maximising the absorption in order to reduce simultaneously both the reflected and transmitted waves.

The purpose of this chapter is to study the problem of perfect absorption of flexural waves in 1D elastic beams with local resonators by using the critical coupling condition. Particularly, the absorption of energy is analysed through the balance between the energy leakage and the inherent losses in the resonators for the two scattering problems: the reflection and the transmission of flexural waves. The presented problem is related to the control of flexural waves in a beam using a passive TVA but with a physical insight that allows the interpretation of the limits of the flexural wave absorption based on both the critical coupling condition and the symmetry of the excited resonances in the resonator. The analysed systems are composed of a main beam and an open resonator simply consisting in a thickness reduction of the main beam. A thin viscoelastic coating is attached to it, leading to a composite material whose loss may be tuned. This composite material is modeled with the Ross-Kerwin-Ungar (RKU) method for beams [154] and is embedded in the main beam. By tuning the losses, it is possible to analyse the

different limits in both scattering problems. In practice, this type of resonator results in simpler geometries than that of the TVA which consists of complicated combinations of mass spring systems simulating a point translational impedance.

The composite is studied by means of an analytical model based on the transfer matrix method. The analytical results, in accordance with the the experimental results, show the limits of the maximal values for the flexural wave absorption and their physical interpretations in both the reflection and transmission problems. The interpretations are based on the eigenvalues of the S-matrix for the propagating waves, represented in the complex frequency plane [153]. An experimental prototype is designed and measured for the reflection problem. The experimental results prove the perfect absorption of flexural waves and validate the analytical predictions.

The chapter is organised as follows. The study presents first a general scattering problem in Section 2.2 in order to show the relevance of the eigenvalues and eigenvectors of the scattering matrix to identify the situations of perfect absorption in the system. In Section 3.2, the theoretical model used to analyse the 1D scattering problems of flexural wave is presented. The physical analysis of the absorption coefficient in the complex frequency plane are presented in Section 2.4. This analysis is based on an analytical model and the concept of critical coupling to obtain a perfect absorption of flexural waves. The experimental set-up used to validate the model for the reflection problem is then presented in Section 2.5 as well as the experimental methodology and results. Finally, Section 2.6 summarises the main results and gives the concluding remarks.

2.2 Scattering problem for 1D configurations

The absorbing devices proposed in this chapter are studied by analysing their scattering properties. Scattering problems differ from usual modal analyses, since it deals with the scattering properties (reflection, transmission and absorption) of waves in the system instead of studying its resonant behaviour. The absorbers studied in this work are therefore embedded in an infinite or semi-infinite medium according to the studied scattering problem, in order to maximise the absorption of incident propagating waves. These media can be seen as waveguides in the same way as in acoustics. This Section aims at presenting the two scattering problems in 1D in order to show the relevance of the eigenvalues and eigenvectors of the scattering matrix to identify the situations of perfect absorption in the systems. The analysis of the problem is achieved in the far-field ($x \to \pm\infty$), i.e. with propagative waves that are related to the carried energy. The reflection and transmission coefficients of the scattering matrix are therefore scalar in this Section. Two cases are presented. A general scattering problem is first treated with three types of scatterers: a mirror symmetric scatterer which corresponds to the one studied later in this chapter, a point symmetric scatterer and a mirror asymmetric scatterer. The specific case of the reflection problem is then presented. The analysis of the scattering problems is based on [125].

Consider an one-dimensional and reciprocal scattering process. The relation between the amplitudes of the incoming (a, d), and outcoming (b, c) waves, on both sides of the scatterer Σ, as shown in Fig. 2.1(a), is given by

$$\begin{pmatrix} c \\ b \end{pmatrix} = \mathbf{S}(f) \begin{pmatrix} a \\ d \end{pmatrix} = \begin{pmatrix} T & R^+ \\ R^- & T \end{pmatrix} \begin{pmatrix} a \\ d \end{pmatrix}, \tag{2.1}$$

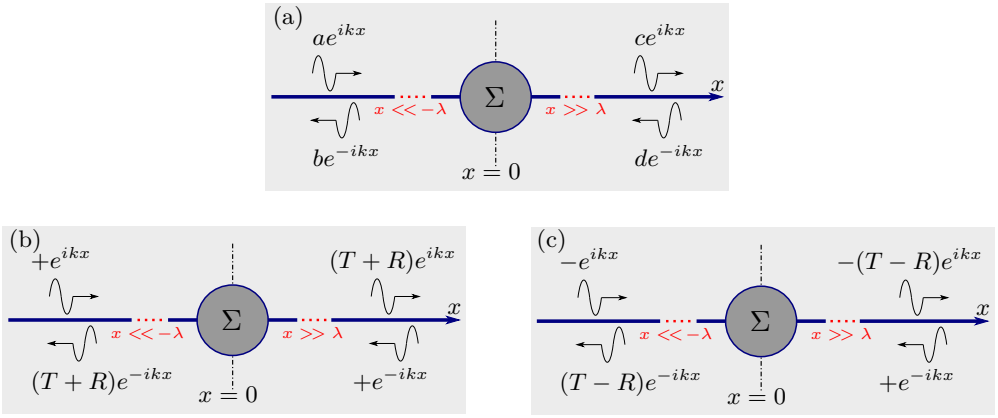

FIGURE 2.1 – (a) Diagram of the scattering process. (b) Symmetric and (c) antisymmetric uncoupled sub-problems for the case of a mirror-symmetric scatterer Σ. The time convention is $e^{-i\omega t}$. (adapted from [125])

where $\mathbf{S}(f)$ is the scattering matrix (S-matrix) of the propagative waves, f is the incident wave frequency, T is the complex transmission coefficient, R^- and R^+ are the complex reflection coefficients for left $(-)$ and right $(+)$ incidence, respectively. In this chapter, the time dependence convention of the harmonic regime is $e^{-i\omega t}$. The eigenvalues of the S-matrix $\psi_{1,2}$ and the eigenvectors $\mathbf{v_{1,2}}$ of the system are expressed respectively as:

$$\psi_{1,2} = T \pm [R^- R^+]^{1/2}, \tag{2.2}$$

and

$$\mathbf{v_1} = \begin{pmatrix} R^+ \\ -\sqrt{R^+R^-} \end{pmatrix}, \qquad \mathbf{v_2} = \begin{pmatrix} \sqrt{R^+R^-} \\ R^+ \end{pmatrix}. \tag{2.3}$$

A zero eigenvalue of the S-matrix corresponds to the case in which the incident waves can be completely absorbed ($b = c = 0$). This case is called coherent perfect absorption (CPA) [36] and happens when $T = \pm\sqrt{R^-R^+}$ and the incident waves a, d correspond to the relevant eigenvector. For an one-sided incident wave, the absorption coefficient is defined as:

$$\alpha^{\pm} = 1 - |R^{\pm}|^2 - |T|^2. \tag{2.4}$$

2.2.1 Mirror symmetric scatterer

The scatterer Σ is considered as mirror symmetric. The reflection coefficients at both ports of Σ are equal in this case such that:

$$R^+ = R^- = R. \tag{2.5}$$

The scattering problem can be reduced to two uncoupled sub-problems by choosing incident waves that are symmetric (see Fig. 2.1(b)) or antisymmetric (see Fig. 2.1(c)). The total reflection coefficients of both problems are therefore respectively:

$$R_s = T + R, \qquad R_a = T - R. \tag{2.6}$$

In particular, the reflection and transmission coefficients of the initial problem in Fig. 2.1(a) can be expressed in terms of R_s and R_a as $R = (R_s + R_a)/2$, and $T = (R_s - R_a)/2$, while the eigenvalues of the S-matrix can be written as $\psi_1 = R_s$ and $\psi_2 = -R_a$. For an one-sided incident wave, the absorption coefficient defined in Eq. (2.4) can be written as:

$$\alpha = \frac{\alpha_s + \alpha_a}{2}, \tag{2.7}$$

where $\alpha_s = 1 - |R_s|^2$ and $\alpha_a = 1 - |R_a|^2$. The total absorption of an incident wave at a given frequency f_{max} by the scatterer (i.e. $\alpha(f_{max}) = 1$) can therefore be achieved provided that the reflection coefficient of both sub-problems equals zero at f_{max}. This has been achieved in Ref. [148] for a mirror symmetric photonic crystal slab covered by a graphene layer and in Ref. [125] for an acoustic mirror symmetric scatterer composed of 2 helmholtz resonators.

2.2.2 Point symmetric scatterer

Σ is now considered as a point scatterer. The length of Σ is therefore reduced to one point at $x = 0$. This case is relevant to the study of absorption by TVA since such devices are attached to the background medium at only one point. Imposing the continuity of the wave-field at this point [125] yields $1 + R = T$ and consequently to $R_a = -1$ according to Eq. (2.6). In this case, the scatterer Σ is transparent to antisymmetric incident waves since $\alpha_a = 0$. The absorption coefficient is then expressed as:

$$\alpha = \frac{\alpha_s}{2}. \tag{2.8}$$

As a consequence, the absorption of the scatterer for an one-sided incident wave at a given frequency f_{max} may not exceed 0.5. In the case where $\alpha(f_{max}) = 0.5$, $\alpha_s(f_{max}) = 1$ which gives $R_s(f_{max}) = \psi_1(f_{max}) = 0$, and $R(f_{max}) = -T(f_{max}) = 1/2$. This case corresponds therefore to the CPA of the two-incident waves problem for symmetric and in phase incoming waves at f_{max}, i.e., $v_2(f_{max})/v_1(f_{max}) = 1$ [188].

2.2.3 Mirror asymmetric scatterer

Σ can be asymmetric in the most general case, such that:

$$R^+ \neq R^-. \tag{2.9}$$

This problem corresponds to the one presented in Fig. 2.1(a) whose the corresponding eigenvalues and eigenvectors are given in Eqs. (2.2) and (2.3) respectively. Therefore, Two absorption coefficients are defined in this case according to the direction where the incident wave is coming from and their expression is given in Eq. (2.4). The eigenvalues of the scattering matrix equal zero when $T = \pm\sqrt{R^+R^-}$. Thus, $T = 0$ and the system presents Unidirectional Perfect One-side Absorption (UNPOA) provided that one of the reflection coefficients reaches zero. From the analysis of the eigenvectors, the direction from which perfect absorption is obtained will correspond to the case of an eigenvector equal to $(0, 0)^T$, where ^{T} is the transpose sign.

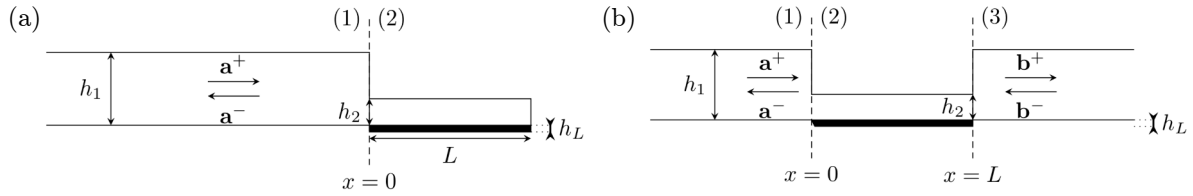

FIGURE 2.2 – Diagrams of the 1D configurations analysed for the reflection and transmission problems for flexural waves. (a) Configuration for the reflection problem. (b) Configuration for the transmission problem.

2.2.4 Complex frequency plane

When the eigenvalues are evaluated in the complex frequency plane [153], poles and zeros can be identified. The pole frequencies correspond to the resonances of the resonator while the zero frequencies correspond to the perfect absorption configuration. Since the systems analysed in this work are invariant under time-reversal symmetry, the scattering matrix, as defined in Eq. (2.1), presents unitary property [128, 133] in the lossless case (i.e., without dissipative losses):

$$\mathbf{S}^*\mathbf{S} = \mathbf{I}. \tag{2.10}$$

The complex frequencies of the eigenvalue poles of the propagative S-matrix are complex conjugates of its zeros. Poles and zeros appear therefore symmetric with respect to the real frequency axis in the lossless case.

2.3 Theoretical model for flexural waves

Two scattering problems are now presented in order to study the absorption of flexural waves by open lossy resonators in 1D systems. The first one is the reflection problem where the absorption by a resonator made of a thinner composite beam located at the termination of a semi-infinite beam is studied (see Fig. 2.2(a)). The second one is the transmission problem where the absorption of the same resonator located between two semi-infinite beams is considered (see Fig. 2.2(b)). Both resonators correspond to mirror symmetric scatterers as described in the previous section. The governing equations used in the model are first introduced in this section. The two scattering problems are then presented. The analytical results shown for the two problems have been tested by numerical simulations, but not shown in this chapter for clarity of the figures. The analytical results are validated experimentally in Section 2.5 later on.

2.3.1 Flexural wave propagation in uniform thin beams

Consider a thin uniform beam whose neutral axis is denoted by the x-axis under Euler-Bernoulli assumptions. According to the Euler–Bernoulli or thin beam theory, the cross-section of the beam, initially orthogonal to its mean axis, remains planar and orthogonal to it, implying therefore that shear strains are neglected. Assuming Euler-Bernoulli conditions, the flexural displacement $W(x,t) = w(x)e^{-i\omega t}$, where ω is the angular frequency, satisfies [113]:

$$D\frac{\partial^4 W(x,t)}{\partial x^4} + m\frac{\partial^2 W(x,t)}{\partial t^2} = 0, \tag{2.11}$$

where $D = EI$ is the flexural rigidity, E the Young modulus, I the second moment of area and m the linear mass. The solution of Eq. (2.11) can be written in the frequency domain as:

$$\left[\frac{\partial^2}{\partial x^2} + k^2\right]\left[\frac{\partial^2}{\partial x^2} + (-ik)^2\right] w(x) = 0, \tag{2.12}$$

where k is the wavenumber and $k^4 = \dfrac{m\omega^2}{D}$. Note that the wavenumber k is real and positive in the lossless case and complex when damping is accounted for. The solution of Eq. (2.12) can be separated in two parts such that:

$$w(x) = w_1(x) + w_2(x),$$

where $w_1(x)$ and $w_2(x)$ are solutions of the following equations respectively:

$$\left[\frac{\partial^2}{\partial x^2} + k^2\right] w_1(x) = 0, \tag{2.13}$$

$$\left[\frac{\partial^2}{\partial x^2} + (-ik)^2\right] w_2(x) = 0. \tag{2.14}$$

The first equation corresponds to the Helmholtz equation governing the propagating flexural waves, while the second equation is the modified Helmholtz equation governing the evanescent waves which are near field waves, the amplitude of which decreases exponentially with distance. The solution of Eq. (2.11) is therefore the sum of the solutions of Eqs. (2.13) and (2.14) that being the sum of four flexural waves:

$$w(x) = a^+ e^{ikx} + a_N^+ e^{-kx} + a^- e^{-ikx} + a_N^- e^{kx}. \tag{2.15}$$

The complex amplitudes of the propagative and evanescent waves are a and a_N respectively, and the signs $^+$ and $^-$ denote the outgoing and ingoing waves respectively. The wave amplitude is expressed in the vector form by convenience:

$$\mathbf{a}^+ = \begin{bmatrix} a^+ \\ a_N^+ \end{bmatrix}, \quad \mathbf{a}^- = \begin{bmatrix} a^- \\ a_N^- \end{bmatrix}. \tag{2.16}$$

The relation between wave amplitudes along a beam with a constant thickness are then described by

$$\mathbf{a}^+(x_0 + x) = \mathbf{f}\ \mathbf{a}^+(\mathbf{x_0}) \ \text{ and } \ \mathbf{a}^-(x_0 + x) = \mathbf{f}^{-1}\mathbf{a}^-(\mathbf{x_0}), \tag{2.17}$$

where the diagonal transfer matrix $\mathbf{f}$ is given by

$$\mathbf{f} = \begin{bmatrix} e^{ikx} & 0 \\ 0 & e^{-kx} \end{bmatrix}. \tag{2.18}$$

2.3.2 Reflection coefficient in a pure reflection problem

Consider an incident plane wave in the configuration described by Fig. 2.2(a), where the system is terminated by a free termination at one end. The displacement $\mathbf{w}$ at any point for

$x < 0$ reads as

$$\mathbf{w}(x<0) = \mathbf{a}^{+} + \mathbf{a}^{-} = \mathbf{a}^{+} + \mathbf{R_r} \cdot \mathbf{a}^{+}, \tag{2.19}$$

where $\mathbf{R_r}$ denotes the reflection matrix of the resonant termination of the beam at $x = 0$. The incident wave is transmitted into the resonant termination and reflected at its end, therefore the matrix $\mathbf{R}_r$ can be evaluated, using the displacement continuity at the interface and at the boundary as [121]:

$$\mathbf{R_r} = \mathbf{a}^{-}\mathbf{a}^{+-1} = \mathbf{r_{12}} + \mathbf{t_{12}} \left((\mathbf{f r_f f})^{-1} - \mathbf{r_{21}} \right)^{-1} \mathbf{t_{21}}, \tag{2.20}$$

where $\mathbf{r_{ij}}$ and $\mathbf{t_{ij}}$ represent the reflection and transmission matrices from section (i) to section (j) of the beam (see Fig. 2.2a). Considering continuity and equilibrium respectively at the section change, these matrices are given by

$$\mathbf{t_{ij}} = \frac{4}{\Delta} \begin{bmatrix} (1+\beta)(1+\gamma) & (-1-i\beta)(1-\gamma) \\ (-1+i\beta)(1-\gamma) & (1+\beta)(1+\gamma) \end{bmatrix}, \tag{2.21}$$

$$\mathbf{r_{ij}} = \frac{2}{\Delta} \begin{bmatrix} -2(\beta^2-1)\gamma + i\beta(1-\gamma)^2 & (1-i)\beta(1-\gamma^2) \\ (1+i)\beta(1-\gamma^2) & -2(\beta^2-1)\gamma - i\beta(1-\gamma)^2 \end{bmatrix}, \tag{2.22}$$

where $\beta = \dfrac{k_j}{k_i}$ and $\gamma = \dfrac{D_j k_j^2}{D_i k_i^2}$ correspond to the ratios of wavenumbers and bending wave impedances, and $\Delta = (1+\beta)^2(1+\gamma)^2 - (1+\beta^2)(1-\gamma)^2$. The reflection matrix $\mathbf{r_f}$ of the free termination is given by

$$\mathbf{r_f} = \begin{bmatrix} i & (1-i) \\ (1+i) & -i \end{bmatrix}. \tag{2.23}$$

$\mathbf{R_r}$ is thus a 2×2 matrix where the diagonal components correspond to the reflection coefficients of the propagative and evanescent waves respectively. It is recalled that the study focuses on the reflection of waves in the far-field ($x \to -\infty$), i.e., on the propagative waves that carry the energy. Only $\mathbf{R_r}(1,1)$ and $\mathbf{R_r}(2,1)$ contribute to the reflected field in the abscence of evanescent incident wave. Moreover, $\mathbf{R_N}(2,1)$ vanishes in the far-field ($x \to -\infty$), as it corresponds to the converted waves from propagative to evanescent waves during the reflexion process. The first term of the reflection matrix $\mathbf{R_r}(1,1) = R_r$ is therefore only considered. The absorption coefficient α_R of propagating waves in the reflection problem can then be written as:

$$\alpha_r = 1 - |R_r|^2, \qquad x \to -\infty. \tag{2.24}$$

Note that R_r is simply equal to 1 for any purely real frequency in the lossless case, i.e. without dissipation, as the energy conservation is fulfilled.

2.3.3 Reflection and transmission coefficients in a 1D symmetric and reciprocal transmission problem

The transmission problem of the structure shown in Fig. 2.2(b) is described in this section, considering $\mathbf{b}^{-} = 0$. Due to the symmetry of the resonator and assuming propagation in the linear regime, the problem is considered as symmetric and reciprocal. The reflection and transmission matrices $\mathbf{R_t}$ and $\mathbf{T_t}$ at $x = 0$ and $x = L$ are used to define the displacements on each side of

the resonator, such as:

$$\mathbf{w}(x<0) = \mathbf{a}^{+} + \mathbf{a}^{-} = \mathbf{a}^{+} + \mathbf{R_t} \cdot \mathbf{a}^{+}, \tag{2.25}$$

$$\mathbf{w}(x>L) = \mathbf{b}^{+} = \mathbf{T_t} \cdot \mathbf{a}^{+}. \tag{2.26}$$

Using the displacement continuity at $x = 0$ and $x = L$ in a similar way as in the previous section, $\mathbf{R_t}$ and $\mathbf{T_t}$ are written as:

$$\mathbf{R_t} = \mathbf{r_{12}} + \mathbf{t_{12}} \left((\mathbf{f r_{23} f})^{-1} - \mathbf{r_{21}} \right)^{-1} \mathbf{t_{21}}, \tag{2.27}$$

$$\mathbf{T_t} = \mathbf{a}^{-}\mathbf{a}^{+^{-1}} = \mathbf{t_{23}}(\mathbf{I} - (\mathbf{f r_{21} f})\mathbf{r_{23}})^{-1}\mathbf{f t_{12}}. \tag{2.28}$$

Therefore the absorption coefficient of the transmission problem is defined as:

$$\alpha_t = 1 - |T_t|^2 - |R_t|^2, \qquad x \to \pm\infty \tag{2.29}$$

where $R_t = \mathbf{R_t}(1,1)$ when $x \to -\infty$ and $T_t = \mathbf{T_t}(1,1)$ when $x \to +\infty$.

2.3.4 Viscoelastic losses in the resonator: the RKU model for beams

The inherent losses of the resonator are introduced by a thin absorbing layer of thickness h_l as shown in Figs 2.2(a) and 2.2(b) and are considered frequency independent. The complex Young Modulus of the absorbing layer is $E_l(1 - i\eta_l)$, where η_l is its loss factor. Using the RKU model for beams [154], this region is modeled as a single composite layer with a given effective bending stiffness D_c written as:

$$D_c = E_2 I_2 \left[(1 - i\eta_2) + e_c h_c^3 (1 - i\eta_l) + \frac{3 + (1 + h_c)^2 e_c h_c [1 - \eta_2\eta_l - i(\eta_2 + \eta_l)]}{1 + e_c h_c (1 - i\eta_l)} \right], \tag{2.30}$$

where the indices 2 and l stand for the parameters of the thin beam and of the absorbing layer respectively, $e_c = E_l/E_2$ and $h_c = h_l/h_2$. The wave number k_c of the composite material can then be written as $k_c^4 = \dfrac{\rho_c h \omega^2}{D_c}$, where $h = h_l + h_2$ and $\rho_c h = \rho_2 h_2 + \rho_l h_l$.

2.4 Limits of absorption for the reflection and transmission problems

This section describes the limits of absorption for flexural waves in the reflection and transmission problem by using open, lossy and symmetric resonators. It provides tools to design absorbers with a maximal absorption in both problems. For this purpose, the eigenvalues of the scattering matrix of the propagative waves are represented in the complex frequency plane as in Ref. [153].The information given by this representation will be exploited to interpret the perfect absorption in terms of the critical coupling condition. In particular, the concept of the zeros and poles of the reflection coefficient in the complex frequency plane is introduced through the analysis of the reflection problems. The material and geometric parameters used in the following sections are described in Tab. 2.1.

	Geometric parameters	Material parameters
Main beam	$h_1 = 5$ mm $b = 2$ cm	$\rho = 2811$ kg.m^{-3} $E = 71.4$ GPa $\eta = 0$ $\nu = 0.3$
Resonator beam	$h_2 = 0.217$ mm $b_2 = 2$ cm $L = 1.6$ cm	$\rho_2 = 2811$ kg.m^{-3} $E_2 = 71.4$ GPa $\eta_2 = 0$ $\nu_2 = 0.3$
Coating layer	$h_l = 1.5$ mm $b_l = 2$ cm $L_l = 1.6$ cm	$E_l = 6.86 \times 10^{-3}$ GPa $\rho_l = 93.3$ kg.m^{-3} η_l $\nu_l = 0.3$

TABLE 2.1 – Geometric and material parameters of the studied systems. The value of η_l depends on the experimental set-up used, see the main text for the values used. b, b_2 and b_l correspond to the width of the system.

2.4.1 Reflection problem

a) Lossless case.

In the reflection problem, where no wave is transmitted, the reflection coefficient R_r represents the scattering of the system. Thus, R_r corresponds directly to both the S-matrix and its associated eigenvalue ($\psi = R_r$). Its zeros correspond to the cases in which the incident wave is totally absorbed. In the lossless case, $|R_r| = 1$ for any purely real frequency and the pole-zero pairs appear at complex conjugate frequencies. Fig. 2.3(a) depicts $\log_{10}(|R_r|)$ in the complex frequency plane. The main beam, the resonator beam and the coating layer have the geometric and material parameters given in Tab. 2.1. Note that the Young moduli are purely real in the lossless case ($\eta = \eta_2 = \eta_l = 0$). As shown in Section 2.2.4, the poles and zeros appear in pairs and are symmetric with respect to the real frequency axis. Moreover the value of $|R_r|$ along the real frequency axis is equal to 1 since no energy is lost in the system and the incoming wave is completely reflected back. It is also worth noting that the imaginary part of the pole in the lossless case represents the amount of energy leakage by the resonator through the main beam [153]. With the time dependence convention used in this chapter, the wave amplitude at the resonance frequency decays as $e^{-\mathrm{Im}(\omega_{pole})t}$. Thus the decay time τ_{leak} can be related with the quality factor due to the leakage as $Q_{leak} = \dfrac{\mathrm{Re}(\omega_{pole})\tau_{leak}}{2} = \dfrac{\mathrm{Re}(\omega_{pole})}{2\mathrm{Im}(\omega_{pole})}$, where the leakage rate can be defined as $\Gamma_{leak} = 1/\tau_{leak} = \mathrm{Im}(\omega_{pole})$. The imaginary part of the poles and zeros increases when the real part of the frequency increases, meaning that more energy leaks out through the resonator at high frequencies.

b) Lossy case.

For the sake of clarity, this section only focuses on the first pole-zero pair of the system previously described. The discussion can nevertheless be extended to any pole-zero pair of the

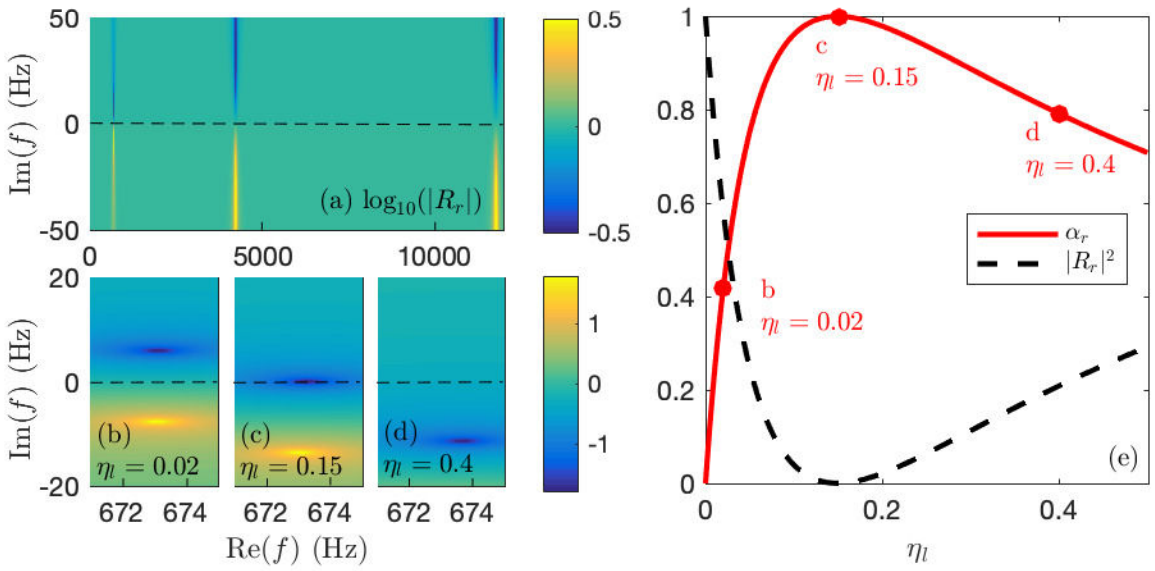

FIGURE 2.3 – Analysis of the scattering in the reflection problem. (a) Representation of $\log_{10}(|R_r|)$ in the complex frequency plane for the lossless case. (b)-(d) $\log_{10}(|R_r|)$ in the complex frequency plane in the lossy case for configurations with $\eta_l = 0.02$, 0.15 and 0.4 respectively. The case when the critical coupling condition is fulfilled ($\eta_l = 0.15$) is represented in (c). (e) Trade-off of the absorption at the first resonance frequency of the resonator as the inherent loss η_l is increased in the system. The points along the absorption curve represent the values of the absorption for the configurations represented in Figs (b)-(d). Red continuous (Black dashed) line represents the absorption (reflection) coefficient as a function of eta_l at 673 Hz, corresponding to the first resonance frequency of the termination.

system in the complex frequency plane. Losses are now introduced into the system by adding an imaginary part to the Young modulus of the damping material such that it can be written as $E_l(1-i\eta_l)$. As a consequence, the symmetry between the poles and zeros with respect to the real frequency axis is broken since the property of Eq. (2.10) is no more satisfied in the lossy case. Figures 2.3b-2.3d depict $\log_{10}(|R_r|)$ in the complex frequency plane around the first resonance frequency for three different increasing values of η_l. Figure 2.3(b) represents the case for which the losses are small ($\eta_l = 0.02$). In this case, the pole-zero pair is quasi-symmetric with respect to the real frequency axis. As the losses in the damping layer increase ($\eta_l = 0.15$ in Fig. 2.3(c) and $\eta_l = 0.4$ in Fig. 2.3(d), the zero moves to the real frequency axis. In particular, the zero of the reflection coefficient is exactly located on the real frequency axis in Fig. 2.3(c). In this situation, the amount of inherent losses in the resonator equals the amount of energy leakage. This situation is known as the critical coupling condition [205] and implies the impedance matching, leading to a perfect absorption.

The value of the absorption coefficient of the first resonant peak as a function of η_l is depicted in Fig. 2.3(e). The position of the zero in the complex frequency plane is directly related to the value of the flexural wave absorption. When the zero approaches the real frequency axis, the value of the absorption is close to one, being equal to 1 when the zero is exactly located in the real frequency axis. It should be noted that the perfect absorption cannot occur once the zero has crossed the real frequency axis. This property might appear counterintuitive since it means that adding a large amount of losses in the system might lead to a deterioration of the absorbing

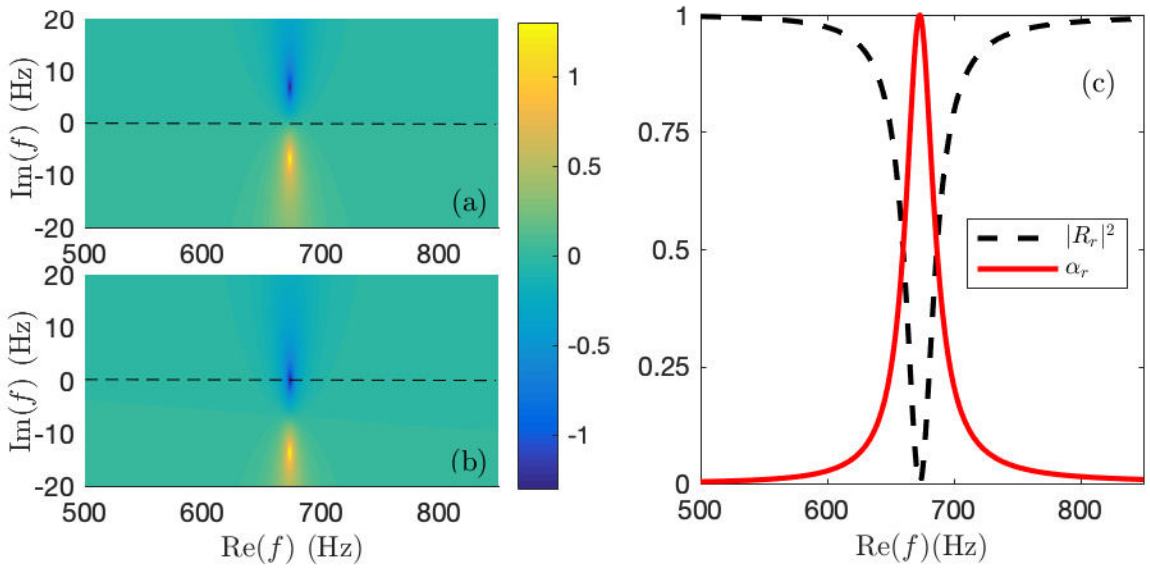

FIGURE 2.4 – Representation of the perfect absorption for the reflection problem. (a), (b) show the representation of the $\log_{10}(|R_r|)$ for the lossless and lossy configurations respectively. (c) Red continuous and black dashed lines show the analytical absorption and reflection coefficients for the critical coupled configuration respectively.

properties of the structure.

c) Design of perfect absorbers for flexural wave in the reflection problem.

A theoretical design for the perfect absorption of flexural waves is shown in this section based on the configuration represented in the Fig. 2.2(b) and the parameters given in Tab. 2.1. Considering that there is no inherent losses in the main beam and the resonator beam ($\eta = \eta_2 = 0$), the loss factor of the coating layer has to be $\eta_l = 0.15$ to obtain a perfect absorption at the first resonance frequency of the system. Figures 2.4(a)-2.4(b) depict $\log_{10}(|R_r|)$ for the lossless and lossy configurations in the complex frequency plane respectively. Figure 2.4b shows particularly the first pole-zero pair of the system in the perfect absorption configuration where the critical coupling condition is fulfilled, showing the zero exactly located on the real frequency axis. Figure 2.4c shows the corresponding absorption (red continuous line) and reflection (black dashed line) coefficients according to real frequencies for the critical coupled configuration. These coefficients are calculated with the analytical model described in previous sections. The incident wave is totally absorbed at the first resonance frequency of the composite beam.

2.4.2 Transmission problem

For the transmission problem, the S-matrix is defined in Eq. (2.1) and has two eigenvalues $\psi_{1,2}$. The scatterer being mirror symmetric, the problem can be reduced to two uncoupled sub-problems: a symmetric problem where $\psi_s = T_t + R_t$ and an anti-symmetric, where $\psi_a = T_t - R_t$. ψ_s corresponds to the eigenvalue of the symmetric problem while ψ_a corresponds to the eigenvalue of the anti-symmetric problem. The absorption coefficient can also be expressed as $\alpha = (\alpha_s + \alpha_a)/2$ where $\alpha_s = 1 - \mid \psi_s \mid^2$ and $\alpha_a = 1 - \mid \psi_a \mid^2$. Similarly to the reflection problem,

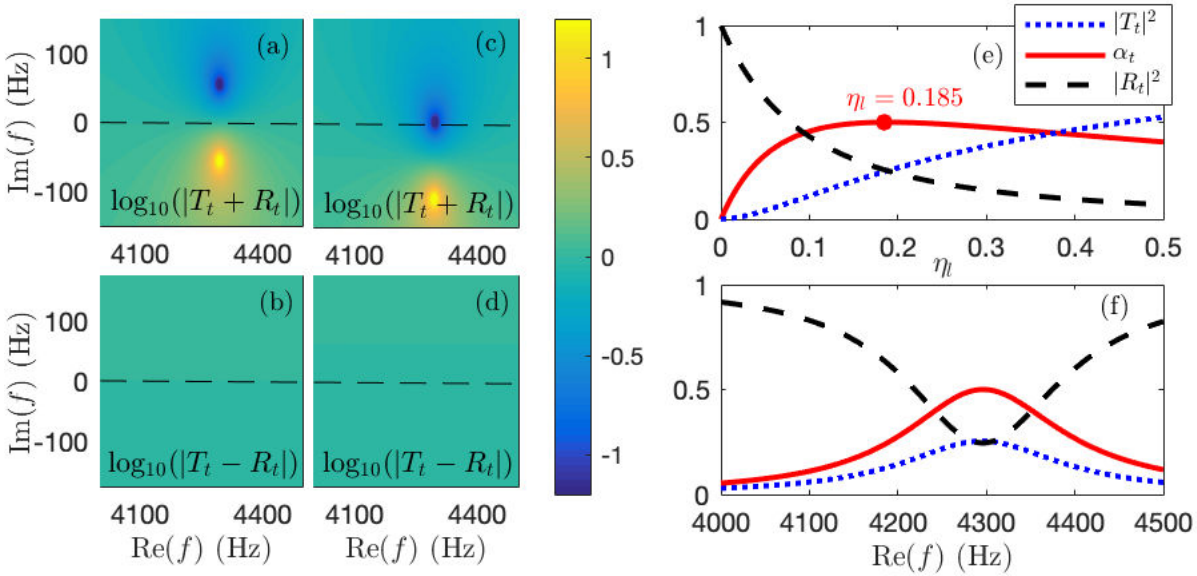

FIGURE 2.5 – Representation of the eigenvalues of the S-matrix for a transmission problem in the lossless and lossy case. (a) and (b) Lossless case for $\log_{10}(|\psi_s|)$ and $\log_{10}(|\psi_a|)$ in the complex frequency plane. (c) and (d) Lossy case for $\log_{10}(|\psi_s|)$ and $\log_{10}(|\psi_a|)$ in the complex frequency plane. (e) Trade-off of the transmission (blue dotted line), reflection (black dashed line) and absorption (red continuous line) for the maximum absorption of the first mode as the loss factor of the coating layer increases. (f) Red continuous, black dashed and blue dotted lines represent the absorption, reflection and transmission coefficients respectively for the half critically coupled configuration.

poles and zeros of ψ_s and ψ_a can be identified in the complex frequency plane. The following sections focuses on the first resonant mode of the beam resonator, the displacement distribution of which is symmetric. The interpretation of the results can nevertheless be applied to the higher order modes with anti-symmetric distributions of the displacement field. It is worth noting that the displacement distribution of the resonant modes changes from symmetric to anti-symmetric as the mode increases due to the geometry of the resonators [97].

a) Lossless case.

Figures 2.5(a) and 2.5(b) show the variation of $\log_{10}(|\psi_s|)$ and $\log_{10}(|\psi_a|)$ evaluated respectively in the complex frequency plane in the lossless case for the first resonant mode. The main beam, the resonator beam and the coating layer of the studied system have still the material and geometric parameters of Tab. 2.1, where $\eta = \eta_2 = \eta_l = 0$ in the lossless case. The symmetric and anti-symmetric problems exhibit pole-zero pairs similarly to the reflection problem in the lossless case. These pairs are also symmetrically positioned with respect to the real frequency axis. The absence of dissipation is shown along the real frequency axis where $|T_t \pm R_t| = 1$ for any real frequency. This section focuses only on the first resonant mode which has a symmetric distribution of the displacement field. Therefore, only the symmetric problem presents a pole-zero pair at the corresponding resonance frequency, while the anti-symmetric one does not.

b) Lossy case.

Unlike the reflection problem, the condition for perfect absorption is stronger in the transmission one and needs to place the zeros of both ψ_s and ψ_a at the same frequency in the real frequency axis. Once this condition is fulfilled, a^+ and b^- correspond to the relevant eigenvector and the system satisfies the Coherent Perfect Absorption (CPA) condition [36, 187, 125]. Losses are introduced in the system in the same way as for the reflection problem, i.e., by increasing the loss factor η_l of the material of the damping layer. Once the losses are introduced, the position of the pole-zero pair of the symmetric eigenvalue in the complex frequency plane shifts towards the upper half space while the anti-symmetric problem remains unchanged without pole-zero pairs, as shown in Figs 2.5(c) and 2.5(d). Therefore, only the zero of the symmetric problem can be placed on the real frequency axis, i.e., only half of the problem can be critically coupled. Figure 2.5(e) shows the dependence of the reflection, transmission and absorption coefficients on the inherent losses in the resonator for the first mode. The maximum absorption obtained is 0.5 since only the symmetric problem is critically coupled ($\alpha = (\alpha_s + \alpha_a)/2 \simeq (1+0)/2 \simeq 1/2$).

c) Design of maximal absorbers for flexural waves in the transmission problem.

Based on the results discussed previously, a configuration with maximal absorption for flexural waves in the transmission problem is designed with the parameters given in Tab. 2.1. As for the reflection problem, no inherent losses are considered in the main beam and the resonator beam ($\eta = \eta_2 = 0$). The loss factor of the coating layer is $\eta_l = 0.185$. The reflection, transmission and absorption for this configuration is analysed in Fig. 2.5(f), showing that the maximum absorption is 0.5 at the resonance frequency of the beam. This result is in accordance with the ones previously obtained [63, 187, 125], even if the resonator is not a point translational impedance. The absorption is limited to 0.5 since only one kind of geometry of resonant mode can be excited. The problem is therefore half critically coupled. To obtain a higher absorption, other strategies based on breaking the symmetry of the resonator [98] or on the use of degenerate resonators are needed [204]. In these cases, both eigenvalues present poles and zeros located at the same real frequencies. It would then be possible to fully critically couple the problem and so obtain a perfect absorption (i.e. $\alpha = 1$) at the appropriate frequency.

2.5 Experimental results

This section presents the experimental results of the reflection coefficient [78, 52] for an aluminum beam system with the configuration described in Section 2.4.1c).

2.5.1 Experimental set-up

The beam is held vertically in order to avoid static deformation due to gravity. The extremity at which the reflection coefficient is estimated is oriented towards the ground (see Fig. 2.6(a)). The used coating layer have been experimentally characterised showing an $\eta_l = 0.15$, which is the value for which perfect absorption can be observed. A photograph of the resonator with the coating layer is shown in Fig. 2.6(b). The measurements are performed along the beam at 21 points equidistant of 5 mm and located on its neutral axis in order to avoid the torsional component. The measurement points are also located sufficiently far from the source and the

extremity of the beam to consider far-field assumption and neglect the contribution of evanescent waves. In this case, far-field assumption is fulfilled at a distance l_f from both the source and the resonator for which the evanescent wave loses 90 % of its initial magnitude. The low frequency limit of the measurements is then estimated using the relation: $e^{-kl_f} = 0.1$. The shaker excites the beam with a sweep sine. The displacement field versus frequency is obtained from the measurements of the vibrometer at each measure point.

2.5.2 Experimental estimation of the reflection coefficient

Consider the flexural displacement $W(x_i, \omega)$ measured at the point $x_i (i \in [0, 20])$ for a given angular frequency ω as

$$W(x_i, \omega) = A(\omega)e^{ikx_i} + B(\omega)e^{-ikx_i}. \tag{2.31}$$

The set of $W(x_i, \omega)$ for each measurement point can be written in a matrix format [52] such as

$$\begin{pmatrix} W(x_0,\omega) \\ W(x_1,\omega) \\ W(x_2,\omega) \\ \vdots \\ W(x_{20},\omega) \end{pmatrix} = \begin{pmatrix} e^{ikx_0} & e^{-ikx_0} \\ e^{ikx_1} & e^{-ikx_1} \\ e^{ikx_2} & e^{-ikx_2} \\ \vdots & \vdots \\ e^{(-ikx_{20})} & e^{(ikx_{20})} \end{pmatrix} \begin{pmatrix} A(\omega) \\ B(\omega) \end{pmatrix}, \tag{2.32}$$

The amplitudes $A(\omega)$ and $B(\omega)$ can then be derived from Eq. (2.32) which forms an overdetermined system. From these amplitudes, the reflection coefficient of the propagative waves can be deduced for any ω as:

$$R_r(\omega) = \frac{A(\omega)}{B(\omega)}. \tag{2.33}$$

2.5.3 Experimental evidence of perfect absorption for flexural waves

Experimental results obtained with the experimental set-up are depicted in Fig. 2.6(c). A drop of reflection is noticed at the first resonant frequency of the termination with a minimum value of $|R_r|^2 = 0.02$ at 667 Hz for the experiment and $|R_r|^2 = 0$ at 673 Hz for the analytical result. The gap between the analytical and experimental resonant frequency is 0.9%. This frequency shift between the model and the experiment is mainly due to the geometric uncertainty in the resonator thickness, induced by the machining process. This geometrical uncertainty induces also an estimation uncertainty of the energy leakage of the resonator. The absorption is then experimentally limited to $\alpha_r = 0.98$. Snapshots of the displacement response of the experimental system are presented in Figs 2.7 and 2.8 for two different frequencies, being $f = 667Hz$ and $f = 800Hz$. A standing wave can be seen in the whole system in Fig. 2.7 since no perfect absorption is provided by the resonator at this specific frequency at one end of the system and a free condition is imposed at the other end. A progressive wave propagating towards the resonator corresponding to the incident wave can be seen in Fig. 2.8. The incident wave is then absorbed by the resonator, avoiding therefore the standing wave. Evidence of perfect absorption for flexural waves by means of critical coupling is shown experimentally here.

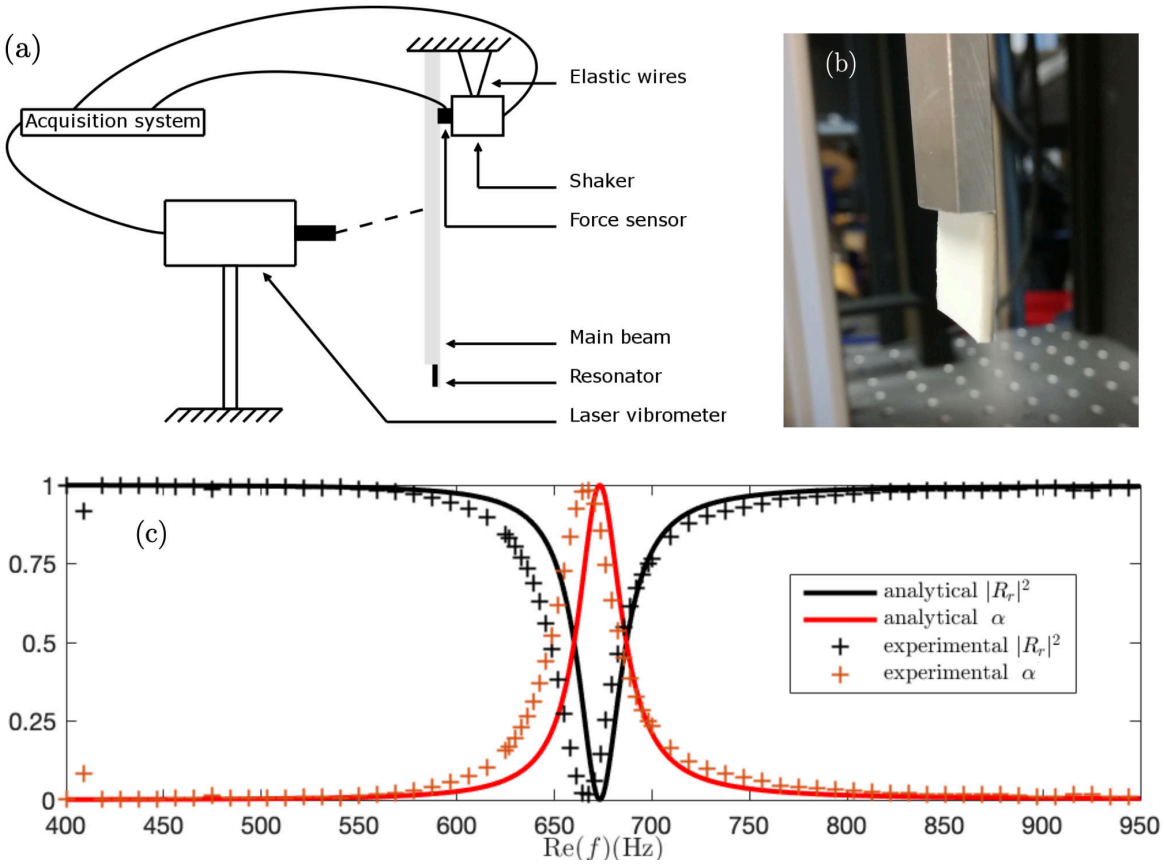

FIGURE 2.6 – (a) Diagram of the experimental set-up. (b) Photograph of the resonator. (c) Black crosses and red open circles show respectively $|R_r|^2$ and α_r for the critical coupled configuration measured with the experimental set-up. Black dashed and red continuous lines show $|R_r|^2$ and α_r calculated with the analytical model.

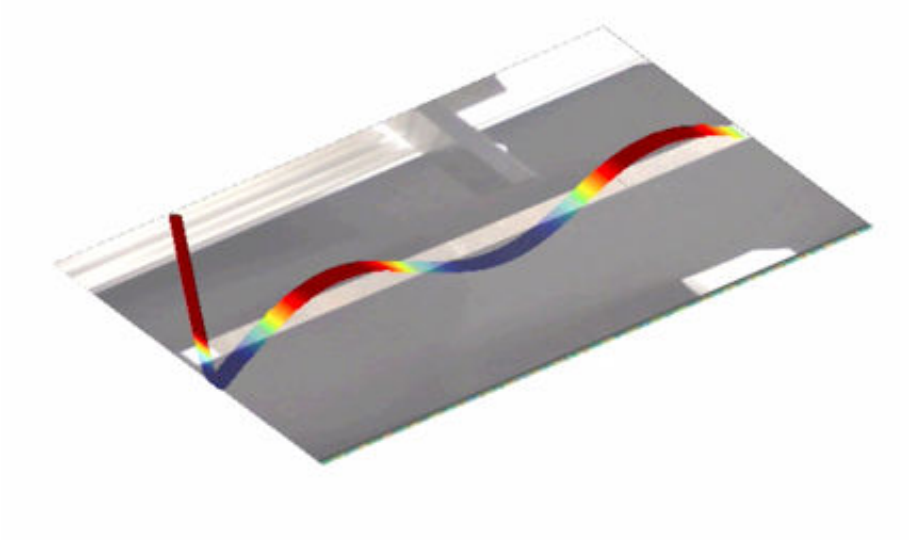

FIGURE 2.7 – Snapshot of the displacement response of the beam system measured with the experimental set-up at 800Hz. The critically coupled resonator is located on the left-hand of the beam system.

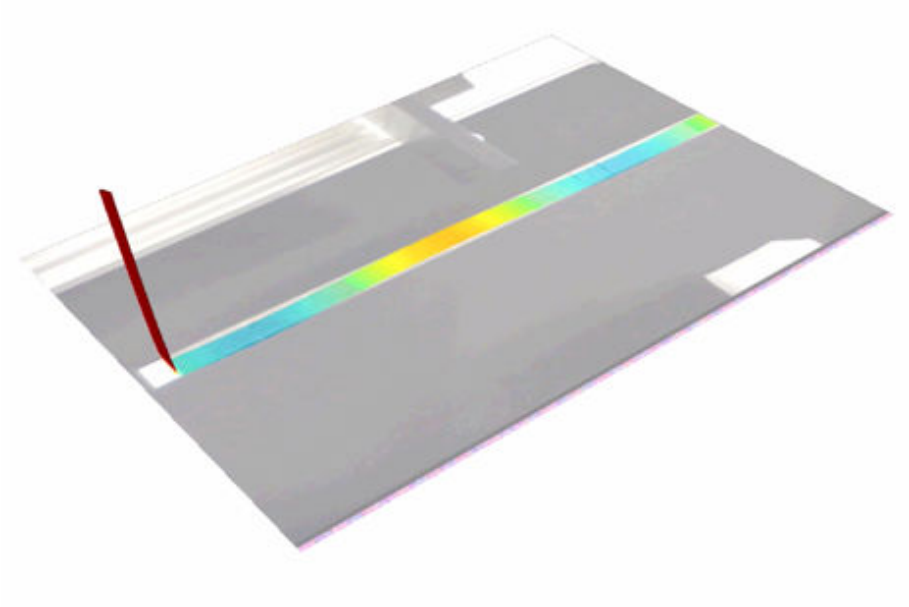

FIGURE 2.8 – Snapshots of the displacement response of the beam system measured with the experimental set-up at 667Hz. The critically coupled resonator is located on the left-hand of the beam system.

2.6 Conclusions

Absorption of propagative flexural waves by means of simple beam structures is analysed in this chapter. The main mechanisms are interpreted in terms of both the critical coupling condition and the symmetries of the resonances for both the reflection and the transmission problems. The positions of the zeros of the eigenvalues of the scattering matrix in the complex frequency plane give informations on the possibility to obtain the perfect absorption. The perfect absorption condition is fulfilled when these zeros are placed on the real frequency axis, meaning that the inherent losses are completely compensating the energy leakage of the system. In the reflection problem, the physical conditions of the problem lead to perfect absorption at low frequencies. In this case a single symmetry for the resonance is excited and perfect absorption can be obtained when the inherent losses of the system balance the energy leakage of the system. In the transmission problem, the requirement to obtain perfect absorption is stronger than for the case in reflection as two kinds of symmetry of the resonances are required to be critically coupled simultaneously. In the case presented in this chapter, or in the general case of point translational impedances, dealing only with one type of symmetry for the resonant modes [63] limits the absorption to 0.5. Two strategies are therefore needed to obtain the perfect absorption in the transmission case: (*i*) breaking the symmetry of the resonator in order to treat the full problem with a single type of symmetry of the resonance mode [98]; (*ii*) using degenerate resonators with two types of symmetries at the same frequency being critically coupled [204]. The resonator used in this study has been chosen as an integral part of the main beam for experimental set-up reasons. However, the presented approach can be applied to any class of 1D resonant-system provided that the resonators are local, open and lossy ones. These properties of the resonator are the essential points to achieve the perfect absorption at low frequency by solving the following problems: increasing the modal density at low frequencies and matching the impedance with the

background medium. The case studied in this chapter performs perfect absorption for a given resonance frequency of the resonator. Its efficiency is therefore tonal. The next step of the work is to design a perfect absorber with a broadband efficiency. To that purpose, the geometry of the resonator is complexified by putting an ABH at the termination of a system.

Chapter 3

Interpretations of the ABH effect by using the complex frequency plane

3.1 Introduction

The representation of the eigenvalues of the scattering matrix in the complex frequency plane has been exploited to interpret and design perfect absorbers of flexural waves in Chapter 2 and in [114]. In the case of a locally resonant termination, such as an ABH termination, the reflection coefficient represents the scattering matrix which is scalar in this kind of problem. As a consequence, the reflection coefficient is the eigenvalue of the problem. Moreover, it has been shown that the reflection coefficient presents pairs of zeros and poles in the complex frequency plane [153, 114]. These zeros and poles are complex conjugates one with respect to the other in the lossless case, thus being symmetric with respect to the real frequency plane. In the ideal case of an ABH in which the thickness is zero, the reflection coefficient should present a continuous number of poles and zeros that coalesce at the real frequency axis. However, this situation is not realistic since the thickness, despite its small value, is nonetheless always finite. In this case, infinite discrete symmetric pairs of poles and zeros appear in the complex frequency plane. At this stage, it is worth noting that the imaginary part of the pole represents the energy leakage between the ABH tip and the main beam as this kind of termination can be interpreted as an open resonator [114].

The damping efficiency of these open resonators can be improved by making use of the inherent losses of the system. In doing so, by taping a layer of viscoelastic material along the thickness profile for instance, the zero and poles can be tuned in the frequency plane. Thus, as shown previously [153, 114], as the losses increase the pairs of zero/pole move along the imaginary frequency axis in the same direction, locating the zeros closer to the real frequency axis. In particular, perfect absorption of the incident wave can be achieved when the zero is located on the real frequency axis, or physically speaking when the energy leakage is perfectly compensated by the added losses, corresponding therefore to the critical coupling condition [205]. Concurrently, it has been shown that the damping efficiency of a practical ABH, also called ABH effect, can be significantly improved by adding a thin layer of viscoelastic material along the ABH profile [106, 107]. The reflection coefficient of such a system has been studied both experimentally [52] and numerically by using various methods detailed in Section 1.2.2c). In general, the ABH effect is characterised by drops of the reflection coefficient at specific frequencies corresponding

to modes of the tapered zone [54]. However, it has not been shown in detail how the losses have to be managed to obtain the perfect absorption of flexural waves.

This chapter focuses on this link between the complex nature of the trapped modes within a 1D ABH and its reflection coefficient drops, in terms of depth and frequency width. More specifically, the purpose of the chapter is to analyse first the absorbing efficiency of the ABH by using the critical coupling condition. The absorption of the ABH termination can be controlled by tuning the losses introduced via the added viscoelastic coating and the geometry of the ABH. Two strategies to optimise the absorption efficiency of an ABH termination at low frequency are then proposed in this chapter, both consisting in applying the critical coupling condition. The first consists in tuning the losses introduced by the viscoelastic layer by shaping its thickness profile in order to achieve the critical coupling condition at several resonances of the ABH. The second strategy is based on the addition of a mass at the extremity of the ABH which decreases the first resonance frequency of the ABH. The critical coupling is then applied at this specific frequency to obtain a low frequency absorption by the termination.

The analysed system is composed of a main beam terminated by an open resonator which corresponds to an ABH of finite length. The ABH termination is discretised by constant thickness piecewise elements. A thin viscoelastic coating is also attached to the ABH creating a composite material. This composite material is modeled with the Ross-Kerwin-Ungar (RKU) method in the same way as in Chapter 2. The vibration response of the composite ABH is studied by means of the Transfer Matrix Method (TMM) [121]. In particular, the eigenvalue of the scattering matrix S, for the propagating waves are analysed in the complex frequency plane [153, 114], providing insightful interpretation on the absorption efficiency of the ABH. All the analytical results are validated against full wave numerical simulations by Finite Element Models, which have been implemented using 2D models of solid mechanics in COMSOL Multiphysics software.

The chapter is organised as follows. In Section 3.2, the theoretical model used to analyse the reflection of flexural wave by a profiled termination is presented for a 1D reflection problem. In Section 3.3, the physical interpretations of the ABH effect of a truncated ABH with a coating layer by using the complex frequency plane in the lossless and lossy cases are presented. Section 3.4 proposes two strategies to optimise the absorption efficiency of an ABH termination at low frequency. The first consists in tuning the losses introduced by the added coating layer in order to apply the critical coupling condition. The second strategy consists in adding a mass at the end of the ABH in order to introduce a degree of freedom in the low frequency regime, where the ABH is not efficient. Finally, Section 3.5 summarises the main results and gives the concluding remarks.

3.2 Theoretical model for the reflection of flexural waves by a profiled termination

This section describes the theoretical model used to study the absorption of flexural waves by a 1D open, lossy, and profiled termination. The model is based on the TMM as proposed by Mace [121] and previously used in Chapter 2 to interpret the perfect absorption of flexural waves of a termination composed of a thin beam of uniform thickness. This method is applied here to calculate the reflection coefficient of finite beam terminations described by $N-1$ piecewise constant property profiles, as depicted in Fig. 3.1.

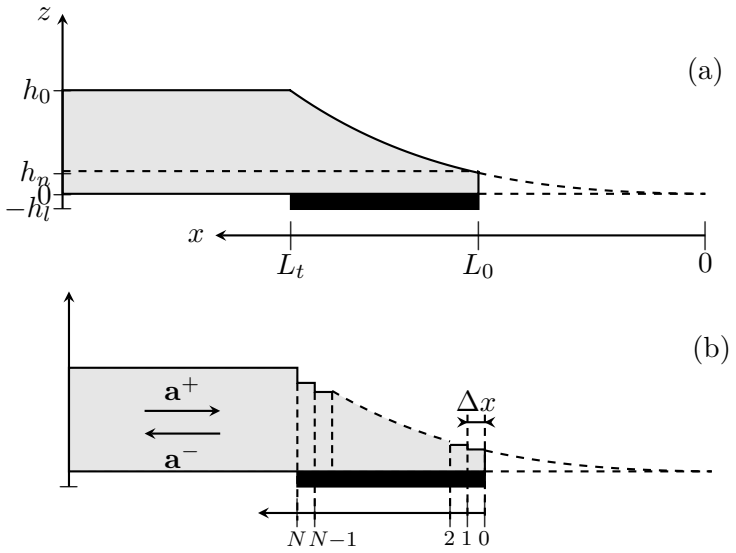

FIGURE 3.1 – (a) Diagrams of the 1D reflection problem for flexural waves with an ABH termination. (b) Spatial discretisation of the thickness profil of the ABH termination.

3.2.1 Reflection problem

Consider a time harmonic ($e^{-i\omega t}$) incident plane wave that impinges the ABH termination from the left (see Fig. 3.1(a)). The ABH is discretised into $N-1$ beams of identical length Δx, but of height h_j, bending stiffness $D_j = EI_j$ where $I_j = bh_j^3/12$ denotes the second moment of area, b being the beam width, and wavenumbers $(k_j)^4 = \dfrac{\rho_j h_j \omega^2}{D_j}$, $j = 0, ..., N$ (see Fig. 3.1(b)). The material of the main beam and the uncoated ABH termination is identical, with E its Young's modulus and ρ its density. The losses are accounted for via a loss factor η, the Young's modulus thus being $E = E(1-i\eta)$. The possible variations of the loss factor against the frequency are ignored in this study, and η is assumed to be constant. This assumption is reasonable in the case of the aluminium beam studied in this chapter. The continuity and equilibrium of the displacement, slope, bending moment and shear force are considered at the interfaces between each consecutive beam. Assuming the Euler-Bernoulli conditions, the flexural displacement $\mathbf{w}$ in the main beam, i.e., for $x > L_t$, reads as

$$\mathbf{w} = \mathbf{a}^+ + \mathbf{a}^- = (\mathbf{I} + \mathbf{R_N}) \cdot \mathbf{a}^+, \tag{3.1}$$

where $\mathbf{a}$ are the complex amplitude vectors of the propagative and evanescent waves, the signs $^+$ and $^-$ denote the ingoing and outgoing waves respectively, $\mathbf{R_N}$ is the reflection matrix at $x = L_t$, i.e. at the interface between the main beam and the ABH termination, and $\mathbf{I}$ is the identity matrix.

The expression of $\mathbf{R_N}$ is a combination of reflection and transmission matrices at the interfaces of all the discrete beams that form the termination. It is obtained iteratively starting from the reflection matrix of the free termination $\mathbf{R_0} = \mathbf{r_{free}}$ given by

$$\mathbf{r_{free}} = \begin{bmatrix} -i & (1-i) \\ (1+i) & -i \end{bmatrix}. \tag{3.2}$$

The iterative scheme takes the following form [121]

$$\mathbf{R_j} = \mathbf{r_{j-1,\,j}} + \mathbf{t_{j-1,\,j}}((\mathbf{f_{j-1}}\mathbf{R_{j-1}}\mathbf{f_{j-1}})^{-1} - \mathbf{r_{j,\,j-1}})^{-1}\mathbf{t_{j,\,j-1}}, \text{for } j = 1 \text{ to } N, \tag{3.3}$$

where $\mathbf{r_{i,j}}$ and $\mathbf{t_{i,j}}$ are the reflection and transmission matrices from section i to section j respectively. Considering the continuity and equilibrium of the displacement, slope, bending moment and shear force, these matrices are given by

$$\mathbf{t_{ij}} = \frac{4}{\Delta_{ij}}\begin{bmatrix} (1+\beta_{ij})(1+\gamma_{ij}) & (-1-i\beta_{ij})(1-\gamma_{ij}) \\ (-1+i\beta_{ij})(1-\gamma_{ij}) & (1+\beta_{ij})(1+\gamma_{ij}) \end{bmatrix}, \tag{3.4}$$

$$\mathbf{r_{ij}} = \frac{2}{\Delta_{ij}}\begin{bmatrix} -2(\beta_{ij}^2-1)\gamma_{ij} + i\beta_{ij}(1-\gamma_{ij})^2 & (1-i)\beta_{ij}(1-\gamma_{ij}^2) \\ (1+i)\beta_{ij}(1-\gamma_{ij}^2) & -2(\beta_{ij}^2-1)\gamma_{ij} - i\beta_{ij}(1-\gamma_{ij})^2 \end{bmatrix}, \tag{3.5}$$

where $\beta_{ij} = \dfrac{k_j}{k_i}$ and $\gamma_{ij} = \dfrac{D_j k_j^2}{D_i k_i^2}$ correspond to the ratios of wavenumbers and bending wave impedances, and $\Delta_{ij} = (1+\beta_{ij})^2(1+\gamma_{ij})^2 - (1+\beta_{ij}^2)(1-\gamma_{ij})^2$. The diagonal transfer matrix in the uniform beams $\mathbf{f_j}$ is expressed as

$$\mathbf{f_j} = \begin{bmatrix} e^{ik_j x} & 0 \\ 0 & e^{-k_j x} \end{bmatrix}. \tag{3.6}$$

$\mathbf{R_N}$ is thus a 2×2 matrix where the upper diagonal component corresponds to the reflection coefficient of the propagative wave. The study focuses on the term $R_N \Leftrightarrow \mathbf{R_N}(1,1)$ that is the only one related to the carried energy. It is recalled that only $\mathbf{R_N}(1,1)$ and $\mathbf{R_N}(2,1)$ contribute to the reflected field in the abscence of evanescent incident wave. Moreover, $\mathbf{R_N}(2,1)$ vanishes in the far-field ($x \to -\infty$), as it corresponds to the converted waves from propagative to evanescent waves during the reflexion process. As the configuration presented in this chapter corresponds to a reflection problem, no wave is transmitted by the termination. In this case, the scattering matrix collapses to a scalar which is the reflection coefficient. Therefore, the reflection coefficient R_N represents the scattering of the system and corresponds directly to both the scattering matrix of the termination and its associated eigenvalue. The absorption coefficient α_R can thus be written as:

$$\alpha_r = 1 - |R_N|^2, \qquad x \to -\infty. \tag{3.7}$$

3.2.2 Introducing viscoelastic losses in the system: the RKU model

A thin viscoelastic layer of identical material, and constant thickness piecewise h_j^l is now added all along the termination length as shown in Fig. 3.1. Each discretised element of the viscoelastic layer coincides with those of the ABH. The losses are assumed to be frequency independent and characterised by a Young's Modulus $E_l(1-i\eta_l)$, where η_l is the loss factor of the viscoelastic material. Using the RKU model [154], the effective bending stiffness D_j^c of the j-th discretised composite beam of the coated tapered area is written as [79]:

$$D_j^c = EI_j\left[(1-i\eta) + e_c\tilde{h}_c^3(1-i\eta_l) + \frac{3+(1+\tilde{h}_c)^2 e_c h_c[1-\eta\eta_l - i(\eta+\eta_l)]}{1+e_c\tilde{h}_c(1-j\eta_l)}\right], \tag{3.8}$$

where the indices j and l stand for the parameters of the uncoated j-th beam of the termination and the absorbing layer respectively, $e_c = E_l/E$ and $\tilde{h}_c = h_j^l/h_j$. In addition, the wave number k_j^c of the j-th composite beam satisfies $(k_j^c)^4 = \dfrac{\rho_j^c h_j^c \omega^2}{D_j^c}$, where $h_j^c = h_j^l + h_j$ is the total composite height and $\rho_j^c = (\rho_j h_j + \rho_l h_l)/h_j^c$ is the density.

3.3 Analysis of R_N in the complex frequency plane to interpret the ABH effect

The absorption of flexural waves by a discretised 1D ABH termination coated by a viscoelastic layer is now analysed in the reflection problem. In this section, the thickness h_j^l of the viscoelastic layer is considered constant such that $h_j^l = h_l$, for $j = 0, ..., N-1$. The eigenvalue of the scattering matrix of the propagative wave reduces to R_N in the current case and is analysed in the complex frequency plane [114, 153]. The material properties and geometric parameters are also given in Tab. 3.1.

	Geometric parameters	Material parameters
Main beam	$h_N = 5$ mm $b = 2$ cm	$\rho = 2700$ kg.m^{-3} $E = 70$ GPa $\eta = 0$
Acoustic Black Hole	$h_0 = 0.1125$ mm $b = 2$ cm $L_t = 20$ cm $L_0 = 3$ cm $N = 201$	ρ_j D_j
Coating layer	$h_l = 0.7$ mm	$E_l = 0.5$ GPa $\rho_l = 950$ kg.m^{-3} η_l

TABLE 3.1 – Geometric and material parameters of the studied systems. The value of the loss factor η_l depends on the experimental set-up used. The parameter b corresponds to the width of the system.

3.3.1 Analysis of lossless ABH terminations with different thickness profiles

Four configurations of termination with different thickness profiles of the uncoated ABH are analysed in this section. The four thickness profiles differ from one another by their power-law χ such that each profile equation reads as :

$$h(x) = h_N \left(\frac{x}{L_t}\right)^{\chi}, \forall x > L_0. \tag{3.9}$$

The analysed orders are linear ($\chi = 1$), quadratic ($\chi = 2$), cubic ($\chi = 3$) and quartic ($\chi = 4$) respectively and are depicted in Fig. 3.2(d). The reflection problem is analysed first for each configuration in the lossless case. In this case, no dissipation is considered and Young moduli are pure real ($\eta = \eta_l = 0$). $\log_{10}(|R_N|)$ of the different thickness profiles are depicted in Fig. 3.2(a)-(d). For each profile order, the poles and zeros are symmetric by pair with respect to the real

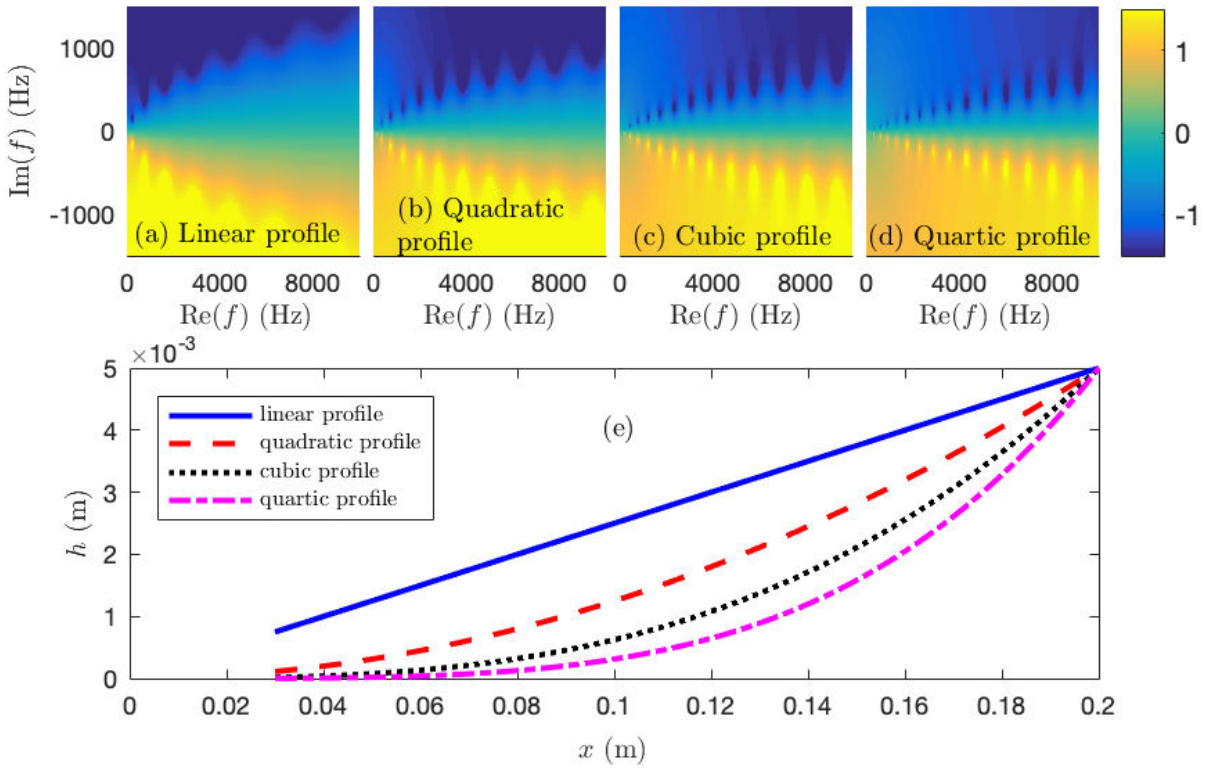

FIGURE 3.2 – (a)-(d) Representation of $\log_{10}(|R_N|)$ in the complex frequency plane for different thickness profiles of ABH in the lossless case (linear, quadratic, cubic and quartic thickness profiles, respectively). (e) Thickness profiles of the ABH studied in (a)-(d).

frequency axis in the lossless case, i.e. the complex frequencies associated to one pair of pole and zero are complex conjugates one from the other. This symmetric distribution comes from the time invariance symmetry of the scattering matrix [153]. The pole frequencies correspond to the resonances of the ABH termination while the zero frequencies correspond to destructive interference phenomena. The value of $|R_N|$ along the real frequency axis is equal to 1 as expected since no energy is lost in the system and the incoming wave is completely reflected back (see Fig. 3.2(d)). Since the ABH terminations are open resonators, the imaginary part of the poles in the lossless case represents the amount of energy leaked by the resonator through the main beam as previously shown in Chapter 2 and in [153]. The quality factor of the resonances can be given by $Q = \frac{\mathrm{Re}(\omega_p)}{2\mathrm{Im}(\omega_p)}$ where ω_p is the complex frequency of the pole.

By observing the general trend of the discrete distribution of poles and zeros, it is possible to note that the imaginary part of the poles (and zeros) increases (decreases) when the real part of the frequency increases, meaning that more energy leaks out through the resonator when the frequency increases. As a consequence, the quality factor of the resonances also decreases as the frequency increases. Two different trends can also be observed according the thickness profiles. On the one hand, the density of poles increases with the order of the profile as shown in Figs. 3.2(a)-(d). On the other hand, the poles/zeros are closer to the real frequency axis as the order of the profile increases, meaning that the modes are more trapped in the termination and that the energy leakage is lower for higher profile orders. As a consequence, the quality factor

Q of the modes increases with the order of the profile, leading to narrower poles and thus zeros.

The previous analysis corresponds to the lossless case. The next stage is to introduce losses in order to shift the zeros to the real frequency axis and design efficient absorbing devices. This situation corresponds to the critical coupling condition at which the introduced losses compensate the energy leakage of the system. Perfect absorption can therefore be observed in that case. In order to do this, a compromise between the density of poles and the quality factor must first be made in order to choose the proper profile. If a low (high) profile order is chosen, the density of poles will be low (high) and the quality factor will be low (high), requiring a big (low) amount of losses to produce a rippled reflection spectrum with broad (narrow) reflection drops. The quadratic profile is chosen here, with $\chi = 2$ which shows a reasonable density of poles with a leakage that can be compensated by realistic materials.

3.3.2 Lossy case

Losses are now introduced into the system by adding an imaginary part to the Young's modulus of the damping material of the viscoelastic coating such that it reads as $E_l(1 - i\eta_l)$. Losses in the uncoated termination and the main beam are neglected ($\eta = 0$). In doing so, the symmetry between the poles and zeros with respect to the real frequency axis is broken [153]. Figures. 3.3(b)-(c) depict $\log_{10}(|R_N|)$ in the complex frequency plane for two different values of η_l, which have to be compared to the lossless case depicted in Fig. 3.3(a) ($\eta_l = 0$). As the losses induced by the damping layer increase ($\eta_l = 2$ in Fig. 3.3(b) and $\eta_l = 4$ in Fig. 3.3(c)), the zeros move to the real frequency axis. Drops of $|R|^2$ appear therefore in Fig. 3.3(d) associated to the resonance frequencies of the ABH termination. The closer to the real frequency axis the zero in the complex frequency plane, the greater the drop of $|R|^2$ with respect to the real frequency with two distinct situations: either the zeros are located in the opposite half space of the poles and there is a lack of loss, or the zeros are located in the same half space as the poles and there is an excess of loss. When the amount of losses exactly compensates the leakage of the system, the corresponding zero of the reflection coefficient is located on the real frequency axis, e.g. at Re(f)=3108 Hz in Fig. 3.3(b). This situation corresponds to the critical coupling condition [205] and implies the impedance matching between the main beam and the resonator, leading to a perfect absorption of the incident wave at this specific real frequency (see Fig. 3.3d). A good agreement between the analytical and numerical results can also be observed in Fig. 2.4(d), therefore validating the analytical model presented in the previous sections.

An overlapping of the zeros on the real frequency axis is observed in Fig. 3.3(b) above the frequency for which the coupling condition is satisfied (3108 Hz). This is due to the geometry of the resonator that leads to low quality factor resonances. The overlapping of the wide zeros results in a broadband quasi-perfect absorption and $|R_N|^2 \simeq 0$ in this frequency range (see Fig. 3.3(d)). This result is one interpretation of the ABH effect at high frequency and is the main contribution of this work. The damping effect of a truncated ABH is the consequence of the critical coupling at one resonance frequency of the ABH and the broadband quasi-perfect absorption at higher frequencies. The critical coupling, and as a consequence the ABH effect of truncated ABH, can be obtained for any power law of thickness profiles, providing that the impedance matching between the main beam and the ABH is achieved by compensating the energy leakage with additional dissipative losses from the viscoelastic layer. However, it is difficult to compensate the leakage with realistic materials for profiles with $\chi < 2$ due to the

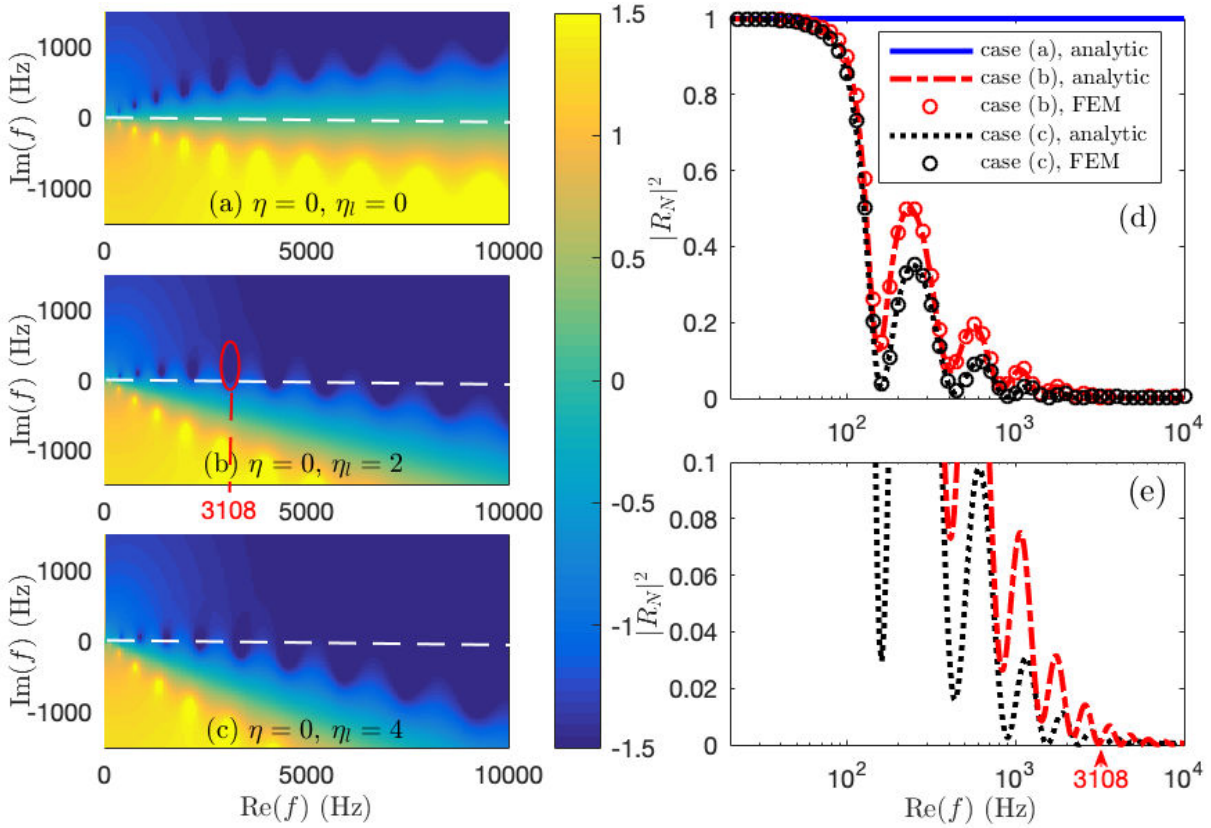

FIGURE 3.3 – (a)-(c) Representation of $\log_{10}(|R_N|)$ in the complex frequency plane for different values of loss factor of the beam η and the viscous layer η_l. (d) Blue continuous, red dash-dotted and black dotted lines show the analytical reflection coefficient according to the real frequency for the configuration of (a),(b) and (c) respectively. Black and red circles show the numerical validations of configuration (b) and (c) respectively. (e) Zoom of the analytical curves of (d).

fact that poles and zeros are far from the real frequency axis in the complex frequency plane, as pointed out by Fig. 3.2(a). In practice, the critical coupling is therefore difficult to attain for such a profile type. For practical application, one interesting goal is to design a system that is critically coupled at the lowest resonance frequency as possible. However, this may require a huge amount of losses, therefore increasing the mass of the system, possibly destroying the higher frequency efficiency. Other strategies should therefore be developed.

3.4 Enhancement of the absorption of an ABH termination

This section proposes methods to enhance the absorption performance of an ABH termination. These methods are based on the use of the complex frequency plane, and can also be applied to any geometry of termination. Two methods are presented. The first one is based on the spatial distribution of the losses introduced by the coating layer by gradually changing its thickness, i.e. h_j^l is also varying with h_j, $j = 0, ..., N-1$. The second one consists in slightly modifying the geometry of the ABH, by adding a mass at the termination end. In this case, the critical coupling at the first zero of the termination may be obtained, leading to a perfect absorption at low frequency.

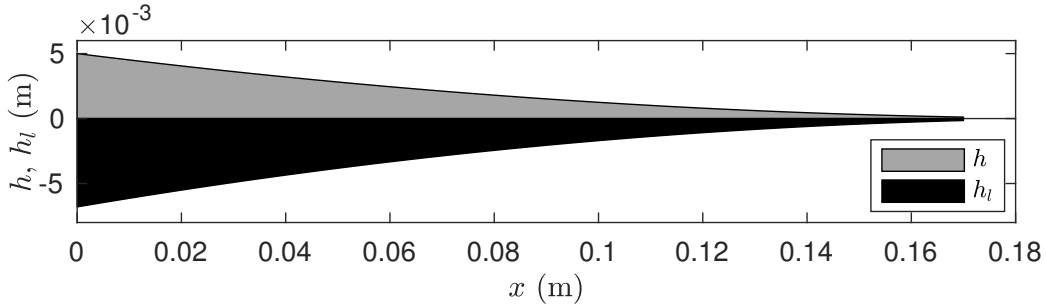

FIGURE 3.4 – Thickness profile of the ABH termination (grey) and the coating layer (black).

3.4.1 Tuning the losses introduced by the coating layer

An enhancement of the absorption properties of an ABH is proposed through tuning the distribution of losses along the ABH termination. Except for the thickness of the coating layer, the geometric and material parameters of the ABH and the coating layer remain the same in this study as in the previous sections (see Tab. 3.1). The thickness profile of the coating layer is shaped so that the losses introduced in the system efficiently compensate the leakage for each resonance of the termination, producing a broadband absorption. The progressive variation of losses is based on a similar phenomenon to graded materials [181]. The incoming wave reduces its speed progressively as it propagates through the ABH. The thickness of the coating layer (and thus the amount of losses) is tapered in such a way that the losses are higher where the wave travels faster. The thickness profile of the coating layer therefore decreases as well as the one of the beam as depicted in Fig. 3.4 and it is defined as:

$$h_l(x) = 1.36 \times h_0 \left(\frac{x}{L_t}\right)^2, \forall x > L_0. \tag{3.10}$$

Figures. 3.5(a)-(b) show the reflection coefficient of the ABH and the coating layer described in Fig. 3.4 in the complex frequency plane in the lossless ($\eta = 0$, $\eta_l = 0$) and lossy ($\eta = 0$, $\eta_l = 2$) cases respectively. As the losses are introduced, the set of zeros are all aligned on the real frequency axis. The critical coupling is therefore performed for each resonance frequency in the analysed frequency band, leading to a total absorption of flexural waves at these particular frequencies. In order to compare, Fig. 3.5(c)-(d) depict the reflection coefficient of the ABH with a coating layer of constant thickness $h_l = 4.7$ mm in the complex frequency plane in the lossless ($\eta = 0$, $\eta_l = 0$) and the lossy cases ($\eta = 0$, $\eta_l = 2$) respectively. Both configurations are designed in such a way that they provide the same absorption performance at the first resonance frequency $f_0 = 185.2$ Hz of the termination in the lossy case. It is worth noting that the quality factor and the density of poles depend on the profile of the coating layer: the uniform coating layer provides a smaller density of poles and smaller quality factors than the profiled one. However larger zeros in the complex frequency plane are present for the uniform profile (see Fig. 3.5(d)).

Contrary to the profiled case, the control of the position of a given zero in the uniform case cannot be achieved independently from the others. This is due to the fact that the losses introduced in the model are frequency independent, and that the thickness of the coating layer and η_l are constant in this case (see Figs. 3.5(c)-(d)). As a result, the distribution of zeros for $\mathrm{Re}(f) > f_0$ is not perfectly aligned on the real frequency axis in the presence of a coating layer

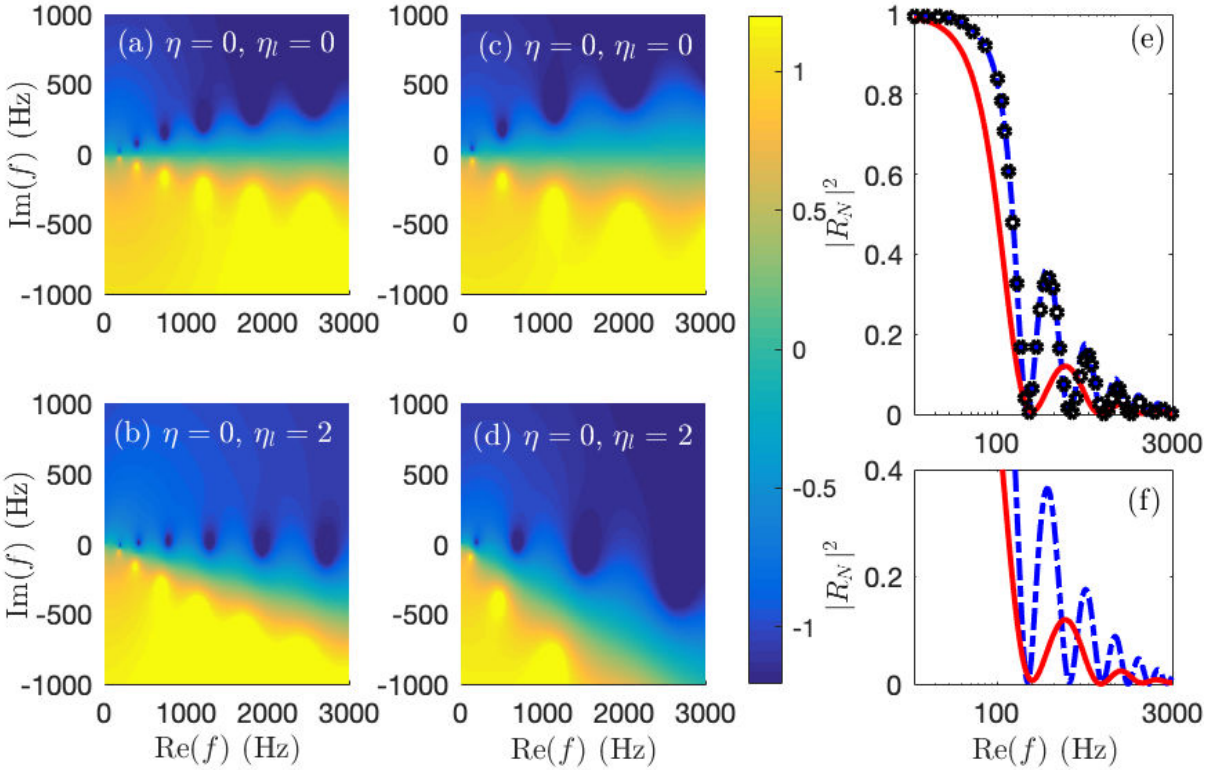

FIGURE 3.5 – (a)-(b) Representation of $\log_{10}(|R_N|)$ of the ABH with the profiled coating layer in the complex frequency plane for the lossless ($\eta = 0$, $\eta_l = 0$) and lossy ($\eta = 0$, $\eta_l = 2$) case respectively. (c)-(d) Representation of $\log_{10}(|R_N|)$ of the ABH with a coating layer of constant thickness ($h_l = 4.7$ mm) in the complex frequency plane for the lossless ($\eta = 0$, $\eta_l = 0$) and lossy ($\eta = 0$, $\eta_l = 2$) case respectively. (e) Blue dash-dotted line and black circles show the reflection coefficient of the ABH with a profiled coating layer according to the real frequencies. Red line shows the analytical reflection coefficient of the ABH with a coating layer of constant thickness ($h_l = 4.7$ mm). (f) Zoom of the analytical curves of (e).

of constant thickness (see the position of the fourth zero in Fig. 3.5(d)). This result highlights the relevance of using profiled coatings to control the position of the zeros independently from the others, and so to produce a cascade of perfect absorption peaks. The reflection coefficients of these two types of ABH terminations are shown in Fig. 3.5(e). The profiled case shows several drops of $|R_N|^2$ corresponding to perfect absorptions. However, the uniform profile has wider peaks due to the lower quality factor of the poles of $|R_N|^2$. The analytical results of the ABH with the profiled coating layer in Fig. 3.5(e) (blue dash-dotted line) are compared with numerical results (red line). The analytical results of the ABH with the profiled coating layer in Fig. 3.5(e) (blue dash-dotted line) are compared with numerical results (red line). A good agreement between both results is noticed.

3.4.2 ABH termination with an added mass

Another parametric analysis based on the complex frequency plane is proposed to improve the absorbing performance of the ABH at low frequencies. The study is carried out by modifying

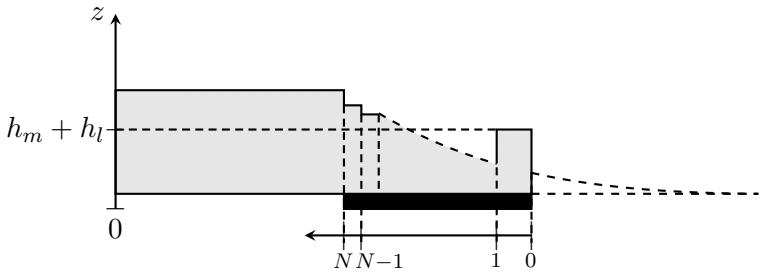

FIGURE 3.6 – Diagram of the spatial discretisation of the ABH with an added mass.

the geometry of the ABH. In particular, a mass is added at the termination end with a varying thickness. The thickness h_m of the mass varies from 0.2 mm to 5 mm. The termination+beam system is still discretised by $N = 201$ beams and the mass consists of increasing the thickness of the 11 first beams of the termination (see Fig. 3.6). The geometric and material parameters of the ABH and the coating layer remain the same as in the previous section and are described in Tab. 3.1. The lossy case is considered here and $\eta = 0$ and $\eta_l = 2$.

Figure. 3.7(a) depicts the reflection coefficient around its first zero in the complex frequency plane for an ABH configuration without added mass. The path of the zero in the complex frequency plane is also depicted according to the increase of the mass thickness in Fig. 3.7(b). As the mass thickness increases, the added mass effect in the termination increases too and the real frequency of the zero decreases. Moreover, the zero moves to the real frequency axis as the mass thickness increases. This is due to a localisation of the mode in the termination, leading to a decrease in leakage and thus a decrease in the absolute value of the imaginary frequency of the zero. In particular, the zero of the reflection coefficient is located on the real frequency axis starting from $h_m = h_N/2$. The critical coupling is therefore obtained and a perfect absorption of the incident wave is observed at $\mathrm{Re}(f) = 80$ Hz and $\mathrm{Re}(f) = 61.5$ Hz for $h_m = h_N/2$ and $h_m = h_N$ respectively (see Fig. 3.7(c)). The analytical results of Fig. 3.7(c) (black dotted, red dashed and blue line) are validated with numerical results (black, red and blue circles), since a good agreement is observed between both models. It is worth noting that the addition of mass does not deteriorate the absorbing properties of the ABH at high frequencies as seen in Fig. 3.7(d). These results highlight the possibility to improve the absorption efficiency of an 1D termination by modifying its geometry and by analysing the position of the zeros of its reflection coefficient in the complex frequency plane.

3.5 Conclusions

Absorption of propagative flexural waves by means of an 1D ABH termination is analysed in this chapter in the case of a reflection problem. The ABH effect is interpreted through the use of the complex frequency plane. The positions of the zeros of the eigenvalues of the scattering matrix in the complex frequency plane provide information on the absorption properties of the ABH. The ABH effect may be interpreted as a consequence of the critical coupling at one resonance frequency of the ABH and of the broadband quasi-perfect absorption at higher frequencies, thanks to the specific geometry of the resonator. This point is the main conclusion of the chapter since it provides a physical explanation of the ABH efficiency. The understanding of this mechanism provides the key to future optimisation procedures of such types of termination.

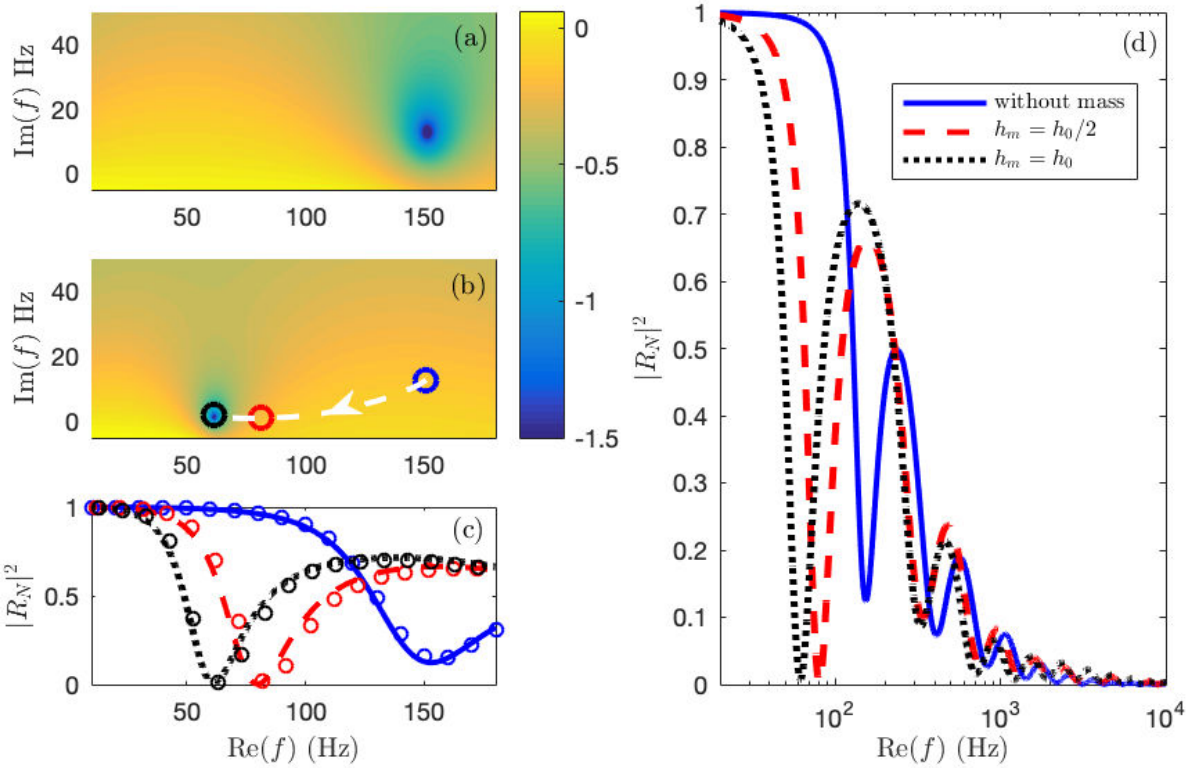

FIGURE 3.7 – (a) Representation of $\log_{10}(|R_N|)$ for the ABH in the complex frequency plane around its first zero. (b) Representation of $\log_{10}(|R_N|)$ in the complex frequency plane around its first zero in the case with an added mass of thickness $h_m = h_l$. White dashed line corresponds to the path of the zero when the thickness of the mass is increased. Blue, red and black circles give the positions of the zero for the configurations ABH ($h_m = h_t$), $h_m = h_0/2$ and $h_m = h_0$ respectively. (c) Blue continuous, red dashed and black dotted lines show the analytical reflection coefficient around the first real resonance frequency for the configurations shown with circles of same color in (b). Blue, red and black circles show the numerical validations. (d) Blue continuous, red dashed and black dotted lines show the analytical reflection coefficient according to the real frequency for the configurations shown with circles of same color in (b).

Two methods are proposed to improve the absorption of a 1D ABH. The first consists in tuning the losses introduced in the system by shaping the thickness profile of the coating layer. In doing so it is possible to control the losses introduced in the resonator according to the real frequency. The second method relies on the addition of a mass at the end of the ABH. The configuration of perfect absorption at the first resonance frequency of the resonator can be obtained and controlled according to the added mass by controlling the position of the corresponding zero in the complex frequency plane.

Chapter 4

Design of the 2D resonant building block by using the critical coupling condition

4.1 Introduction

The critical coupling condition has been presented in the case of 1D beam systems, and has been used to show the perfect absorption of flexural waves in the reflection problem in Chapters 2 and 3. These scattering problems are characterised by a scattering matrix and its eigenvalues, and the position of the zeros of the scattering matrix eigenvalues in the complex frequency plane gives informations on the possibility to obtain the critical coupling condition. It has been shown in previous chapters that the critical coupling condition is fulfilled when a zero is placed on the real frequency axis, meaning that the inherent losses of the system are completely compensating its energy leakage, producing therefore a perfect absorption peak at this specific frequency in the reflection problem. Following this procedure, a perfect absorber at one given frequency in a reflection problem has been designed in Chapter 2 by means of a simple beam termination on top of which a coating layer has been attached. Then, a 1D broadband absorber has been obtained in Chapter 3 by using an ABH termination and by combining the concept of critical coupling with the ABH effect.

The next step of the study is to extend the perfect absorption of flexural waves in 2D systems. Flexural waves propagating in a thin plate are therefore considered instead of a beam, and the resonant inclusion consists of a penetrable circular scatterer embedded in an infinite or semi-infinite thin plate. This penetrable scatterer presents leakage and adding a coating layer on it, as done for 1D resonators in previous chapters, allows the control of its inherent losses. A direct extension of the critical coupling condition in 2D can therefore be performed for the particular case of a concentric incident wave propagating towards the centre of the scatter.

The purpose of this chapter is to study the problem of perfect absorption of flexural waves in 2D thin plates with a local resonator by using the critical coupling condition. Particularly, the energy absorption of the first axisymmetric mode of a circular resonator is analysed through the balance between the energy leakage and the inherent losses of the resonator for the case of a concentric incident wave propagating towards the centre of the resonator. The presented problem is related to the problem of perfect absorption of flexural waves in 1D elastic beams

treated in Chapter 2. The analysed systems are composed of an infinite thin plate and an open resonator consisting in a circular reduction of the thickness of the plate. A thin viscoelastic coating is attached to the resonator in order to introduce losses, leading to a composite material whose losses may be tuned. This composite material is modeled with the Ross-Kerwin-Ungar (RKU) model for plates [154] and is embedded in the hosting plate. By tuning the losses in the same way as in Chapter 2, it is possible to analyse the scattering problem in 2D and design a 2D perfect absorber for a concentric incident wave. The composite is studied by means of a semi-analytical model based on the scattering method, and the interpretations are based on the eigenvalue of the S-matrix for the propagating waves, which is directly the reflection coefficient in this case, represented in the complex frequency plane [153]. A numerical model based on Finite Element formalism is also implemented and validates the analytical predictions. The results obtained in this chapter will be used to design a periodic array of penetrable circular scatterers embedded in an infinite or semi-infinite 2D thin plate. This system constitutes a metaplate whose resonant building block is composed of the penetrable and dissipative scatterers. This problem will be detailed in Chapter 5. The geometry of the resonator then becomes more complex by considering an axysimmetric profiled inclusion using the multilayer scattering approach. It consists of discretising the thickness profile of the resonator into a finite number of layers, and allows to compute the scattering coefficients as well as the propagative and evanescent field amplitudes at each layer. The study is applied in the case of a 2D ABH resonator and shows the efficiency of the method for more complex axisymmetric inclusion.

The chapter is organised as follows. In order to introduce the notations, the study first summarises the governing polar equations and their solutions for the flexural wave propagation in a uniform thin plate in Section 4.2. In Section 4.3, the scattering problem of an concentric incident wave propagating towards the centre of a composite scatterer is treated. The extension of the critical coupling condition for a 2D problem for the $n = 0$ axisymmetric mode of the scatterer is then applied in Section 4.4. The multilayer scattering problem of flexural waves by a 2D profiled scatterer is presented in Section 4.5. This allows to embed any kind of scatterer with radially varying properties in the hosting plate and shows the adaptibility of the method for more complex systems. This model is based on the multilayer scattering model [27]. Finally, Section 4.7 summarises the main results and gives the concluding remarks of the chapter.

4.2 Flexural wave propagation in a uniform thin plate in polar coordinate

This section first aims at introducing the flexural motion equations of thin plates according to the Kirchhoff-Love assumptions. These assumptions possess analogue limitations as the Euler-Bernoulli model in beam theory. However, it is sufficient to cover most of the situations encountered in engineering and are good first approximations to describe the phenomena of flexural wave propagation in thin plates. All these equations can be found in [81, 175, 113], among others. This section summarises them and defines notations for the main purpose of this chapter.

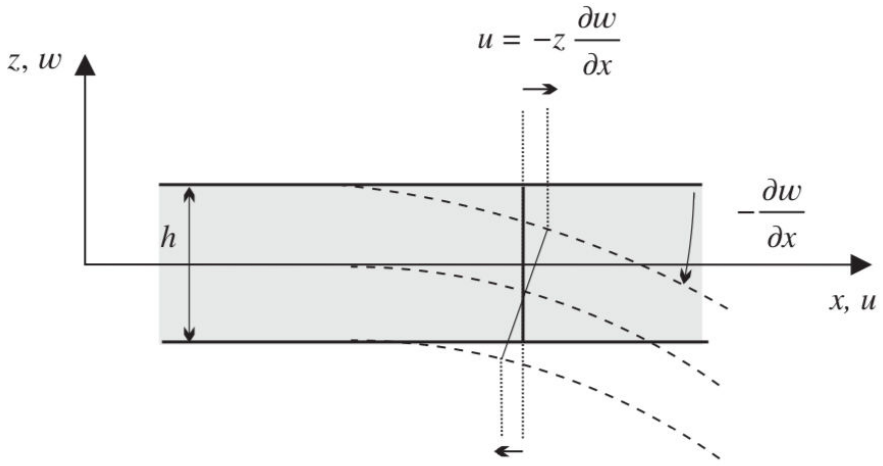

FIGURE 4.1 – Kinematic of the thin plate deformation (from [81]).

4.2.1 Equation for flexural waves in a uniform thin plate

A thin uniform plate according to the Kirchhoff-Love theory is now considered. The assumptions given by this theory are the following [81]:

1. The thickness h of the plate is small compared to its other dimensions and the plate possesses a mean plane.
2. Only the transverse displacement w is considered.
3. The stresses in the transverse directions are neglected.
4. The cross-sections, initially orthogonal to the mean plane, remain plane and orthogonal (see Fig. 4.1), implying that transverse shear strains are neglected.
5. The displacements u and v represented in Fig. (4.1) in the mean plane result from two effects:
   — an initial uniform displacement field over the thickness which results from a loading of the plate in its plane;
   — the rotation of the cross-section.

The differential equation of motion for the transverse displacement $W(r,\theta,t)$ of a plate in the polar coordinate system (O,r,θ) is given by

$$D\Delta^2 W(r,\theta,t) + \rho h \frac{\partial^2 W(r,\theta,t)}{\partial t^2} = q, \tag{4.1}$$

where $D = \frac{Eh^3}{12(1-\nu^2)}$ is the flexural rigidity, ρ the mass density, h the plate thickness and q the external forces applied to the plate. In absence of external forces, Eq (4.1) can be expressed in the harmonic domain with the time convention $W(r,\theta,t) = w(r,\theta)e^{-i\omega t}$ as:

$$\Delta^2 w(r,\theta) - \frac{\rho h \omega^2}{D} w(r,\theta) = 0,$$

$$\Leftrightarrow (\nabla^2\nabla^2 - k^4) w(r,\theta) = [\nabla^2 + k^2][\nabla^2 - k^2] w(r,\theta) = 0, \tag{4.2}$$

where $k^4 = \frac{\rho h \omega^2}{D}$ is the wave number. The solution of Eq. (4.2) can be split in two parts:

$$w(r,\theta) = w_\pi(r,\theta) + w_\epsilon(r,\theta),$$

where $w_\pi(r,\theta)$ and $w_\epsilon(r,\theta)$ are solutions of the following equations, respectively:

$$[\nabla^2 + k^2] w_\pi(r,\theta) = 0, \tag{4.3}$$

$$[\nabla^2 - k^2] w_\epsilon(r,\theta) = 0. \tag{4.4}$$

The first equation corresponds to the Helmholtz equation in which $w_\pi(r,\theta)$ refers to the propagative waves, while the second equation is the modified Helmholtz equation where $w_\epsilon(r,\theta)$ refers to the evanescent waves.

4.2.2 General solution of the flexural motion equation in cylindrical coordinates

a) Expression of w_π

Equation (4.3) is now considered to compute $w_\pi(r,\theta)$. A variable separation is applied first, such that:

$$w_\pi(r,\theta) = R(r)\Theta(\theta). \tag{4.5}$$

By reinjecting Eq. (4.5) into Eq. (4.3) one can obtain:

$$\left(\frac{\partial^2 R}{\partial r^2} + \frac{1}{r}\frac{\partial R}{\partial r}\right)\Theta + \frac{R}{r^2}\frac{\partial \Theta}{\partial \theta} + k^2 R\Theta = 0. \tag{4.6}$$

Equation. (4.6) can therefore be separated into two equations, a first one according to the radial function R and a second according to the angular function Θ:

$$\begin{cases} \dfrac{\partial^2 \Theta}{\partial \theta^2} + \alpha^2 \Theta = 0, \\ \dfrac{\partial^2 R}{\partial r^2} + \dfrac{1}{r}\dfrac{\partial R}{\partial r} + \left(k^2 - \dfrac{\alpha^2}{r^2}\right) R = 0. \end{cases} \tag{4.7}$$

The general solution of the equation satisfied by Θ takes the form of exponential functions $e^{\pm i\alpha\theta}$. However, any point M in the plate having the polar coordinates (r,θ) coincides with the point having the polar coordinates $(r,\theta + 2n\pi)$ where $n \in \mathbb{Z}$. Since the wavefield is uniquely defined at each point of the plate, the solution Θ is 2π-periodic, which implies that $\alpha = n \in \mathbb{Z}$. Furthermore, the differential equation satisfied by R with $\alpha = n \in \mathbb{Z}$ is called the Bessel equation of integer order $n \in \mathbb{Z}$. Any solution of this equation can be written as the linear combination of two independent particular solutions called the Bessel functions of the first and second kind. The expressions of Θ and R can therefore be expressed as:

$$\begin{cases} \Theta_n(\theta) = C_{1n} e^{in\theta}, \\ R_n(r) = C_{2n} \mathrm{J}_n(kr) + C_{3n} \mathrm{Y}_n(kr), \end{cases} \tag{4.8}$$

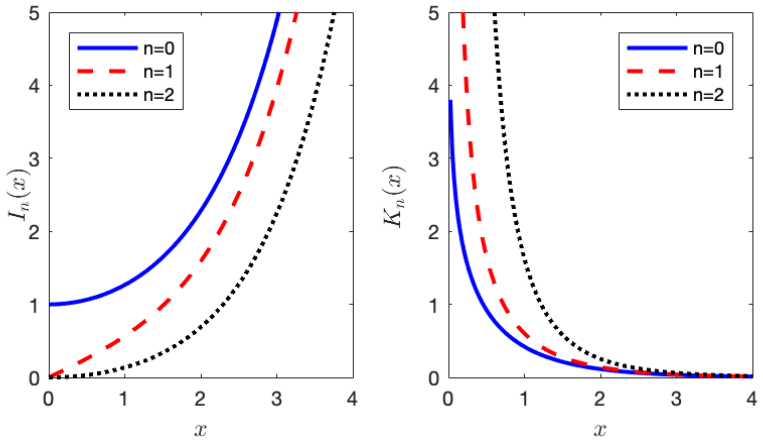

FIGURE 4.2 – Variation of $\mathrm{I}_n(x)$ and $\mathrm{K}_n(x)$ for several orders.

where J_n and Y_n are the Bessel functions of the first and second kind, respectively. By reinjecting both expressions of Eq. (4.8) into Eq. (4.5), the general solution w_π is given by:

$$w_\pi(r,\theta) = \left[A_{\mathrm{J},n}\mathrm{J}_n(kr) + A_{\mathrm{Y},n}\mathrm{Y}_n(kr)\right] e^{in\theta}. \tag{4.9}$$

The amplitudes $A_{\mathrm{J},n}$ and $A_{\mathrm{Y},n}$ are determined according to the boundary conditions of the studied system. The Bessel functions $\mathrm{J}_n(kr)$ and $\mathrm{Y}_n(kr)$ can be seen as standing decaying waves. This can be proven by writing their asymptotic limits as $kr \to \infty$:

$$\mathrm{J}_n(kr) \to \sqrt{\frac{2}{\pi kr}}\cos(kr-\phi_n) \qquad \text{and} \qquad \mathrm{Y}_n(kr) \to \sqrt{\frac{2}{\pi kr}}\sin(kr-\phi_n), \tag{4.10}$$

where $\phi_n = n\frac{\pi}{2} + \frac{\pi}{4}$. In the same way as the complex exponential functions are formed from sine and cosine functions, the Hankel functions of first and second kind $\mathrm{H}_n^{(1)}(kr)$ and $\mathrm{H}_n^{(2)}(kr)$ can be expressed as function of $\mathrm{J}_n(kr)$ and $\mathrm{Y}_n(kr)$, such that: $\mathrm{H}_n^{(1)}(kr) = \mathrm{J}_n(kr) + i\mathrm{Y}_n(kr)$ and $\mathrm{H}_n^{(2)}(kr) = \mathrm{J}_n(kr) - i\mathrm{Y}_n(kr)$. As linear combinations of Bessel functions, the Hankel functions also satisfy the Bessel equation, Eq. (4.7), such that:

$$w_\pi(r,\theta) = \left[A_{\mathrm{H}^{(1)},n}\mathrm{H}_n^{(1)}(kr) + A_{\mathrm{H}^{(2)},n}\mathrm{H}_n^{(2)}(kr)\right] e^{in\theta}. \tag{4.11}$$

$\mathrm{H}_n^{(1)}(kr)$ and $\mathrm{H}_n^{(2)}(kr)$ can be seen as outgoing and ingoing propagating waves respectively according to the time convention $e^{-i\omega t}$. This can also be proven by writing their asymptotic limits as $kr \to \infty$:

$$\mathrm{H}_n^{(1)}(kr) \to \sqrt{\frac{2}{\pi kr}}e^{ikr-\phi_n} \qquad \text{and} \qquad \mathrm{H}_n^{(2)}(kr) \to \sqrt{\frac{2}{\pi kr}}e^{-ikr-\phi_n}. \tag{4.12}$$

These functions will be of importance later in this chapter for the computation of the 2D reflection coefficient, since it requires a decomposition of the fields into ingoing and outgoing waves.

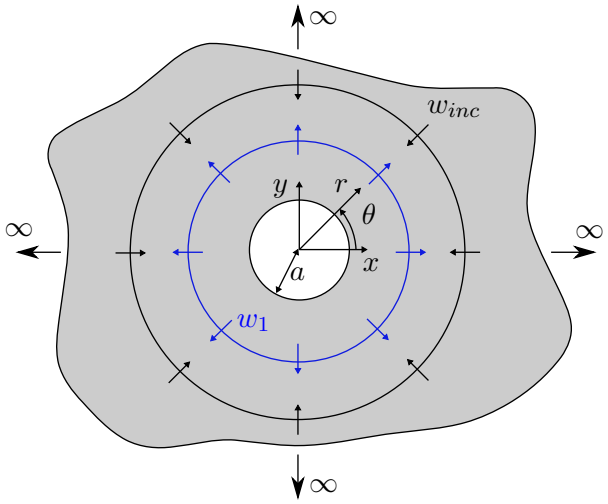

FIGURE 4.3 – Diagram of the 2D scattering problem with a concentric incident wave propagating towards the centre of the resonator.

b) Expression of w_ϵ

The steps to express w_ϵ are similar to those for w_π except that a modified Bessel equation is obtained for the radial part. The solution is therefore expressed as a linear combination of modified Bessel functions of first and second kind $\mathrm{I}_n(x) = i^{-n}\mathrm{J}_n(ix)$ and $\mathrm{K}_n(x) = \frac{\pi i^{n+1}}{2}\mathrm{I}_n(ix)$:

$$w_\epsilon(r,\theta) = \left[A_{\mathrm{I},n}\mathrm{I}_n(kr) + A_{\mathrm{K},n}\mathrm{K}_n(kr)\right] e^{in\theta}, \tag{4.13}$$

Again, the amplitudes $A_{\mathrm{I},n}$ and $A_{\mathrm{K},n}$ are determined according to the boundary conditions of the studied system, and the computation procedure is equivalent to that of propagative amplitudes. Here, the modified Bessel functions describe the evanescent field in the plate as the shapes of the functions are similar to pure real exponential functions (see Fig.4.2).

4.3 Scattering of a uniform circular inclusion in a thin plate

A 2D scattering problem in an infinite thin plate is now presented in order to study the absorption of flexural waves by a 2D open inclusion. This inclusion is also both uniform and circular. This problem has already been treated by Pao and Mow [141] in the case of an incident plane wave. The results for the limiting cases of a rigid inclusion and a cavity have been given by Norris and Vemula [134] and are summarised in Appendix B. This section concerns the particular scattering case of an concentric incident wave propagating towards the centre of a composite scatterer S of radius a (see Figs. 4.3 and 4.4). It aims at introducing the analytical equations and their solutions used in the model to design a 2D perfect absorber. The plate properties are denoted by the index 1 and the uncoated scatterer properties by the index 0. The expressions of the displacement fields in the system are expressed with the polar coordinate system (O, r, θ) whose origin is aligned with the centre of the scatterer (see Fig. 4.3 and 4.4). The RKU model for a plate is first introduced in this section to model the composite material properties of the resonator. The governing equations of the problem and their solutions are then introduced. The boundary conditions are finally presented in order to compute the amplitude of the fields.

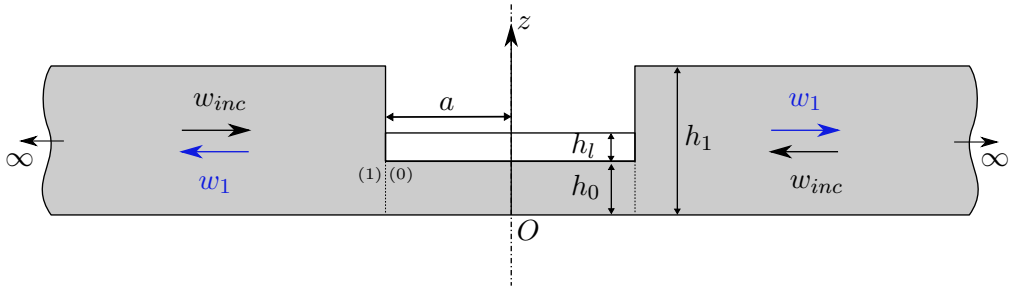

FIGURE 4.4 – Side view of the scattering problem.

4.3.1 Viscoelastic losses in the resonator: the RKU model for plates

The inherent losses of the resonator are introduced by a thin absorbing layer of thickness h_l and are considered frequency independent. The complex Young's Modulus of the absorbing layer is $E_l(1-i\eta_l)$ according to the chosen time convention, where η_l is its loss factor. Using the RKU model for a plate [154] , this region is modeled as a single composite layer with a given effective wave number k_0^p written as:

$$k_0^p = \left(\frac{12\omega^2\rho_0(1-\nu_0^2)}{E_0 h_0^2} \left[\frac{1+\rho_r^p h_r^p}{(1-i\eta_0)+1-i\eta_l)h_r^p E_r^p \alpha^p} \right] \right)^{1/4}, \tag{4.14}$$

where the indices 0 and l stand for the parameters of the uncoated resonator and of the absorbing layer respectively, $\rho_r^p = \frac{\rho_l}{\rho_0}$, $h_r^p = \frac{h_l}{h_0}$, $E_r^p = \frac{E_l}{E_0}$ and $\alpha^p = 3 + 6h_r + 4h_r^2$. The flexural bending stiffness D_0^p can then be written as

$$D_0^p = \frac{h_0^3}{12(1-\nu_0^2)} E_0 \left[(1 + h_r E_r \alpha) - j\left(\eta_0 + \nu_l h_r E_r \alpha\right) \right]. \tag{4.15}$$

The mass density of the composite material corresponds to the mean value of the mass density of the resonator and the absorbing layer, such that:

$$\rho_0^p = \frac{\rho_0 h_0 + \rho_l h_l}{h_0^p}, \tag{4.16}$$

where $h_0^p = h_0 + h_l$, and the Poisson coefficient of the composite is the same as the uncoated resonator's:

$$\nu_0^p = \nu_0. \tag{4.17}$$

4.3.2 Governing equations and their solutions

The flexural displacement field in the plate $w(r,\theta)$ and in the composite scatterer $w_0^p(r,\theta)$ are governed by the following equations respectively:

$$\begin{cases} (\nabla^2\nabla^2 - k_1^4)w(r,\theta) = 0, & \forall r > a, \\ (\nabla^2\nabla^2 - (k_0^p)^4)w_0^p(r,\theta) = 0, & \forall r < a. \end{cases} \tag{4.18}$$

where $k_1^4 = \frac{\rho_1 h_1 \omega^2}{D_1}$, and $(k_0^p)^4$ is defined in Section 4.3.1. The displacement field $w(r,\theta)$ in the plate can be defined as the sum of the incident field $w_{inc}(r,\theta)$ and the scattered field $w_1(r,\theta)$ by using the superposition principle, such that:

$$w(r,\theta) = w_{inc}(r,\theta) + w_1(r,\theta). \tag{4.19}$$

The incident field corresponds to a concentric wave of unitary amplitude which converges towards the centre of the scatterer. Therefore, its expression is given by a Hankel function of the second kind at the order $n = 0$ according to Eq. (4.12) and the time convention used in this chapter:

$$w_{inc}(r) = A_{\mathrm{H},0}^{inc}\mathrm{H}_0^{(2)}(k_1 r), \tag{4.20}$$

where $A_{\mathrm{H},0}^{inc} = 1$. The general expression of w_1 and w_0^p is given by making the sum of Eq. (4.9) and Eq. 4.13 at the order $n = 0$. However, the scattered field at $r > a$ must be represented by outgoing waves and must satisfy the Sommerfeld radiation condition. This condition is fulfilled by $\mathrm{H}_0(k_1 r)$ and $\mathrm{K}_0(k_1 r)$, as shown in Section 4.2.2a), and the scattered field w_1 in the plate is expressed as:

$$w_1 = A_{\mathrm{H},0}\mathrm{H}_0^{(1)}(k_1 r) + A_{\mathrm{K},0}\mathrm{K}_0(k_1 r), \qquad r > a. \tag{4.21}$$

Furthermore, $\mathrm{H}_0(kr)$ and $\mathrm{K}_0(kr)$ are singular as $r \to 0$. The displacement field w_0^p in the composite scatterer is then composed of a sum of a Bessel function and a modified Bessel function of first kind at the order $n = 0$, such that:

$$w_0^p = A_{\mathrm{J},0}\mathrm{J}_0(k_0^p r) + A_{\mathrm{I},0}\mathrm{I}_0(k_0^p r), \qquad r < a. \tag{4.22}$$

It is reminded that these expressions correspond to the case of a concentric incident wave propagating towards the centre of a composite scatterer ($n = 0$) and are a particular case of Norris and Vemula's work [134]. The generalisation of the expressions in the case of an incident plane wave is summarised in Appendix B.

4.3.3 Boundary conditions

Now that the displacement fields have been expressed according to the polar coordinate system (O, r, θ), the boundary condition at the interface between the scatterer and the surrounding plate at $r = a$ can be applied to compute the scattering coefficients $A_{\mathrm{H},0}$, $A_{\mathrm{K},0}$, $A_{\mathrm{J},0}$ and $A_{\mathrm{I},0}$ from the incident amplitude $A_{\mathrm{H},0}^{inc}$. Four boundary conditions at $r = a$ are distinguished according to the Khirchhoff theory, and by ignoring the discontinuities of the mean planes between the inclusion and the surrounding plate:

— displacement continuity

$$w = w_0^p, \tag{4.23}$$

— displacement normal derivative continuity

$$\frac{\partial w}{\partial r} = \frac{\partial w_0^p}{\partial r}, \tag{4.24}$$

— bending moment continuity

$$M\left(w\right) = M_0^p\left(w_0^p\right), \tag{4.25}$$

— (Kirchhoff) shear force continuity

$$V\left(w\right) = V_0^p\left(w_0^p\right), \tag{4.26}$$

with [175]

$$M_i(w_i) = -D_i\frac{\partial^2 w_i}{\partial r^2} - D_i\nu_i\left(\frac{1}{r}\frac{\partial w_i}{\partial r} + \frac{1}{r^2}\frac{\partial^2 w_i}{\partial\theta^2}\right), \tag{4.27}$$

and

$$V_i(w_i) = -D_i\frac{\partial}{\partial r}\nabla^2 w_i - D_i(1-\nu_i)\frac{1}{r^2}\frac{\partial^2}{\partial\theta^2}\left(\frac{\partial w_i}{\partial r} - \frac{w_i}{r}\right), \tag{4.28}$$

where the index i can take the values 1 or $^p_0$, which denote the plate and the composite scatterer, respectively. Applying these continuity conditions leads to the equation system [134]:

$$\mathbf{A_0}.\mathbf{x_0} = \mathbf{B_0}, \tag{4.29}$$

with

$$\mathbf{A_0} = \begin{pmatrix} \mathrm{H}_0^{(1)}(\varepsilon_1) & \mathrm{K}_0(\varepsilon_1) & -\mathrm{J}_0(\varepsilon_0^p) & -\mathrm{I}_0(\varepsilon_0^p) \\ \mathrm{H}_0^{(1)'}(\varepsilon_1) & \mathrm{K}_0'(\varepsilon_1) & -\kappa\mathrm{J}_0'(\varepsilon_0^p) & -\kappa\mathrm{I}_0'(\varepsilon_0^p) \\ S^1_{\mathrm{H}_0} & S^1_{\mathrm{K}_0} & -\mathcal{D}S^p_{\mathrm{J}_0} & -\mathcal{D}S^p_{\mathrm{I}_0} \\ T^1_{\mathrm{H}_0} & T^1_{\mathrm{K}_0} & -\mathcal{D}T^p_{\mathrm{J}_0} & -\mathcal{D}T^p_{\mathrm{I}_0} \end{pmatrix},$$

$$\mathbf{x_0} = \begin{pmatrix} A_{\mathrm{H},0} \\ A_{\mathrm{K},0} \\ A_{\mathrm{J},0} \\ A_{\mathrm{I},0} \end{pmatrix}, \qquad \mathbf{B_0} = -\begin{pmatrix} \mathrm{H}_0^{(2)}(\varepsilon_1) \\ \mathrm{H}_0^{(2)'}(\varepsilon_1) \\ S^1_{\mathrm{H}_0^{(2)}} \\ T^1_{\mathrm{H}_0^{(2)}} \end{pmatrix},$$

$\kappa = \frac{k_0^p}{k_1}$, $\varepsilon_1 = k_1 a$, $\varepsilon_0^p = k_0^p a = \kappa\varepsilon_1$ and $\mathcal{D} = \frac{D_0^p}{D_1}$.

$$S^p_{X_n} = \left[n^2(1-\nu_0) \mp \varepsilon_0^{p2}\right] X_n(\varepsilon_0^p) - (1-\nu_0)\varepsilon_0^p X_n'(\varepsilon_0^p), \tag{4.30}$$

$$S^1_{X_n} = \left[n^2(1-\nu_1) \mp \varepsilon_1^2\right] X_n(\varepsilon_1) - (1-\nu_1)\varepsilon_1 X_n'(\varepsilon_1), \tag{4.31}$$

$$T^p_{X_n} = n^2(1-\nu_0)X_n(\varepsilon_0^p) - \left[n^2(1-\nu_0) \pm (\varepsilon_0^p)^2\right] X_n'(\varepsilon_0^p), \tag{4.32}$$

$$T^1_{X_n} = n^2(1-\nu_1)X_n(\varepsilon_1) - \left[n^2(1-\nu_1) \pm (\varepsilon_1)^2\right] X_n'(\varepsilon_1), \tag{4.33}$$

Here, prime denotes $\frac{\partial}{\partial r}$. The upper sign in Eqs. (4.30)-(4.33) is taken when $X_n = \mathrm{J}_n$ or $\mathrm{H}_n^{(1)}$

	Geometric parameters	Material parameters
Host plate	$h_1 = 5$ mm	$\rho_1 = 2800$ kg.m^{-3} $E_1 = 70$ GPa $\eta_1 = 0$ $\nu_1 = 0.3$
Inclusion	$h_0 = 0.84$ mm $a = 10$ cm	$\rho_0 = 2800$ kg.m^{-3} $E_0 = 70$ GPa $\nu_0 = 0.3$ $\eta_0 = 0$
Coating layer	$h_l = 0.7$ mm	$E_l = 0.5$ GPa $\rho_l = 950$ kg.m^{-3} $\nu_l = 0.3$ η_l

TABLE 4.1 – Geometric and material parameters of the studied systems. The value of η_l depends on the experimental set-up used, see main text for the values used.

while the lower sign is taken when $X_n = \mathrm{I}_n$ or K_n. The solution of the equation system (4.29) gives the scattering coefficients $A_{\mathrm{H},0}$, $A_{\mathrm{K},0}$, $A_{\mathrm{J},0}$ and $A_{\mathrm{I},0}$ for $n = 0$. This system is still valid for any order $n \in \mathbb{Z}$ provided that the order is replaced for every Bessel and Hankel function.

4.4 Extension of the critical coupling condition in a 2D problem for the $n = 0$ axisymmetric mode

This section describes the extension of the critical coupling condition in a 2D problem for the $n = 0$ axisymmetric mode of a uniform circular scatterer. It provides tools to design absorbers with a maximal absorption when the incident wave is concentric and defined by a Hankel function of the second kind at the order $n = 0$. For this purpose, the reflection coefficient of the propagative waves ($r \to \infty$), which is the only reflection coefficient related to the carried energy, is first defined for the specific case of an incident wave propagating towards the centre of the scatterer. The incident wave is therefore described by a Hankel function of the second kind: $w_{inc} = \mathrm{H}_n^{(2)}(k_1 r)$. The reflection coefficient is then represented in the complex frequency plane. The information given by this representation will be exploited to interpret the perfect absorption in terms of the critical coupling condition, as introduced in Chapter 2. The concept of the zeros and poles of the reflection coefficient in the complex frequency plane is once again shown in this section through the analysis of the reflection problem. The open resonator is represented by a circular reduction of the thickness of the plate, the material and geometric parameters of which are described in Tab. 4.1.

4.4.1 Reflection coefficient in 2D scattering problems

The reflection coefficient describes how much an incident wave is reflected by a discontinuity. It is closely related to the transmission coefficient which corresponds to the amount of energy that is transmitted through the discontinuity. These coefficients can be easily defined for a 1D

reflection problem by doing the ratio between the reflected or transmitted wave amplitude over the incident wave amplitude. Note that the incident wave interacts entirely with the discontinuity and the amount of its energy that is not reflected is transmitted or absorbed by the discontinuity. These coefficients can be computed for 2D systems in which the discontinuity is a plane separating two media. In this case, the reflection coefficient corresponds to the amount of energy that is coming back to the medium where it comes from. However, the definition of the 2D reflection coefficient is not straightforward when the discontinuity separates a circular medium from an infinite medium, since one part of the incident wave may not interact with the circular medium and remain undisturbed. The term *scattered wave* instead of *reflected wave* is therefore used. The scattering-cross section Q_{sc} is generally used to evaluate the energy deviated or scattered by the scatterer. This quantity is defined as the ratio between the total energy flux of the scattered field and the flux per unit length of the incident field [134] and is given by:

$$Q_{sc} = \frac{1}{2}\int_0^{2\pi} \mid f(\theta) \mid^2 \mathrm{d}\theta, \tag{4.34}$$

where $f(\theta)$ is the far-field ($r \to \infty$) magnitude of the scattered field.

In the particular scattering problem of an incident wave propagating towards the centre of a circular scatterer given by the expression of Eq. (4.20), the incident wave interacts completely with the scatterer and its energy is either reflected or transmitted through the edge of the scatterer. The scattered field corresponds therefore to a reflected field and the scattering-cross section is equivalent to a 2D reflection coefficent. In this case, the reflected field represents the field that diverges from the centre of the scatterer. The reflection coefficient of the propagative waves τ_0 is then the ratio between the amplitude of the wave diverging from the scatterer centre over the amplitude of the wave converging towards the scatterer centre, such that:

$$\tau_0 = \frac{A_{\mathrm{H},0}}{A^{inc}_{\mathrm{H},0}}. \tag{4.35}$$

It is worth noting that even if the incident wave can be transmitted through the scatterer edge, this problem corresponds to a reflection problem and τ_0 represents the scattering of the system since no wave is transmitted by the resonator itself.

4.4.2 Analysis of τ_0 in the complex frequency plane for the lossless case

As mentioned in the previous section, the reflection coefficient τ_0 represents the scattering of the system in the reflection problem since no wave is transmitted by the resonator. Thus, τ_0 corresponds directly to both the S-matrix and its associated eigenvalue, and its zeros correspond to the cases in which the incident wave is totally absorbed (see Section 2.2). In the lossless case, $|\tau_0| = 1$ for any purely real frequency and the pole-zero pairs appear at complex conjugate frequencies. Figure 4.5 depicts $\log_{10}(|\tau_0|)$ in the complex frequency plane for the lossless case. The plate, the resonator and the coating layer have the geometric and material parameters given in Tab. 2.1. Note again that the Young's moduli are purely real in the lossless case ($\eta_0 = \eta_1 = \eta_l = 0$). Similarly to the case of a 1D beam resonator studied in Section 2.4.1a), the poles and zeros appear in pairs and are symmetric with respect to the real frequency axis. The imaginary part of the pole in the lossless case represents the amount of energy leakage by the resonator through

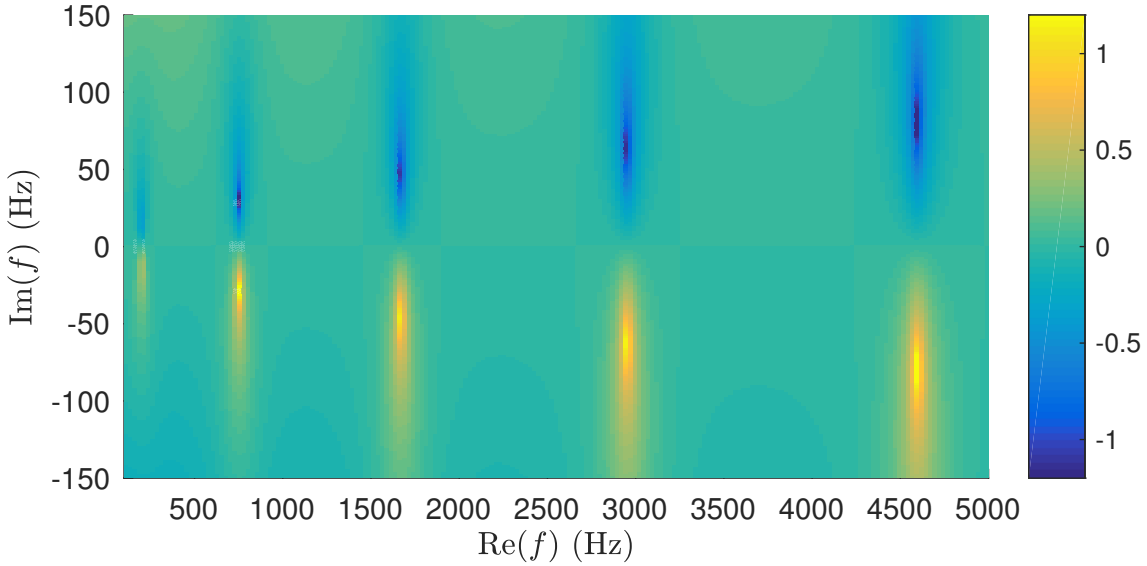

FIGURE 4.5 – Representation of log10($|\tau_0|$) in the complex frequency plane for the lossless case. The real frequency of each pole corresponds only to the resonance frequency of the axisymmetric modes of the resonator since the incident wave imposes axisymmetric displacements at its edge.

the surrounding plate [153]. Moreover, the incident wave imposes axisymmetric displacements at the edge of the resonator. The only modes that are excited are therefore the ones with an axisymmetric modeshape. As a result, the real frequency of each pole in Fig 4.5 corresponds only to the resonance frequency of one axisymmetric modes of the resonator.

a) Perfect absorption of 2D flexural waves for the $n = 0$ axisymmetric mode of a uniform circular resonator

A theoretical design for the perfect absorption of flexural waves is shown in this section based on the configuration represented in Fig. 4.3 and the parameters given in Tab. 4.1. Considering that there are no inherent losses in the resonator and the surrounding plate ($\eta_0 = \eta_1 = 0$), the loss factor of the coating layer has to be $\eta_l = 2$ to obtain a perfect absorption at the first resonance frequency corresponding to the first axisymmetric mode ($n = 0$) of the resonator. This value has been found by increasing progressively the losses until attaining the perfect absorption as the zero reaches the real frequency axis.

Figures 4.6(a)-4.6(b) depict $\log_{10}(|\tau_0|)$ for the lossless and lossy configurations in the complex frequency plane, respectively. In particular, Fig. 4.6(b) shows the first pole-zero pair of the system in the perfect absorption configuration where the critical coupling condition is fulfilled, showing the zero exactly located on the real frequency axis. This particular configuration corresponds to the situation where the amount of inherent losses in the resonator equals the amount of energy leakage (see Section 2.4.1 for more details). Figure 4.6(c) shows the corresponding reflection (red dashed line) and absorption (black continuous line) coefficients and the scattering-cross section (blue dotted line) according to real frequencies for the critical coupled configuration. $\alpha \approx 1$ and $|\tau_0| \approx 0$ at the first resonance frequency of the composite inclusion (at Re(f) = 184.9 Hz), meaning that the incident wave is totally absorbed at this specific frequency. The analytical reflection coefficient $|\tau_0|$ is also compared in Fig. 4.6(c) with numerical results (magenta crossed

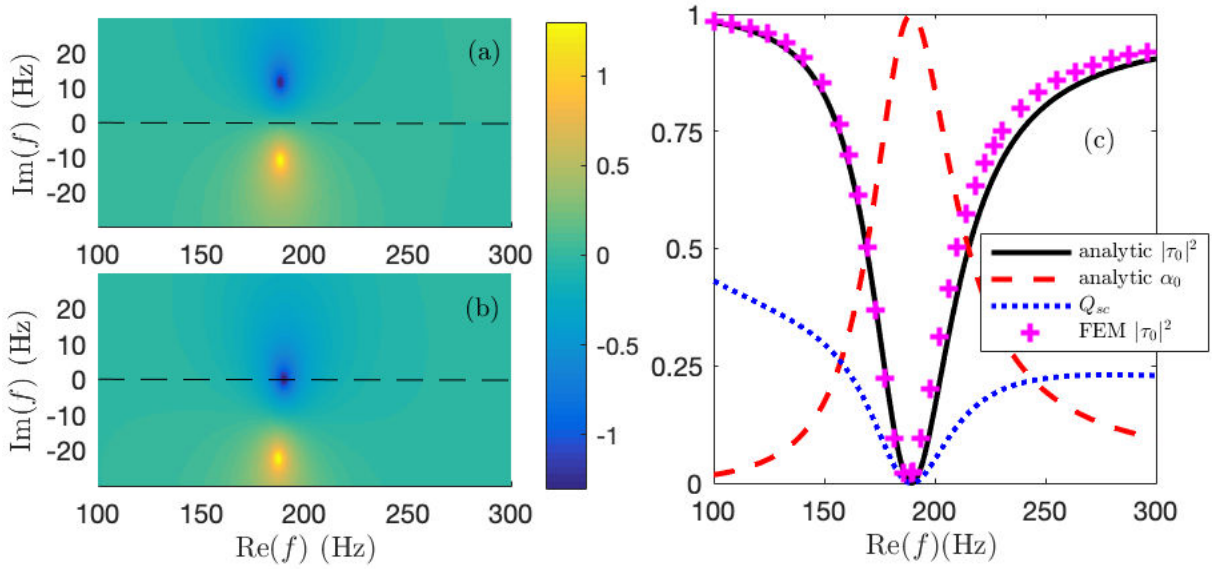

FIGURE 4.6 – Representation of the perfect absorption for the reflection problem. (a), (b) show the representation of the $\log_{10}(|\tau_0|)$ for the lossless and lossy configurations respectively. (c) Black continuous and red dashed lines show the analytical reflection and absorption coefficients for the critical coupled configuration respectively. Blue dotted line corresponds to the scattering cross-section and the magenta crossed line corresponds to the reflection coefficient obtained using a FEM model.

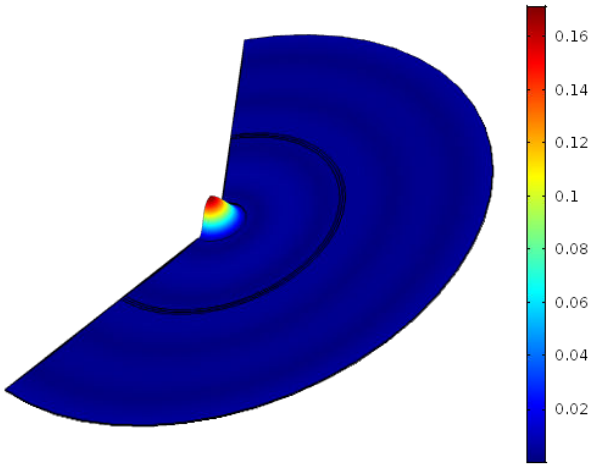

FIGURE 4.7 – Displacement response (in m) of the circular resonator embedded at the centre of a circular plate for the critically coupled configuration ($\mathrm{Re}(f) = 184.9$ Hz, $\eta_l = 2$), using a 2D axisymmetric model of solid mechanics in COMSOL software. The concentric incident wave is simulated by imposing a load at the edge of the circular plate.

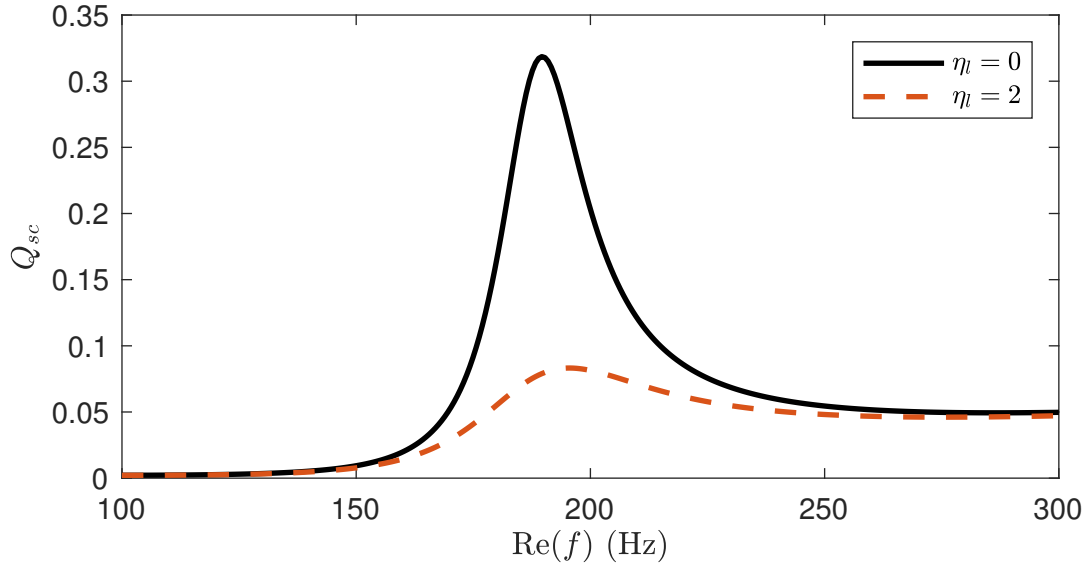

FIGURE 4.8 – Representation of Q_{sc} in the lossless (continuous black line) and lossy (red dashed line, $\eta_l = 2$) cases for an incident wave defined by a Bessel function of the first kind at the order $n = 0$. The parameters of the inclusion are given in Tab. 4.1. The lossy case corresponds to the critically coupled configuration of the inclusion when the incident wave is described by a Hankel function of the second kind $\mathrm{H}_n^{(2)}(x)$.

line) obtained with a FEM model. The FEM model has been implemented by using a 2D axisymmetric model of solid mechanics in COMSOL software. The geometry of the model is composed of a circular plate at the centre of which is placed the inclusion. The concentric incident wave is simulated by imposing a load at the edge of the circular plate. A good agreement of both results can be noticed, which validates the analytic model. The scattering-cross section (blue dotted line) in Fig. 4.6(c) also has a zero value at the first resonance frequency of the inclusion. This result highlights that it is as relevant to use Q_{sc} as τ_0 to study the absorption of the inclusion in the particular case of an incident wave converging towards the centre of the inclusion and described by a Hankel function of the second kind $\mathrm{H}_n^{(2)}(x)$.

b) Remarks on the scattering-cross section

The previous section highlights that it is as relevant to use Q_{sc} as τ_0 to study the absorption of the inclusion in the particular case of an incident wave converging towards the centre of the inclusion and described by a Hankel function of the second kind $\mathrm{H}_n^{(2)}(x)$. However, most of the scattering problems are studied with an incident plane wave defined as a linear combination of Bessel functions of the first kind $\mathrm{J}_n(x)$. In this case, the study of absorption by using Q_{sc} has to be taken with precaution due to the properties of the Bessel function of the first kind. To illustrate this point, the same scattering problem as presented in Fig. 4.3 is studied again except that a Bessel function of the first kind at the order $n = 0$ is considered instead of a Hankel function of the second kind : $w_{inc} = \mathrm{J}_0(k_1 r)$.

The parameters of the scatterer remain the same as before and are given in Tab. 4.1. Therefore, the scatterer should still totally absorb all the wave which converges toward its centre at $\mathrm{Re}(f) \approx 184.9$ Hz, as shown in Fig. 4.6c. Figure 4.8 depicts Q_{sc} in the lossless (continuous black

line) and lossy (red dashed line, $\eta_l = 2$) case. The lossy case corresponds to the critically coupled configuration of the inclusion when the incident wave is described by a Hankel function of the second kind $\mathrm{H}_n^{(2)}(x)$. A maximum of Q_{sc} in the lossy case instead of a minimum is observed at the first resonance frequency of the scatterer in Fig. 4.8. The maximum of absorption can no longer be observed as a minimum of Q_{sc}. This result is due to the properties of the incident wave $\mathrm{J}_0(k_1 r)$, which can be expressed as a linear combination of a Hankel function of the first kind and a Hankel function of the second kind, such that:

$$\mathrm{J}_0(k_1 r) = \frac{1}{2}\left(\mathrm{H}_0^{(1)}(k_1 r) + \mathrm{H}_0^{(2)}(k_1 r)\right). \tag{4.36}$$

This means that $\mathrm{J}_0(k_1 r)$ is composed of a converging and a diverging component according to Eqs.(4.12). In this case, the definitions of τ_0 and Q_{sc} given in Section 4.4.1, are not equivalent anymore since the incident wave contains a diverging component. A reflection coefficient for the propagative wave can nonetheless be computed in this case by separating the diverging and the converging component of the incident field of (4.36). Considering again an incident wave of unitary amplitude $w_{inc} = \mathrm{J}_0(k_1 r)$, the total converging field w_{conv} in the plate corresponds to one part of the incident wave and can be written as:

$$w_{conv} = \frac{1}{2}\mathrm{H}_0^{(1)}(k_1 r). \tag{4.37}$$

The diverging field w_{div} in the plate which corresponds to the scattered field and the other part of the incident wave, is expressed as:

$$w_{div} = \left(\frac{1}{2} + A_{\mathrm{H},0}\right)\mathrm{H}_0^{(2)}(k_1 r). \tag{4.38}$$

The reflection coefficient τ_0' takes therefore the form:

$$\tau_0' = 2A_{\mathrm{H},0} + 1. \tag{4.39}$$

This observation can be extended to any order $n \in \mathbb{Z}$ of Bessel function and to the case of an incident plane wave. These results highlight that Q_{sc} cannot be related to the absorption of a scatterer for a general scattering problem with an incident plane wave.

4.5 Multilayer scattering of flexural waves by a 2D profiled scatterer

Now, the problem becomes more complex by studying the scattering of a penetrable scatterer S with a radially varying thickness profile and coated by a viscoelastic layer. The scatterer is perfectly bonded to the plate along the boundary r_N. The model used for that purpose is the multi-layer scattering method, where the continuous variation of the parameters of the system uncoated scatterer+infinite plate has been discretised in a finite number N of homogeneous axisymmetric layers [27]. The layers are numbered, such that the surrounding plate corresponds to $j = N$ and the core layer corresponds to $j = 0$. This method consists of a semi-analytical approach that provides the scattering coefficients of each layer. The uncoated layers are distributed into concentric rings of identical length δ_r, but of radially varying height h_j, bending

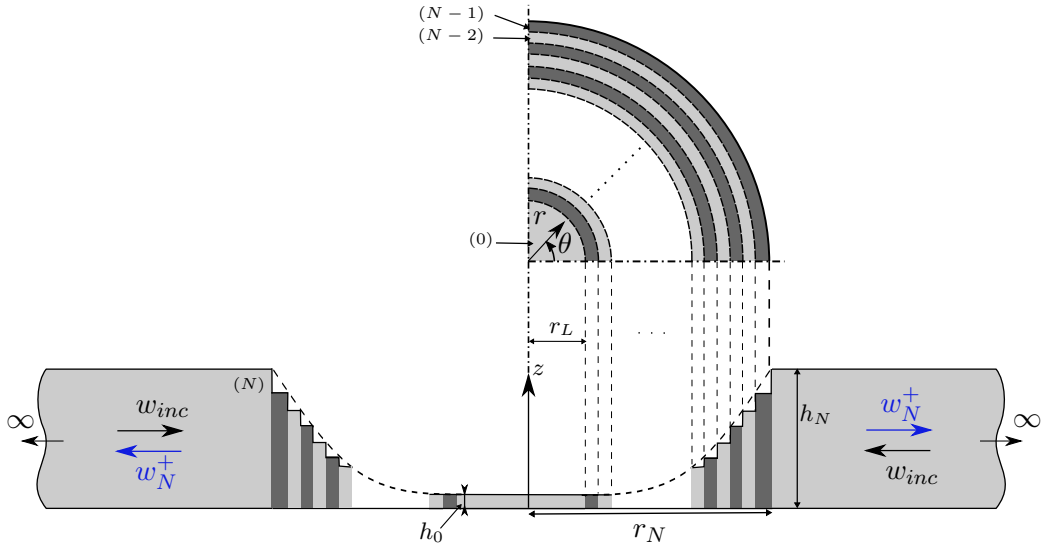

FIGURE 4.9 – Diagram of the 2D scattering problem with a concentric incident wave propagating towards the centre of a resonator with radially varying thickness.

stiffness $D_j = \frac{Eh_j^3}{12(1-\nu_j^2)}$, and wavenumber $k_j^2 = \omega\sqrt{\frac{\rho h_j}{D_j}}$, $j = 0, ..., N$ as shown in Fig. 4.9. The materials of the plate and the uncoated scatterer are identical, with E the Young's modulus and ρ its density. The losses are accounted for via a loss factor η, the Young's modulus thus being $E = E(1 - i\eta)$. A concentric incident wave w_{inc} propagating in layer N toward the centre of the scatterer is considered. It is defined by a Hankel function of the second kind at the order $n = 0$ as written in Eq. (4.20). The scatterer thickness varies between $r_0 < r < r_N$ by following a quadratic law, leading to an ABH thickness profile defined as:

$$h(r_j) = h_N \left(\frac{r}{r_N}\right)^2, \forall r < r_N. \tag{4.40}$$

A plateau of constant thickness h_0 is therefore considered for all $r < r_0$ (see Fig. 4.9).

4.5.1 The RKU model for the multi-layered resonator

The inherent losses of the multi-layered resonator are introduced by a thin absorbing layer of thickness h_l and are considered frequency independent similarly to previous sections. The complex Young's Modulus of the absorbing layer is still expressed as $E_l(1-i\eta_l)$. Using the RKU model [154] for a plate, each coated layer j is modeled as a single composite layer with a given effective wave number k_j^p written as:

$$k_j^p = \left(\frac{12\omega^2\rho_j(1-\nu_j^2)}{E_j h_j^2}\left[\frac{1+\rho_{j,r}^p h_{j,r}^p}{(1-i\eta_j)+1-i\eta_l)h_{j,r}^p E_{j,r}^p \alpha^p}\right]\right)^{1/4}, \tag{4.41}$$

where the indices j and l stand for the parameters of the uncoated j-th layer and of the absorbing layer respectively, $\rho_{j,r}^p = \frac{\rho_l}{\rho_j}$, $h_{j,r}^p = \frac{h_l}{h_j}$, $E_{j,r}^p = \frac{E_l}{E_j}$ and $\alpha^p = 3 + 6h_r + 4h_r^2$. The flexural bending

stiffness D_1^p can then be written as:

$$D_j^p = \frac{h_j^3}{12(1-\nu_j^2)} E_j \left[(1 + h_{j,r} E_{j,r} \alpha) - j \left(\eta_j + \nu_l h_{j,r} E_{j,r} \alpha \right) \right]. \tag{4.42}$$

The mass density of the composite material is expressed as:

$$\rho_j^p = \frac{\rho_j h_j + \rho_l h_l}{h_j^p}, \tag{4.43}$$

where $h_j^p = h_j + h_l$, and the Poisson coefficient of the composite is supposed to be the same as the uncoated resonator's:

$$\nu_j^p = \nu_j. \tag{4.44}$$

4.5.2 Governing equations

A polar coordinate system aligned with the centre of the inclusion is now considered. The equation of flexural motion in the scatterer+plate system is still modeled by using the Kirchoff-Love approximation [81]. Assuming time harmonic behaviour ($e^{-i\omega t}$) and no external forces, the equation of the flexural displacement w_j^p at each coated ring can be written along the z-axis as:

$$\left[\nabla^2 \nabla^2 - (k_j^p)^4 \right] w_j^p(r, \theta) = 0. \tag{4.45}$$

The flexural field w_j^p of the j-th coated layer is described as the sum of the field w_j^{p-} transmitted by the $(j+1)$-th layer with the field w_j^{p+} scattered by the $(j-1)$-th layer:

$$w_j^p = w_j^{p-} + w_j^{p+} = A_{\mathrm{J},0}^{(j)} \mathrm{J}_0(k_j^p r) + A_{\mathrm{I},0}^{(j)} \mathrm{I}_0(k_j^p r) + A_{\mathrm{H},0}^{(j)} \mathrm{H}_0^{(1)}(k_j^p r) + A_{\mathrm{K},0}^{(j)} \mathrm{K}_0(k_j^p r). \tag{4.46}$$

The notation $^-$ describes a converging propagation of the fields towards the centre of S and $^+$ denotes a diverging propagation. However, this definition is not valid for the layer 0 due to the singularity of $\mathrm{H}_n(z)$ and $\mathrm{K}_n(z)$ when $z = 0$. The field of the layer 0 has then to be described as:

$$w_0 = A_{\mathrm{J},0}^{(0)} \mathrm{J}_0(k_0 r) + A_{\mathrm{I},0}^{(0)} \mathrm{I}_0(k_0 r). \tag{4.47}$$

The field of layer N, corresponding to the surrounding plate, is given by the sum of the incident field w_{inc} with the field w_N^+ scattered by the first layer of the scatterer:

$$w_N = w_{inc} + w_N^+ = A_{\mathrm{H},0}^{inc} \mathrm{H}_0^{(2)}(k_N r) + A_{\mathrm{H},0}^{(N)} \mathrm{H}_0^{(1)}(k_N r) + A_{\mathrm{K},0}^{(N)} \mathrm{K}_0(k_N r). \tag{4.48}$$

For the sake of clarity, the amplitudes $A_{\mathrm{J},0}^{(j)}$ and $A_{\mathrm{I},0}^{(j)}$ are now gathered in a vector $\mathbf{W}_{\mathbf{0,j}}^- = \begin{pmatrix} A_{\mathrm{J},0}^{(j)} \\ A_{\mathrm{I},0}^{(j)} \end{pmatrix}$, and the amplitudes $A_{\mathrm{H},0}^{(j)}$ and $A_{\mathrm{K},0}^{(j)}$ in $\mathbf{W}_{\mathbf{0,j}}^+ = \begin{pmatrix} A_{\mathrm{H},0}^{(j)} \\ A_{\mathrm{K},0}^{(j)} \end{pmatrix}$.

4.5.3 Scattering matrix

The scattering problem of a scatterer with radially varying properties cannot be studied by extending the problem of a uniform scatterer as shown in Section 4.4 due to the presence of ingoing and outgoing waves at each layer. A multilayer scattering approach is therefore adopted to characterise this problem. This approach gives the relation between the converging and diverging amplitudes at each interface between two consecutive layers j and $j+1$, such that:

$$\begin{pmatrix} \mathbf{W^-_{0,j}} \\ \mathbf{W^+_{0,j+1}} \end{pmatrix} = \begin{pmatrix} \mathbf{T^-_{0,j+1}} & \mathbf{R^-_{0,j+1}} \\ \mathbf{R^+_{0,j+1}} & \mathbf{T^+_{0,j+1}} \end{pmatrix} \begin{pmatrix} \mathbf{W^-_{0,j+1}} \\ \mathbf{W^+_{0,j}} \end{pmatrix} = \mathbf{S_{j+1}} \begin{pmatrix} \mathbf{W^-_{0,j+1}} \\ \mathbf{W^+_{0,j}} \end{pmatrix}, \tag{4.49}$$

where $\mathbf{S_j + 1}$ is the scattering matrix of interface $j+1$, $\mathbf{T^-_{0,j+1}}$ and $\mathbf{T^+_{0,j+1}}$ are respectively the converging and diverging transmission coefficients at interface $j+1$, and $\mathbf{R^-_{0,j+1}}$ and $\mathbf{R^+_{0,j+1}}$ the converging and diverging reflection coefficients. As the scattering problem implies propagative and evanescent waves, the scattering matrix involves coefficients of size 2×2. The coefficients are computed using the continuity conditions at each interface [40]. The steps to compute the scattering coefficients as well as the propagative and evanescent field amplitudes at each layer of the scatterer are detailed in Appendix C according to [27]. The reflection coefficient of the propagative waves at each layer j may be defined as the ratio of the amplitude of the converging propagative wave in the j-th layer $A^j_{\mathrm{J},0}$ over the amplitude of the propagative scattered wave in the j-th layer $A^{(j)}_{\mathrm{H},0}$, such that:

$$\tau_0^j = \frac{A^j_{\mathrm{J},0}}{A^{(j)}_{\mathrm{H},0}}. \tag{4.50}$$

The difference between τ_0^j and the propagative term of $\mathbf{R^+_{0,j}}$ is that the latter characterises the reflection of propagative and evanescent waves at a given interface j regardless of the other interfaces, while τ_0^j characterises the reflection of the propagative waves in the system composed of j layers. The global reflection coefficient τ_0^N of the ABH for the propagative waves is determined by making the ratio of the incident wave amplitude $A^{inc}_{\mathrm{H},0}$ over the amplitude of the propagative scattered wave in the plate $A^{(N)}_{\mathrm{H},0}$ and can be written as:

$$\tau_0^N = \frac{A^{(inc)}_{\mathrm{H},0}}{A^{(N)}_{\mathrm{H},0}}. \tag{4.51}$$

4.6 Perfect absorption of 2D flexural waves for the $n = 0$ axisymmetric mode of a 2D ABH

A theoretical design for the perfect absorption of flexural waves is shown in this section based on the configuration represented in Fig. 4.10 and the parameters given in Tab. 4.2. Considering that there are no inherent losses in the uncoated resonator and the surrounding plate ($\eta = 0$), the loss factor of the coating layer has to be $\eta_l = 0.35$ to obtain a perfect absorption at the first resonance frequency corresponding to the axisymmetric mode ($n = 0$) of the ABH. This value has been found, similarly to the case of a uniform circular resonator, by increasing progressively the losses until attaining the perfect absorption as the zero reaches the real frequency axis.

Figures 4.10(a)-4.10(b) depict $\log_{10}(|\tau_0^N|)$ for the lossless and lossy configurations in the com-

	Geometric parameters	Material parameters
Host plate	$h_N = 5$ mm	$\rho = 2800$ kg.m^{-3} $E = 70$ GPa $\eta = 0$ $\nu = 0.3$
Acoustic Black Hole	$h_0 = 0.2$ mm $r_0 = 2$ cm $r_N = 10$ cm $N = 151$	ρ_j D_j
Coating layer	$h_l = 0.7$ mm	$E_l = 0.5$ GPa $\rho_l = 950$ kg.m^{-3} η_l $\nu_l = 0.3$

TABLE 4.2 – Geometric and material parameters of the multi-layer scattering problem. The value of η_l depends on the experimental set-up used, see main text for the values used.

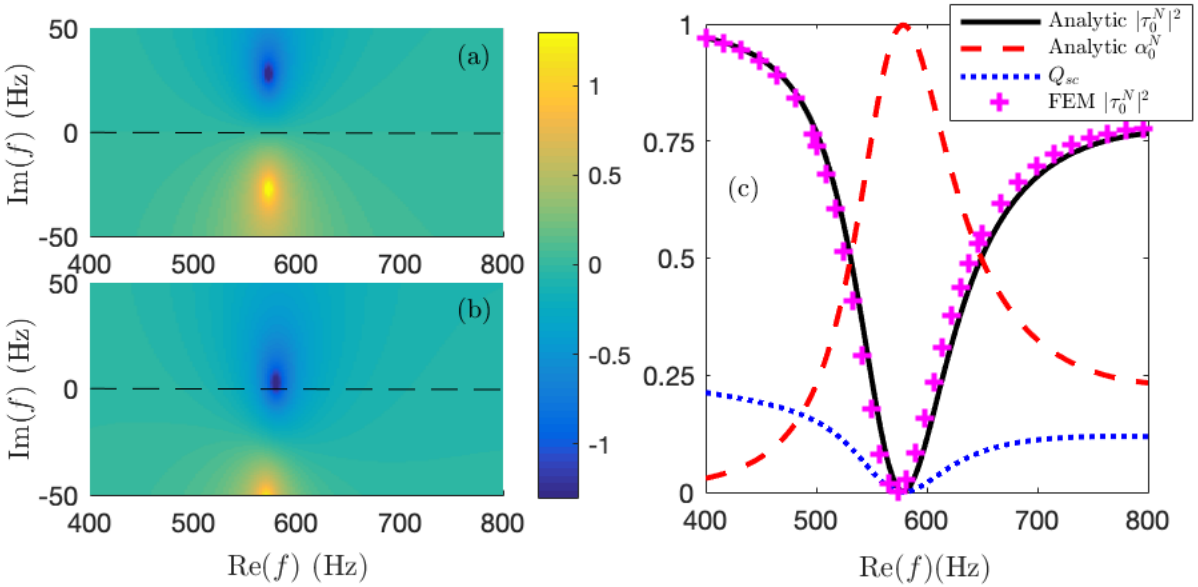

FIGURE 4.10 – Representation of the perfect absorption for the reflection problem. (a), (b) show the representation of the $\log_{10}(|\tau_0^N|)$ for the lossless and lossy configurations respectively. (c) Black continuous and red dashed lines show the analytical reflection and absorption coefficients for the critical coupled configuration respectively. Blue dotted line corresponds to the scattering cross-section and the magenta crossed line to the reflection coefficient obtained using a FEM model.

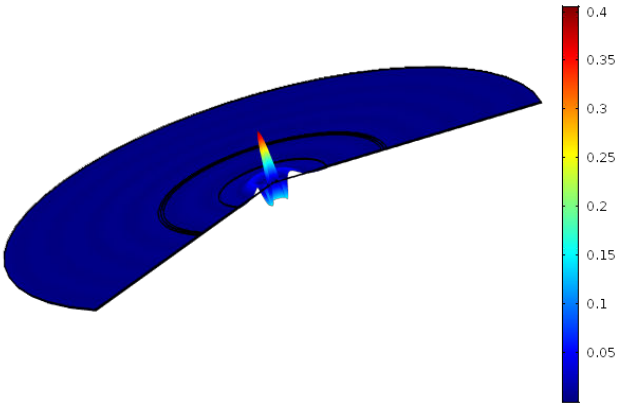

FIGURE 4.11 – Displacement response of the ABH (in m) embedded at the centre of a circular plate for the critically coupled configuration ($\mathrm{Re}(f) = 580$ Hz, $\eta_l = 0.45$), using a 2D axisymmetric model of solid mechanics in COMSOL software. The concentric incident wave is simulated by imposing a load at the edge of the circular plate.

plex frequency plane respectively. Similarly to Fig. 4.6(b), Fig. 4.10(b) shows the first pole-zero pair of the system in the perfect absorption configuration where the critical coupling condition is fulfilled, showing the zero exactly located on the real frequency axis. Therefore, the amount of inherent losses in the resonator equals the amount of energy leakage in this situation (see Section 2.4.1 for more details). Figure 4.10(c) shows the corresponding reflection (red dashed line) and absorption (black continuous line) coefficients and the scattering-cross section (blue dotted line) according to real frequencies for the critical coupled configuration. $\alpha_0^N \approx 1$ and $|\tau_0^N| \approx 0$ at the first resonance frequency of the composite inclusion (at $\mathrm{Re}(f) \approx 580$ Hz), meaning that the incident wave is totally absorbed at this specific frequency see (Fig.4.11) . The analytic reflection coefficient $|\tau_0^N|$ is also compared in Fig. 4.10c with numerical results (magenta crossed line) obtained with a FEM model. The configuration of the FEM model is the same as for the Section a) except that an ABH is placed at the centre of the circular plate. Again, a good agreement of both results can be noticed, which validates the analytical model. The scattering-cross section (blue dotted line) in Fig. 4.10c also has a zero value at the first resonance frequency of the inclusion, showing also the perfect absorption at this frequency. These results show the adaptability of the method for any radially inhomogeneous structure.

4.7 Conclusions

The extension of the critical coupling condition in a 2D problem for the $n = 0$ axisymmetric mode of a 2D penetrable scatterer is analysed in this chapter. A first scattering problem of a uniform circular inclusion with a concentric incident wave propagating towards the centre of the resonator is presented. Similarly to the 1D problem presented in Chapter 2, the position in the complex frequency plane of the zeros of the eigenvalues of the scattering matrix of the penetrable scatterer provides information on the possibility to obtain the perfect absorption. The perfect absorption condition is fulfilled when these zeros are placed on the real frequency axis, meaning that the inherent losses are completely compensating the energy leakage of the

system. The results also highlight that the scattering-cross section Q_{sc} cannot be related to the absorption of a scatterer for a general scattering problem with an incident plane wave due to the properties of the Bessel functions that describe the incident wave. The adaptability of the method for more complex geometries is shown by studying the scattering problem of an ABH, and is validated by means of FEM models. Again, the presented approach can be applied to any class of 2D resonant-systems provided that the resonators are local, open and lossy. The problems presented in this chapter are the preliminary steps to the extension of the problem of perfect absorption of flexural waves in 2D metaplates in which inclusions or complex scatterers, such as ABHs, are embedded. The metaplates consist of an array of penetrable circular scatterers embedded in an infinite or semi-infinite 2D thin plate. The penetrable scatterers that compose the resonant building block of the metaplate are designed using the method presented in this chapter in order to maximise their absorption properties.

Chapter 5

Scattering of flexural waves by a critically coupled array of 2D resonators

The resonant block of the metaplate was previously designed in Chapter 4 making use of the critical coupling conditions by solving the scattering of a concentric incident wave by a circular resonator embedded in an infinite plate. In order to get closer to practical problems encountered in mechanical engineering, these resonant blocks are now periodically arranged to form an array to design the metaplate. If several resonators, or more generally obstacles, are considered, *the field scattered from one obstacle will induce further scattered fields from all the other obstacles, which will induce further scattered fields from all the other obstacles, and so on* [122]. All these recursive interactions of fields with two or more obstacles constitute what is called *Multiple scattering*, and a variety of mathematical techniques for solving such a problem exist: the main techniques involve separation of variables, integral equations and T-matrices [122]. Note that the difference between multiple scattering and single scattering relies not only on the number of obstacles that are in the system, but also on whether or not the interactions between the scattered field by each obstacles is accounted for. The single scattering can be considered when the spacing between the several obstacles is large compared to their size and the wavelength of the incident wave. In this case, *the total scattered field is just the sum of the fields scattered by the individual [obstacles], each of which is acted on by the [incident] field in isolation from the other [obstacles]* [19].

The multiple scattering theory has been widely used in various fields of wave physics, from electromagnetisms, to water waves, acoustics and elastodynamics [122]. The studied obstacles can be randomly [143] or periodically distributed. In this latter, a crystal or an array is formed. They can also be rigid as well as penetrable, involving elastic [123], porous [85] or poroelastic [5, 189] materials. Such systems with penetrable obstacles thus become locally resonant, present original properties, and are part of the metamaterial class as presented in Section 1.3.

This chapter focuses on the scattering of flexural waves by an infinite critically coupled array of circular inclusions embedded in a thin plate. More specifically, the purpose of the chapter is to analyse the absorbing efficiency of this array in two configurations. The first configuration

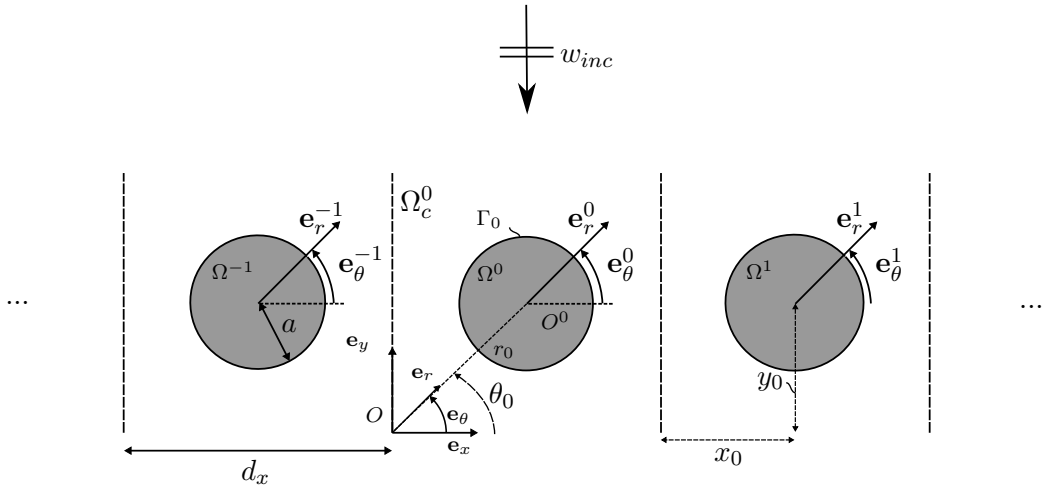

FIGURE 5.1 – Sketch of the 2D scattering problem by an infinite array of circular inclusions.

corresponds to a 2D transmission problem in which the array is embedded in an infinite thin plate, whereas the second corresponds to a 2D reflection problem in which the scattered field by the array interacts with a simply supported plane boundary in a semi-infinite thin plate. The excitation takes the form of an incident plane wave which is normal to the axis of the array. The resonators consist of circular reductions of the thickness of the plate on which a thin viscoelastic coating is attached. The resonator geometry and constitutive materials remain the same as those of the resonators designed in Chapter 4. The scattered field by the array is studied by means of the multiple scattering theory. In particular, the reflection, transmission and absorption coefficients of the array are analysed for the propagating waves and are validated using a 3D semi-periodic FEM model of solid mechanics in COMSOL software.

This chapter is organised as follows. In Section 5.1, the scattering of an infinite array of circular inclusions is presented for the 2D transmission and reflection problem. Section 5.2 presents and discuss the critically coupled transmission and reflection problems. Finally, Section 5.3 summarises the main results and gives the concluding remarks.

5.1 Scattering by an infinite row of circular inclusions.

This section aims at presenting the semi-analytical model used to study the scattering properties of an infinite array of circular inclusions coated by a viscoelastic layer embedded in a thin plate. The formalism consided in [157] is adapted here for flexural waves. A semi-infinite unit cell Ω_c^0 of width d_x is considered in a plate of constant thickness h, flexural rigidity D, and mass density ρ. This unit cell is attached to a global Cartesian coordinate system $(O, \mathbf{e}_x, \mathbf{e}_y)$ and a polar coordinate system $(O, \mathbf{e}_r, \mathbf{e}_\theta)$ (see Fig.5.1). The position vector according to these coordinate systems is written as $\mathbf{x} = x\mathbf{e}_x + y\mathbf{e}_y = r\mathbf{e}_r + \theta\mathbf{e}_\theta$. A circular inclusion of radius a, thickness h_0 and denoted by Ω^0 is placed in the unit cell Ω_c^0. The centre of Ω^0 is located at the point $\mathbf{x}_0$ of coordinates $\mathbf{x}_0 = x_0\mathbf{e}_x + y_0\mathbf{e}_y = d_x/2\mathbf{e}_x + y_0\mathbf{e}_y$. A polar coordinate system $(O^0, \mathbf{e}_r^0, \mathbf{e}_\theta^0)$ is also attached to the centre of the inclusion. The inclusion is coated by a viscoelastic layer of constant thickness h_l. This composite region is modeled by means of the RKU model introduced in Section 4.3.1. The infinite array consists of the d_x-periodic repetition of the unit cell Ω_c^0 along the direction $\mathbf{e}_x$. The j-th repetition of the unit cell is denoted Ω_c^j where $j \in \mathbb{Z}$, and is included in

the cartesian domain $x \in [0 + jd_x; d_x + jd_x]$ and $y = y_0$. A polar coordinate system $(O^j, \mathbf{e}_r^j, \mathbf{e}_\theta^j)$ is attached to the centre of each circular inclusion Ω_j of coordinates $\mathbf{x}_j = x_j\mathbf{e}_x + y_j\mathbf{e}_y = r_j\mathbf{e}_r + \theta_j\mathbf{e}_\theta$. The position vector according to the coordinate systems attached to each inclusion Ω_j is written as $\mathbf{r}^j = r^j\mathbf{e}_r^j + \theta^j\mathbf{e}_\theta^j$.

5.1.1 The incident wave w_{inc}

The incident field w_{inc} is considered as a propagative plane wave of unitary amplitude and frequency f propagating along the direction $-\mathbf{e}_y$ (i.e. $\theta_{inc} = -\pi/2$) in all this chapter. The propagation of the incident wave is therefore normal to the array, and can be written using the time convention $e^{-i\omega t}$ as:

$$w_{inc}(\mathbf{x}) = e^{i\mathbf{k}.\mathbf{x}} = e^{-iky}, \tag{5.1}$$

where $\mathbf{k} = -k\mathbf{e}_y$ is the wavevector and $k = \left(\frac{\rho h\omega^2}{D}\right)^{1/4}$ the wavenumber. The position vector $\mathbf{x}$ can furthermore be expressed as $\mathbf{x} = \mathbf{x}_j + \mathbf{r}^j$ where $\mathbf{r}^j = r^j\cos\theta^j\mathbf{e}_x + r^j\sin\theta^j\mathbf{e}_y$. As a result, Eq. (5.1) becomes:

$$w_{inc}(\mathbf{x}) = e^{i\mathbf{k}\mathbf{x}_j}e^{-ikr^j\sin\theta^j} = e^{i\mathbf{k}\mathbf{x}_j}e^{ikr^j\cos(\theta^j+\frac{\pi}{2})}, \tag{5.2}$$

where $e^{i\mathbf{k}\mathbf{x}_j}$ plays the role of a complex amplitude which depends on the position $\mathbf{x}_j$ of the centre of the inclusion Ω^j in the global Cartesian coordinate system. The term $e^{ikr^j\cos(\theta^j+\frac{\pi}{2})}$ can be expand upon Bessel functions using the Jacobi-Anger expansion [2], such that:

$$e^{ikr^j\cos(\theta^j+\frac{\pi}{2})} = \sum_{n\in\mathbb{Z}}(-1)^n\mathrm{J}_n(kr^j)e^{in\theta^j}. \tag{5.3}$$

The substitution of Eq. (5.3) in Eq. (5.1) leads to the following expansion of the incident field upon the Bessel functions in the polar coordinate system $(O^j, \mathbf{e}_r^j, \mathbf{e}_\theta^j)$ attached to the inclusion Ω^j:

$$w_{inc}(\mathbf{r}^j) = \sum_{n\in\mathbb{Z}} A_{\mathrm{J},n}^{inc,j}\mathrm{J}_n(kr^j)e^{in\theta^j} \tag{5.4}$$

with

$$A_{\mathrm{J},n}^{inc,j} = e^{i\mathbf{k}\mathbf{x}_j}\sum_{n\in\mathbb{Z}}(-1)^n. \tag{5.5}$$

The generalisation of these expressions to the case of an incident wave with an arbitrary incident angle is given in Appendix B.0.1 .

5.1.2 Quasi-periodicity

The displacement field in the system is governed by the biharmonic equation of motion given in Eq.(4.2), and is written as the sum of the incident wave w_{inc} and the scattered field w_{sc} by the array. The latter is the sum of the scattered fields w_{sc}^j by each inclusion Ω^j, thus the total displacement field reads as:

$$w = w_{inc} + w_{sc} = w_{inc}(\mathbf{x}) + \sum_{j\in\mathbb{Z}} w_{sc}^j(\mathbf{r}^j). \tag{5.6}$$

Each scattered field w_{sc}^j is first expanded upon outgoing propagating and evanescent waves in its own cylindrical coordinate system using Hankel functions of the first kind and Bessel functions

of the second kind:

$$w_{sc}^{j}(\mathbf{r}^{j}) = \sum_{n\in\mathbb{Z}} \left[A_{\mathrm{H},n}^{j} \mathrm{H}_{n}^{(1)}(kr^{j}) + A_{\mathrm{K},n}^{j} \mathrm{K}_{n}(kr^{j}) \right] e^{in\theta^{j}}, \tag{5.7}$$

where $A_{\mathrm{H},n}^{j}$ and $A_{\mathrm{K},n}^{j}$ are the propagative and evanescent scattering coefficients of Ω^{j}, respectively. The number of scattering coefficients to determine can be reduced in this case by exploiting both the quasi-periodicity of the array along $\mathbf{e}_x$ and the normal plane incidence feature of the excitation, i.e., $\mathbf{k} = -k\mathbf{e}_y$. Both conditions involve that the scattered coefficients of each inclusion are equal due to the Floquet-Bloch condition:

$$A_{\mathrm{H},n}^{j} = A_{\mathrm{H},n} \qquad \text{and} \qquad A_{\mathrm{K},n}^{j} = A_{\mathrm{K},n} \qquad j \in \mathbb{Z}. \tag{5.8}$$

Note that this relation is no more valid when the angle of the incident plane wave is arbitrary and that a phase-shift has to be accounted for via the Floquet-Bloch condition. As a consequence of Eq (5.8), it is sufficient to determine the scattering coefficients of one inclusion Ω^{j} to solve the problem.

5.1.3 Lattice sum

The scattering coefficients of the inclusion Ω^{0} are now determined. The total scattered displacement field w_{sc} takes therefore the following form:

$$w_{sc}(\mathbf{r}^{j}) = \sum_{j\in\mathbb{Z}} \sum_{n\in\mathbb{Z}} \left[A_{\mathrm{H},n}^{0} \mathrm{H}_{n}^{(1)}(kr^{j}) + A_{\mathrm{K},n}^{0} \mathrm{K}_{n}(kr^{j}) \right] e^{in\theta^{j}}. \tag{5.9}$$

The Graf's addition theorem is then used to express the scattered fields by each inclusion Ω^{j}, with $j \in \mathbb{Z}^{*}$, in the local polar coordinate system $(O^{0}, \mathbf{e}_{r}^{0}, \mathbf{e}_{\theta}^{0})$ attached to Ω^{0} (see Appendix D.1 for more details on the Graf's addition theorem):

$$\begin{aligned} w_{sc}(\mathbf{r}^{0}) = & \sum_{n\in\mathbb{Z}} \left[A_{\mathrm{H},n}^{0} \mathrm{H}_{n}^{(1)}(kr^{0}) + A_{\mathrm{K},n}^{0} \mathrm{K}_{n}(kr^{0}) \right] e^{in\theta^{0}} \\ & + \sum_{n\in\mathbb{Z}} \sum_{q\in\mathbb{Z}} \left[A_{\mathrm{H},q}^{0} S_{n-q}^{\mathrm{H}} \mathrm{J}_{n}(kr^{0}) e^{in\theta^{0}} + A_{\mathrm{K},q}^{0} S_{n-q}^{\mathrm{K}} \mathrm{I}_{n}(kr^{0}) \right] e^{in\theta^{0}}, \quad \text{with } r^{0} < d_x - a \cap \Omega_{c}^{0}, \end{aligned} \tag{5.10}$$

and S_{n-q}^{H} and S_{n-q}^{K} are written as:

$$S_{n-q}^{\mathrm{H}} = \sum_{j>0} \mathrm{H}_{n-q}^{(1)}(kjd) \left(1 + (-1)^{n-q}\right), \tag{5.11}$$

$$S_{n-q}^{\mathrm{K}} = \sum_{j>0} \mathrm{K}_{n-q}(kjd) \left((-1)^{n} + (-1)^{q}\right). \tag{5.12}$$

In particular, Eq. (5.11) is known as Lattice sum or Schlömilch serie. Such a serie arises naturally in scattering problems where the scatterer is an infinite periodic structure and accounts for the contribution of the fields scattered by Ω^{j}, where $j \in \mathbb{Z}^{*}$, to the near-field close to Ω^{0} [116]. The form of the serie as written in Eq. (5.11) is unsuitable for numerical computation due to its very slow convergence. However, it can be transformed into another expression which is amenable

for computation [116, 177](see Appendix D.2 for more details on the transformation of S^{H}_{n-q}). Note that this slow convergence concerns only S^{H}_{n-q} and not S^{K}_{n-q}, since $\mathrm{K}_n(x)$ is exponentially decaying with the increasing argument x. Using the appropriate expression of Schlömilch serie, the total displacement field in the polar coordinate system $(O^0, \mathbf{e}^0_r, \mathbf{e}^0_\theta)$ takes the following form in the vicinity of Ω^0 ($r^0 < d_x - a \cap \Omega^0_c$) :

$$w(\mathbf{r}^0) = \sum_{n\in\mathbb{Z}} \left[A^0_{\mathrm{H},n}\mathrm{H}^{(1)}_n(kr^0) + A^0_{\mathrm{K},n}\mathrm{K}_n(kr^0) + \left(A^{inc,0}_{\mathrm{J},n} + \mathcal{A}^0_{\mathrm{H},n}\right)\mathrm{J}_n(kr^0) + \mathcal{A}^0_{\mathrm{K},n}\mathrm{I}_n(kr^0)\right] e^{in\theta^0}, \tag{5.13}$$

where

$$\mathcal{A}^0_{\mathrm{H},n} = \sum_{q\in\mathbb{Z}} A^0_{\mathrm{H},q} S^{\mathrm{H}}_{n-q} \quad \text{and} \quad \mathcal{A}^0_{\mathrm{K},n} = \sum_{q\in\mathbb{Z}} A^0_{\mathrm{K},q} S^{\mathrm{K}}_{n-q}. \tag{5.14}$$

5.1.4 Boundary conditions and scattering coefficients

The scattering coefficients of Ω^0 are determined by means of the boundary conditions at the interface Γ_0 between the scatterer and the surrounding plate (see Fig. 5.1). Equation (5.13) is similar to the expression of the displacement field in the case of the scattering by an isolated inclusion. The procedure to apply the boundary conditions at Γ_0 is therefore exactly the same as presented in Section 4.3.3. Hence, applying the boundary conditions at Γ_0 for a given order n of Bessel function leads to the following equation system:

$$\mathbf{A^0_n}.\mathbf{x^0_n} = \mathbf{B^0_n}.\mathbf{a^0_n}, \tag{5.15}$$

with

$$\mathbf{A^0_n} = \begin{pmatrix} \mathrm{H}^{(1)}_n(\varepsilon) & \mathrm{K}_n(\varepsilon) & -\mathrm{J}_n(\varepsilon^p_0) & -\mathrm{I}_n(\varepsilon^p_0) \\ \mathrm{H}^{(1)\prime}_n(\varepsilon) & \mathrm{K}_n{}'(\varepsilon) & -\kappa^0\mathrm{J}_0{}'(\varepsilon^p_0) & -\kappa^0\mathrm{I}_0{}'(\varepsilon^p_0) \\ S_{\mathrm{H}_n} & S^p_{\mathrm{K}_n} & -\mathcal{D}^0 S^p_{\mathrm{J}_n} & -\mathcal{D}^0 S^p_{\mathrm{I}_n} \\ T_{\mathrm{H}_n} & T^p_{\mathrm{K}_n} & -\mathcal{D}^0 T^p_{\mathrm{J}_n} & -\mathcal{D}^0 T^p_{\mathrm{I}_n} \end{pmatrix},$$

$$\mathbf{x^0_n} = \begin{pmatrix} A^0_{\mathrm{H},n} \\ A^0_{\mathrm{K},n} \\ A^0_{\mathrm{J},n} \\ A^0_{\mathrm{I},n} \end{pmatrix} \quad , \quad \mathbf{B^0_n} = -\begin{pmatrix} \mathrm{J}_n(\varepsilon) & \mathrm{I}_n(\varepsilon) \\ \mathrm{J}_n{}'(\varepsilon) & \mathrm{I}_n{}'(\varepsilon) \\ S_{\mathrm{J}_n} & S_{\mathrm{I}_n} \\ T_{\mathrm{J}_n} & T_{\mathrm{I}_n} \end{pmatrix} \quad , \quad \mathbf{a^0_n} = \begin{pmatrix} A^{inc,0}_{\mathrm{J},n} + \mathcal{A}^0_{\mathrm{H},n} \\ \mathcal{A}^0_{\mathrm{K},n} \end{pmatrix},$$

where $\kappa^0 = k^p_0/k$, $\varepsilon = ka$, $\varepsilon^p_0 = k^p_0 a = \kappa^0\varepsilon$ and $\mathcal{D}^0 = D^p_0/D$ and

$$S^i_{X_n} = \left[n^2(1-\nu_i) \mp \varepsilon_i^2\right] X_n(\varepsilon_i) - (1-\nu_i)\varepsilon_i X'_n(\varepsilon_i), \tag{5.16}$$

$$T^i_{X_n} = n^2(1-\nu_i)X_n(\varepsilon_i) - \left[n^2(1-\nu_i) \pm \varepsilon_i^2\right] X'_n(\varepsilon_i), \tag{5.17}$$

where the indice i is either equal to p or is null. The upper sign in Eqs.(5.16) and Eq. (5.17) is taken when $X_n = \mathrm{J}_n$ or $\mathrm{H}^{(1)}_n$ while the lower sign is taken when $X_n = \mathrm{I}_n$ or K_n. In the case where the scattered field is expanded upon N orders of Hankel functions and modified Bessel functions of the second kind ($n \in [-N; N]$, $N \in \mathbb{Z}$), the scattering coefficients are determined

from Eq. (5.15) by solving the following system:

$$\begin{cases} A^0_{\mathrm{H}_{-N}} - T^{-N}_{11}\sum\limits_{q\in\mathbb{Z}} A^0_{\mathrm{H}_q} S^{\mathrm{H}}_{-N-q} - T^{-N}_{12}\sum\limits_{q\in\mathbb{Z}} A^0_{\mathrm{K}_q} S^{\mathrm{K}}_{-N-q} = T^{-N}_{11} A^{inc,0}_{\mathrm{J},-N} \\ A^0_{\mathrm{K}_{-N}} - T^{-N}_{21}\sum\limits_{q\in\mathbb{Z}} A^0_{\mathrm{H}_q} S^{\mathrm{H}}_{-N-q} - T^{-N}_{22}\sum\limits_{q\in\mathbb{Z}} A^0_{\mathrm{K}_q} S^{\mathrm{K}}_{-N-q} = T^{-N}_{21} A^{inc,0}_{\mathrm{J},-N} \\ \vdots \\ A^0_{\mathrm{H}_0} - T^{0}_{11}\sum\limits_{q\in\mathbb{Z}} A^0_{\mathrm{H}_q} S^{\mathrm{H}}_{0-q} - T^{0}_{12}\sum\limits_{q\in\mathbb{Z}} A^0_{\mathrm{K}_q} S^{\mathrm{K}}_{0-q} = T^{0}_{11} A^{inc,0}_{\mathrm{J},0} \\ A^0_{\mathrm{K}_0} - T^{0}_{21}\sum\limits_{q\in\mathbb{Z}} A^0_{\mathrm{H}_q} S^{\mathrm{H}}_{0-q} - T^{0}_{22}\sum\limits_{q\in\mathbb{Z}} A^0_{\mathrm{K}_q} S^{\mathrm{K}}_{0-q} = T^{0}_{21} A^{inc,0}_{\mathrm{J},0} \\ \vdots \\ A^0_{\mathrm{H}_N} - T^{N}_{11}\sum\limits_{q\in\mathbb{Z}} A^0_{\mathrm{H}_q} S^{\mathrm{H}}_{N-q} - T^{N}_{12}\sum\limits_{q\in\mathbb{Z}} A^0_{\mathrm{K}_q} S^{\mathrm{K}}_{N-q} = T^{N}_{11} A^{inc,0}_{\mathrm{J},N} \\ A^0_{\mathrm{K}_N} - T^{N}_{21}\sum\limits_{q\in\mathbb{Z}} A^0_{\mathrm{H}_q} S^{\mathrm{H}}_{N-q} - T^{N}_{22}\sum\limits_{q\in\mathbb{Z}} A^0_{\mathrm{K}_q} S^{\mathrm{K}}_{N-q} = T^{N}_{21} A^{inc,0}_{\mathrm{J},N} \end{cases}, \tag{5.18}$$

where

$$\mathbf{T^n} = \begin{bmatrix} T^n_{11} & T^n_{12} \\ T^n_{21} & T^n_{22} \\ T^n_{31} & T^n_{32} \\ T^n_{41} & T^n_{42} \end{bmatrix} = \left(\mathbf{A^0_n}\right)^{-1} \cdot \mathbf{B^0_n}. \tag{5.19}$$

The sums are truncated in practice to $n \in [-N; N]$ by using the following numerical recipe [10]:

$$N = \mathrm{floor}(4.05(ka)^{1/3} + ka) + 10, \tag{5.20}$$

to ensure their convergence. Note that this truncation concerns only the Hankel functions of the first kind and the Bessel functions of the second kind in the scattered field, and that the lattice sum which runs over the spatial repetition of the unit cell is evaluated independently of this truncation.

5.1.5 Reflection and transmission coefficients

a) General expressions

The reflection and transmission coefficients of the array are now computed. These coefficients provide the global behaviour of the inclusion array submitted to an incident field in the Cartesian coordinate system. To derive these coefficients, the system composed of the infinite plate and the array is divided into 3 domains (see Fig. 5.2):

— Ω_c corresponds to the array of d_x-periodic repetitions of Ω^0_c,

— Ω^+ corresponds to the upper half-space, i.e., above the array, where the incident wave initially propagates and is reflected from the array,

— Ω^- corresponds to the lower half-space, i.e., below the array, where the transmitted waves propagate away from the array.

The displacement fields w^+ in Ω^+ and w^- in Ω^- are then expanded upon plane waves. However, due to the d_x-periodicity of the array, only the discret set of wavevectors $k^\mu_x\mathbf{e}_x \pm k^\mu_y\mathbf{e}_x$ and $\gamma^\mu_x\mathbf{e}_x \pm \gamma^\mu_y\mathbf{e}_x$ is admissible [18, 74], where the Bloch wavevector reduces to $k^\mu_x = \gamma^\mu_x = \frac{2\pi\mu}{d_x}$ because the incident wave is normal to the array, $k^\mu_y = \sqrt{k^2 - k^{\mu 2}_x}$ and $\gamma^\mu_y = \sqrt{(ik)^2 - \gamma^{\mu 2}_x}$ where

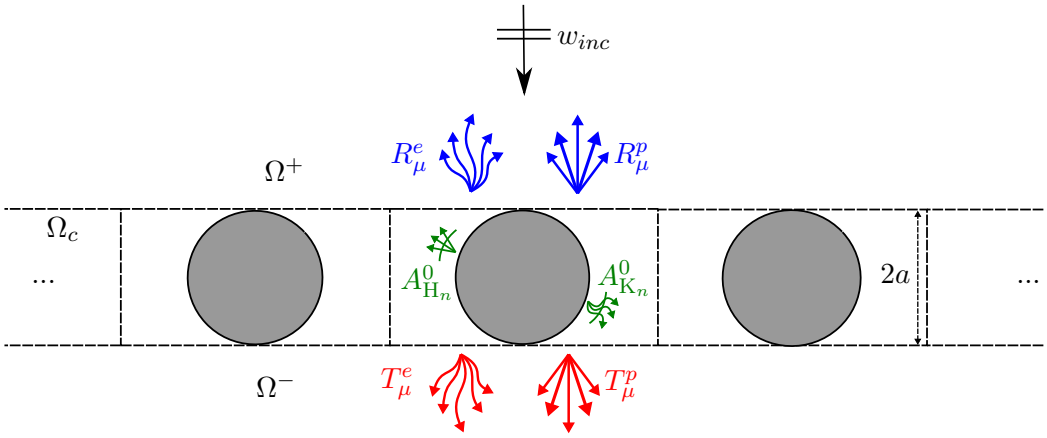

FIGURE 5.2 – Sketch of the scattering coefficients, reflection coefficients and transmission coefficients in the scattering problem.

$\mu \in \mathbb{Z}$. Therefore, the expansion of the displacement fields upon Bloch waves are:

$$w^+(\mathbf{x}) = \sum_{\mu\in\mathbb{Z}} \delta_{\mu 0} e^{ik_x^\mu x - ik_y^\mu (y-(y_0+a))} + R^p_\mu e^{ik_x^\mu x + ik_y^\mu (y-(y_0+a))} + R^e_\mu e^{i\gamma_x^\mu x + i\gamma_y^\mu (y-(y_0+a))}, \qquad (x,y)\in\Omega^+ \tag{5.21a}$$

$$w^-(\mathbf{x}) = \sum_{\mu\in\mathbb{Z}} T^p_\mu e^{ik_x^\mu x - ik_y^\mu y-(y_0-a))} + T^e_\mu e^{i\gamma_x^\mu x - i\gamma_y^\mu (y-(y_0-a))}. \qquad (x,y)\in\Omega^- \tag{5.21b}$$

R^p_μ, R^e_μ, T^p_μ and T^e_μ are the complex amplitudes of the propagative and evanescent outgoing plane waves radiated from the array in $\Omega^\pm$. The relation between the Bloch waves amplitudes R^p_μ, R^e_μ, T^p_μ and T^e_μ and the scattering coefficients $A^0_{\mathrm{H}_n}$ and $A^0_{\mathrm{K}_n}$ determined from Eq. (5.18) is derived by means of the Green-Kirchhoff Integral Theorem, which is detailed in [157]. After derivations, the Bloch wave amplitudes take the form:

$$R^p_\mu = \sum_{n\in\mathbb{Z}} A^0_{\mathrm{H}_n} K^{p+}_{\mu n} e^{-ik_x^\mu x_0 + ik_y^\mu a}, \tag{5.22a}$$

$$R^e_\mu = \sum_{n\in\mathbb{Z}} A^0_{\mathrm{K}_n} K^{e+}_{\mu n} e^{-i\gamma_x^\mu x_0 + i\gamma_y^\mu a}, \tag{5.22b}$$

$$T^p_\mu = \delta_{\mu 0} e^{ik_x^\mu x - ik_y^\mu (y-(y_0+a))} + \sum_{n\in\mathbb{Z}} A^0_{\mathrm{H}_n} K^{p-}_{\mu n} e^{-ik_x^\mu x_0 + ik_y^\mu y_0}, \tag{5.22c}$$

$$T^e_\mu = \sum_{n\in\mathbb{Z}} A^0_{\mathrm{K}_n} K^{e-}_{\mu n} e^{-i\gamma_x^\mu x_0 + i\gamma_y^\mu y_0}, \tag{5.22d}$$

with

$$K^{p\pm}_{\mu n} = \frac{2(-i)^n}{d_x k_y^\mu} e^{i\pm n\theta_\mu}, \tag{5.23a}$$

$$K^{e\pm}_{\mu n} = \frac{i\pi}{d_x \gamma_y^\mu} e^{i\pm n\alpha_\mu}, \tag{5.23b}$$

where $ke^{i\theta_\mu} = k_x^\mu + ik_y^\mu$ and $\gamma e^{i\alpha_\mu} = \gamma_x^\mu + i\gamma_y^\mu$. Due to the unitary amplitude of the incident wave, the global reflection, transmission and absorption coefficient of the lattice can be expressed as

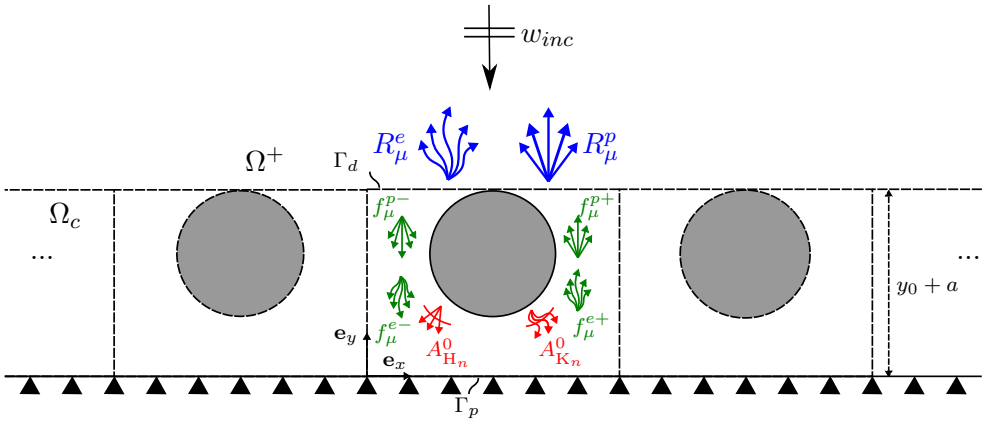

FIGURE 5.3 – Sketch of the scattering problem with a simply supported plane.

[85]:

$$|R_T|^2 = \sum_{\mu\in\mathbb{Z}} \frac{\mathrm{Re}\left(k_y^\mu\right)}{k_y^0} \left|R_\mu^p\right|^2, \tag{5.24}$$

$$|T_T|^2 = \sum_{\mu\in\mathbb{Z}} \frac{\mathrm{Re}\left(k_y^\mu\right)}{k_y^0} \left|T_\mu^p\right|^2, \tag{5.25}$$

$$\alpha_T = 1 - |R_T|^2 - |T_T|^2. \tag{5.26}$$

b) Interaction of the array with a plane boundary

The interaction of the array with a plane boundary Γ_p parallel to the array and located at $y = 0$ is now studied (see Fig. 5.3). This study is possible thanks to the expansion of the scattered field w_{sc} upon Bloch waves expressed in Eqs. (5.21a) and (5.21b). A simply supported condition is chosen here to avoid the conversion of wave types from propagative to evanescent and vice-versa [48], and so make the calculation easier. The incident wave remains the same as the previous study and is still expressed by Eq. (5.1). The half-space Ω^+ is now only considered. The displacement field w^+ in Ω^+ keeps the same form as in Eq. (5.21a). However, the expression of the reflection coefficients differs from that of Eq. (5.22a) and 5.22b due to the presence of the plane boundary. The displacement field inside the unit cell Ω_c^0 takes the form:

$$\begin{aligned} w_c^0(\mathbf{x}) = &\sum_{\mu\in\mathbb{Z}} f_\mu^{p+} e^{ik_x^\mu x + ik_y^\mu y} + f_\mu^{p-} e^{ik_x^\mu x - ik_y^\mu y} + f_\mu^{e+} e^{i\gamma_x^\mu x + i\gamma_y^\mu y} + f_\mu^{e-} e^{i\gamma_x^\mu x - i\gamma_y^\mu y} \\ &+ \sum_{n\in\mathbb{Z}} A^0_{\mathrm{H}_n} K^{p\pm}_{\mu n} e^{-ik_x^\mu x_0 \pm ik_y^\mu a} e^{ik_x^\mu x + \pm ik_y^\mu (y-(y_0+a))} \\ &+ A^0_{\mathrm{K}_n} K^{e\pm}_{\mu n} e^{-i\gamma_x^\mu x_0 \mp i\gamma_y^\mu a} e^{i\gamma_x^\mu x \pm i\gamma_y^\mu (y-(y_0+a))}, \end{aligned} \tag{5.27}$$

where the upper signs are taken when $y > y_0 + a$ and the lower signs when $0 < y < y_0 - a$. f_μ^{p+} and f_μ^{p-} account for the amplitudes of the ingoing and outgoing propagative Bloch waves in Ω_c^0, respectively, whereas f_μ^{e+} and f_μ^{e-} correspond to the amplitudes of the ingoing and outgoing evanescent Bloch waves in Ω_c^0, respectively. The scattering coefficients in w^+ as well as the waves amplitudes of w_c^0 are determined by means of the boundary conditions at Γ_d, Γ_p, and Γ_0. The

boundary conditions at Γ_p and the continuity conditions at Γ_d implies:

$$\begin{cases} \displaystyle\int_0^{d_x} w_c^0 e^{-ik_x^\nu x} dx = \int_0^{d_x} w^+ e^{-ik_x^\nu x} dx \\ \displaystyle\int_0^{d_x} \frac{\partial w_c^0}{\partial y} e^{-ik_x^\nu x} dx = \int_0^{d_x} \frac{\partial w^+}{\partial y} e^{-ik_x^\nu x} dx \end{cases}, \qquad y \in \Gamma_d, \tag{5.28}$$

and

$$\begin{cases} \displaystyle\int_0^{d_x} w_c^0 e^{-ik_x^\nu x} dx = 0 \\ \displaystyle\int_0^{d_x} \frac{\partial^2 w_c^0}{\partial y^2} e^{-ik_x^\nu x} dx = 0 \end{cases}, \qquad y \in \Gamma_p. \tag{5.29}$$

Applying the boundary conditions at Γ_d, Γ_p and making use of the orthogonality relation $\displaystyle\int_0^{d_x} e^{ik_x^\mu x} e^{-ik_x^\nu x} dx = 2\pi d_x \delta_{\nu\mu}$, the amplitudes f_μ^{p+}, f_μ^{p-}, f_μ^{e+} and f_μ^{e-}, and the propagative and evanescent reflection coefficients R_μ^p and R_μ^e can be expressed as:

$$f_\mu^{p+} = -\delta_{q0} e^{ik_y^\mu (y_0+a)} - \sum_{n\in\mathbb{Z}} A_{\mathrm{H}_n}^0 K_{\mu n}^{p-} e^{-ik_x^\mu x_0 + ik_y^\mu y_0}, \tag{5.30a}$$

$$f_\mu^{p-} = \delta_{\mu 0} e^{ik_y^\mu (y_0+a)}, \tag{5.30b}$$

$$f_\mu^{e+} = -\sum_{n\in\mathbb{Z}} A_{\mathrm{K}_n}^0 K_{\mu n}^{e-} e^{-i\gamma_x^\mu x_0 + i\gamma_y^\mu y_0}, \tag{5.30c}$$

$$f_\mu^{e-} = 0, \tag{5.30d}$$

$$R_\mu^p = -\delta_{\mu 0} e^{i2k_y^\mu (y_0+a)} + \sum_{n\in\mathbb{Z}} A_{\mathrm{H}_n}^0 e^{ik_y^\mu (y_0+a)} (K_{\mu n}^{p+} e^{-ik_x^\mu x_0 - ik_y^\mu y_0} - K_{\mu n}^{p-} e^{-ik_x^\mu x_0 + ik_y^\mu y_0}), \tag{5.30e}$$

$$R_\mu^e = \sum_{n\in\mathbb{Z}} A_{\mathrm{K}_n}^0 e^{i\gamma_y^\mu (y_0+a)} (K_{\mu n}^{e+} e^{-i\gamma_x^\mu x_0 - i\gamma_y^\mu y_0} - K_{\mu n}^{e-} e^{-ik_x^\mu x_0 + i\gamma_y^\mu y_0}). \tag{5.30f}$$

f_μ^{p-} and f_μ^{e-} accounts therefore for the incident wave amplitudes in Ω_c^0, whereas f_μ^{p+} and f_μ^{e+} accounts for the reflection at Γ_p of the incident wave and the scattered field by Ω^0. The scattering coefficients A_{H_n} and A_{K_n} of Ω^0 are again determined by means of the boundary conditions at Γ_0. However, it requires beforehand to expand the exponential terms of w_c^0 upon Bessel functions in the coordinate system $(O^0, \mathbf{e}_r^0, \mathbf{e}_\theta^0)$ by using the Jacobi-Anger expansion, such that:

$$f_\mu^{p+} e^{ik_x^\mu x + ik_y^\mu y} = \sum_{n\in\mathbb{Z}} F_{\mu n}^{p+} \mathrm{J}_n(kr^0) e^{in\theta^0}, \tag{5.31a}$$

$$f_\mu^{e+} e^{i\gamma_x^\mu x + i\gamma_y^\mu y} = \sum_{n\in\mathbb{Z}} F_{\mu n}^{e+} \mathrm{I}_n(kr^0) e^{in\theta^0}. \tag{5.31b}$$

with

$$F_{\mu n}^{p+} = \left(-\delta_{\mu 0} e^{ik_y^\mu (y_0+a)} - \sum_{m\in\mathbb{Z}} A_{\mathrm{H}_m}^0 K_{\mu m}^{p-} e^{-ik_x^\mu x_0 + ik_y^\mu y_0} \right) i^n e^{-in\theta_\mu} e^{ik_x^\mu x_0 + ik_y^\mu y_0}, \tag{5.32a}$$

$$F_{\mu n}^{e+} = -\sum_{m\in\mathbb{Z}} A_{\mathrm{K}_m}^0 K_{\mu m}^{e-} e^{-i\gamma_x^\mu x_0 + i\gamma_y^\mu y_0} (-1)^n e^{-in\alpha_\mu} e^{i\gamma_x^\mu x_0 + i\gamma_y^\mu y_0}. \tag{5.32b}$$

Hence, applying the boundary condition at Γ_0 for a given order n of Bessel function leads to the following equation system:

$$\mathbf{A_n^0}.\mathbf{x_n^0} = \mathbf{B_n^0}.\mathbf{a_n^{0r}}, \tag{5.33}$$

with $\mathbf{a_n^{0r}} = \left(A_{\mathrm{J},n}^{inc,0} + \mathcal{A}_{\mathrm{H},n}^0 + \sum_{\mu\in\mathbb{Z}} F_{\mu n}^{p+}; \mathcal{A}_{\mathrm{K},n}^0 + \sum_{\mu\in\mathbb{Z}} F_{\mu n}^{e+}\right)^{\mathrm{T}}$ and where $^{\mathrm{T}}$ is the transpose sign. If the scattered field is expanded upon N orders of Hankel functions and modified Bessel functions of the second kind, the scattering coefficients are determined from Eq. (5.33) by solving the following system:

$$\begin{cases}
A_{\mathrm{H}_{-N}}^0 - T_{11}^{-N}\mathcal{S}_{-N}^H - T_{12}^{-N}\mathcal{S}_{-N}^K = T_{11}^{-N}\left(A_{\mathrm{J},-N}^{inc,0} - \sum_{\mu\in\mathbb{Z}} \delta_{\mu 0} e^{ik_y^\mu(y_0+a)} i^{-N} e^{iN\theta_\mu} e^{ik_x^\mu x_0 + ik_y^\mu y_0}\right) \\
A_{\mathrm{K}_{-N}}^0 - T_{21}^{-N}\mathcal{S}_{-N}^H - T_{22}^{-N}\mathcal{S}_{-N}^K = T_{21}^{-N}\left(A_{\mathrm{J},-N}^{inc,0} - \sum_{\mu\in\mathbb{Z}} \delta_{\mu 0} e^{ik_y^\mu(y_0+a)} i^{-N} e^{iN\theta_\mu} e^{ik_x^\mu x_0 + ik_y^\mu y_0}\right) \\
\vdots \\
A_{\mathrm{H}_0}^0 - T_{11}^{0}\mathcal{S}_{0}^H - T_{12}^{0}\mathcal{S}_{0}^K = T_{11}^{0}\left(A_{\mathrm{J},0}^{inc,0} - \sum_{\mu\in\mathbb{Z}} \delta_{\mu 0} e^{ik_y^\mu(y_0+a)} e^{ik_x^\mu x_0 + ik_y^\mu y_0}\right) \\
A_{\mathrm{K}_0}^0 - T_{21}^{0}\mathcal{S}_{0}^H - T_{22}^{0}\mathcal{S}_{0}^K = T_{21}^{0}\left(A_{\mathrm{J},0}^{inc,0} - \sum_{\mu\in\mathbb{Z}} \delta_{\mu 0} e^{ik_y^\mu(y_0+a)} e^{ik_x^\mu x_0 + ik_y^\mu y_0}\right) \\
\vdots \\
A_{\mathrm{H}_N}^0 - T_{11}^{N}\mathcal{S}_{N}^H - T_{12}^{N}\mathcal{S}_{N}^K = T_{11}^{N}\left(A_{\mathrm{J},N}^{inc,0} - \sum_{\mu\in\mathbb{Z}} \delta_{\mu 0} e^{ik_y^\mu(y_0+a)} i^{N} e^{-iN\theta_\mu} e^{ik_x^\mu x_0 + ik_y^\mu y_0}\right) \\
A_{\mathrm{K}_N}^0 - T_{21}^{N}\mathcal{S}_{N}^H - T_{22}^{N}\mathcal{S}_{N}^K = T_{21}^{N}\left(A_{\mathrm{J},N}^{inc,0} - \sum_{\mu\in\mathbb{Z}} \delta_{\mu 0} e^{ik_y^\mu(y_0+a)} i^{N} e^{-iN\theta_\mu} e^{ik_x^\mu x_0 + ik_y^\mu y_0}\right)
\end{cases}, \tag{5.34}$$

with

$$\mathcal{S}_n^H = \sum_{q\in\mathbb{Z}} A_{\mathrm{H}_q}^0 \left(S_{n-q}^{\mathrm{H}} - \sum_{\mu\in\mathbb{Z}} e^{i2k_y^\mu y_0} K_{\mu q}^{p-} i^n e^{-in\theta_\mu}\right), \tag{5.35a}$$

$$\mathcal{S}_n^K = \sum_{q\in\mathbb{Z}} A_{\mathrm{K}_q}^0 \left(S_{n-q}^{\mathrm{K}} - \sum_{\mu\in\mathbb{Z}} e^{i2\gamma_y^\mu y_0} K_{\mu q}^{e-} (-1)^n e^{-in\theta_0}\right). \tag{5.35b}$$

The reflection and absorption coefficient of the lattice can then be expressed as:

$$|R_R|^2 = \sum_{\mu\in\mathbb{Z}} \frac{\mathrm{Re}\left(k_y^\mu\right)}{k_y^0} \left|R_\mu^p\right|^2, \tag{5.36}$$

$$\alpha_R = 1 - |R_R|^2. \tag{5.37}$$

5.2 Scattering by an infinite array of circular resonators

The following two scattering problems are now considered: the first one is named the transmission problem and involves both the reflection and transmission coefficients and the second one is named the reflection problem by backed infinite array of circular resonators and only involves reflection. Both problems are depicted in Figs. 5.2 and 5.3, respectively. The resonators in both problems consist of homogeneous circular reductions of the plate thickness on top of which a coating layer is placed, similarly to the resonators studied in Section 4.4. The geometry and material parameters of the composite resonators are the same as those in Section 4.4 whose values are detailed in Table 4.1. These resonators are critically coupled at their first axisymmetric mode when excited by a converging wave. They also totally absorb this concentric incident wave, when isolated, at the corresponding eigenfrequency: $Re(f_0) = 184.9$Hz (see Chapter 4 for more details). The study focuses only on the reflection and transmission of waves in the far-field, $(y \to \pm\infty)$, that is to say, on the propagative waves that carry the energy. The expansion of the displacement fields upon Bloch waves is truncated such that $\mu \in [-20 : 20]$.

5.2.1 Transmission problem

The same configuration as in Fig. 5.2 is considered for the transmission problem with $d_x = 24$ cm. Therefore, the expansion of the scattered field upon the scattering coefficients $A^0_{\mathrm{H},n}$ and $A^0_{\mathrm{K},n}$ is truncated at $N = 15$ orders ($n \in [-15 : 15]$) by applying Eq. (5.20). The propagative reflection coefficients $|R_T|^2$, the transmission coefficient $|T_T|^2$ and the absorption coefficient $\alpha_T = 1 - |R_T|^2 - |T_T|^2$ are evaluated around the frequency $\mathrm{Re}(f_0) = 184.9$ Hz by using the multiple scattering model presented above. The lattice sums S^{H}_{n-q} and S^{K}_{n-q} are also expanded upon 2000 terms.

Figure 5.4 depicts $|R_T|^2$, $|T_T|^2$ and $\alpha_T = 1-|R_T|^2-|T_T|^2$ using the multiple scattering model and a FEM model. The FEM model is implemented by using a 3D model of solid mechanics in COMSOL software. The geometry of the model is composed of one unit cell of the infinite array of circular inclusions. The periodicity along $\mathbf{e}_x$ is simulated using Floquet conditions, whereas the infinite length along $\mathbf{e}_y$ with Perfectly Matched Layers (PML) (see Fig. 5.5). The incident plane wave is simulated by imposing a load at an edge parallel to the axis of the array.

The absorption coefficient α_T reaches 0.5 at most at $\mathrm{Re}(f) = 196$Hz in Fig. 5.4. This frequency corresponds approximately to the resonance frequency of the first axi-symmetric mode of the composite resonators. These results are similar to those obtained in the 1D transmission problem presented in Section 2.4.2c). This absorption limit of 0.5 is, once again, due to the fact that a single symmetric mode is excited here and that the system is thus half critically coupled (see Chapter 2.2). The solutions to increase the absorption are the same as those presented in Section 2.4.2c) which are: breaking the symmetry of the resonator[98] or using degenerate resonators[204]. A good agreement between the analytical and numerical results highlights the adaptibility of the critical coupling method applied to flexural waves for the 2D transmission problem.

5.2.2 Reflection problem

The configuration of Fig. 5.3 is now considered for the reflection problem. The width of the unit cell is $d_x = 24$ cm, $y_0 = 12$ cm and the expansion of the scattered field is still truncated such

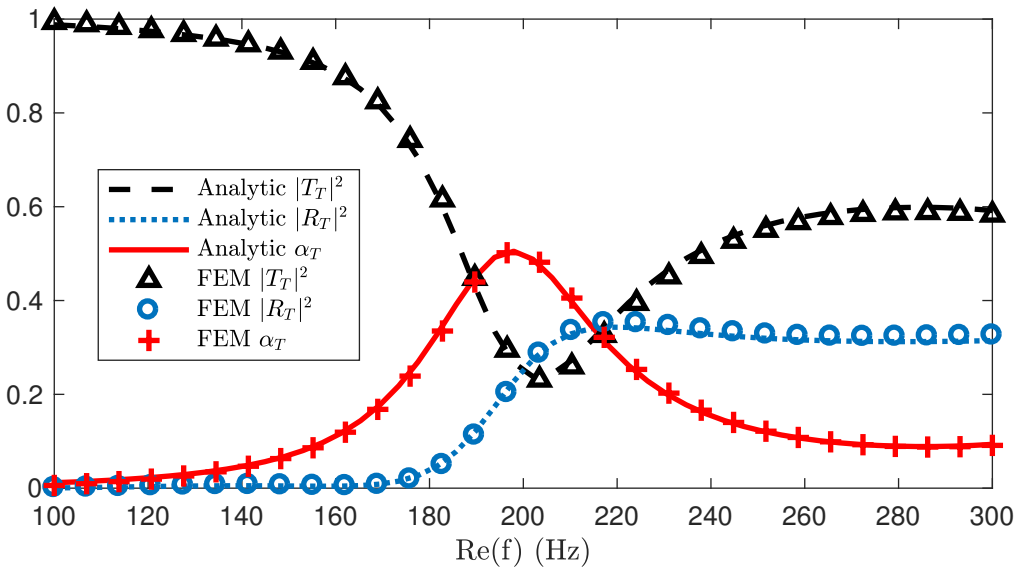

FIGURE 5.4 – Representation of $|R_T|^2$,$|T_T|^2$ and α_T around the first eigenfrequency of the critically coupled resonators. Black dashed, blue dotted and red solid lines show the analytical transmission, reflection and absorption coefficients $|R_T|^2$,$|T_T|^2$ and α_T respectively, whereas black triangle, blue circles and red crossed lines correspond to the transmission, reflection and absorption coefficients computed by means of a FEM model.

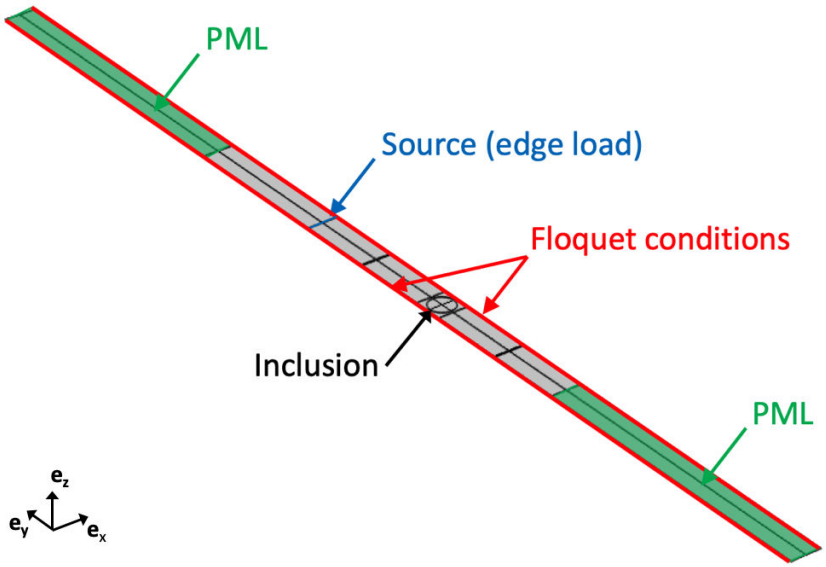

FIGURE 5.5 – 3D FEM model of the unit cell of the infinite array of inclusions used in COMSOL software to numerically compute $|R_T|^2$, $|T_T|^2$ and α_T. The periodicity along $\mathbf{e}_x$ is simulated using Floquet conditions and the infinite length along $\mathbf{e}_y$ with Perfectly Matched Layers (PML).

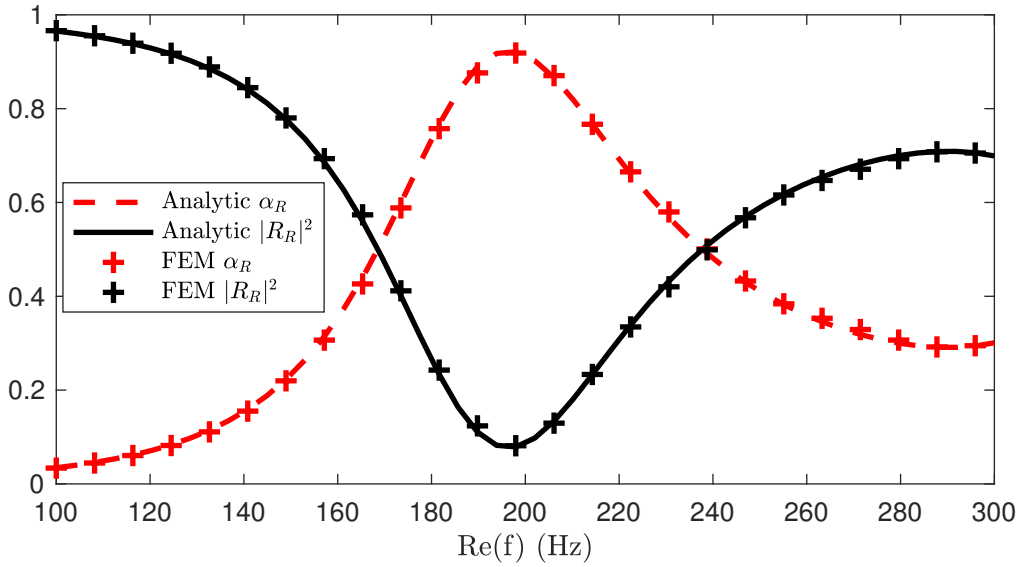

FIGURE 5.6 – Representation of $|R_R|^2$ and α_R around the first eigenfrequency of the critically coupled resonators placed in unit cells of width $d_x = 24$ cm and $y_0 = 12$ cm. Black and red solid lines show the analytical reflection and absorption coefficients $|R_R|^2$ and α_R respectively, whereas black and red crossed lines correspond to the reflection and absorption coefficients computed by means of a FEM model respectively.

that $n \in [-15 : 15]$. The propagative reflection coefficient $|R_R|^2$ and the absorption coefficient α_R are evaluated around the frequency $Re(f_0) = 184.9Hz$ by using the multiple scattering model with a plane simple supported boundary presented above and by using a FEM model whose configuration is depicted in Fig. 5.7. Note that the simply supported condition is simulated in the FEM model by imposing a displacement equal to 0 along $\mathbf{e}_z$ at the corresponding face.

Figure 5.6 depicts $|R_R|^2$ and α_R around the first eigenfrequency of the resonators. The perfect absorption is still not reached in this case since α_R equals 0.92 at most at $\mathrm{Re}(f) = 196$Hz. This may be explained by the interaction between the boundary and the resonator which alter the resonant behaviour of the latter, and more particularly its inherent losses. The resonator positions are therefore slightly moved along $\mathbf{e}_y$ axis in order to increase their absorbing efficiency. Figure 5.8 depicts $|R_R|^2$ and α_R of the resonator array located at $x_0 = 12$ cm and $y_0 = 16.3$ cm in unit cells of width $d_x = 24$ cm. An enhancement of the absorption is therefore noticed ($\alpha_R = 0.98$ at $\mathrm{Re}(f) = 196$ Hz). The frequency of the maximum of absorption is slightly modified due to the coupling between the resonator and the boundary. These results highlight the adaptibility of the critical coupling method applied to flexural waves for 2D reflection problem.

5.3 Conclusions

The absorption of a propagative flexural plane waves by an infinite array of circular resonators in 2D thin plates is analysed in this chapter. The absorbing efficiency of this system is analysed by means of the reflection, transmission and absorption coefficients using the multiple scattering method for both the reflection and the transmission problems. In the transmission problem, the physical conditions imply only one type of symmetry of the resonant modes, and limit the

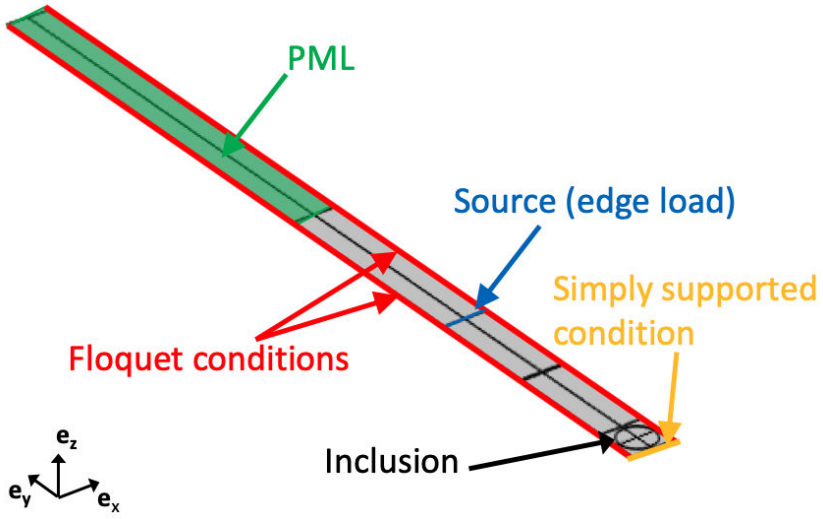

FIGURE 5.7 – 3D FEM model of the unit cell of the infinite array of inclusions used in COMSOL software to numerically compute $|R_R|^2$ and α_R. The periodicity along $\mathbf{e}_x$ is simulated using Floquet conditions and the semi-infinite length along $\mathbf{e}_y$ with Perfectly Matched Layers (PML). The simply supported condition is simulated by imposing a displacement equal to 0 along $\mathbf{e}_z$ at the corresponding face.

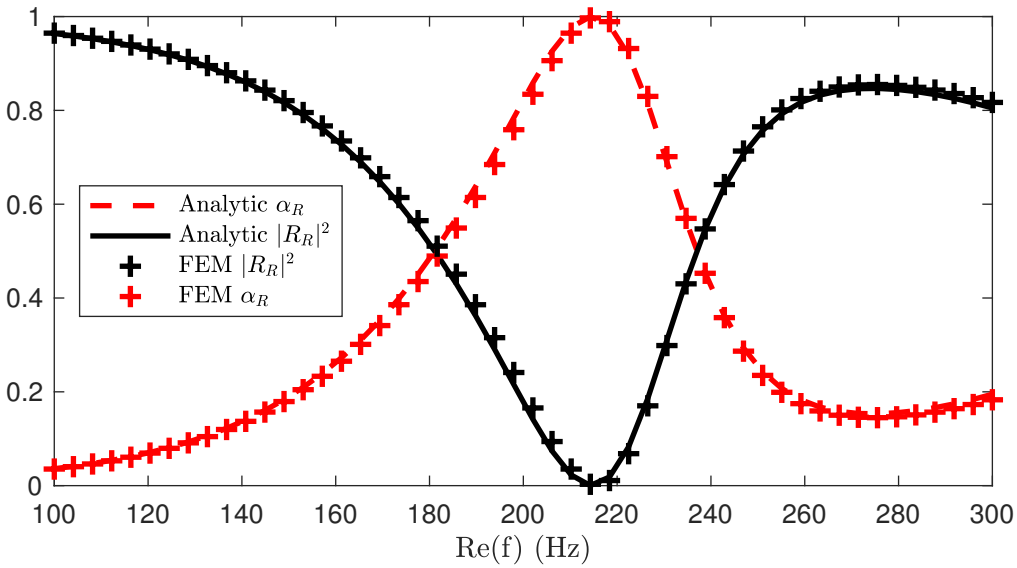

FIGURE 5.8 – Representation of $|R_R|^2$ and α_R around the first eigenfrequency of the critically coupled resonators centred in unit cells of width $d_x = 24$ cm and $y_0 = 16.3$ cm. Black and red solid lines show the analytical reflection and absorption coefficients $|R_R|^2$ and α_R respectively, whereas black and red crossed lines correspond to the reflection and absorption coefficients computed by means of a FEM model respectively.

absorption of the array to 0.5. The strategies to obtain a perfect absorption in the 2D case would be the same as in the 1D case (see Chapter 2): (*i*) breaking the symmetry of the resonator in order to treat the full problem with a single type of symmetry of the resonance mode [98]; (*ii*) using degenerate resonators with two types of symmetries at the same frequency [204]. In the reflection problem, perfect absorption is possible. To that purpose, the distance between the resonators and the boundary has to be slightly increased to reduce their coupling. The results of this chapter highlight the adaptibility of the critical coupling method applied to flexural waves for 2D problems. The resonators used in this chapter, the type of incident wave and the boundary conditions have been chosen as simple as possible to show the adaptability of the method for 2D problem and give the key feature for future designs of 2D subwavelength perfect absorbers for flexural waves. Further studies could be considered by analysing the absorption of the array submitted to several incidence angles and to other boundary conditions than simple supported. More complex axi-symmetric geometries, such as pits of power law profile as ABHs, could also be used by means of the method presented in Section 4.5. The absorbing mechanisms presented in this chapter may also be combined with other mechanisms, such as bandgaps obtained by periodically arranging the resonators along $\mathbf{e}_x$ and $\mathbf{e}_y$.

Chapter 6

Conclusions and perspectives

The main objective of this thesis was to understand, analyse and design 1D and 2D passive damping lightweight systems which can mitigate flexural waves at low frequencies, and more particularly with systems whose characteristic dimensions are much smaller than the wavelength of the incident wave. Particular interest has been accorded to the design of subwavelength perfect absorbers which have proven their efficiency in audible acoustic metamaterials, and the problem of subwavelength perfect absorption adapted for flexural waves has been investigated. The thesis has been constructed following a bottom-up approach based on the understanding of the critical coupling condition, which gives the rules for designing subwavelength perfect absorbers, and the extension of this particular condition to the case of flexural waves.

Among other damping systems, this thesis has paid attention to the Acoustic Black Holes (ABH). Such systems consist in continuously decreasing the thickness of the plate or beam by following a power-law, and provide good wave control and absorption at high frequencies. The thesis has investigated the combination of the ABH effect at high frequencies with the subwavelength perfect absorption mechanisms obtained at low frequencies.

The main contributions presented in this dissertation are summarised below as well as perspectives for future works.

6.1 Conclusions

6.1.1 Subwavelength absorbers for flexural waves

The absorption of propagative flexural waves by means of simple composite beam structures has firstly been discussed in Chapter 2. The mechanisms of energy absorption have been interpreted in terms of both the critical coupling conditions and the symmetries of the resonances for both the reflection and the transmission problems. In particular, the complex frequencies of the zeros of the scattering matrix eigenvalues in the complex frequency plane has proven to be a relevant tool for determining the possibility of achieving perfect absorption. The condition of perfect absorption is fulfilled when these zeros are placed on the real frequency axis, meaning that the inherent losses are completely compensating the energy leakage of the system. This condition is also called the critical coupling condition. The perfect absorption has been obtained for the reflection problem since it only involves a single symmetry of the resonances. In the transmission problem, the requirement to obtain perfect absorption is stronger as two kinds of symmetries of the resonances are required to be critically coupled simultaneously. In the case

presented in Chapter 2, dealing only with one type of symmetry for the resonant modes limits the absorption to 0.5. All the analytical results in Chapter 2 have been validated numerically using FEM models and an experimental validation of the reflection problem have also been performed. The presented approach can be applied to any class of 1D resonant-system provided that the resonators are local, open and lossy ones. These properties of the resonator are the essential points to achieve the perfect absorption at low frequency in addition to solving the following problems: increasing the modal density at low frequencies and matching the impedance with the background medium. These results pave the way to the design of simple resonators for efficient flexural wave absorption by means of the critical coupling condition, showing also the limits of absorption induced by the geometry used. More complex 1D geometries have also been considered in Chapter 3 by using 1D composite ABHs, showing the adaptability of the method.

The extension of the critical coupling conditions in a 2D problem for the $n = 0$ axisymmetric mode of a 2D penetrable scatterer has been analysed in Chapter 4. A first scattering problem of an uniform circular inclusion with a concentric incident wave propagating towards the centre of the resonator has been presented, and the perfect absorption has been performed by fulfilling the critical coupling condition similarly to a 1D system. The results have also highlighted that the scattering-cross section Q_{sc} cannot be related to the absorption of a scatterer for a general scattering problem with an incident plane wave due to the properties of the Bessel functions that describe the incident wave. The adaptability of the method for more complex geometries has then been shown by studying the scattering problem of an ABH using a multilayer scattering model, and has been validated by means of a FEM model. The presented approach can, once again, be adapted to any class of 2D resonant-systems provided that the resonators are local, open and lossy.

The 2D uniform circular resonator designed in Chapter 4 has been embedded in the form of an infinite array in a plate, also called metaplate, and two scattering problems have been studied by using the multiple scattering method: the reflection problem in a semi-infinite plate and the transmission problem in an infinite plate. In the transmission problem, the physical conditions have, once again, implied only one type of symmetry of the resonant modes. The absorption of the array is therefore limited to 0.5 as for the 1D cases treated in Chapter 2. In the reflection problem, perfect absorption is possible at low frequencies. To that purpose, the distance between the resonators and the boundary have been slightly increased due to their coupling. These results highlight the adaptibility of the critical coupling method applied to flexural waves for 2D problems and give the key feature for future design of 2D subwavelength perfect absorbers for flexural waves.

6.1.2 Interpretation of the ABH effect by using the complex frequency plane

A new physical insight of the ABH efficiency has emerged through the study of the critical coupling of a 1D ABH. The ABH effect has been interpreted through the use of the complex frequency plane in Chapter 3. The geometry of the ABH leads to low quality factor resonances and, as a consequence, to wide zeros of its scattering matrix eigenvalues in the complex frequency plane. The ABH effect may therefore be interpreted as a consequence of the critical coupling at one resonance frequency of the ABH and of the broadband quasi-perfect absorption at higher

frequencies, thanks to the specific geometry of the resonator. This point is the main contribution of the dissertation on the ABH effect, and sheds new light on how to interpret the ABH effect in beams. The understanding of this mechanism provides a guidance tool for the design and the optimisation of ABH terminations. Two methods have been proposed to improve the absorption of 1D ABHs using the concept of critical coupling. The first consisted in tuning the losses introduced in the system by shaping the thickness profile of the coating layer. In doing so it is possible to control the losses introduced in the resonator according to the real frequency. The second method relies on the addition of a mass at the end of the ABH and was based on the work of Aklouche *et al.* [3]. The configuration of perfect absorption at the first resonance frequency of the resonator can be obtained and tuned according to the added mass by controlling the position of the corresponding zero in the complex frequency plane.

6.2 Perspectives

Type of inherent losses. The problem of subwavelength perfect absorption adapted for flexural waves has been treated in this dissertation. One key point to obtain perfect absorption is to completely compensate the energy leakage of the system with its inherent losses. The inherent losses of the resonators have been controlled in this thesis by placing a layer of viscoelastic material on them. The use of such materials may be labourious from the experimental point of view to controle precisely the amount of losses introduced into the system, since their properties depend on the temperature and on the way they are glued on the structure. Moreover, the modification of the losses in the system implies to change the viscoelastic material which can also be arduous. The investigation for other methods to control more effectively the inherent losses of the resonators is therefore of great interest. The use of Shape Memory Polymers (SMP), whose properties are tuned by temperature control, would be relevant for instance. The damping properties of such materials are strongly temperature dependent. In particular, SMP soften and become more dissipative when the increasing temperature reaches the glass transition temperature of the material. This particular temperature is localised in the transition state where the material changes from a glassy state to a rubbery state. The application of SMP in the case of a 1D reflection problem by an ABH termination has already been done in the work of Ouisse *et al.* [138]. Their work has shown the possibility to improve the acoustic black hole effect through the control of the SMP loss factor by varying the temperature. It would be interesting to combine these types of material with the concept of perfect absorption treated in this dissertation for future designs of subwavelength perfect absorbers for flexural waves. Another kind of system that could be used is semi-active systems made of piezoelectric transducers whose damping properties can be tuned according to the frequency. This strategy is investigated by Guillaume Raybaud in the framework of its PhD thesis in the Acoustic Laboratory of Le Mans University with the Project ANR eTNAA -17-CE08-0035-01 (2017-2021) at the time of writing this dissertation.

Perfect absorption for the transmission problem. The absorption in the transmission problems treated in this thesis is limited to 0.5 since the physical conditions implied only one type of symmetry of the resonant modes and lead to a half critically coupled problem. Several strategies based on breaking the symmetry of the resonator [98] or on the use of degenerate resonators [204] have been proposed in acoustics and have proven effective. In these cases, both eigenvalues of the scattering matrix present poles and zeros located at the same real

frequencies. It would then be possible to fully critically couple the problem and so obtain a perfect absorption at the appropriate frequency. Such strategies could be adapted in the case of flexural waves in future works to obtain the perfect absorption for the transmission problem. A simple way to break the symmetry of the resonator in the case of beam structures is to consider a resonator made of two beams with different thicknesses, for instance. Perfect absorption from degenerated resonators can be obtained when the interaction of their transmission response leads to destructive interferences, while their impedance matching to the propagating medium implies no back scattering.

Multiple scattering problem. This thesis has dealt with scattering problem of flexural waves by a critically coupled array of 2D resonators. The angle of the incident wave and the boundary conditions have been chosen as simple as possible (an incident wave normal to the axis of the array and a simply supported condition have been considered) to show the adaptability of the method of perfect absorption for 2D problem. Further studies could be considered by analysing the absorption of the array submitted to several incidence angles and to other boundary conditions than simple supported. More complex axi-symmetric geometries, such as ABHs, could also be used by means of the multi-layer scattering method presented in Section 4.5. The absorbing mechanisms presented in Chapter 5 may also be combined with other mechanisms, such as bandgaps obtained by periodically arranging the resonators along $\mathbf{e}_x$ and $\mathbf{e}_y$. Finally, the interaction between the boundary and the resonators has not been further investigated due to a lack of time. Further investigations on the influence of this interaction on the resonator properties could also be interesting for future design of metaplate.

Appendices

Appendix A

Published article

IOP Publishing New J. Phys. 21 (2019) 053003 https://doi.org/10.1088/1367-2630/ab1761

New Journal of Physics
The open access journal at the forefront of physics

Deutsche Physikalische Gesellschaft DPG
IOP Institute of Physics

Published in partnership with: Deutsche Physikalische Gesellschaft and the Institute of Physics

OPEN ACCESS

RECEIVED
9 January 2019

REVISED
20 March 2019

ACCEPTED FOR PUBLICATION
9 April 2019

PUBLISHED
6 May 2019

PAPER

Limits of flexural wave absorption by open lossy resonators: reflection and transmission problems

J Leng[1], F Gautier[1], A Pelat[1], R Picó[2], J-P Groby[1] and V Romero-García[1]

[1] Laboratoire d'Acoustique de l'Université du Mans, LAUM—UMR 6613 CNRS,Le Mans Université, Avenue Olivier Messiaen, F-72085 LE MANS CEDEX 9, France
[2] Instituto para la Gestión Integral de zonas Costeras (IGIC),Universitat Politècnica de València, Paranimf 1, E-46730, Gandia, Spain

E-mail: vicente.romero@univ-lemans.fr

Keywords: perfect absorption, acoustic metamaterials, locally resonant structures

Supplementary material for this article is available online

Abstract

The limits of flexural wave absorption by open lossy resonators are analytically and numerically reported in this work for both the reflection and transmission problems. An experimental validation for the reflection problem is presented. The reflection and transmission of flexural waves in 1D resonant thin beams are analyzed by means of the transfer matrix method. The hypotheses, on which the analytical model relies, are validated by experimental results. The open lossy resonator, consisting of a finite length beam thinner than the main beam, presents both energy leakage due to the aperture of the resonators to the main beam and inherent losses due to the viscoelastic damping. Wave absorption is found to be limited by the balance between the energy leakage and the inherent losses of the open lossy resonator. The perfect compensation of these two elements is known as the critical coupling condition and can be easily tuned by the geometry of the resonator. On the one hand, the scattering in the reflection problem is represented by the reflection coefficient. A single symmetry of the resonance is used to obtain the critical coupling condition. Therefore the perfect absorption can be obtained in this case. On the other hand, the transmission problem is represented by two eigenvalues of the scattering matrix, representing the symmetric and anti-symmetric parts of the full scattering problem. In the geometry analyzed in this work, only one kind of symmetry can be critically coupled, and therefore, the maximal absorption in the transmission problem is limited to 0.5. The results shown in this work pave the way to the design of resonators for efficient flexural wave absorption.

1. Introduction

Recent studies in audible acoustics have focused on wave absorption at low frequencies by means of subwavelength locally resonant materials. In particular, the design of broadband subwavelength perfect absorbers, whose dimensions are much smaller than the wavelength of the frequency to be attenuated, has recently been proposed [1–5]. Such devices can totally absorb the energy of an incident wave and require solving the twofold but often contradictory problem: (i) increasing the density of states at low frequencies and (ii) matching the impedance with the background medium. On the one hand, the use of local resonators is a successful approach for increasing the density of states at low frequencies with reduced dimensions, as it has been shown in the field of metamaterials [6–13]. On the other hand, the local resonators of such metamaterials are open and lossy ones, implying energy leakage and inherent losses. In these systems the impedance matching can be controlled by the ratio between the inherent losses of the resonator and the leakage of energy [14]. Particularly, the perfect compensation of the leakage by the losses is known as the critical coupling condition [15] and has been widely used to design perfect absorbers in different fields of physics [16, 17] other than acoustics.

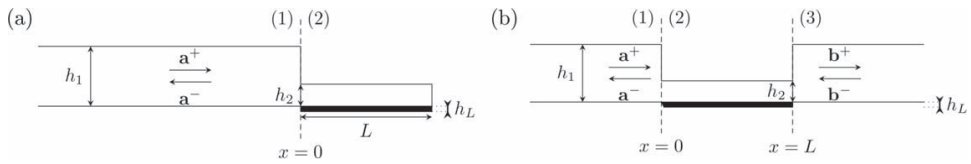

Figure 1. Diagrams of the 1D configurations analyzed for the reflection and transmission problems for flexural waves. (a) Configuration for the reflection problem. (b) Configuration for the transmission problem.

The critical coupling condition is also relevant for applications in vibrations owing to the increasing need for damping materials at low frequencies in several branches of industry [10]. Current passive solutions in this field are mainly based on the use of viscoelastic coatings [18]. Another solution yields in the tuned vibration absorber (TVA) [19–21] that is used to control flexural waves in beams. The tuning of the resonance frequency of an undamped TVA has been analyzed [20], showing that complete suppression of the flexural wave transmission can be achieved. In most cases, TVA have been used to minimize the transmission of a propagating wave [20], resulting in practice in heavy treatments at low frequencies. Less attention has been paid to the case of maximizing the absorption in order to reduce simultaneously both the reflected and transmitted waves.

The purpose of this work is to study the problem of perfect absorption of flexural waves in 1D elastic beams with local resonators by using the critical coupling condition. Particularly, the absorption of energy is analyzed through the balance between the energy leakage and the inherent losses in the resonators for the two scattering problems: the reflection and the transmission of flexural waves. The presented problem is related to the control of flexural waves in a beam using a passive TVA but with a physical insight that allows the interpretation of the limits of the flexural wave absorption based on both the critical coupling conditions and the symmetry of the excited resonances in the resonator. The analyzed systems are composed of a main beam and an open resonator simply consisting in a reduction of the thickness of the main beam. A thin viscoelastic coating is attached to it, leading to a composite material whose loss may be tuned. This composite material is modeled with the Ross–Kerwin–Ungar (RKU) method [22] and is embedded in the main beam. By tuning the losses, it is possible to analyze the different limits in both scattering problems. In practice, this type of resonator results in simpler geometries than that of the TVA which consists of complicated combinations of mass spring systems simulating a point translational impedance.

The composite is studied by means of an analytical model based on the transfer matrix method. The analytical results, in accordance with the the experimental results, show the limits of the maximal values for the flexural wave absorption and their physical interpretations in both the reflection and transmission problems. The interpretations are based on the eigenvalues of the *S*-matrix for the propagating waves, represented in the complex frequency plane [1]. An experimental prototype is designed and measured for the reflection problem. The experimental results prove the perfect absorption of flexural waves and validate the analytical predictions.

The work is organized as follows. In section 2, the theoretical model used to analyze the 1D scattering problems of flexural wave is presented. The physical analysis of the absorption coefficient in the complex frequency plane are presented in section 3. This analysis is based on an analytical model and the concept of critical coupling to obtain a perfect absorption of flexural waves. The experimental set-up used to validate the model for the reflection problem is then presented in section 4 as well as the experimental methodology and results. Finally, section 5 summarizes the main results and gives the concluding remarks.

2. Theoretical models

This section describes the theoretical model used to study the absorption of flexural waves by open lossy resonators in 1D systems, following the approach of Mace [23]. The governing equations used in the model are first introduced. Two scattering problems are then presented. The first one is the reflection problem where the absorption by a resonator made of a thinner composite beam located at the termination of a semi-infinite beam is studied (figure 1(a)). The second one is the transmission problem where the absorption of the same resonator located between two semi-infinite beams is considered (figure 1(b)). The analytical results shown for the two problems have been tested by numerical simulations, but not shown in the article for clarity of the figures, later on the analytical results are validated experimentally in the section 4.

2.1. Flexural wave propagation in uniform beams

Consider a thin uniform beam whose neutral axis is denoted by the x-axis. Assuming Euler-Bernoulli conditions, the flexural displacement $w(x, t)$ satisfies [24]:

$$D\frac{\partial^4 w}{\partial x^4} + m\frac{\partial^2 w}{\partial t^2} = 0, \tag{1}$$

where $D = EI$ is the flexural rigidity, E the Young modulus, I the second moment of area and m the linear mass. Assuming time harmonic solution of the form $e^{i\omega t}$, where ω is the angular frequency, the solution of equation (1) can be written in the frequency domain as the sum of four flexural waves:

$$w(x) = a^+ e^{-ikx} + a_N^+ e^{-kx} + a^- e^{ikx} + a_N^- e^{kx}. \tag{2}$$

The complex amplitudes of the propagative and evanescent waves are a and a_N respectively, and the signs $^+$ and $^-$ denote the outgoing and ingoing waves respectively. The evanescent component is a near field component, the amplitude of which decreases exponentially with distance. The flexural wavenumber k is given by $k^4 = \frac{m\omega^2}{D}$, which is real and positive in the lossless case and complex when damping is accounted for. The wave amplitude is expressed in the vector form by convenience:

$$\mathbf{a}^+ = \begin{bmatrix} a^+ \\ a_N^+ \end{bmatrix}, \quad \mathbf{a}^- = \begin{bmatrix} a^- \\ a_N^- \end{bmatrix}. \tag{3}$$

The relation between wave amplitudes along a beam with a constant thickness are then described by

$$\mathbf{a}^+(x_0 + x) = \mathbf{f}\mathbf{a}^+(\mathbf{x_0}) \text{ and } \mathbf{a}^-(x_0 + x) = \mathbf{f}^{-1}\mathbf{a}^-(\mathbf{x_0}), \tag{4}$$

where the diagonal transfer matrix $\mathbf{f}$ is given by

$$\mathbf{f} = \begin{bmatrix} e^{-ikx} & 0 \\ 0 & e^{-kx} \end{bmatrix}. \tag{5}$$

2.2. Reflection coefficient in a pure reflection problem

Consider an incident plane wave in the configuration described by the figure 1(a), where the system is terminated by a free termination at one end. The displacement $\mathbf{w}$ at any point for $x < 0$ reads as

$$\mathbf{w}(x < 0) = \mathbf{a}^+ + \mathbf{a}^- = \mathbf{a}^+ + \mathbf{R_r} \cdot \mathbf{a}^+, \tag{6}$$

where $\mathbf{R_r}$ denotes the reflection matrix of the resonant termination of the beam at $x = 0$. The incident wave is transmitted into the resonant termination and reflected at its end, therefore the matrix $\mathbf{R}_r$ can be evaluated, using the displacement continuity at the interface and at the boundaries as [23]:

$$\mathbf{R_r} = \mathbf{a}^-\mathbf{a}^{+-1} = \mathbf{r_{12}} + \mathbf{t_{12}}((\mathbf{f r_f f})^{-1} - \mathbf{r_{21}})^{-1}\mathbf{t_{21}}, \tag{7}$$

where $\mathbf{r_{ij}}$ and $\mathbf{t_{ij}}$ represent the reflection and transmission matrices from sections (i)–(j) of the beam (see figure 1(a)). Considering continuity and equilibrium respectively at the section change, these matrices are given by

$$\mathbf{t_{ij}} = \frac{4}{\Delta}\begin{bmatrix} (1+\beta)(1+\gamma) & (-1+1i\beta)(1-\gamma) \\ (-1-i\beta)(1-\gamma) & (1+\beta)(1+\gamma) \end{bmatrix}, \tag{8}$$

$$\mathbf{r_{ij}} = \frac{2}{\Delta}\begin{bmatrix} -2(\beta^2-1)\gamma - 1i\beta(1-\gamma)^2 & (1+i)\beta(1-\gamma^2) \\ (1-i)\beta(1-\gamma^2) & -2(\beta^2-1)\gamma + i\beta(1-\gamma)^2 \end{bmatrix}, \tag{9}$$

where $\beta = \frac{k_j}{k_i}$ and $\gamma = \frac{D_j k_j^2}{D_i k_i^2}$ correspond to the ratios of wavenumbers and bending wave impedances, and $\Delta = (1+\beta)^2(1+\gamma)^2 - (1+\beta^2)(1-\gamma)^2$. The reflection matrix $\mathbf{r_f}$ of the free termination is given by

$$\mathbf{r_f} = \begin{bmatrix} -\imath & (1+\imath) \\ (1-\imath) & \imath \end{bmatrix}. \tag{10}$$

$\mathbf{R_r}$ is thus a 2×2 matrix where the diagonal components correspond to the reflection coefficients of the propagative and evanescent waves respectively. The study focuses on the reflection of waves in the far-field ($x \to -\infty$), i.e. on the propagative waves that carry the energy. The first term of the reflection matrix $\mathbf{R_r}(1,1) \equiv R_r$ is therefore only considered since $\mathbf{R_r}(1,2)$, $\mathbf{R_r}(2,1)$, $\mathbf{R_r}(2,2) \to 0$ when $x \to -\infty$. The absorption coefficient α_R of propagating waves in the reflection problem can then be written as:

$$\alpha_r = 1 - |R_r|^2, \qquad x \to -\infty. \tag{11}$$

In the lossless case, i.e. without dissipation, R_r is simply equal to 1 for any purely real frequency as the energy conservation is fulfilled.

2.3. Reflection and transmission coefficients in a 1D symmetric and reciprocal transmission problem

The transmission problem of the structure shown in figure 1(b) is described in this section, considering $\mathbf{b}^- = 0$. Due to the symmetry of the resonator and assuming propagation in the linear regime, the problem is considered as symmetric and reciprocal. The reflection and transmission matrices $\mathbf{R_t}$ and $\mathbf{T_t}$ at $x = 0$ and $x = L$ are used to

Table 1. Geometric and material parameters of the studied systems. The value of η_l depends on the experimental set-up used, see main text for the used values retrieved from experiments.

	Geometric parameters	Material parameters
Main beam	$h_1 = 5$ mm	$\rho = 2811$ kg m^{-3}
	$b = 2$ cm	E=71.4 GPa
		$\eta = 0$
		$\nu = 0.3$
Resonator beam	$h_2 = 0.217$ mm	$\rho_2 = 2811$ kg m^{-3}
	$b_2 = 2$ cm	E_2=71.4 GPa
	L=1.6 cm	$\eta_2 = 0$
		$\nu_2 = 0.3$
Coating layer	$h_l = 1.5$ mm	$E_l = 6.86 \times 10^{-3}$ GPa
	$b_l = 2$ cm	$\rho_l = 93.3$ kg m^{-3}
	$L_l = 1.6$ cm	η_l
		$\nu_l = 0.3$

define the displacements on each side of the resonator such as:

$$\mathbf{w}(x < 0) = \mathbf{a}^+ + \mathbf{a}^- = \mathbf{a}^+ + \mathbf{R_t} \cdot \mathbf{a}^+, \tag{12}$$

$$\mathbf{w}(x > L) = \mathbf{b}^+ = \mathbf{T_t} \cdot \mathbf{a}^+. \tag{13}$$

Using the displacement continuity at $x = 0$ and $x = L$ in a similar way as in the previous section, $\mathbf{R_t}$ and $\mathbf{T_t}$ are written as

$$\mathbf{R_t} = \mathbf{r_{12}} + \mathbf{t_{12}}((\mathbf{fr_{23}\,f})^{-1} - \mathbf{r_{21}})^{-1}\mathbf{t_{21}}, \tag{14}$$

$$\mathbf{T_t} = \mathbf{a}^-\mathbf{a}^{+-1} = \mathbf{t_{23}}(\mathbf{I} - (\mathbf{fr_{21}\,f})\mathbf{r_{23}})^{-1}\mathbf{ft_{12}}. \tag{15}$$

Therefore the absorption coefficient of the transmission problem is defined as

$$\alpha_t = 1 - |T_t|^2 - |R_t|^2, \quad x \to \pm\infty \tag{16}$$

where $R_t = \mathbf{R_t}(1,1)$ when $x \to -\infty$ and $T_t = \mathbf{T_t}(1,1)$ when $x \to +\infty$.

2.4. Viscoelastic losses in the resonator: the RKU model

The inherent losses of the resonator are introduced by a thin absorbing layer of thickness h_l as shown in figures 1(a), (b) and are considered frequency independent. The complex Young Modulus of the absorbing layer is $E_l(1 + i\eta_l)$, where η_l is its loss factor. Using the RKU model [22], this region is modeled as a single composite layer with a given effective bending stiffness D_c written as:

$$D_c = E_2 I_2 \left[(1 + j\eta_2) + e_c h_c^3 (1 + j\eta_l) + \frac{3 + (1 + h_c)^2 e_c h_c [1 - \eta_2\eta_l + j(\eta_2 + \eta_l)]}{1 + e_c h_c (1 + j\eta_l)} \right], \tag{17}$$

where the indices 2 and l stand for the parameters of the thin beam and of the absorbing layer respectively, $e_c = E_l/E_2$ and $h_c = h_l/h_2$. The wave number k_c of the composite material can then be written as $k_c^4 = \frac{\rho_c h \omega^2}{D_c}$, where $h = h_l + h_2$ and $\rho_c h = \rho_2 h_2 + \rho_l h_l$.

3. Limits of absorption for the reflection and transmission problems

This section describes the limits of absorption for flexural waves in the reflection and transmission problem by using open, lossy and symmetric resonators. It provides tools to design absorbers with a maximal absorption in both problems. For this purpose, the eigenvalues of the scattering matrix of the propagative waves are represented in the complex frequency plane as in [1]. The material and geometric parameters used in the following sections are described in table 1.

3.1. Properties of the *S*-matrix

Consider a two-port, 1D, symmetric and reciprocal scattering process for the systems described in figure 1(b) in the case where $x \to \pm\infty$. The relation between the amplitudes a^+ and b^- of the incoming waves and a^- and b^+ of the outgoing waves when $x \to \pm\infty$ is given by

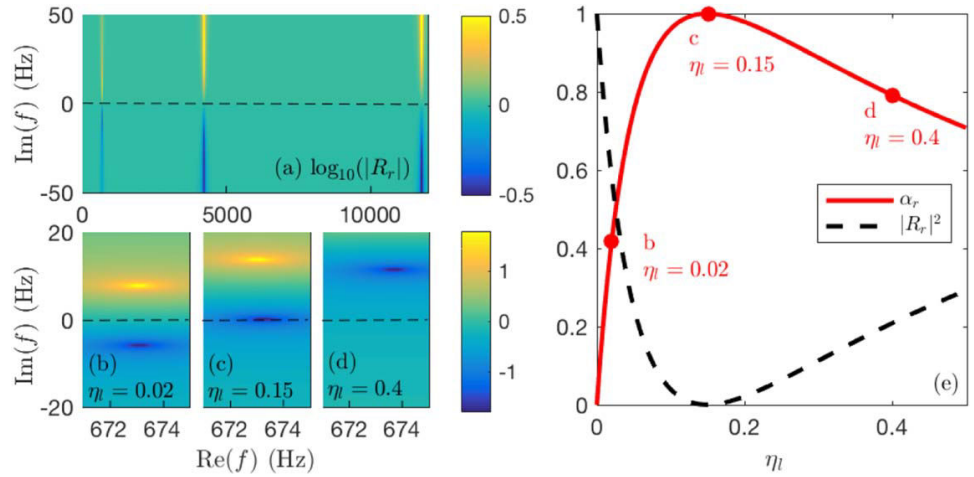

Figure 2. Analysis of the scattering in the reflection problem. (a) Representation of $\log_{10}(|R_r|)$ in the complex frequency plane for the lossless case. (b)–(d) $\log_{10}(|R_r|)$ in the complex frequency plane in the lossy case for configurations with $\eta_l = 0.02, 0.15$ and 0.4 respectively. The case when the critical coupling condition is fulfilled ($\eta_l = 0.15$) is represented in (c). (e) Trade-off of the absorption at the first resonance frequency of the resonator as the inherent loss η_l is increased in the system. The points along the absorption curve represent the values of the absorption for the configurations represented in figures (b)–(d). Red continuous (Black dashed) line represents the absorption (reflection) coefficient as a function of eta_l at 673 Hz, corresponding to the first resonance frequency of the termination.

$$\begin{pmatrix} a^- \\ b^+ \end{pmatrix} = \mathbf{S}(\omega)\begin{pmatrix} b^- \\ a^+ \end{pmatrix} = \begin{bmatrix} T_t & R_t \\ R_t & T_t \end{bmatrix}\begin{pmatrix} b^- \\ a^+ \end{pmatrix}, \quad x \to \pm\infty, \tag{18}$$

where **S** is the scattering matrix or the *S*-matrix of the propagative waves. The complex eigenvalues of the *S*-matrix are $\psi_{1,2} = T_t \pm R_t$. An eigenvalue of the *S*-matrix equal to zero implies that the incident wave is completely absorbed ($a^- = b^+ = 0$). This happens when $T_t = \pm R_t$ and the incident waves $[a^+, b^-]$ correspond to the relevant eigenvector. When the eigenvalues are evaluated in the complex frequency plane [1], poles and zeros can be identified. The pole frequencies correspond to the resonances of the resonator (zeros of the denominator of the eigenvalues) while the zero frequencies (zeros of the numerator of the eigenvalues) correspond to the perfect absorption configuration. In the case of a reflection problem, the eigenvalues are reduced to the reflection coefficient.

Since the systems analyzed in this work are invariant under time-reversal symmetry, the scattering matrix, as defined in equation (18), presents unitary property [25] in the lossless case (i.e. without dissipative losses):

$$\mathbf{S}^*\mathbf{S} = \mathbf{I}. \tag{19}$$

The complex frequencies of the eigenvalue poles of the propagative *S*-matrix are complex conjugates of its zeros. Poles and zeros appear therefore symmetric with respect to the real frequency axis in the lossless case.

3.2. Reflection problem

3.2.1. Lossless case

In the reflection problem, where no wave is transmitted, the reflection coefficient R_r represents the scattering of the system. Thus, R_r corresponds directly to both the *S*-matrix and its associated eigenvalue ($\psi = R_r$). Its zeros correspond to the cases in which the incident wave is totally absorbed. In the lossless case, $|R_r| = 1$ for any purely real frequency and the pole-zero pairs appear at complex conjugate frequencies. Figure 2(a) depicts $\log_{10}(|R_r|)$ in the complex frequency plane. The main beam, the resonator beam and the coating layer have the geometric and material parameters given in table 1. Note that the Young moduli are purely real in the lossless case ($\eta = \eta_2 = \eta_l = 0$). As shown in section 3.1, the poles and zeros appear in pairs and are symmetric with respect to the real frequency axis. Moreover the value of $|R_r|$ along the real frequency axis is equal to 1. It is also worth noting that the imaginary part of the pole in the lossless case represents the amount of energy leakage by the resonator through the main beam [1]. With the time dependence convention used in this work, the wave amplitude at the resonance frequency decays as $e^{-\mathrm{Im}(\omega_{\mathrm{pole}})t}$. Thus the decay time τ_{leak} can be related with the quality factor due to the leakage as $Q_{\mathrm{leak}} = \frac{\mathrm{Re}(\omega_{\mathrm{pole}})\tau_{\mathrm{leak}}}{2} = \frac{\mathrm{Re}(\omega_{\mathrm{pole}})}{2\mathrm{Im}(\omega_{\mathrm{pole}})}$, where the leakage rate can be defined as $\Gamma_{\mathrm{leak}} = 1/\tau_{\mathrm{leak}} = \mathrm{Im}(\omega_{\mathrm{pole}})$. The imaginary part of the poles and zeros increases when the real part of the frequency increases, meaning that more energy leaks out through the resonator at high frequencies.

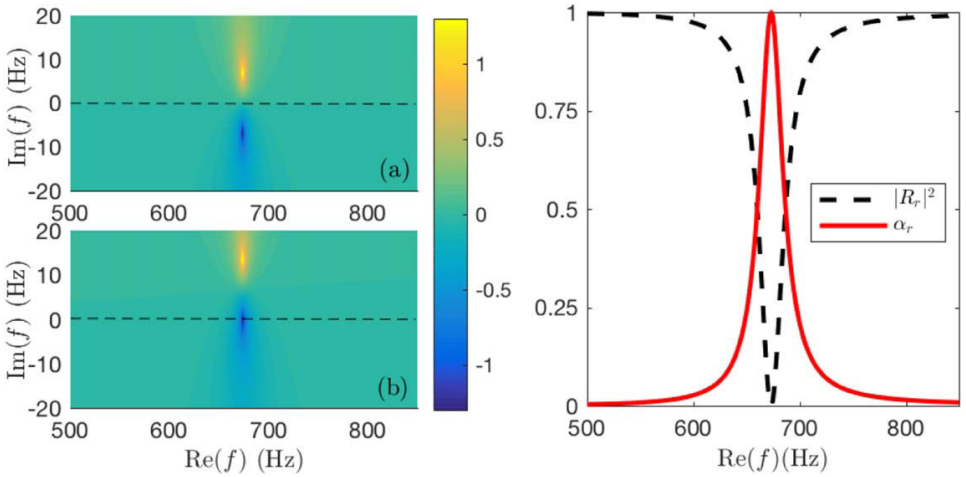

Figure 3. Representation of the perfect absorption for the reflection problem. (a), (b) Show the representation of the $\log_{10}(|R_r|)$ for the lossless and lossy configurations respectively. (c) Red continuous and black dashed lines show the analytical absorption and reflection coefficients for the critical coupled configuration respectively.

3.2.2. Lossy case

For the sake of clarity, this section only focuses on the first pole-zero pair of the system previously described. The discussion can nevertheless be extended to any pole-zero pair of the system in the complex frequency plane. Losses are now introduced into the system by adding an imaginary part to the Young modulus of the damping material such that it can be written as $E_l(1 + i\eta_l)$.

As a consequence, the symmetry between the poles and zeros with respect to the real frequency axis is broken, since the property of equation (19) is no more satisfied in the lossy case. Figures 2(b)–(d) depict $\log_{10}(|R_r|)$ in the complex frequency plane around the first resonance frequency for three different increasing values of η_l. Figure 2(b) represents the case for which the losses are small ($\eta_l = 0.02$). In this case, the pole-zero pair is quasi-symmetric with respect to the real frequency axis. As the losses in the damping layer increase ($\eta_l = 0.15$ in figure 2(c) and $\eta_l = 0.4$ in figure 2(d)), the zero moves to the real frequency axis. In particular, the zero of the reflection coefficient is exactly located on the real frequency axis in figure 2(c). In this situation, the amount of inherent losses in the resonator equals the amount of energy leakage. This situation is known as the critical coupling condition [15] and implies the impedance matching, leading to a perfect absorption.

The value of the absorption coefficient of the first resonant peak as a function of η_l is depicted in figure 2(e). The position of the zero in the complex frequency plane is directly related to the value of the flexural wave absorption. When the zero approaches the real frequency axis, the value of the absorption is close to one, being equal to 1 when the zero is exactly located in the real frequency axis. It should be noted that the perfect absorption cannot occur once the zero has crossed the real frequency axis. This property might appear counterintuitive since it means that adding a large amount of losses in the system might lead to a deterioration of the absorbing properties of the structure.

3.2.3. Design of perfect absorbers for flexural wave in the reflection problem

A theoretical design for the perfect absorption of flexural waves is shown in this section based on the configuration represented in the figure 1(b) and the parameters given in table 1. Considering that there is no inherent losses in the main beam and the resonator beam ($\eta = \eta_2 = 0$), the loss factor of the coating layer has to be $\eta_l = 0.15$ to obtain a perfect absorption at the first resonance frequency of the system.

Figures 3(a), (b) depict $\log_{10}(|R_r|)$ for the lossless and lossy configurations in the complex frequency plane respectively. Figure 3(b) shows particularly the first pole-zero pair of the system in the perfect absorption configuration where the critical coupling condition is fulfilled, showing the zero exactly located on the real frequency axis. Figure 3(c) shows the corresponding absorption (red continuous line) and reflection (black dashed line) coefficients according to real frequencies for the critical coupled configuration. These coefficients are calculated with the analytical model described in previous sections. The incident wave is totally absorbed at the first resonance frequency of the composite beam.

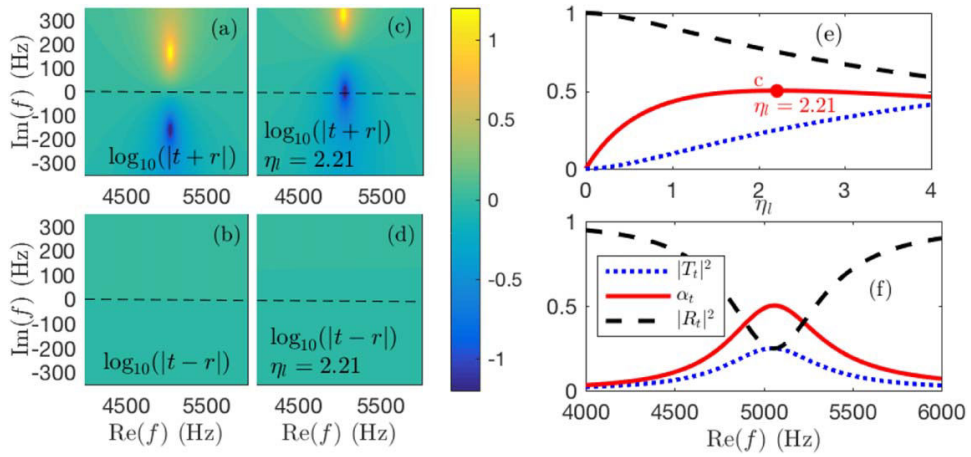

Figure 4. Representation of the eigenvalues of the *S*-matrix for a transmission problem in the lossless and lossy case. (a) and (b) Lossless case for $\log_{10}(|\psi_s|)$ and $\log_{10}(|\psi_a|)$ in the complex frequency plane. (c) and (d) Lossy case for $\log_{10}(|\psi_s|)$ and $\log_{10}(|\psi_a|)$ in the complex frequency plane. (e) Trade-off of the transmission (blue dotted line), reflection (black dashed line) and absorption (red continuous line) for the maximum absorption of the first mode as the loss factor of the coating layer increases. (f) Red continuous, black dashed and blue dotted lines represent the absorption, reflection and transmission coefficients respectively for the half critically coupled configuration.

3.3. Transmission problem

For the transmission problem, the *S*-matrix is defined in equation (18) and has two eigenvalues $\psi_{1,2}$. The scatterer being mirror symmetric, the problem can be reduced to two uncoupled sub-problems: a symmetric problem where $\psi_s = T_t + R_t$ and an anti-symmetric, where $\psi_a = T_t - R_t$.

ψ_s corresponds to the reflection coefficient of the symmetric problem while ψ_a corresponds to the reflection coefficient of the anti-symmetric problem. The absorption coefficient can also be expressed as $\alpha = (\alpha_s + \alpha_a)/2$ where $\alpha_s = 1 - |\psi_s|^2$ and $\alpha_a = 1 - |\psi_a|^2$. Similarly to the reflection problem, poles and zeros of ψ_s and ψ_a can be identified in the complex frequency plane. The following sections focuses on the first resonant mode of the beam resonator, the displacement distribution of which is symmetric. The interpretation of the results can nevertheless be applied to the higher order modes with anti-symmetric distributions of the displacement field. It is worth noting that the displacement distribution of the resonant modes changes from symmetric to anti-symmetric as the mode increases due to the geometry of the resonators [26].

3.3.1. Lossless case

Figures 4(a) and (b) show the variation of $\log_{10}(|\psi_s|)$ and $\log_{10}(|\psi_a|)$ evaluated respectively in the complex frequency plane in the lossless case for the first resonant mode. The main beam, the resonator beam and the coating layer of the studied system have still the material and geometric parameters of table 1, where $\eta = \eta_2 = eta_l = 0$ in the lossless case. The symmetric and anti-symmetric problems exhibit pole-zero pairs similarly to the reflection problem in the lossless case. These pairs are also symmetrically positioned with respect to the real frequency axis. The absence of dissipation is shown along the real frequency axis where $|T_t \pm R_t| = 1$ for any real frequency. This section focuses only on the first resonant mode which has a symmetric distribution of the displacement field. Therefore, only the symmetric problem presents a pole-zero pair at the corresponding resonance frequency, while the anti-symmetric one does not.

3.3.2. Lossy case

Unlike the reflection problem, the condition for perfect absorption is stronger in the transmission one and needs to place the zeros of both ψ_s and ψ_a at the same frequency in the real frequency axis. Once this condition is fulfilled, a^+ and b^- correspond to the relevant eigenvector and the system satisfies the coherent perfect absorption condition [2, 9, 27].

Losses are introduced in the system in the same way as for the reflection problem, i.e. by increasing the loss factor η_l of the material of the damping layer. Once the losses are introduced, the position of the pole-zero pair of the symmetric eigenvalue in the complex frequency plane shifts towards the upper half space while the anti-symmetric problem remains unchanged without pole-zero pairs, as shown in figures 4(c) and (d). Therefore, only the zero of the symmetric problem can be placed on the real frequency axis, i.e. only half of the problem can be critically coupled. Figure 4(e) shows the dependence of the reflection, transmission and absorption coefficient

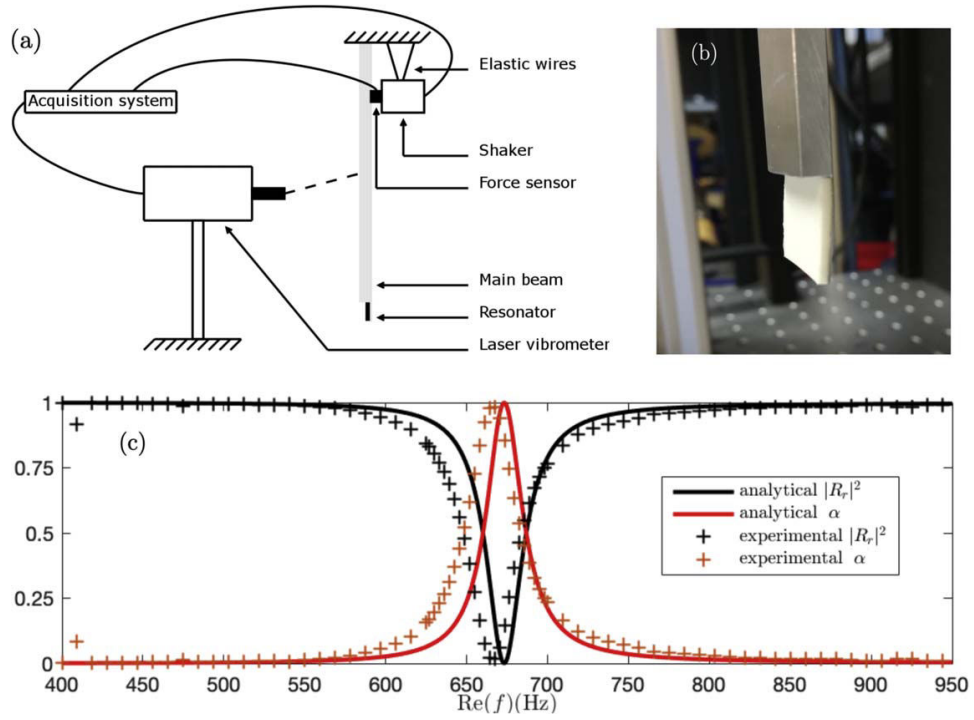

Figure 5. (a) Diagram of the experimental set-up. (b) Photograph of the resonator. (c) Black crosses and red open circles show respectively $|R_r|^2$ and α_r for the critical coupled configuration measured with the experimental set-up. Black dashed and red continuous lines show $|R_r|^2$ and α_r calculated with the analytical model.

on the inherent losses in the resonator for the first mode. The maximum absorption obtained is 0.5 since only the symmetric problem is critically coupled ($\alpha = (\alpha_s + \alpha_a)/2 \simeq (1 + 0)/2 = 1/2$).

3.3.3. Design of maximal absorbers for flexural wave in the transmission problem

Based on the results discussed previously, a configuration with maximal absorption for flexural waves in the transmission problem is designed with the parameters given in table 1. As for the reflection problem, no inherent losses are considered in the main beam and the resonator beam ($\eta = \eta_2 = 0$). The loss factor of the coating layer is $\eta_l = 2.21$. The reflection, transmission and absorption for this configuration is analyzed in figure 4(f), showing that the maximum absorption is 0.5 at the resonance frequency of the beam. This result is in accordance with the ones previously obtained [2, 9, 21], even if the resonator is not a point translational impedance. The absorption is limited to 0.5 since only one kind of geometry of resonant mode can be excited. The problem is therefore half critically coupled. To obtain a higher absorption, other strategies based on breaking the symmetry of the resonator [5] or on the use of degenerate resonators are needed [28]. In these cases, both eigenvalues present poles and zeros located at the same real frequencies. It would then be possible to fully critically couple the problem and so obtain a perfect absorption (i.e. $\alpha = 1$) at the appropriate frequency.

4. Experimental results

This section presents the experimental results of the reflection coefficient [29, 30] for an aluminum beam system with the configuration described in section 3.2.3.

4.1. Experimental set-up

The beam is held vertically in order to avoid static deformation due to gravity. The extremity at which the reflection coefficient is estimated is oriented towards the ground (see figure 5(a)). The used coating layer have been experimentally characterized showing an $\eta_l = 0.15$, which is the value for which perfect absorption can be observed. A photograph of the resonator with the coating layer is shown in figure 5(b). The measurements are performed along the beam at 21 points equidistant of 5 mm and located on its neutral axis in order to avoid the torsional component. The measurement points are also located sufficiently far from the source and the

extremity of the beam to consider far-field assumption and neglect the contribution of evanescent waves. In this case, far-field assumption is fulfilled at a distance l_f from both the source and the resonator for which the evanescent wave loses 90% of its initial magnitude. The low frequency limit of the measurements is then estimated using $e^{kl_f} = 0.1$. The shaker excites the beam with a sweep sine. The displacement field versus frequency is obtained from the measurements of the vibrometer at each measure point.

4.2. Experimental estimation of the reflection coefficient

Consider the flexural displacement $W(x_i, \omega)$ measured at the point $x_i (i \in [0,\ 20])$ for a given angular frequency ω as

$$W(x_i,\ \omega) = A(\omega)\mathrm{e}^{-\mathrm{i}kx_i} + B(\omega)\mathrm{e}^{\mathrm{i}kx_i}. \tag{20}$$

The set of $W(x_i, \omega)$ for each measurement point can be written in a matrix format [30] such as

$$\begin{pmatrix} W(x_0,\ \omega) \\ W(x_1,\ \omega) \\ W(x_2,\ \omega) \\ \vdots \\ W(x_{20},\ \omega) \end{pmatrix} = \begin{pmatrix} \mathrm{e}^{(-\mathrm{i}kx_0)} & \mathrm{e}^{(\mathrm{i}kx_0)} \\ \mathrm{e}^{(-\mathrm{i}kx_1)} & \mathrm{e}^{(\mathrm{i}kx_1)} \\ \mathrm{e}^{(-\mathrm{i}kx_2)} & \mathrm{e}^{(\mathrm{i}kx_2)} \\ \vdots & \vdots \\ \mathrm{e}^{(-\mathrm{i}kx_{20})} & \mathrm{e}^{(\mathrm{i}kx_{20})} \end{pmatrix} \begin{pmatrix} A(\omega) \\ B(\omega) \end{pmatrix}. \tag{21}$$

The amplitudes $A(\omega)$ and $B(\omega)$ can then be derived from equation (21) which forms an overdetermined system. From these amplitudes, the reflection coefficient of the propagative waves can be deduced for any ω as:

$$R_r(\omega) = \frac{A(\omega)}{B(\omega)}. \tag{22}$$

4.3. Experimental evidence of perfect absorption for flexural waves

Experimental results obtained with the experimental set-up are depicted in figure 5(c). A drop of reflection is noticed at the first resonant frequency of the termination with a minimum value of $|R_r|^2 = 0.02$ at 667 Hz for the experiment and $|R_r|^2 = 0$ at 673 Hz for the analytical result. The gap between the analytical and experimental resonant frequency is 0.9%. This frequency shift between the model and the experiment is mainly due to the geometric uncertainty in the resonator thickness, induced by the machining process. This geometrical uncertainty induces also an estimation uncertainty of the energy leakage of the resonator. The absorption is then experimentally limited to $\alpha_r = 0.98$. Evidence of perfect absorption for flexural waves by means of critical coupling is shown experimentally here.

Three experimental scans of the whole beam at 500, 670 and 800 Hz have been measured[3]. At 500 or 800 Hz the reflection coefficient is very close to one. The standing waves in the main beam are visible at these frequencies. At 670 Hz, the termination absorbs totally the incident waves. There is therefore no standing waves and the waves are propagating in the main beam.

5. Conclusions

Absorption of propagative flexural waves by means of simple beam structures is analyzed in this work. The main mechanisms are interpreted in terms of both the critical coupling conditions and the symmetries of the resonances for both the reflection and the transmission problems. The positions of the zeros of the eigenvalues of the scattering matrix in the complex frequency plane give informations on the possibility to obtain the perfect absorption. The perfect absorption condition is fulfilled when these zeros are placed on the real frequency axis, meaning that the inherent losses are completely compensating the energy leakage of the system. In the reflection problem, the physical conditions of the problem lead to perfect absorption at low frequencies. In this case a single symmetry for the resonance is excited and perfect absorption can be obtained when the inherent losses of the system balance the energy leakage of the system. In the transmission problem, the requirement to obtain perfect absorption is stronger than for the case in reflection as two kinds of symmetries of the resonances are required to be critically coupled simultaneously. In the case presented in this work, or in the general case of point translational impedances, dealing only with one type of symmetry for the resonant modes [21] limits the absorption to 0.5. Therefore for the perfect absorption in the transmission case, two strategies are needed: (i) breaking the symmetry of the resonator in order to treat the full problem with a single type of symmetry of the resonance mode [5]; (ii) using degenerate resonators with two types of symmetries at the same frequency being critically coupled [28]. The resonator used in this study has been chosen as an integral part of the main beam for

[3] See supplementary material is available online at stacks.iop.org/NJP/21/053003/mmedia: videos 500 Hz.avi, 670 Hz.avi and 800 Hz.avi

experimental set-up reasons. However, the presented approach can be applied to any class of 1D resonant-system provided that the resonators are local, open and lossy ones. These properties of the resonator are the essential points to achieve the perfect absorption at low frequency by solving the following problems: increasing the density of states at low frequencies and matching the impedance with the background medium.

Acknowledgments

The authors thank Mathieu Sécail-Geraud and Julien Nicolas for the development of the experimental set-up. The work has been founded by the RFI Le Mans Acoustic (Région Pays de la Loire) within the framework of the Metaplaque project. This article is based upon work from COST action DENORMS CA 15125, supported by COST (European Cooperation in Science and Technology). The work was partly supported by the Spanish Ministry of Economy and Innovation (MINECO) and European Union FEDER through project FIS2015-65998-C2-2 and by project AICO/2016/060 by Consellería de Educación, Investigación, Cultura y Deporte de la Generalitat Valenciana.

ORCID iDs

V Romero-García https://orcid.org/0000-0002-3798-6454

References

[1] Romero-García V, Theocharis G, Richoux O and Pagneux V 2016 Use of complex frequency plane to design broadband and sub-wavelength absorbers *J. Acoust. Soc. Am.* **139** 3395–403
[2] Merkel A, Theocharis G, Richoux O, Romero-García V and Pagneux V 2015 Control of acoustic absorption in one-dimensional scattering by resonant scatterers *App. Phys. Lett.* **107** 244102
[3] Groby J-P, Pommier R and Aurégan Y 2016 Use of slow sound to design perfect and broadband passive sound absorbing materials *J. Acoust. Soc. Am.* **139** 1660–71
[4] Jiménez N, Huang W, Romero-García V, Pagneux V and Groby J-P 2016 Ultra-thin metamaterial for perfect and quasi-omnidirectional sound absorption *Appl. Phys. Lett.* **109** 121902
[5] Jiménez N, Romero-García V, Pagneux V and Groby J-P 2017 Rainbow-trapping absorbers: Broadband, perfect and asymmetric sound absorption by subwavelength panels for transmission problems *Sci. Rep.* **7** 13595
[6] Fang N, Xi D, Xu J, Ambati M, Srituravanich W, Sun C and Zhang X 2006 Ultrasonic metamaterials with negative modulus *Nat. Mater.* **5** 452
[7] Liu Z, Zhang X, Mao Y, Zhu Y Y, Yang Z, Chan C T and Sheng P 2000 Locally resonant sonic materials *Science* **289** 1734–6
[8] Skelton E A, Craster R V, Colombi A and Colquitt D J 2018 The multi-physics metawedge: graded arrays on fluid-loaded elastic plates and the mechanical analogues of rainbow trapping and mode conversion *New J. Phys.* **20** 053017
[9] Wei P, Croënne C, Tak Chu S and Li J 2014 Symmetrical and anti-symmetrical coherent perfect absorption for acoustic waves *Appl. Phys. Lett.* **104** 121902
[10] Duan Y, Luo J, Wang G, Hang Z H, Hou B, Li J, Sheng P and Lai Y 2015 Theoretical requirements for broadband perfect absorption of acoustic waves by ultra-thin elastic meta-films *Sci. Rep.* **5** 12139
[11] Theocharis G, Richoux O, Romero-García V, Merkel A and Tournat V 2014 Limits of slow sound propagation and transparency in lossy, locally resonant periodic structures *New J. Phys.* **16** 093017
[12] Colombi A, Ageeva V, Smith R J, Clare A, Patel R, Clark M, Colquitt D, Roux P, Guenneau S and Craster R V 2017 Enhanced sensing and conversion of ultrasonic rayleigh waves by elastic metasurfaces *Sci. Rep.* **7** 6750
[13] Pal R J and Ruzzene M 2017 Edge waves in plates with resonators: an elastic analogue of quantum valley hall effect *New J. Phys.* **19** 025001
[14] Bliokh K Y, Bliokh Y P, Freilikher V, Savel'ev S and Nori F 2008 Colloquium: unusual resonators: plasmonics, metamaterials, and random media *Rev. Mod. Phys.* **80** 1201
[15] Yariv A 2000 universal relations for coupling of optical power between microresonators and dielectric waveguides *Electron. Lett.* **36** 321–2
[16] Xu Y, Li Y, Lee R K and Yariv A 2000 Scattering-theory analysis of waveguide-resonator coupling *Phys. Rev.* E **62** 7389
[17] Cai M, Painter O and Vahala K J 2000 Observation of critical coupling in a fiber taper to a silica-microsphere whispering-gallery mode system *Phys. Rev. Lett.* **85** 74
[18] Teng T-L and Hu N-K 2001 Analysis of damping characteristics for viscoelastic laminated beams *Comput. Method Appl.* M **190** 3881–92
[19] Den Hartog J P 1985 *Mechanical Vibrations* (New York: Dover)
[20] Brennan M J 1999 Control of flexural waves on a beam using a tunable vibration neutraliser *J. Sound Vib.* **222** 389–407
[21] El-Khatib H M, Mace B R and Brennan M J 2005 Suppression of bending waves in a beam using a tuned vibration absorber *J. Sound Vib.* **288** 1157–75
[22] Ross D, Ungar E L and Kerwin E M 1960 Damping of plate flexural vibrations by means of viscoelastic laminae *Structural Damping* (Oxford: Pergamon) pp 49–57
[23] Mace B R 1984 Wave reflection and transmission in beams *J. Sound Vib.* **97** 237–46
[24] Leissa A W 1969 *Tabulated Numerical Results of Theories of Plate Vibration* (Washington, DC: NASA)
[25] Norris A N 1998 Reflection and transmission of structural waves at an interface between doubly curved shells *Acta Acust. United Ac.* **84** 1066–76
[26] Jiménez N, Romero-García V, Pagneux V and Groby J-P 2017 Quasiperfect absorption by subwavelength acoustic panels in transmission using accumulation of resonances due to slow sound *Phys. Rev.* B **95** 014205

[27] Chong Y D, Ge L, Cao H and Stone A D 2010 Coherent perfect absorbers: time-reversed lasers *Phys. Rev. Lett.* **105** 053901
[28] Yang M, Meng C, Fu C, Li Y, Yang Z and Sheng P 2015 Subwavelength total acoustic absorption with degenerate resonators *Appl. Phys. Lett.* **107** 104104
[29] Gautier F, Moulet M-H and Pascal J-C 2006 Reflection, transmission and coupling of longitudinal and flexural waves at beam junctions. part i: measurement methods *Acta Acust. United Ac.* **92** 982–97
[30] Denis V, Gautier F, Pelat A and Poittevin J 2015 Measurement and modelling of the reflection coefficient of an acoustic black hole termination *J. Sound Vib.* **349** 67–79

Appendix B

Scattering of an uniform circular inclusion in a thin plate

Chapter 4 deals with the particular scattering problem of a concentric incident wave converging towards the centre of a circular scatterer. This appendix summarise a more general scattering problem with an incident plane wave scattered by a cavity according to the work of Norris and Vemula [134]. The scattered field of an incident plane wave w_{inc} by an isolated circular scatterer S of radius a is considered. The material properties of the scatterer are assumed randomly different from the surrounding plate. The scatterer properties are denoted by the subscript 0 and the plate properties by the subscript 1. The expressions of the displacements field in the system are expressed with the polar coordinate system (O, r, θ) whose the origin is aligned with the centre of the scatterer. The flexural displacement field in the plate $w(r, \theta)$ and in the scatterer $w_0(r, \theta)$ are governed by the following equations respectively:

$$\begin{cases} (\nabla^2\nabla^2 - k_1^4)w(r,\theta) = 0, \\ (\nabla^2\nabla^2 - k_0^4)w_0(r,\theta) = 0, \end{cases} \tag{B.1}$$

where $k_0^4 = \frac{\rho h_0 \omega^2}{D_0}$ and $k_1^4 = \frac{\rho_1 h_0 \omega^2}{D_1}$. The displacement field $w(r, \theta)$ in the plate is defined as the sum of an incident field $w_{inc}(r, \theta)$ and a scattered field $w_0(r, \theta)$ such that:

$$w(r,\theta) = w_{inc}(r,\theta) + w_1(r,\theta). \tag{B.2}$$

B.0.1 Expression of the incident propagative plane wave

The incident wave w_{inc} is considered as a propagative plane wave with unitary amplitude and wave vector $\mathbf{k_1}$. Assuming that a cartesian coordinate system is aligned with the centre of the scatterer, the position vector reads as

$$\mathbf{x} = x\mathbf{e}_x + y\mathbf{e}_y. \tag{B.3}$$

w_{inc} can then be written as:

$$w_{inc}(\mathbf{x}) = e^{i\mathbf{k}\cdot\mathbf{x}}, \tag{B.4}$$

with $\mathbf{k} = k_{1x}\mathbf{e}_x + k_{1y}\mathbf{e}_y$. To satisfy the first equation of B.1, the relation $k_{1x}^2 + k_{1y}^2 = k_1^2$ must hold. The wavenumber components can therefore be written in the form $k_{1x} = k_1\cos(\theta_{inc})$ and $k_{1x} =$

$k_1 \sin(\theta_{inc})$, where the angle θ_{inc} characterises the direction of propagation of the incident wave, while the position vector reads in the polar coordinate system as $\mathbf{x} = r\cos(\theta)\mathbf{e}_x + r\sin(\theta)\mathbf{e}_y$,. As a result, Eq.B.4 becomes from Eq.B.3 :

$$w_{inc}(r,\theta) = e^{ik_1 r\{\cos(\theta)\cos(\theta_{inc})+\sin(\theta)\sin(\theta_{inc})\}} = e^{ik_1 r\cos(\theta-\theta_{inc})}. \tag{B.5}$$

This expression can be expand upon Bessel functions using the Jacobi-Anger expansion [2] such that:

$$w_{inc}(r,\theta) = \sum_{n=-\infty}^{+\infty} A^{inc}_{\mathrm{J},n}\mathrm{J}_n(k_1 r)e^{in\theta} \qquad , r > a, \tag{B.6}$$

where $A^{inc}_{\mathrm{J},n} = i^n e^{-in\theta_{inc}}$ is the incident amplitude.

B.0.2 Expression of w_0 and w_1

The general expressions of w_0 is given by summing Eq.4.9 and Eq. 4.13. However, as $\mathrm{H}_n(k_0 r)$ and $\mathrm{K}_n(k_0 r)$ are singular as $r \to 0$, the displacement field w_0 in the scatterer S is only composed of a linear combination of Bessel functions and modified Bessel functions of first kind such that:

$$w_0 = \sum_{n=-\infty}^{+\infty} \left[A_{\mathrm{J},n}\mathrm{J}_n(k_0 r) + A_{\mathrm{I},n}\mathrm{I}_n(k_0 r)\right] \mathrm{e}^{in\theta} \qquad , r < a. \tag{B.7}$$

$\mathrm{H}_n(k_1 r)$ and $\mathrm{K}_n(k_1 r)$ represents the outgoing waves in the system when $r > a$ and satisfy the Sommerfeld radiation condition as shown in Section 4.2.2. The scattered field w_1 in the plate is therefore expressed as:

$$w_1 = \sum_{n=-\infty}^{+\infty} \left[A_{\mathrm{H},n}\mathrm{H}_n(k_1 r) + A_{\mathrm{K},n}\mathrm{K}_n(k_1 r)\right] e^{in\theta} \qquad , r > a. \tag{B.8}$$

B.0.3 Boundary conditions

Now that the displacement fields have been expressed according to the polar coordinate system (O, r, θ), the boundary condition at the interface between the scatterer and the surrounding plate (at $r = a$) can be applied to compute the scattering coefficients $A_{\mathrm{H},n}$, $A_{\mathrm{K},n}$, $A_{\mathrm{J},n}$ and $A_{\mathrm{I},n}$ from the incident amplitude $A^{inc}_{\mathrm{J},n}$. Four boundary conditions at $r = a$ are distinguished according to Khirchhoff theory:

— displacement continuity

$$w(a,\theta) = w_0(a,\theta), \tag{B.9}$$

— displacement normal derivative continuity

$$\frac{\partial w(a,\theta),}{\partial r} = \frac{\partial w_0(a,\theta),}{\partial r}, \tag{B.10}$$

— bending moment continuity

$$M\left(w(a,\theta)\right) = M_0\left(w_1(a,\theta)\right), \tag{B.11}$$

— the (Kirchhoff) shear force continuity

$$V\left(w(a,\theta)\right) = V_0\left(w_1(a,\theta)\right), \tag{B.12}$$

with [175]

$$M_i(w) = -D_i\frac{\partial^2 w}{\partial r^2} - D_i\nu_i\left(\frac{1}{r}\frac{\partial w}{\partial r} + \frac{1}{r^2}\frac{\partial^2 w}{\partial \theta^2}\right), \tag{B.13}$$

and

$$V_i(w) = -D_i\frac{\partial}{\partial r}\nabla^2 w - D_i(1-\nu_i)\frac{1}{r^2}\frac{\partial^2}{\partial\theta^2}\left(\frac{\partial w}{\partial r} - \frac{w}{r}\right), \tag{B.14}$$

where the subscripts $i = 0, 1$ denotes the scatterer and the plate respectively. Applying these continuity conditions leads to the system of equations[134]:

$$\mathbf{A_n}.\mathbf{x_n} = \mathbf{B_n}.\mathbf{a_n} \tag{B.15}$$

where

$$\mathbf{A_n} = \begin{pmatrix} \mathrm{H}_n(\varepsilon_1) & \mathrm{K}_n(\varepsilon_1) & -\mathrm{J}_n(\varepsilon_0) & -\mathrm{I}_n(\varepsilon_0) \\ \mathrm{H'}_n(\varepsilon_1) & \mathrm{K'}_n(\varepsilon_1) & -\kappa\mathrm{J'}_n(\varepsilon_0) & -\kappa\mathrm{I'}_n(\varepsilon_0) \\ S^1_{\mathrm{H}_n} & S^1_{\mathrm{K}_n} & -\mathcal{D}S^0_{\mathrm{J}_n} & -\mathcal{D}S^0_{\mathrm{I}_n} \\ T^1_{\mathrm{H}_n} & T^1_{\mathrm{K}_n} & -\mathcal{D}T^0_{\mathrm{J}_n} & -\mathcal{D}T^0_{\mathrm{I}_n} \end{pmatrix}$$

$$\mathbf{x_n} = \begin{pmatrix} A_{\mathrm{H},n} \\ A_{\mathrm{K},n} \\ A_{\mathrm{J},n} \\ A_{\mathrm{I},n} \end{pmatrix}, \qquad \mathbf{B_n} = -\begin{pmatrix} \mathrm{J}_n(\varepsilon_1) & \mathrm{I}_n(\varepsilon_1) \\ \mathrm{J'}_n(\varepsilon_1) & \mathrm{I'}_n(\varepsilon_1) \\ S^1_{\mathrm{J}_n} & S^1_{\mathrm{I}_n} \\ T^1_{\mathrm{J}_n} & T^1_{\mathrm{I}_n} \end{pmatrix}, \qquad \mathbf{a_n} = \begin{pmatrix} A^{inc}_{\mathrm{J},n} \\ 0 \end{pmatrix},$$

$\kappa = \frac{k_0}{k_1}$, $\varepsilon_1 = k_1 a$, $\varepsilon_0 = k_0 a = \kappa\varepsilon_1$ et $\mathcal{D} = \frac{D_1}{D_0}$.

$$S^i_{X_n} = \left[n^2(1-\nu_i) \mp \varepsilon_i^2\right] X_n(\varepsilon_i) - (1-\nu_i)\varepsilon_i X'_n(\varepsilon_i), \tag{B.16}$$

$$T^i_{X_n} = n^2(1-\nu_i)X_n(\varepsilon_i) - \left[n^2(1-\nu_i) \pm \varepsilon_i^2\right] X'_n(\varepsilon_i), \tag{B.17}$$

The upper sign in Eq. (B.16) and Eq. (B.17) is taken when $X_n = \mathrm{J}_n$ or H_n while the lower sign is taken when $X_n = \mathrm{I}_n$ or K_n. The solution of the equation system (B.15) gives the scattering coefficients $A_{\mathrm{H},n}$, $A_{\mathrm{K},n}$, $A_{\mathrm{J},n}$ and $A_{\mathrm{I},n}$ for a given function order n. In the case where the solution is a linear combination of N order, the system has to be solved N times for each function order.

Appendix C

Computation of the scattering coefficients and the scattering field finside a 2D scatterer with varying properties

Section 4.5 deals with the particular scattering problem of a concentric incident wave converging towards the centre of a circular scatterer with radially varying thickness.This appendix aims to show the computation steps to obtain the scattering coefficients as well as the propagative and evanescent field amplitudes of a more general problem where the structure is radially homogeneous, that is, its parameters depend only on the radial coordinate. The problem is also generalized to any Bessel function order $n \in \mathbb{Z}$. The model used to that purpose is the multilayer scattering method, where the continuous variation of the parameters has been discretized in a number N of homogeneous cylindrically symmetric layers [27]. The layers are numbered such that the surrounding plate corresponds to $j = N$ and the core layer corresponds to $j = 0$.

C.1 Expression of the scattered amplitudes inside the scatterer according to the scattering coefficients.

The flexural amplitudes $\mathbf{W^-_{n,j}}$ et $\mathbf{W^+_{n,j}}$ at layer j can be related to the incident wave from the recurrence relation of Eq. (4.49), such that:

$$\mathbf{W^-_{n,j-1}} = \mathbf{T^-_{n,j}}.\mathbf{W^-_{n,j}} - \mathbf{R^-_{n,j}}.\mathbf{W^+_{n,j-1}} \tag{C.1}$$

$$\mathbf{W^+_{n,j}} = \mathbf{R^+_{n,j}}.\mathbf{W^-_{n,j}} + \mathbf{T^+_{n,j}}.\mathbf{W^+_{n,j-1}} \tag{C.2}$$

Defining the elastic 'impedance' matrix $\mathbf{Z_{nj}}$ as the term which link the diverging field with the converging field in the same layer ($\mathbf{W^+_{n,j}} = \mathbf{Z_{n,j}}.\mathbf{W^-_{n,j}}$) and replacing this term in Eqs. (C.1) and (C.2), one can obtain:

$$\mathbf{W^-_{n,j-1}} = \left(\mathbf{Id} - \mathbf{R^-_{n,j}}.\mathbf{Z_{n,j-1}}\right)^{-1} \mathbf{T^-_{n,j}}.\mathbf{W^-_{n,j}} \tag{C.3}$$

$$\mathbf{W^-_{n,j-1}} = \left(\mathbf{T^+_{n,j}}..\mathbf{Z_{n,j-1}}\right)^{-1}.\left(\mathbf{Z_{n,j}} - \mathbf{R^+_{n,j}}\right).\mathbf{W^-_{n,j}}. \tag{C.4}$$

These two relations give a recursive relation between $\mathbf{W^-_{n,j-1}}$ and $\mathbf{W^-_{n,j}}$ and a second between $\mathbf{Z_{n,j}}$ and $\mathbf{Z_{n,j-1}}$ such that:

$$\mathbf{Z_{n,j}} = \mathbf{R^+_{n,j}} + \mathbf{T^+_{n,j}}.\mathbf{Z_{n,j-1}}.\mathbf{X_{n,j-1}}, \tag{C.5}$$

$$\mathbf{X_{n,j-1}} = \left(\mathbf{Id} - \mathbf{R^-_{n,c}}.\mathbf{Z_{n,j-1}}\right)^{-1}.\mathbf{T^-_{n,j}}, \tag{C.6}$$

where $\mathbf{W^-_{n,j-1}} = \mathbf{X_{n,j-1}}.\mathbf{W^-_{n,j}}$. Assuming that all the scattering coefficients are known, the first iteration to compute all the $\mathbf{Z_{n,j}}$ and $\mathbf{X_{n,j}}$ might be done between layer 1 and layer 0. Layer à0 is described by a combination of Bessel and modified Bessel function of the first kind. Therefore, it is possible to write from Eqs.(C.1) and (C.2):

$$\mathbf{X_{n,0}} = \mathbf{T^-_{n,1}}$$

$$\mathbf{Z_{n,0}} = \mathbf{R^+_{n,1}}$$

As a result, it might be possible to express the amplitude of all the converging and diverging fields as a function of the incident field outside the scatterer and its scattering coefficients, in the same way as transfer functions.

C.1.1 Computation of the scattering coefficients inside the scatterer

The scattering coefficients are obtained applying the continuity conditions between each interface. These conditions are the same as presented in Section B.0.3 and have to satisfy two types of incidence: converging incidence and diverging incidence. The first case leads to the computation of a diverging reflection and a converging transmission, and the second one to a converging reflection and a diverging transmission.

Converging incident wave: Applying the continuity conditions at the interface between the layers $j-1$ and j at $r = r_{j-1}$ with a converging incident wave leads to the following equation system :

$$\mathbf{A_{n,j}}\mathbf{x_{n,j}} = \mathbf{B_{n,j}}\mathbf{a_{n,j}}, \tag{C.7}$$

where

$$\mathbf{A_{n,j}} = \begin{pmatrix} \mathrm{H}_n(\varepsilon_j) & \mathrm{K}_n(\varepsilon_j) & -\mathrm{J}_n(\varepsilon_{j-1}) & -\mathrm{I}_n(\varepsilon_{j-1}) \\ \mathrm{H'}_n(\varepsilon_j) & \mathrm{K'}_n(\varepsilon_j) & -\kappa_n \mathrm{J'}_n(\varepsilon_{j-1}) & -\kappa_l \mathrm{I'}_n(\varepsilon_{j-1}) \\ S^j_{\mathrm{H}_n} & S^j_{\mathrm{K}_n} & -D_j S^{j-1}_{\mathrm{J}_n} & -D_j S^{l+1}_{\mathrm{I}_n} \\ T^j_{\mathrm{H}_n} & T^j_{\mathrm{K}_n} & -D_j T^{l+1}_{\mathrm{J}_n} & -D_j T^{l+1}_{\mathrm{I}_n} \end{pmatrix},$$

$$\mathbf{x_{n,j}} = \begin{pmatrix} A^{(j)}_{\mathrm{H},n} \\ A^{(j)}_{\mathrm{K},n} \\ A^{(j-1)}_{\mathrm{J},n} \\ A^{(j-1)}_{\mathrm{I},n} \end{pmatrix}, \quad \mathbf{B_{n,j}} = - \begin{pmatrix} \mathrm{J}_n(\varepsilon_j) & \mathrm{I}_n(\varepsilon_j) \\ \mathrm{J'}_n(\varepsilon_j) & \mathrm{I'}_n(\varepsilon_j) \\ S^j_{\mathrm{J}_n} & S^j_{\mathrm{I}_n} \\ T^j_{\mathrm{J}_n} & T^j_{\mathrm{I}_n} \end{pmatrix}, \quad \mathbf{a_{n,j}} = \begin{pmatrix} A^{(j)}_{\mathrm{J},n} \\ A^{(j)}_{\mathrm{I},n} \end{pmatrix},$$

with $\kappa_j = \frac{k_{j-1}}{k_j}$, $\varepsilon_j = k_j r_{j-1}$, $\varepsilon_{j-1} = k_{l+1} r_{j-1}$ et $D_j = \frac{D_{j-1}}{D_j}$. Note that the expression of $\mathbf{a_{n,j}}$ is not valid when $j = N$ in the case where the incident wave in the plate is defined with a Hankel function of the second kind. In this case, $\mathbf{a_{n,N}} = \begin{pmatrix} A^{(N)}_{\mathrm{H},0} \\ 0 \end{pmatrix}$. Writing $\mathbf{x_{n,j}} = \begin{pmatrix} \mathbf{W^+_{n,j}} \\ \mathbf{W^-_{n,j-1}} \end{pmatrix}$,$\mathbf{a_{n,j}} = \begin{pmatrix} \mathbf{W^+_{n,j}} \end{pmatrix}$, we get:

$$(C.7) \Rightarrow \begin{pmatrix} \mathbf{W^+_{n,j}} \\ \mathbf{W^-_{n,j-1}} \end{pmatrix} = \begin{pmatrix} \mathbf{R^+_{n,j}} \\ \mathbf{T^-_{n,j}} \end{pmatrix} \begin{pmatrix} \mathbf{W^-_{n,j}} \end{pmatrix} \tag{C.8}$$

These coefficients are directly computed from the material properties of the system and from Bessel, Hankel and modified Bessel functions. This means that the coefficients are totally independant of the field in the system.

Diverging incident wave: Applying the continuity conditions at the interface between the j-th and $j-1$-th layers at $r = r_{j-1}$ with a diverging incident wave leads to the following system of equations :

$$\mathbf{A'_{n,j}} \mathbf{x'_{n,j}} = \mathbf{B'_{n,j}} \mathbf{a'_{n,j}}, \tag{C.9}$$

where

$$\mathbf{A'_{n,j}} = \begin{pmatrix} \mathrm{J}_n(\varepsilon_{j-1}) & \mathrm{I}_n(\varepsilon_{j-1}) & -\mathrm{H}_n(\varepsilon_j) & -\mathrm{K}_n(\varepsilon_j) \\ \mathrm{J'}_n(\varepsilon_{j-1}) & \mathrm{I'}_n(\varepsilon_{j-1}) & -\kappa_{1j}\mathrm{H'}_n(\varepsilon_j) & -\kappa_{1j}\mathrm{K'}_n(\varepsilon_j) \\ S^{j-1}_{\mathrm{J}_n} & S^{j-1}_{\mathrm{I}_n} & -D_{j-1}S^{j}_{\mathrm{H}_n} & -D_{j-1}S^{j}_{\mathrm{K}_n} \\ T^{j-1}_{\mathrm{J}_n} & T^{j-1}_{\mathrm{I}_n} & -D_{j-1}T^{j}_{\mathrm{H}_n} & -D_{j-1}T^{j}_{\mathrm{K}_n} \end{pmatrix}$$

$$\mathbf{x'_{n,j}} = \begin{pmatrix} A^{(j-1)}_{\mathrm{H},n} \\ A^{(j-1)}_{\mathrm{K},n} \\ A^{(j)}_{\mathrm{J},n} \\ A^{(j)}_{\mathrm{I},n} \end{pmatrix}, \quad \mathbf{B'_{n,j}} = -\begin{pmatrix} \mathrm{H}_n(\varepsilon_{j-1}) & \mathrm{K}_n(\varepsilon_{j-1}) \\ \mathrm{H'}_n(\varepsilon_{j-1}) & \mathrm{K'}_n(\varepsilon_{j-1}) \\ S^{j-1}_{\mathrm{H}_n} & S^{j-1}_{\mathrm{K}_n} \\ T^{j-1}_{\mathrm{H}_n} & T^{j-1}_{\mathrm{K}_n} \end{pmatrix}, \quad \mathbf{a'_{n,j}} = \begin{pmatrix} A^{(j-1)}_{\mathrm{J},n} \\ A^{(j-1)}_{\mathrm{I},n} \end{pmatrix},$$

with $\kappa_{1j} = \frac{k_{j-1}}{k_j}$, $\varepsilon_j = k_j R_{j-1}$, $\varepsilon_{j-1} = k_{j-1} R_{j-1}$ and $D_j = \frac{D_{j-1}}{D_j}$. As for (C.8), we can get from (C.9):

$$\begin{pmatrix} \mathbf{W^-_{n,j-1}} \\ \mathbf{W^+_{n,j}} \end{pmatrix} = \begin{pmatrix} \mathbf{R^-_{n,j}} \\ \mathbf{T^+_{n,j}} \end{pmatrix} \cdot \begin{pmatrix} \mathbf{W^+_{n,j}} \end{pmatrix} \tag{C.10}$$

This system has no physical meaning when it is solved for layer 0, since the scattered field and the incident field are both described by a linear combination of Bessel and modified Bessel functions. Furthermore, It is useless to compute the coefficient of layer 0 because they are not used to compute $\mathbf{X_n}$ et $\mathbf{Z_n}$.

Appendix D

Mathematical tools for multiple scattering

Chapter 5 deals with multiple scattering problems with an infinite row of circular critically coupled resonators. This appendix aims to detail the mathematical tools used to study this problem.

D.1 Graf's addition theorem

The Graf's addition theorem is used in Chapter 5 to express all the fields scattered by each inclusion Ω^j, with $j \in \mathbb{Z}^*$, according to the local polar coordinate system $(O^0, \mathbf{e}_r^0, \mathbf{e}_\theta^0)$ attached to Ω^0. This theorem is a particular case of the Neumann's addition theorem and allows to apply the coordinate change of Bessel, Hankel and modified Bessel functions from one coordinate system to another at a given order. Let's consider two polar coordinate systems (O_1, r_1, θ_1) and (O_2, r_2, θ_2) whose origins are spaced at a distance b and angle βas shown in Fig. D.1.

The Graf's addition theorem of J_n,I_n from the coordinate system (O_1, r_1, θ_1) to (O_2, r_2, θ_2)

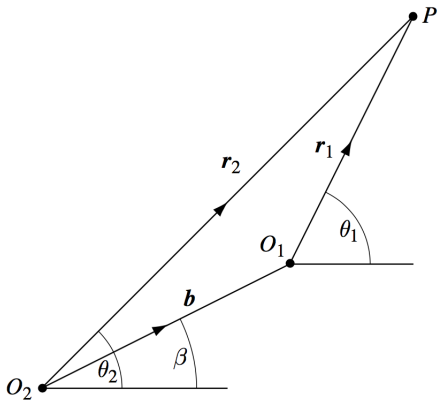

FIGURE D.1 – Configuration of the two polar coordinate systems.

takes the following form:

$$\mathrm{S}_n(kr_1)e^{in\theta_1} = \sum_{m=-\infty}^{+\infty} \mathrm{S}_{n-m}(kb)e^{i(n-m)\beta}\mathrm{S}_m(kr_2)e^{im\theta_2}, \tag{D.1}$$

where S = J or I. The expressions for the Hankel function H_n and modified Bessel function of the second kind K_n require to distinguish two cases according to whether the wave is convergent or divergent from the origin of the reference coordinate system

$$\mathrm{H}_n(kr_1)e^{in\theta_1} = \sum_{m=-\infty}^{+\infty} \mathrm{H}_{n-m}(kb)e^{i(n-m)\beta}\mathrm{J}_m(kr_2)e^{im\theta_2} \qquad , r_2 < b, \tag{D.2}$$

$$\mathrm{H}_n(kr_1)e^{in\theta_1} = \sum_{m=-\infty}^{+\infty} \mathrm{J}_{n-m}(kb)e^{i(n-m)\beta}\mathrm{H}_m(kr_2)e^{im\theta_2} \qquad , r_2 > b, \tag{D.3}$$

$$\mathrm{K}_n(kr_1)e^{in\theta_1} = \sum_{m=-\infty}^{+\infty} (-1)^m\mathrm{K}_{n-m}(kb)e^{i(n-m)\beta}\mathrm{I}_m(kr_2)e^{im\theta_2} \quad , r_2 < b, \tag{D.4}$$

$$\mathrm{K}_n(kr_1)e^{in\theta_1} = \sum_{m=-\infty}^{+\infty} (-1)^{n-m}\mathrm{I}_{n-m}(kb)e^{i(n-m)\beta}\mathrm{K}_m(kr_2)e^{in\theta_2} \quad , r_2 > b. \tag{D.5}$$

D.2 Transformation of the Schlömilch series

The Schlömilch series arises naturally in scattering problems where the scatterer is an infinite periodic structure. They account for the contribution of the fields scattered by all the repetitions of the inclusion to the near-field close to this inclusion. The form of the serie as written in Eq. 5.11 is unsuitable for numerical computation due to its very slow convergence. However, Linton and Twersky showed than it can be transformed into a new expression which is amenable to computation [116, 177]. This sections aims to summarise the transformations of the Schlömilch series that are used to treat the scattering problems of Chapter. 5. The Schlömilch serie encountered in Chapter. 5 concerns the Hankel function and takes the form:

$$S_{n-q}^{\mathrm{H}} = \sum_{j>0} \mathrm{H}_{n-q}^{(1)}(kjd)\left(1 + (-1)^{n-q}\right). \tag{D.6}$$

As $\mathrm{H}_{q-n}^{(1)}(kjd) = (-1)^{n-q}\mathrm{H}_{n-q}^{(1)}(kjd)$, $S_{n-q}^{\mathrm{H}} = S_{q-n}^{\mathrm{H}}$. Furthermore, the transformation of this serie takes several forms whether the order $|n-q|$ is even, odd or 0 (see Ref. [116, 177] for more details on these conditions). If $n - q = 0$:

$$S_0^{\mathrm{H}} = -1 - \frac{2i}{pi}\left(C + ln\left(\frac{kd}{4\pi}\right)\right) + \frac{2}{kd\sin\Phi_0} + {\sum_{m\in\mathbb{Z}}}'\left(\frac{2}{kd\sin\Phi_0} + \frac{i}{\pi|m|}\right), \tag{D.7}$$

where $\Phi_m = \arccos\left(\cos\theta_{inc} + \frac{2m\pi}{kd}\right)$ and C is the Euler constant.
If $|n-q|$ is even,

$$S_{n-q}^{\mathrm{H}} = 2 - (-1)^N \sum_{m\in\mathbb{Z}} \frac{e^{i(n-q)\mathrm{sign}(m)\Phi_m}}{kd\sin\Phi_m} + 2i\lambda_N, \tag{D.8}$$

where $N = (n-q)/2$, sign(m) is the signe of m with the convention sign$(0) = +1$ and

$$\lambda_N = \frac{1}{2\pi} \sum_{m=0}^{N} \frac{(-1)^m 2^{2m} (N+m-1)!}{(2m)!(N-m)!} \left(\frac{2\pi}{kd}\right)^{2m} B_{2m}(0), \tag{D.9}$$

with B_m the Bernoulli polynomial.
If $|n-q|$ is odd,

$$S^{\mathrm{H}}_{n-q} = 2 - (-1)^M i \sum_{m\in\mathbb{Z}} \frac{e^{i(2M-1)\mathrm{sign}(m)\Phi_m}}{kd \sin\Phi_m} + 2\lambda_M, \tag{D.10}$$

where $M = (n-q+1)/2$ and

$$\lambda_M = \frac{1}{\pi} \sum_{m=0}^{M-1} \frac{(-1)^m 2^{2m} (M+m-1)!}{(2m+1)!(M-m-1)!} \left(\frac{2\pi}{kd}\right)^{2m+1} B_{2m+1}(0). \tag{D.11}$$

References

[1] Science for environment policy: Noise abatement approaches. `https://ec.europa.eu/environment/integration/research/newsalert/pdf/noise_abatement_approaches_FB17_en.pdf`. Accessed: 2019-09-20.

[2] M. Abramowitz. Handbook of mathematical functions with formulas, graphs, and mathematical tables, nbs. *Applied Math. Series*, 55:232, 1964.

[3] O. Aklouche. *Réduction des niveaux vibratoires d'un panneau au moyen de trous noirs acoustiques structurés en réseau périodique: conception d'une méta-plaque*. PhD thesis, Université du Maine, 2017.

[4] O. Aklouche, A. Pelat, S. Maugeais, and F. Gautier. Scattering of flexural waves by a pit of quadratic profile inserted in an infinite thin plate. *Journal of Sound and Vibration*, 375:38–52, 2016.

[5] A. Alevizaki, R. Sainidou, P. Rembert, B. Morvan, and N. Stefanou. Phononic crystals of poroelastic spheres. *Physical Review B*, 94(17):174306, 2016.

[6] N.D. Anh, H. Matsuhisa, L.D. Viet, and M. Yasuda. Vibration control of an inverted pendulum type structure by passive mass–spring-pendulum dynamic vibration absorber. *Journal of Sound and Vibration*, 307(1-2):187–201, 2007.

[7] M.F. Ashby. *Acoustic metamaterials and phononic crystals*. Butterworth Heinemann, 2004.

[8] M. Badreddine Assouar, M. Senesi, M. Oudich, M. Ruzzene, and Z. Hou. Broadband plate-type acoustic metamaterial for low-frequency sound attenuation. *Applied Physics Letters*, 101(17):173505, 2012.

[9] T. Bailey and J.E. Hubbard. Distributed piezoelectric-polymer active vibration control of a cantilever beam. *Journal of Guidance, Control, and Dynamics*, 8(5):605–611, 1985.

[10] P.W. Barber and S.C. Hill. *Light scattering by particles: computational methods*, volume 2. World scientific, 1990.

[11] J.J. Bayod. Experimental study of vibration damping in a modified elastic wedge of power-law profile. *Journal of Vibration and Acoustics*, 133(6):061003, 2011.

[12] B.S. Beck, K.A. Cunefare, M. Ruzzene, and M. Collet. Experimental analysis of a cantilever beam with a shunted piezoelectric periodic array. *Journal of Intelligent Material Systems and Structures*, 22(11):1177–1187, 2011.

[13] J. Becker, O. Fein, M. Maess, and L. Gaul. Finite element-based analysis of shunted piezoelectric structures for vibration damping. *Computers & structures*, 84(31-32):2340–2350, 2006.

[14] S. Behrens, S.O.R. Moheimani, and A.J. Fleming. Multiple mode current flowing passive piezoelectric shunt controller. *Journal of sound and vibration*, 266(5):929–942, 2003.

[15] M. Berardengo, S. Manzoni, and A.M. Conti. Multi-mode passive piezoelectric shunt damping by means of matrix inequalities. *Journal of Sound and Vibration*, 405:287–305, 2017.

[16] J.L. Black, C.C. Mei, and M.C.G. Bray. Radiation and scattering of water waves by rigid bodies. *Journal of Fluid Mechanics*, 46(1):151–164, 1971.

[17] K.Y. Bliokh, Y.P. Bliokh, V. Freilikher, S. Savel'ev, and F. Nori. Colloquium: Unusual resonators: Plasmonics, metamaterials, and random media. *Rev. Mod. Phys.*, 80(4):1201, 2008.

[18] F. Bloch. Über die quantenmechanik der elektronen in kristallgittern. *Zeitschrift für physik*, 52(7-8):555–600, 1929.

[19] C.F. Bohren and D.R. Huffman. *Absorption and scattering of light by small particles*. John Wiley & Sons, 2008.

[20] E.P. Bowyer and V.V. Krylov. Damping of flexural vibrations in turbofan blades using the acoustic black hole effect. *Applied Acoustics*, 76:359–365, 2014.

[21] E.P. Bowyer, D.J. O'Boy, V.V. Krylov, and F. Gautier. Experimental investigation of damping flexural vibrations in plates containing tapered indentations of power-law profile. *Applied Acoustics*, 74(4):553–560, 2013.

[22] M.J. Brennan. Characteristics of a wideband vibration neutralizer. *Noise Control Engineering Journal*, 45(5):201–207, 1997.

[23] M.J. Brennan. Control of flexural waves on a beam using a tunable vibration neutraliser. *Journal of Sound and Vibration*, 222(3):389–407, 1999.

[24] M.J. Brennan. Control of flexural waves on a beam using a tunable vibration neutraliser. *Jour. Sound Vib.*, 222(3):389–407, 1999.

[25] L. Brillouin. *Wave propagation in periodic structures: electric filters and crystal lattices*. Courier Corporation, 2003.

[26] L.W. Cai and S.A. Hambric. Multiple scattering of flexural waves on thin plates. *Journal of Vibration and Acoustics*, 138(1):011009, 2016.

[27] L.W. Cai and J. Sánchez-Dehesa. Acoustical scattering by radially stratified scatterers. *The Journal of the Acoustical Society of America*, 124(5):2715–2726, 2008.

[28] M. Cai, O. Painter, and K.J. Vahala. Observation of critical coupling in a fiber taper to a silica-microsphere whispering-gallery mode system. *Phys. Rev. Lett.*, 85(1):74, 2000.

[29] F. Casadei, B.S. Beck, K.A. Cunefare, and M. Ruzzene. Vibration control of plates through hybrid configurations of periodic piezoelectric shunts. *Journal of Intelligent Material Systems and Structures*, 23(10):1169–1177, 2012.

[30] G.J. Chaplain and R.V. Craster. Flat lensing by graded line meta-arrays. *Physical Review B*, 99(22):220102, 2019.

[31] G.J. Chaplain, M.P. Makwana, and R.V. Craster. Rayleigh–bloch, topological edge and interface waves for structured elastic plates. *Wave Motion*, 86:162–174, 2019.

[32] C. Charles, B. Bonello, and F. Ganot. Propagation of guided elastic waves in 2d phononic crystals. *Ultrasonics*, 44:e1209–e1213, 2006.

[33] H. Chen and C.T. Chan. Acoustic cloaking in three dimensions using acoustic metamaterials. *Applied physics letters*, 91(18):183518, 2007.

[34] S. Chen, G. Wang, J. Wen, and X. Wen. Wave propagation and attenuation in plates with periodic arrays of shunted piezo-patches. *Journal of Sound and Vibration*, 332(6):1520–1532, 2013.

[35] T. Chen, M. Ruzzene, and A. Baz. Control of wave propagation in composite rods using shape memory inserts: theory and experiments. *Journal of Vibration and control*, 6(7):1065–1081, 2000.

[36] Y.D. Chong, L. Ge, H. Cao, and A.D. Stone. Coherent perfect absorbers: time-reversed lasers. *Physical review letters*, 105(5):053901, 2010.

[37] D. Chronopoulos, M. Ichchou, B. Troclet, and O. Bareille. Efficient prediction of the response of layered shells by a dynamic stiffness approach. *Composite Structures*, 97:401–404, 2013.

[38] D. Chronopoulos, B. Troclet, O. Bareille, and M. Ichchou. Modeling the response of composite panels by a dynamic stiffness approach. *Composite Structures*, 96:111–120, 2013.

[39] C.C. Claeys, K. Vergote, P. Sas, and W. Desmet. On the potential of tuned resonators to obtain low-frequency vibrational stop bands in periodic panels. *Journal of Sound and Vibration*, 332(6):1418–1436, 2013.

[40] A. Climente, D. Torrent, and J. Sánchez-Dehesa. Omnidirectional broadband insulating device for flexural waves in thin plates. *Journal of Applied Physics*, 114(21):214903, 2013.

[41] A. Climente, D. Torrent, and J. Sánchez-Dehesa. Gradient index lenses for flexural waves based on thickness variations. *Applied Physics Letters*, 105(6):064101, 2014.

[42] A. Colombi, V. Ageeva, R.J. Smith, A. Clare, R. Patel, M. Clark, D. Colquitt, P. Roux, S. Guenneau, and R.V. Craster. Enhanced sensing and conversion of ultrasonic rayleigh waves by elastic metasurfaces. *Sci. Rep.*, 7(6750), 2017.

[43] D. Colton and R. Kress. *Inverse acoustic and electromagnetic scattering theory*, volume 93. Springer Science & Business Media, 2012.

[44] L. Cremer and M. Heckl. *Structure-borne sound: structural vibrations and sound radiation at audio frequencies*. Springer Science & Business Media, 2013.

[45] M.J. Crocker. General introduction to noise and vibration effects on people and hearing conservation. *Handbook of Noise and Vibration Control*, pages 301–307, 2007.

[46] C. J Cross and S. Fleeter. Shunted piezoelectrics for passive control of turbomachine blading flow-induced vibrations. *Smart materials and Structures*, 11(2):239, 2002.

[47] J. Cuenca. *Wave models for the flexural vibrations of thin plates-Model of the vibrations of polygonal plates by the image source method-Vibration damping using the acoustic black hole effect*. PhD thesis, 2009.

[48] J. Cuenca, F. Gautier, and L. Simon. Harmonic green's functions for flexural waves in semi-infinite plates with arbitrary boundary conditions and high-frequency approximation for convex polygonal plates. *Journal of Sound and Vibration*, 331(6):1426–1440, 2012.

[49] F. dell'Isola, C. Maurini, and M. Porfiri. Passive damping of beam vibrations through distributed electric networks and piezoelectric transducers: prototype design and experimental validation. *Smart Materials and Structures*, 13(2):299, 2004.

[50] J.P. Den Hartog. *Mechanical vibrations*. Courier Corporation, 1985.

[51] J. Deng, L. Zheng, P. Zeng, Y. Zuo, and O. Guasch. Passive constrained viscoelastic layers to improve the efficiency of truncated acoustic black holes in beams. *Mechanical Systems and Signal Processing*, 118:461–476, 2019.

[52] V. Denis, F. Gautier, A. Pelat, and J. Poittevin. Measurement and modelling of the reflection coefficient of an acoustic black hole termination. *J. Sound Vib.*, 349:67–79, 2015.

[53] V. Denis, A. Pelat, and F. Gautier. Scattering effects induced by imperfections on an acoustic black hole placed at a structural waveguide termination. *Journal of Sound and Vibration*, 362:56–71, 2016.

[54] V. Denis, A. Pelat, F. Gautier, and B. Elie. Modal overlap factor of a beam with an acoustic black hole termination. *Journal of Sound and Vibration*, 333(12):2475–2488, 2014.

[55] V. Denis, A. Pelat, C. Touzé, and F. Gautier. Improvement of the acoustic black hole effect by using energy transfer due to geometric nonlinearity. *International Journal of Non-Linear Mechanics*, 94:134–145, 2017.

[56] J. Der Hagopian, L. Gaudiller, and B. Maillard. Hierarchial control of hydraulic active suspensions of a fast all-terrain military vehicle. *Journal of Sound and Vibration*, 222(5):723–752, 1999.

[57] P.A. Deymier. *Acoustic metamaterials and phononic crystals*, volume 173. Springer Science & Business Media, 2013.

[58] E.K. Dimitriadis, C.R. Fuller, and C.A. Rogers. Piezoelectric actuators for distributed vibration excitation of thin plates. *Journal of Vibration and Acoustics*, 113(1):100–107, 1991.

[59] P.A.M. Dirac. The lorentz transformation and absolute time. *Physica*, 19(1—12):888–896, 1953.

[60] J.J. Dosch, D.J. Inman, and E. Garcia. A self-sensing piezoelectric actuator for collocated control. *Journal of Intelligent material systems and Structures*, 3(1):166–185, 1992.

[61] Y. Duan, J. Luo, G. Wang, Z.H. Hang, B. Hou, J. Li, P. Sheng, and Y. Lai. Theoretical requirements for broadband perfect absorption of acoustic waves by ultra-thin elastic meta-films. *Sci. Rep.*, 5(12139), 2015.

[62] H.M. El-Khatib, B.R. Mace, and M.J. Brennan. Suppression of bending waves in a beam using a tuned vibration absorber. *Journal of Sound and Vibration*, 288(4-5):1157–1175, 2005.

[63] H.M. El-Khatib, B.R. Mace, and M.J. Brennan. Suppression of bending waves in a beam using a tuned vibration absorber. *J. Sound Vib.*, 288(4):1157–1175, 2005.

[64] S.l. Elliott and M.E. Johnson. Radiation modes and the active control of sound power. *J. Acoust. Soc. Am.*, 94(4):2194–2204, 1993.

[65] D.V. Evans and R. Porter. Penetration of flexural waves through a periodically constrained thin elastic plate in vacuo and floating on water. *Journal of Engineering Mathematics*, 58(1-4):317–337, 2007.

[66] D.J. Ewins. *Modal testing: theory and practice*, volume 15. Research studies press Letchworth, 1984.

[67] N. Fang, D. Xi, J. Xu, M. Ambati, W. Srituravanich, C. Sun, and X. Zhang. Ultrasonic metamaterials with negative modulus. *Nat. Mater.*, 5(6):452, 2006.

[68] M. Farhat, S. Guenneau, and S. Enoch. Ultrabroadband elastic cloaking in thin plates. *Physical review letters*, 103(2):024301, 2009.

[69] M. Farhat, S. Guenneau, and S. Enoch. High directivity and confinement of flexural waves through ultra-refraction in thin perforated plates. *EPL (Europhysics Letters)*, 91(5):54003, 2010.

[70] M. Farhat, S. Guenneau, S. Enoch, and A.B. Movchan. Cloaking bending waves propagating in thin elastic plates. *Physical Review B*, 79(3):033102, 2009.

[71] M. Farhat, S. Guenneau, S. Enoch, A.B. Movchan, and G.G. Petursson. Focussing bending waves via negative refraction in perforated thin plates. *Applied Physics Letters*, 96(8):081909, 2010.

[72] P. A. Feurtado and S. C. Conlon. Investigation of boundary-taper reflection for acoustic black hole design. *J. Noise Cont. Eng.*, 63(5):460, 2015.

[73] R.P Feynman and F.L. Vernon Jr. The theory of a general quantum system interacting with a linear dissipative system. *Annals of Physics*, 24:118–173, 1963.

[74] G. Floquet. Sur les équations différentielles linéaires à coefficients périodiques. In *Annales scientifiques de l'École normale supérieure*, volume 12, pages 47–88, 1883.

[75] S. Foucaud, G. Michon, Y. Gourinat, A. Pelat, and F. Gautier. Artificial cochlea and acoustic black hole travelling waves observation: Model and experimental results. *Journal of Sound and Vibration*, 333(15):3428–3439, 2014.

[76] H. Frahm. Device for damping vibrations of bodies., April 18 1911. US Patent 989,958.

[77] F. Gautier, J. Cuenca, V.V. Krylov, and L. Simon. Experimental investigation of the acoustic black hole effect for vibration damping in elliptical plates. *Journal of the Acoustical Society of America*, 123(5):3318, 2008.

[78] F. Gautier, M.H. Moulet, and J.C. Pascal. Reflection, transmission and coupling of longitudinal and flexural waves at beam junctions. part i: measurement methods. *Acta Acust. United Ac.*, 92(6):982–997, 2006.

[79] V.B. Georgiev, J. Cuenca, F. Gautier, L. Simon, and V.V. Krylov. Damping of structural vibrations in beams and elliptical plates using the acoustic black hole effect. *Journal of sound and vibration*, 330(11):2497–2508, 2011.

[80] M. Geradin and D. Rixen. Théorie des vibrations, applicationa la dynamique des structures 2e édition, 1996.

[81] M. Géradin and D.J. Rixen. *Mechanical vibrations: theory and application to structural dynamics*. John Wiley & Sons, 2014.

[82] C. Goffaux, F. Maseri, J.O. Vasseur, B. Djafari-Rouhani, and Ph. Lambin. Measurements and calculations of the sound attenuation by a phononic band gap structure suitable for an insulating partition application. *Applied physics letters*, 83(2):281–283, 2003.

[83] J.P. Groby, W. Huang, A. Lardeau, and Y. Aurégan. The use of slow waves to design simple sound absorbing materials. *J. Appl. Phys.*, 117(12):124903, 2015.

[84] J.P. Groby, R. Pommier, and Y. Aurégan. Use of slow sound to design perfect and broadband passive sound absorbing materials. *J. Acoust. Soc. Am.*, 139(4):1660–1671, 2016.

[85] J.P. Groby, A. Wirgin, and E. Ogam. Acoustic response of a periodic distribution of macroscopic inclusions within a rigid frame porous plate. *Waves in Random and Complex Media*, 18(3):409–433, 2008.

[86] J.L. Guyader and C. Lesueur. Acoustic transmission through orthotropic multilayered plates, part i: Plate vibration modes. *Journal of Sound and Vibration*, 58(1):51–68, 1978.

[87] N.W. Hagood and A. von Flotow. Damping of structural vibrations with piezoelectric materials and passive electrical networks. *Journal of Sound and Vibration*, 146(2):243–268, 1991.

[88] S. Halkjær, O. Sigmund, and J.S. Jensen. Maximizing band gaps in plate structures. *Structural and Multidisciplinary Optimization*, 32(4):263–275, 2006.

[89] S.G. Haslinger, N.V. Movchan, A.B. Movchan, and R.C. McPhedran. Transmission, trapping and filtering of waves in periodically constrained elastic plates. *Proceedings of the Royal Society A: Mathematical, Physical and Engineering Sciences*, 468(2137):76–93, 2011.

[90] O. Heaviside. *Electromagnetic theory*, volume 3. Cosimo, Inc., 2008.

[91] K.M. Ho, C.T. Chan, and C.M. Soukoulis. Existence of a photonic gap in periodic dielectric structures. *Physical Review Letters*, 65(25):3152, 1990.

[92] J.C. Hsu and T.-T. Wu. Lamb waves in binary locally resonant phononic plates with two-dimensional lattices. *Applied physics letters*, 90(20):201904, 2007.

[93] W. Huang, H. Zhang, D.J. Inman, J. Qiu, C. ES Cesnik, and H. Ji. Low reflection effect by 3d printed functionally graded acoustic black holes. *Journal of Sound and Vibration*, 450:96–108, 2019.

[94] M.I. Hussein, M.J. Leamy, and M. Ruzzene. Dynamics of phononic materials and structures: Historical origins, recent progress, and future outlook. *Applied Mechanics Reviews*, 66(4):040802, 2014.

[95] L. Jaouen, A. Renault, and M. Deverge. Elastic and damping characterizations of acoustical porous materials: Available experimental methods and applications to a melamine foam. *Applied acoustics*, 69(12):1129–1140, 2008.

[96] N. Jiménez, W. Huang, V. Romero-García, V. Pagneux, and J.P. Groby. Ultra-thin metamaterial for perfect and quasi-omnidirectional sound absorption. *Appl. Phys. Lett.*, 109(12):121902, 2016.

[97] N. Jiménez, V. Romero-García, V. Pagneux, and J.-P. Groby. Quasiperfect absorption by subwavelength acoustic panels in transmission using accumulation of resonances due to slow sound. *Phys. Rev. B*, 95:014205, 2017.

[98] N. Jiménez, V. Romero-García, V. Pagneux, and J.P. Groby. Rainbow-trapping absorbers: Broadband, perfect and asymmetric sound absorption by subwavelength panels for transmission problems. *Sci. Rep.*, 7(1):13595, 2017.

[99] C. Jiu-Jiu, Q. Bo, and C. Jian-Chun. Complete band gaps for lamb waves in cubic thin plates with periodically placed inclusions. *Chinese Physics Letters*, 22(7):1706, 2005.

[100] S. John. Strong localization of photons in certain disordered dielectric superlattices. *Physical review letters*, 58(23):2486, 1987.

[101] M.E. Johnson and S.J. Elliott. Active control of sound radiation using volume velocity cancellation. *J. Acoust. Soc. Am.*, 98(4):2174–2186, 1995.

[102] D. I.G. Jones. *Handbook of viscoelastic vibration damping*. John Wiley & Sons, 2001.

[103] M. Kadic, T. Bückmann, N. Stenger, M. Thiel, and M. Wegener. On the practicability of pentamode mechanical metamaterials. *Applied Physics Letters*, 100(19):191901, 2012.

[104] A.O. Krushynska, V.G. Kouznetsova, and M.G.D. Geers. Towards optimal design of locally resonant acoustic metamaterials. *Journal of the Mechanics and Physics of Solids*, 71:179–196, 2014.

[105] V.V. Krylov. Propagation of plate bending waves in the vicinity of one-and two-dimensional acoustic 'black holes'. 2007.

[106] V.V. Krylov and F.J.B.S. Tilman. Acoustic 'black holes' for flexural waves as effective vibration dampers. *Journal of Sound and Vibration*, 274(3-5):605–619, 2004.

[107] V.V. Krylov and R.E.T.B. Winward. Experimental investigation of the acoustic black hole effect for flexural waves in tapered plates. *Journal of Sound and Vibration*, 300(1-2):43–49, 2007.

[108] M.S. Kushwaha. Stop-bands for periodic metallic rods: Sculptures that can filter the noise. *Applied Physics Letters*, 70(24):3218–3220, 1997.

[109] M.S. Kushwaha, P. Halevi, L. Dobrzynski, and B. Djafari-Rouhani. Acoustic band structure of periodic elastic composites. *Physical review letters*, 71(13):2022, 1993.

[110] C. Lagarrigue, J.P. Groby, and V. Tournat. Sustainable sonic crystal made of resonating bamboo rods. *The Journal of the Acoustical Society of America*, 133(1):247–254, 2013.

[111] J.C. Lee and J.C. Chen. Active control of sound radiation from rectangular plates using multiple piezoelectric actuators. *Applied Acoustics*, 57(4):327–343, 1999.

[112] J.Y. Lee and W. Jeon. Vibration damping using a spiral acoustic black hole. *The Journal of the Acoustical Society of America*, 141(3):1437–1445, 2017.

[113] A. W. Leissa. *Tabulated numerical results of theories of plate vibration*. NASA, Washington, DC, United States., 1969.

[114] J. Leng, F. Gautier, A. Pelat, R. Picó, J.P. Groby, and V. Romero-Garcia. Limits of flexural wave absorption by open lossy resonators: reflection and transmission problems. *New Journal of Physics*, 21(5):053003, 2019.

[115] C.K. Liew, M. Veidt, D.T. Chavara, A.J. Ruys, C. Young, and M. McCreery. Metal-polymer functionally graded materials for removing guided wave reflections at beam end boundaries. In *Proceedings of the 5th Australasian Congress on Applied Mechanics*, page 539. Engineers Australia, 2007.

[116] C.M. Linton. Schlömilch series that arise in diffraction theory and their efficient computation. *Journal of Physics A: Mathematical and General*, 39(13):3325, 2006.

[117] B. Liu, J.L. Silverberg, A.A. Evans, C.D. Santangelo, R.J. Lang, T.C. Hull, and I. Cohen. Topological kinematics of origami metamaterials. *Nature Physics*, 14(8):811, 2018.

[118] L. Liu and M.I. Hussein. Wave motion in periodic flexural beams and characterization of the transition between bragg scattering and local resonance. *Journal of Applied Mechanics*, 79(1):011003, 2012.

[119] X. Liu, Z.and Zhang, Y. Mao, Y.Y. Zhu, Z. Yang, Ch. T. Chan, and P. Sheng. Locally resonant sonic materials. *science*, 289(5485):1734–1736, 2000.

[120] C.J. Luke and P.A. Martin. Fluid–solid interaction: acoustic scattering by a smooth elastic obstacle. *SIAM Journal on Applied Mathematics*, 55(4):904–922, 1995.

[121] B.R. Mace. Wave reflection and transmission in beams. *J. Sound Vib.*, 97(2):237–246, 1984.

[122] P.A. Martin. *Multiple scattering: interaction of time-harmonic waves with N obstacles*. Number 107. Cambridge University Press, 2006.

[123] R.C. McPhedran and A.B. Movchan. The rayleigh multipole method for linear elasticity. *Journal of the Mechanics and Physics of Solids*, 42(5):711–727, 1994.

[124] R.C. McPhedran, A.B. Movchan, and N.V. Movchan. Platonic crystals: Bloch bands, neutrality and defects. *Mechanics of materials*, 41(4):356–363, 2009.

[125] A. Merkel, G. Theocharis, O. Richoux, V. Romero-García, and V. Pagneux. Control of acoustic absorption in one-dimensional scattering by resonant scatterers. *App. Phys. Lett.*, 107(24):244102, 2015.

[126] Lezza A. Mignery. Designing automotive dash panels with laminated metal. *SAE transactions*, pages 3349–3353, 1999.

[127] M.A. Mironov. Propagation of a flexural wave in a plate whose thickness decreases smoothly to zero in a finite interval. *Soviet Physics Acoustics-USSR*, 34(3):318–319, 1988.

[128] M.H. Moulet. *Les jonctions en mécanique vibratoire: représentation par matrice de diffusion et caractérisation expérimentale pour des poutres assemblées*. PhD thesis, Université du Maine, 2003.

[129] D. Mousanezhad, S. Babaee, H. Ebrahimi, R. Ghosh, A.S. Hamouda, K. Bertoldi, and A. Vaziri. Hierarchical honeycomb auxetic metamaterials. *Scientific reports*, 5:18306, 2015.

[130] A.B. Movchan, N.V. Movchan, and R.C. McPhedran. Bloch–floquet bending waves in perforated thin plates. *Proceedings of the Royal Society A: Mathematical, Physical and Engineering Sciences*, 463(2086):2505–2518, 2007.

[131] N.O. Myklestad. The concept of complex damping. *Journal of Applied Mechanics-Transactions of the ASME*, 19(3):284–286, 1952.

[132] Ahid D. Nashif, David I. G. Jones, and John P. Henderson. *Vibration Damping,*. New York : Wiley, 1985.

[133] A.N. Norris. Reflection and transmission of structural waves at an interface between doubly curved shells. *Acta Acust. United Ac.*, 84(6):1066–1076, 1998.

[134] A.N. Norris and C. Vemula. Scattering of flexural waves on thin plates. *Journal of sound and vibration*, 181(1):115–125, 1995.

[135] H. Oberst and K. Frankenfeld. Über die dämpfung der biegeschwingungen dünner bleche durch fest haftende beläge. *Acta Acustica united with Acustica*, 2(6):181–194, 1952.

[136] R. Ohayon and C. Soize. Méthodes numériques avancées en vibroacoustique basses et moyennes fréquences. *Revue Européenne des éléments finis*, 8(5-6):607–637, 1999.

[137] M. Oudich, M. Senesi, M.B. Assouar, M. Ruzenne, J.H. Sun, B. Vincent, Z. Hou, and T.T. Wu. Experimental evidence of locally resonant sonic band gap in two-dimensional phononic stubbed plates. *Physical Review B*, 84(16):165136, 2011.

[138] M. Ouisse, D. Renault, P. Butaud, and E. Sadoulet-Reboul. Damping control for improvement of acoustic black hole effect. *Journal of Sound and Vibration*, 454:63–72, 2019.

[139] D.J. O'Boy and A.P. Dowling. Tyre/road interaction noise—numerical noise prediction of a patterned tyre on a rough road surface. *Journal of Sound and Vibration*, 323(1-2):270–291, 2009.

[140] R.J. Pal and M. Ruzzene. Edge waves in plates with resonators: an elastic analogue of quantum valley hall effect. *New J. Phys.*, 19(025001), 2017.

[141] Y.H. Pao and C.C. Mow. Diffraction of elastic waves and dynamic stress concentrations. crane, russak & company. *Inc., New York*, pages 601–612, 1973.

[142] J. Park and D.L. Palumbo. A new approach to identify optimal properties of shunting elements for maximum damping of structural vibration using piezoelectric patches. 2004.

[143] W.J. Parnell and P.A. Martin. Multiple scattering of flexural waves by random configurations of inclusions in thin plates. *Wave Motion*, 48(2):161–175, 2011.

[144] J.B. Pendry. Negative refraction makes a perfect lens. *Physical review letters*, 85(18):3966, 2000.

[145] J.B. Pendry, A.J. Holden, D.J. Robbins, and W.J. Stewart. Magnetism from conductors and enhanced nonlinear phenomena. *IEEE transactions on microwave theory and techniques*, 47(11):2075–2084, 1999.

[146] R. Penrose. A generalized inverse for matrices. In *Mathematical proceedings of the Cambridge philosophical society*, volume 51, pages 406–413. Cambridge University Press, 1955.

[147] F. Pierron, G. Vert, R. Burguete, S. Avril, R. Rotinat, and M.R. Wisnom. Identification of the orthotropic elastic stiffnesses of composites with the virtual fields method: sensitivity study and experimental validation. *Strain*, 43(3):250–259, 2007.

[148] J.R. Piper, V. Liu, and S. Fan. Total absorption by degenerate critical coupling. *Applied Physics Letters*, 104(25):251110, 2014.

[149] A. Preumont. *Vibration control of active structures*, volume 2. Springer, 1997.

[150] A. Preumont, A. François, P. De Man, N. Loix, and K. Henrioulle. Distributed sensors with piezoelectric films in design of spatial filters for structural control. *Journal of Sound and Vibration*, 282(3-5):701–712, 2005.

[151] M.D. Rao. Recent applications of viscoelastic damping for noise control in automobiles and commercial airplanes. *Journal of Sound and Vibration*, 262(3):457–474, 2003.

[152] J.N. Reddy. A simple higher-order theory for laminated composite plates. *Journal of applied mechanics*, 51(4):745–752, 1984.

[153] V. Romero-García, G. Theocharis, O. Richoux, and V. Pagneux. Use of complex frequency plane to design broadband and sub-wavelength absorbers. *J. Acoust. Soc. Am.*, 139(6):3395–3403, 2016.

[154] D. Ross, E.L. Ungar, and E.M. Kerwin. Damping of plate flexural vibrations by means of viscoelastic laminae. *Structural damping*, pages 49–87, 1960.

[155] J.E. Ruzicka. Structural damping. pages 49–57, 1960.

[156] J.V. Sanchez-Perez, C. Rubio, R. Martinez-Sala, R.l Sanchez-Grandia, and V. Gomez. Acoustic barriers based on periodic arrays of scatterers. *Applied Physics Letters*, 81(27):5240–5242, 2002.

[157] L. Schwan and J.-P. Groby. *Fundamentals and Applications of Acoustic Metamaterials: From Seismic to Radio Frequency*, volume 1, chapter Introduction to Multiple Scattering Theory, pages 143–182. John Wiley & Sons, New Jersey, 2019.

[158] L. Schwan, O. Umnova, C. Boutin, and J.P. Groby. Nonlocal boundary conditions for corrugated acoustic metasurface with strong near-field interactions. *Journal of Applied Physics*, 123(9):091712, 2018.

[159] M.R. Shepherd, P.A. Feurtado, and S.C. Conlon. Multi-objective optimization of acoustic black hole vibration absorbers. *The Journal of the Acoustical Society of America*, 140(3):EL227–EL230, 2016.

[160] M. Sigalas and E.N. Economou. Band structure of elastic waves in two dimensional systems. *Solid state communications*, 86(3):141–143, 1993.

[161] M.M. Sigalas and E.N. Economou. Elastic and acoustic wave band structure. *Journal of Sound Vibration*, 158:377–382, 1992.

[162] M.M. Sigalas and E.N. Economou. Elastic waves in plates with periodically placed inclusions. *Journal of Applied Physics*, 75(6):2845–2850, 1994.

[163] E.A. Skelton, R.V. Craster, A. Colombi, and D.J. Colquitt. The multi-physics metawedge: graded arrays on fluid-loaded elastic plates and the mechanical analogues of rainbow trapping and mode conversion. *New J. Phys.*, 20(053017), 2018.

[164] D.R. Smith, W.J. Padilla, D.C. Vier, S.C. Nemat-Nasser, and S. Schultz. Composite medium with simultaneously negative permeability and permittivity. *Physical review letters*, 84(18):4184, 2000.

[165] D.R. Smith, D.C. Vier, N. Kroll, and S. Schultz. Direct calculation of permeability and permittivity for a left-handed metamaterial. *Applied Physics Letters*, 77(14):2246–2248, 2000.

[166] M.J.A. Smith, R.C. McPhedran, C.G. Poulton, and M.H. Meylan. Negative refraction and dispersion phenomena in platonic clusters. *Waves in Random and Complex Media*, 22(4):435–458, 2012.

[167] J.C. Snowdon. Vibration of cantilever beams to which dynamic absorbers are attached. *The Journal of the Acoustical Society of America*, 39(5A):878–886, 1966.

[168] J.C. Snowdon. Dynamic vibration absorbers that have increased effectiveness. *Journal of Engineering for Industry*, 96(3):940–945, 1974.

[169] J.Q. Sun, M.R. Jolly, and M.A. Norris. Passive, adaptive and active tuned vibration absorbers – a survey. *J. Mech. Design*, 117(B):234–242, 1995.

[170] L. Tang and L. Cheng. Enhanced acoustic black hole effect in beams with a modified thickness profile and extended platform. *Journal of Sound and Vibration*, 391:116–126, 2017.

[171] L. Tang, L. Cheng, H. Ji, and J. Qiu. Characterization of acoustic black hole effect using a one-dimensional fully-coupled and wavelet-decomposed semi-analytical model. *Journal of Sound and Vibration*, 374:172–184, 2016.

[172] T.L. Teng and N.K. Hu. Analysis of damping characteristics for viscoelastic laminated beams. *Comput. Method Appl. M.*, 190(29-30):3881–3892, 2001.

[173] American Society For Testing and Materials. *Standard test method for measuring vibration-damping properties of materials*. ASTM International, 2010.

[174] G. Theocharis, O. Richoux, V. Romero-García, A. Merkel, and V. Tournat. Limits of slow sound propagation and transparency in lossy, locally resonant periodic structures. *New J. Phys.*, 16(9):093017, 2014.

[175] S.P. Timoshenko and S. Woinowsky-Krieger. *Theory of plates and shells*. McGraw-hill, 1959.

[176] G. Trainiti, J.J. Rimoli, and M. Ruzzene. Wave propagation in periodically undulated beams and plates. *International Journal of Solids and Structures*, 75:260–276, 2015.

[177] V. Twersky. Elementary function representations of schlömilch series. *Archive for Rational Mechanics and Analysis*, 8(1):323–332, 1961.

[178] E.E. Ungar. Loss factors of viscoelastically damped beam structures. *The Journal of the Acoustical Society of America*, 34(8):1082–1089, 1962.

[179] E.E. Ungar and Edward M. Kerwin Jr. Plate damping due to thickness deformations in attached viscoelastic layers. *The Journal of the Acoustical Society of America*, 36(2):386–392, 1964.

[180] J.O. Vasseur, P.A. Deymier, B. Djafari-Rouhani, Y. Pennec, and A.C. Hladky-Hennion. Absolute forbidden bands and waveguiding in two-dimensional phononic crystal plates. *Physical Review B*, 77(8):085415, 2008.

[181] C. Vemula, A.N. Norris, and G.D. Cody. Attenuation of waves in plates and bars using a graded impedance interface at edges. *Journal of Sound and Vibration*, 196(1):107–127, 1996.

[182] V.G. Veselago. The electrodynamics of substances with simultaneously negative values of ϵ and μ. *Physics-Uspekhi*, 10(4):509–514, 1968.

[183] T.T. W., Z.-G. Huang, T.C. Tsai, and T.C. Wu. Evidence of complete band gap and resonances in a plate with periodic stubbed surface. *Applied Physics Letters*, 93(11):111902, 2008.

[184] Y.F. Wang, Y.S. Wang, and X.X. Su. Large bandgaps of two-dimensional phononic crystals with cross-like holes. *Journal of Applied Physics*, 110(11):113520, 2011.

[185] Z. Wang and A.N. Norris. Waves in cylindrical shells with circumferential submembers: a matrix approach. *Journal of Sound and Vibration*, 181(3):463, 1995.

[186] T. Wassereau, F. Ablitzer, C. Pézerat, and J.L. Guyader. Experimental identification of flexural and shear complex moduli by inverting the timoshenko beam problem. *Journal of Sound and Vibration*, 399:86–103, 2017.

[187] P. Wei, C. Croënne, S. Tak Chu, and J. Li. Symmetrical and anti-symmetrical coherent perfect absorption for acoustic waves. *Appl. Phys. Lett.*, 104(12):121902, 2014.

[188] P. Wei, C. Croënne, Sai T.C., and Jensen Li. Symmetrical and anti-symmetrical coherent perfect absorption for acoustic waves. *Applied Physics Letters*, 104(12):121902, 2014.

[189] T. Weisser, J.P. Groby, O. Dazel, F. Gaultier, E. Deckers, S. Futatsugi, and L. Monteiro. Acoustic behavior of a rigidly backed poroelastic layer with periodic resonant inclusions by a multiple scattering approach. *The Journal of the Acoustical Society of America*, 139(2):617–629, 2016.

[190] J. Wen, G. Wang, D. Yu, H. Zhao, and Y. Liu. Theoretical and experimental investigation of flexural wave propagation in straight beams with periodic structures: Application to a vibration isolation structure. *Journal of Applied Physics*, 97(11):114907, 2005.

[191] J.M. Whitney and C.T. Sun. A higher order theory for extensional motion of laminated composites. *Journal of Sound and Vibration*, 30(1):85–97, 1973.

[192] M.L. Williams, R.F. Landel, and J.D. Ferry. The temperature dependence of relaxation mechanisms in amorphous polymers and other glass-forming liquids. *Journal of the American Chemical society*, 77(14):3701–3707, 1955.

[193] J.L. Wojtowicki, L. Jaouen, and R. Panneton. New approach for the measurement of damping properties of materials using the oberst beam. *Review of scientific instruments*, 75(8):2569–2574, 2004.

[194] S.Y. Wu. Method for multiple mode piezoelectric shunting with single pzt transducer for vibration control. *Journal of intelligent material systems and structures*, 9(12):991–998, 1998.

[195] W. Xiao, G.W. Zeng, and Y.S. Cheng. Flexural vibration band gaps in a thin plate containing a periodic array of hemmed discs. *Applied Acoustics*, 69(3):255–261, 2008.

[196] Y. Xiao, J. Wen, L. Huang, and X. Wen. Analysis and experimental realization of locally resonant phononic plates carrying a periodic array of beam-like resonators. *Journal of Physics D: Applied Physics*, 47(4):045307, 2013.

[197] Y. Xiao, J. Wen, and X. Wen. Flexural wave band gaps in locally resonant thin plates with periodically attached spring–mass resonators. *Journal of Physics D: Applied Physics*, 45(19):195401, 2012.

[198] Y. Xiao, J. Wen, and X. Yu, D.and Wen. Flexural wave propagation in beams with periodically attached vibration absorbers: band-gap behavior and band formation mechanisms. *Journal of Sound and Vibration*, 332(4):867–893, 2013.

[199] Y. Xu, Y. Li, R.K. Lee, and A. Yariv. Scattering-theory analysis of waveguide-resonator coupling. *Phys. Rev. E*, 62(5):7389, 2000.

[200] E. Yablonovitch. Inhibited spontaneous emission in solid-state physics and electronics. *Physical review letters*, 58(20):2059, 1987.

[201] S. Yan, A.M. Lomonosov, and Z. Shen. Numerical and experimental study of lamb wave propagation in a two-dimensional acoustic black hole. *Journal of Applied Physics*, 119(21):214902, 2016.

[202] S.L. Yan, A.M. Lomonosov, and Z.H. Shen. Evaluation of an acoustic black hole's structural characteristics using laser-generated lamb waves. *Laser Physics Letters*, 13(2):025003, 2016.

[203] B. Yang, S. W. Nunez, T.E. Welch, and J.R. Schwaegler. Laminate dash ford taurus noise and vibration performance. Technical report, SAE Technical Paper, 2001.

[204] M. Yang, C. Meng, C. Fu, Y. Li, Z. Yang, and P. Sheng. Subwavelength total acoustic absorption with degenerate resonators. *Appl. Phys. Lett.*, 107(10):104104, 2015.

[205] A. Yariv. Universal relations for coupling of optical power between microresonators and dielectric waveguides. *Electron. Lett.*, 36(4):321–322, 2000.

[206] L. Zhao and F. Semperlotti. Embedded acoustic black holes for semi-passive broadband vibration attenuation in thin-walled structures. *Journal of Sound and Vibration*, 388:42–52, 2017.

[207] L. Zhou, T.and Tang, H. Ji, J. Qiu, and L. Cheng. Dynamic and static properties of double-layered compound acoustic black hole structures. *International Journal of Applied Mechanics*, 9(05):1750074, 2017.

[208] T. Zhou and L. Cheng. A resonant beam damper tailored with acoustic black hole features for broadband vibration reduction. *Journal of Sound and Vibration*, 430:174–184, 2018.

[209] H. Zhu and F. Semperlotti. Improving the performance of structure-embedded acoustic lenses via gradient-index local inhomogeneities. *International Journal of Smart and Nano Materials*, 6(1):1–13, 2015.

[210] H. Zhu and F. Semperlotti. Two-dimensional structure-embedded acoustic lenses based on periodic acoustic black holes. *Journal of Applied Physics*, 122(6):065104, 2017.

Titre : Contrôle des ondes de flexion au moyen d'absorbeurs parfaits sub-longueur d'onde : application au Trou Noir Acoustique

Mots-clés : contrôle passif d'onde, onde de flexion, métamatériau, structure localement résonante, absorption parfaite, couplage critique, trou noir acoustique

Résumé : Le contrôle des vibrations à basse fréquence adapté aux structures légères est un défi scientifique et technologique en raison de contraintes économiques et écologiques de plus en plus strictes. De récentes études en acoustique ont portées sur l'absorption totale d'ondes basses fréquences à l'aide d'absorbeurs parfaits sub-longueurs d'onde. Ces métamatériaux sont obtenus en exploitant la condition de couplage critique. Une généralisation de cette méthode pour le domaine élastodynamique serait d'un grand intérêt pour répondre aux exigences du contrôle des vibrations de structures légères à basse fréquence.

Cette thèse vise à adapter le problème d'absorption parfaite des ondes de flexion dans des systèmes 1D et 2D avec des résonateurs locaux en utilisant la condition de couplage critique. Une étude préliminaire sur des systèmes 1D à géométries simples sont d'abord proposée. Celle-ci propose une méthode de conception de résonateurs simples pour une absorption efficace des ondes de flexion. Une complexification du système 1D est ensuite considérée avec l'étude du couplage critique de Trou Noir Acoustique (TNA) 1D. Ceci a motivé l'interprétation de l'effet TNA à l'aide du concept de couplage critique afin de présenter des outils clés à de futures procédures d'optimisation pour ce type de terminaisons. La condition de couplage critique est ensuite étendue aux systèmes 2D. L'absorption parfaite par le premier mode axisymétrique d'un résonateur circulaire inséré dans une plaque mince infinie est analysée. La diffusion multiple par une ligne de résonateurs circulaires insérés dans une plaque mince 2D infinie ou semi-infinie, appelée métaplaque, est aussi considérée dans l'optique de se rapprocher d'une application industrielle. A travers cette thèse, des modèles analytiques, des simulations numériques et des expériences sont présentés pour valider le comportement physique des systèmes présentés.

Title: Controlling flexural waves using subwavelength perfect absorbers: application to Acoustic Black Holes

Keywords: Passive wave control, flexural waves, metamaterials, locally resonant structures, perfect absorption, critical coupling, acoustic Black hole

Abstract: The vibration control adapted to light structures is a scientific and technological challenge due to increasingly stringent economic and ecological standards. Meanwhile, recent studies in audible acoustics have focused on broadband wave absorption at low frequencies by means of subwavelength perfect absorbers. Such metamaterials can totally absorb the energy of an incident wave. The generalisation of this method for applications in elastodynamics could be of great interest for the vibration control of light structures.

This thesis aims at adapting the perfect absorption problem for flexural waves in 1D and 2D systems with local resonators using the critical coupling condition. A study of 1D systems with simple geometries is first proposed. This provides methods to design simple resonators for an effective absorption of flexural waves. The 1D systems then become more complex by studying the critical coupling of 1D Acoustic Black Holes (ABH). The ABH effect is then interpreted using the concept of critical coupling, and key features for future optimisation procedures of ABHs are presented. The critical coupling condition is then extended to 2D systems. The perfect absorption by the first axisymmetric mode of a circular resonator inserted in a thin plate is analysed. Multiple scattering by an array of circular resonators inserted in an infinite or semi-infinite 2D thin plate, called metaplate, is also considered to get close to practical applications. Through this thesis, analytical models, numerical simulations and experiments are shown to validate the physical behaviour of the systems presented.